Université Fédérale
Toulouse Midi-Pyrénées

THÈSE

En vue de l'obtention du

DOCTORAT DE L'UNIVERSITÉ DE TOULOUSE

Délivré par :

Université Toulouse 3 Paul Sabatier (UT3 Paul Sabatier)

Cotutelle internationale avec "Anadolu University"

Présentée et soutenue par :
Yasemin CELIK

le jeudi 26 février 2015

Titre :

PRODUCTION OF GRAPHENE BASED MATERIALS AND THEIR POTENTIAL APPLICATIONS

École doctorale et discipline ou spécialité :
ED SDM : Sciences et génie des matériaux - CO034

Unité de recherche :
CIRIMAT Institut Carnot

Directeur/trice(s) de Thèse :

Dr. Emmanuel FLAHAUT
Prof. Dr. Ender SUVACI

Jury :
Dr. Alain PENICAUD, Université de Bordeaux : Rapporteur
Prof. Dr. Servet TURAN, Anadolu University : Examinateur
Prof. Dr. Burhanettin CICEK, Ankara University : Examinateur
Dr. Emmanuel FLAHAUT, Université de Toulouse : Directeur de thèse
Prof. Dr. Ender SUVACI, Anadolu University : Directeur de thèse

PRODUCTION OF GRAPHENE BASED MATERIALS AND THEIR POTENTIAL APPLICATIONS

Yasemin CELIK
PhD Thesis

Joint Supervision of Thesis (Cotutelle) between Anadolu University, Turkey and Université Toulouse III Paul Sabatier, France
Ceramic Engineering/Materials Science and Engineering
February–2015

This thesis study has been financially supported by Anadolu University Scientific Research Projects Commission under the project numbers 1101F005 and 1110F155.

To my husband Ali,

My parents Ayşe & Orhan, and

My brother Ahmet Yılmaz

ABSTRACT

PhD Dissertation

PRODUCTION OF GRAPHENE BASED MATERIALS AND THEIR POTENTIAL APPLICATIONS

Yasemin CELIK

Joint Supervision of Thesis (Cotutelle) between Anadolu University and Université Toulouse III Paul Sabatier
Ceramic Engineering/Materials Science and Engineering

Supervisors: Prof. Dr. Ender SUVACI, Dr. Emmanuel FLAHAUT
2015, 214 pages

Graphene is a promising material for many applications due to its unique properties. However, properties and yield of graphene-based materials show variations depending on which production route is used. Therefore, an appropriate production method has to be preferred according to the requirements of a specific application. In this thesis study, graphene-based materials have been successfully produced by liquid phase exfoliation (LPE) and chemical vapor deposition (CVD), which are promising graphene production methods in terms of quality, scalability, cost and applicability of the produced material to relevant applications, and a fundamental understanding on graphene production has been developed.

LPE route allows one to produce graphene-based materials at a large-scale for applications such as nanocomposites. The challenge of this method is to increase graphene concentration as much as possible while maintaining the quality of the graphene flakes. Therefore, a comparative study, at which three different graphite-based powders were investigated as starting materials for an effective exfoliation process in isopropyl alcohol (IPA), was performed. High concentration (~1.1 mg/ml), few-layer (<5 layers) graphene-based dispersions were prepared by sonication in IPA within 90 min by utilizing a high surface area graphite nano-powder. This graphene-based material was then incorporated into Al_2O_3 matrix nanocomposites as a reinforcing/filler phase. Ceramic matrix nanocomposites which exhibit anisotropic mechanical, thermal and electrical properties have been successfully prepared by spark plasma sintering.

On the other hand, large-area graphene films, which are promising for electronic applications, were synthesized via low-pressure CVD method over Cu-foils. The influence of ramping atmosphere and Cu foil characteristics on the impurity level, quality of the synthesized graphene films and their thickness uniformity was investigated. High quality CVD-grown graphene films with a significantly reduced disorder level were used for device fabrication and characterized in terms of their electrical resistance at room temperature as a function of gate voltage and transport property measurements in Quantum Hall Effect (QHE) regime (at low temperature and high magnetic field) by pulsed magnetic field experiments. The preliminary results confirmed that single layer graphene with a relatively high electronic mobility reaching up to ~46500 cm^2/Vs at room temperature was successfully produced.

Keywords: Liquid phase exfoliation, chemical vapor deposition, nanocomposites, electronic applications

RÉSUMÉ

Thèse de Doctorat

SYNTHÈSE DE MATÉRIAUX À BASE DE GRAPHÈNE ET LEURS APPLICATIONS POTENTIELLES

Yasemin CELIK

Université Toulouse III Paul Sabatier Cotutelle Internationale avec Anadolu University
Génie des Céramique/Sciences et Génie des Matériaux

Directeurs: Prof. Dr. Ender SUVACI, Dr. Emmanuel FLAHAUT
2015, 214 pages

Le graphène est un matériau prometteur pour de nombreuses applications du fait de ses propriétés exceptionnelles. Cependant, à la fois les propriétés et les rendements des graphènes et dérivés sont très variables et dépendants de la méthode de production utilisée. De ce fait, la méthode de production doit être développée en accord avec les besoins liés à l'application visée. Dans cette thèse, différents nanomatériaux dérivés du graphène ont été préparés en employant deux méthodes différentes, l'exfoliation en milieu liquide et la synthèse directe par dépôt chimique catalytique en phase vapeur (CVD), et une compréhension fondamentale sur la production de graphène a été acquise. Ces deux méthodes sont prometteuses en termes de qualité, de possibilité de production à grande échelle, de cout de production et enfin d'applications des différents "graphènes" obtenus.

D'une part, l'exfoliation en milieu liquide permet de produire des dérivés du graphène tels que le few-layer graphene (FLG (<5 feuillets)) à relativement grande échelle, pour des applications telles que les nanocomposites. Le défi principal consiste à augmenter la concentration en FLG autant que possible, tout en conservant une bonne qualité. De ce fait, une étude comparative de l'exfoliation dans l'alcool isopropylique de 3 poudres de graphite différentes a été entreprise. Des suspensions de FLG de concentration élevée (~1,1 mg/ml) ont été obtenues en partant de poudre de graphite de surface spécifique élevée, par sonication dans l'alcool isopropylique (cuve, 90 min). Ces nanoparticules ont ensuite été incorporées dans des nanocomposites à matrice alumine. Ainsi, nous avons préparé par frittage SPS des nanocomposites à matrice céramique possédant des propriétés mécaniques, thermiques et électriques anisotropes.

D'autre part, des films de graphène alliant une grande surface, prometteurs pour des applications dans le domaine de l'électronique, ont été synthétisés par CVD basse pression sur des feuilles de Cu. L'influence de l'atmosphère pendant le traitement thermique et la nature du catalyseur sur le niveau d'impuretés, la qualité des films de graphène synthétisés et leur uniformité en termes de nombre de feuillets a été étudiée. Des films de graphène CVD de haute qualité (très peu de désordre de structure) ont été utilisés pour la réalisation de dispositifs. Ces derniers ont été caractérisés à température ambiante en mesurant leur résistance électrique en fonction de la tension grille ainsi que par des mesures de transport en régime d'effet Hall quantique (basse température et forts champs magnétiques - pulsés). Les résultats préliminaires obtenus confirment que du graphène mono-feuillet possédant une bonne mobilité électronique atteignant jusqu'à 46500 cm^2/Vs à température ambiante a pu être synthétisé avec succès.

Mots-clés: Graphène, exfoliation en milieu liquide, dépôt chimique catalytique en phase vapeur, nanocomposites, applications électroniques

ÖZET

Doktora Tezi

GRAFEN ESASLI MALZEMELERİN ÜRETİMİ VE POTANSİYEL UYGULAMALARI

Yasemin ÇELİK

Anadolu Üniversitesi ile Toulouse III Paul Sabatier Üniversitesi arasında Çift Diploma Doktora Programı
Seramik Mühendisliği/Malzeme Bilimi ve Mühendisliği

Danışmanlar: Prof. Dr. Ender SUVACI, Dr. Emmanuel FLAHAUT
2015, 214 sayfa

Grafen benzersiz özellikleri sayesinde pek çok uygulama alanı için umut vadeden bir malzemedir. Bununla birlikte, grafen-esaslı malzemelerin özellikleri ve miktarı hangi üretim yöntemi ile üretildiğine bağlı olarak farklılık gösterir. Bu nedenle, grafen-esaslı malzemelerin, kullanılacağı uygulama alanının gereksinimlerine bağlı olarak uygun bir üretim yöntemi ile üretilmesi gerekmektedir. Bu tez çalışmasında, grafen esaslı malzemeler kalite, verim, maliyet ve elde edilen malzemenin uygulanabilirliği açılarından en avantajlı yöntemler olan sıvı faz eksfoliasyonu (tabakalara ayırma) ve kimyasal buharla biriktirme yöntemleri kullanılarak başarıyla üretilmiş ve grafen üretimi üzerine temel bir anlayış kazanılmıştır.

Sıvı faz eksfoliasyonu, nanokompozit uygulamaları için yüksek miktarda grafen-esaslı malzeme üretimine imkan sağlamaktadır. Bu yöntemde aşılması gereken sorun, kaliteyi koruyarak grafen konsantrasyonunu mümkün olduğunca artırabilmektir. Bu amaçla, izopropil alkol (IPA) içerisinde etkin bir eksfoliasyon elde edebilmek için üç farklı grafit-esaslı tozun başlangıç malzemesi olarak kullanıldığı karşılaştırmalı bir çalışma gerçekleştirilmiştir. Yüksek konsantrasyona sahip (~1.1 mg/ml), birkaç tabakalı (<5 tabaka) grafen levhalardan oluşan dispersiyonlar, yüksek yüzey alanına sahip bir nano-grafit tozunun IPA içerisinde 90 dk sonikasyon işlemine maruz bırakılması ile üretilmiştir. Bu malzeme daha sonra Al_2O_3 matris nanokompozitlerde takviye faz olarak kullanılmış; sonuç olarak, anizotropik mekanik, ısıl ve elektriksel özellik gösteren seramik matris nanokompozitler spark plazma sinterleme yöntemi ile başarıyla üretilmiştir.

Diğer taraftan, elektronik uygulamalar için gelecek vadeden, geniş alana sahip grafen filmler düşük-basınç kimyasal buharla biriktirme yöntemi ile Cu folyolar üzerinde sentezlenmiştir. Isıtma atmosferinin ve Cu folyo özelliklerinin sentezlenen grafen filmlerin kalitesi, kalınlığı ve safsızlık miktarı üzerine olan etkileri incelenmiştir. Hata oranı önemli ölçüde azaltılmış kaliteli grafen filmleri aygıt üretiminde kullanılmıştır. Bu aygıtların oda sıcaklığındaki elektriksel direnç ve Quantum Hall Etkisi rejimindeki (düşük sıcaklık ve yüksek manyetik alan) taşınım özellikleri ölçülmüştür. Ön sonuçlar, oda sıcaklığında yüksek elektronik hareketliliğe sahip (~46500 cm^2/Vs) tek tabakalı grafenin başarıyla üretildiğini göstermiştir.

Anahtar Kelimeler: Sıvı faz eksfoliasyonu, kimyasal buharla biriktirme, nanokompozitler, elektronik uygulamalar

ACKNOWLEDGEMENTS

I would like to express my sincere gratitude to my supervisor Prof. Dr. Ender Suvaci for his supervision, encouragement, support and advice. I am also thankful to him for believing in me.

I am also grateful to my supervisor Dr. Emmanuel Flahaut for his supervision, support and help, as well as for introducing me to many valuable scientists and collaborators, who are experts in their field.

I would like to extend my gratitude to Dr. Walter Escoffier (from LNCMP-T, Toulouse) for device fabrication, pulsed magnetic field experiments and invaluable discussions on the results. I also would like to thank Lucien Datas for HRTEM analyses which were performed at 'service commun TEMSCAN', UPS.

I am also thankful to my jury members Prof. Dr. Servet Turan, Prof. Dr. Burhanettin Cicek and Dr. Alain Penicaud for their valuable time and suggestions.

I also thank Dr. Pascal Puech (CEMES, Toulouse) for discussions on Raman analyses, Dr. Daniel Monceau and his PhD student Aurelien Fabas (CIRIMAT ENSIACET, Toulouse) for assistance in the usage of HSC Chemistry Software, Prof. Dr. R. Mustafa Oksuzoglu and his research group (Anadolu University) for assistance in sheet resistance measurements of thin films, Prof. Dr. Mujdat Caglar and his PhD student Serif Ruzgar (Anadolu University) for their help in electrical resistance measurements of nanocomposites, Mustafa Cobanli from Ceramic Research Center for TGA analyses and C_p measurements, and Seyfi Yamak (Anadolu University) for providing maintenance for the devices in the lab.

I would like to thank all my research group members (past and present) for their encouragement and help, as well as for their friendship.

I am grateful to my husband Dr. Ali Celik, who is also a colleague of mine, for his endless support, patience and love, and for his invaluable contributions to nanocomposite studies, SEM analyses and helpful discussions. I am also eternally grateful to my parents, Ayse and Orhan Bozkaya, and my brother Ahmet Yilmaz Bozkaya for their endless support, encouragement and help throughout my life.

I also gratefully acknowledge the financial support from Anadolu University Scientific Research Projects Commission under the project numbers 1101F005 and 1110F155.

TABLE OF CONTENTS

Page

LIST OF FIGURES

LIST OF TABLES

LIST OF ABBREVIATIONS

(C)CVD	:	(Catalytic) chemical vapor deposition
(HR)TEM	:	High resolution transmission electron microscopy
0D	:	Zero-dimensional
1D	:	One-dimensional
3D	:	Three-dimensional
Ar	:	Argon
BSE	:	Back-scattered electron
C_2H_2	:	Acetylene
CH_4	:	Methane
CMOS	:	Complementary metal-oxide-semiconductor
CNP	:	Charge neutrality point
CNT(s)	:	Carbon nanotube(s)
Cu	:	Copper
DI	:	De-ionized
DLS	:	Dynamic light scattering
EDM	:	Electro discharge machining
EDX	:	Energy dispersive x-ray spectroscopy
EG	:	Expanded graphite
ELS	:	Electrophoretic light scattering
FEG-SEM	:	Field emission gun – scanning electron microscopy
FFT(s)	:	Fast Fourier transform(s)
FWHM	:	Full width at half maximum
GNP(s)	:	Graphite nanoplatelet(s)
GNS(s)	:	Graphite nanosheet(s)
GO	:	Graphene oxide
GPL(s)	:	Graphene platelet(s)
H_2	:	Hydrogen
HIP	:	Hot isostatic press
HOPG	:	Highly oriented pyrolytic graphite
IPA	:	Isopropyl alcohol
LPE	:	Liquid phase exfoliation
MFC	:	Mass flow controller

MLG	:	Multilayer graphene
MWNTs	:	Multi-wall carbon nanotubes
Ni	:	Nickel
NMP	:	N-methyl-2-pyrrolidone
OLEDs	:	Organic light emitting diodes (OLEDs)
PA	:	Primary artificial (nano-graphite powder)
PMMA	:	Poly methyl methacrylate
QHE	:	Quantum Hall Effect
RD	:	Relative density
r-GO	:	Reduced graphene oxide
SE	:	Secondary electron
SEFG	:	Surface enhanced flake graphite
SENB	:	Single edge notch beam
SPS	:	Spark plasma sintering
SWNTs	:	Single-wall carbon nanotubes
TGA	:	Thermo-gravimetric analysis
TIM	:	Thermal interface material
TS	:	Tip sonication
XRD	:	X-ray diffractometer
y_0	:	Partial amount of non-sedimenting stable phase
A_1	:	Partial amount of sedimenting phase 1
A_2	:	Partial amount of sedimenting phase 2
τ_1	:	Time constant for first sedimenting phase
τ_2	:	Time constant for second sedimenting phase
σ_{el}	:	Electrical conductivity
$R_{(s)}$	:	Resistance. Subscript refers to sheet resistance.
t	:	Thickness of the film
C	:	Concentration (mg/ml)
A	:	Absorbance
α'	:	Absorption coefficient
l	:	Cell length
D	:	Diameter of the film
ρ	:	Density (2.2 g/cm^3 for graphene)
V	:	Volume of dispersion

$D_{Moiré}$	:	Periodicity of Moiré pattern
d	:	Lattice constant (0.246 nm for HOPG)
θ	:	Rotation angle between two layers of hexagonal lattice
I_D/I_G	:	Intensity ratio of the D-band to that of the G-band
I_{2D}/I_G	:	Intensity ratio of the 2D-band to that of the G-band
σ_f	:	Flexural strength. Subscript *c* refers to nanocomposite.
HV	:	Vickers hardness
K_{IC}	:	Fracture toughness. Subscript *m* and *c* refer to monolithic material and nanocomposite, respectively.
P	:	Indentation load
a	:	Length of indentation half diagonal
c	:	Average crack length measured at the tips of crack trace
E	:	Elastic modulus
ρ_{el}	:	Electrical resistivity. Subscript *m* and *c* refer to monolithic material and nanocomposite, respectively.
S	:	Cross-sectional area
σ_0		A parameter depending on the electrical conductivity of the filler material
t_c	:	Critical exponent
ϕ	:	Volume fraction of filler
ϕ_c	:	Critical volume fraction of filler (percolation threshold)
k	:	Thermal conductivity
C_p	:	Specific heat
α	:	Thermal diffusivity
$k_{in\text{-}plane}/k_{through\text{-}thickness}$	:	In-plane to through-thickness thermal conductivity ratio
B1	:	Batch-1
B2	:	Batch-2
V_g	:	Gate voltage
R_{xy}	:	Hall resistance
μ	:	Field effect mobility
n_0	:	Residual carrier density at charge neutrality point

1. INTRODUCTION AND STATEMENT OF THE PROBLEM

Carbon, the building block of life on Earth, is a unique element, the atoms of which can form up to four directional covalent bonds with other atoms leading to formation of extraordinary materials. Diamond and graphite are well-known three-dimensional allotropes of carbon; while fullerene and carbon nanotube are the zero- and one-dimensional forms of it, respectively. The discovery of fullerene molecules in 1985 by Kroto et al. [1] and afterwards carbon nanotubes in 1991 by Iijima [2] were breakthroughs in the field of nanotechnology which stimulated both fundamental research and potential applications on carbon nanomaterials. Two-dimensional form of carbon, so-called 'graphene', was first fabricated and isolated in 2004 by Novoselov et al. [3] using mechanical exfoliation method, and its unique electrical properties were successfully revealed. Until that date, 2D materials were thought as thermodynamically unstable, according to theoretical calculations [4, 5]. Although in 1962, Boehm et al. [6] reported that they obtained extremely thin carbon foils by reduction of graphite oxide, there were experimental difficulties in isolating and identifying single layer pristine graphene. The isolation and successfully characterization of graphene by Novoselov et al. [3] has paved the way for not only exploring the outstanding properties of graphene but also for development of other two-dimensional materials [7]. Graphene is a single atom-thick plane of carbon atoms arranged in a two-dimensional honeycomb lattice. In spite of having an atomic thickness, it is the strongest (thermodynamically stable) material ever known [8]. It is an excellent electrical conductor, which shows room temperature ballistic transport [9] and has an extremely high intrinsic thermal conductivity at room temperature, which is among the highest of any known materials for sufficiently large, suspended flakes [10]. Due to these unique properties, graphene is a promising material for many applications such as field effect transistors, transparent electrodes, sensors, energy storage systems and composites. However, production of high quality graphene-based materials at industrial scale is a prerequisite for making the potential applications of graphene real. There are numerous methods being used for graphene production; however, the number of layers, lateral size,

quality and the yield of graphene-based materials show variations depending on which production route is used. Therefore, an appropriate graphene production method should be preferred according to the requirements of a specific application.

Graphene is commonly produced by either bottom-up techniques, such as chemical vapor deposition (CVD) on metal substrates [11] and epitaxial growth on SiC [12] or by top-down approaches where graphene sheets are isolated from graphite by mechanical exfoliation using Scotch tape [3], chemical exfoliation methods, such as graphite oxide [13] and liquid phase exfoliation [14] routes. Among these methods, mechanical exfoliation gives the highest-quality graphene when the best-quality graphite is used; however, this method has extremely low yield; therefore, it can only be used for fundamental research. Bottom-up techniques, especially CVD, enable one to produce large area, planar graphene films with relatively low defect density and are well-suited for flexible transparent electrodes and electronic applications where the growth can be patterned precisely in combination with lithographical methods. However, the CVD-synthesized graphene film is mostly transferred from the grown substrate onto arbitrary (dielectric) substrates for further applications. The mobility of the CVD-synthesized graphene is limited by disorders, defects and impurities originating from both the synthesis process and the transfer technique. Therefore, it is required to enhance the transport properties of CVD graphene while growing it uniformly at a large-area. On the other hand, chemical exfoliation methods, e.g., liquid phase exfoliation (LPE) of graphite, are promising for large-scale production of graphene-based materials (lower quality compared to CVD-graphene) at low cost for applications where accurate positioning of the layers is not required, such as composite materials, conductive inks and energy storage. However, obtaining high quality few-layer (<5 layers) graphene materials in a large scale and with a reasonable lateral size is the main challenge of LPE routes.

Although the CVD and the LPE routes are the most promising graphene production methods in terms of quality, scalability, cost and the applicability of the produced material to relevant applications, the current challenges of these

methods have to be overcome in order to make the potential applications of graphene real. Therefore, the research objectives of this thesis are:

i. To gain a fundamental understanding of two basic graphene production routes: liquid phase exfoliation, which is a top-down technique and chemical vapor deposition, which is a bottom-up technique.
ii. To determine the critical parameters of these techniques, influencing the quality, number of layers, lateral size, uniformity and the scalability of graphene-based materials.
iii. To produce graphene-based materials with required properties (by taking into account the determined critical parameters) for specific applications such as nanocomposites and electronic devices using the appropriate graphene production method, and to show the applicability of the produced graphene materials in these applications.

In the framework of these objectives, this thesis has been organized in two main parts and is divided into 7 Chapters:

(1) Production of graphene-based materials by LPE method, characterization and application to ceramic matrix nanocomposites.

Chapter 2 gives a general overview of properties, production methods, characterization and potential applications of graphene. **Chapter 3** presents the challenges in LPE methods and reports a comparative study at which three different graphite-based powders are investigated as starting materials for an effective exfoliation process in a low boiling point solvent. A detailed characterization of the produced graphene-based materials in terms of their stability and concentration in dispersions, number of layers, lateral size and quality are reported, and the graphene-based material which shows a more promising combination of quality and quantity is determined. **In Chapter 4**, incorporation of this selected graphene-based material into Al_2O_3 matrix nanocomposites as a reinforcing/filler phase is discussed. The effect of this reinforcing/filler material on mechanical, electrical and thermal properties of the nanocomposites is discussed by taking into account the anisotropy and proposing relevant mechanisms for each material property.

(2) Synthesis of graphene by CVD method, characterization, optimization of the process conditions and application to electronic devices.

Chapter 5 details the experiments of graphene synthesis via low-pressure CVD method and discusses the influence of catalyst material type (Cu foil) and impurities originating from catalyst material on quality, number of layers and uniformity of graphene films. Effects of ramping atmosphere and catalyst pre-cleaning on amount and type of impurities are reported. Optimization of transfer of the synthesized graphene from Cu foil onto dielectric substrates is also discussed. **Chapter 6** reports device fabrication from the CVD-grown graphene samples synthesized in Chapter 5 and electrical characterization of these devices to reveal the mobility of the CVD-graphene samples. Resistance measurements of the devices at room temperature as a function of back gate voltage and transport property measurements in Quantum Hall Effect (QHE) regime (at low temperature and high magnetic field) by pulsed magnetic field experiments are discussed in this Chapter. **Chapter 7** gives an overview of the general conclusions of this thesis study and a viewpoint of future work.

Chapters 3-6 start with a literature review of the corresponding part followed by experimental procedure, results and discussion, and conclusion sections in order.

At the scope of the Joint Supervision of Thesis, the experiments of graphene production by LPE and CVD methods and the characterization of the produced graphene-based materials, as well as nanocomposite production and characterization were performed in Anadolu University, Eskisehir, Turkey. For the CVD experiments and the characterization of the graphene-based materials, a laboratory including CVD equipment and Raman-AFM combined system was established in Anadolu University, Department of Materials Science and Engineering with the financial support supplied by Anadolu University Scientific Research Projects Commission under the Project number of 1110F155. Transmission electron microscopy (TEM) and high resolution TEM analyses were performed in Université Paul Sabatier, Toulouse, France with the help of Lucien Datas and Pierre Lonchambon at service commun TEMSCAN. Device fabrication

from the CVD-grown graphene samples were performed in AIME (Center for Micro-Nano Electronics) and LAAS (Laboratory for Analysis and Architecture of Systems) in Toulouse. Room temperature resistance and high field magneto-transport measurements of the prepared devices were conducted in Laboratoire National des Champs Magnétiques Intenses (LNCMI-Toulouse) in collaboration with Dr. Walter Escoffier, LNCMI, Toulouse, France.

2. GRAPHENE BACKGROUND

2.1. Properties of Graphene

Graphene, a single atom-thick plane of carbon atoms, is the basic building block for graphitic materials of all other dimensionalities (i.e., zero-dimensional (0D) fullerenes, one-dimensional (1D) nanotubes and three-dimensional (3D) graphite) [9]. The length of the C-C bonds in a planar graphene sheet is 0.1421 nm and the interlayer distance is 0.34 nm for layer numbers ≥2. The unique properties of graphene arise from its hexagonal lattice, in which sp^2 hybridized carbon atoms are arranged in a honeycomb network. The four valence electrons of graphene are distributed in the 2s and 2p orbitals. The s, p_x and p_y orbitals hybridize to form three planar orbitals with bond angles of 120° with respect to each other, leading to σ-bonds which are responsible for the strong in-plane covalent bonds within the graphene sheet (Fig. 2.1). Graphene owes its outstanding mechanical properties to these σ-bonds. The remaining p_z orbital is perpendicular to this planar plane and form π-bonds, which are responsible for weak van der Waals interactions between graphene sheets and for unusual electronic properties of graphene (Fig. 2.1). Each carbon atom contributes with one electron to the π-band resulting in a half filled system.

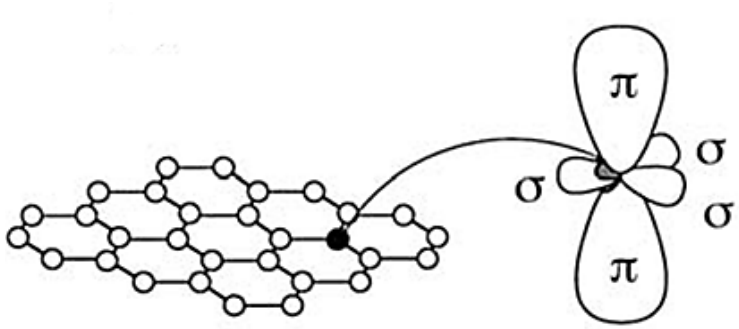

Figure 2.1. Illustration of the valence orbitals. It shows three in-plane σ bonds/atom and π-bonds perpendicular to the plane [15].

The unit cell of graphene contains two identical carbon atoms (A and B) (Fig. 2.2(a)). Therefore, the energy spectrum of graphene comprises of a filled π-band (lower energy valence band) and an empty π^*-band (higher energy conduction band). The conduction band touches the valence band at the corners of the corresponding Brillouin zone (the primitive unit cell in reciprocal space) (Fig. 2.2(b)). These points are known as Dirac points (K and K' points), which indicate the Fermi level. The energy spectrum of graphene is defined by six double cones near the Dirac points, where energy dispersion is linear (Fig. 2.2(c)). As a consequence of this linear dispersion, charge carriers in graphene behave like massless Dirac fermions [16, 17].

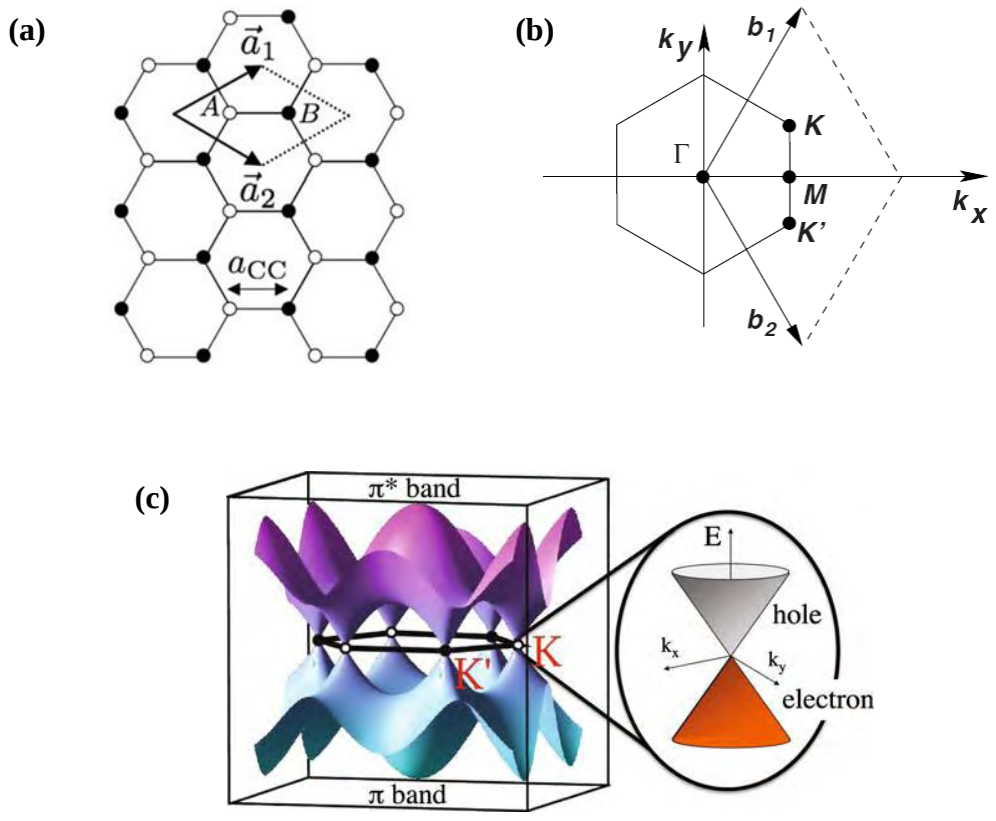

Figure 2.2. (a) The hexagonal lattice of graphene [15], **(b)** The corresponding Brillouin zone [17] and **(c)** Electronic band structure of single layer graphene [15].

Since graphene does not have an energy band-gap, and density of states at the Fermi level is zero, it exhibits a semi-metal character and is referred to as zero-gap semiconductor. The band structure of graphene is the basis of its unique electronic properties. It shows room-temperature ambipolar characteristics, i.e., charge carriers can be tuned between holes and electrons depending on the nature of the gate voltage [3, 9]. The mobility of charge carriers in suspended graphene is very high, so that indicating ballistic transport [9]. Recently measured electron mobility for graphene reaches up to ~150 000 $cm^2V^{-1}s^{-1}$ for carrier concentrations of ~10^{11} cm^{-2} [18], which is comparable to the calculated theoretical value of 200 000 $cm^2V^{-1}s^{-1}$ [19]. This mobility value is much larger than that of any other material and is promising for electronic applications such as high-speed transistors and integrated circuits. It should be noted that these exceptional properties usually belong to pristine graphene measured under idealized conditions. However, under realistic conditions, the mobility is strongly affected by impurities and structural defects which cause scattering of charge carriers [20]. Another consequence of massless Dirac fermions is the unusual Quantum Hall Effect (QHE) observed in graphene at large magnetic fields [16, 21] indicating the graphene's extreme electronic quality [9]. Graphene also exhibits a superior intrinsic thermal conductivity (~5000 $W.m^{-1}.K^{-1}$) at room temperature in suspended form, that is higher than that of any known material [10]. The measurements for supported graphene on SiO_2/Si revealed a thermal conductivity of ~600 $W.m^{-1}.K^{-1}$ at room temperature [22]. This value is below the one reported for suspended graphene, but it still exceeds the thermal conductivity of Si (~145 $W.m^{-1}.K^{-1}$) and Cu (~400 $W.m^{-1}.K^{-1}$) at room temperature [23]. Graphene has optical transparency of ~97.7%. The opacity increases with number of layers (each graphene layer adds another 2.3% absorption of incident white light) [24], and remarkable mechanical strength and flexibility with a Young's modulus of 1.0 TPa and intrinsic strength of 130 GPa [8] indicating that it is stronger than the strongest steel. Moreover, it exhibits a very high theoretical specific surface area of 2630 m^2/g [25].

Similar to single layer graphene, bilayer graphene is also a zero-gap semiconductor. However, bilayer graphene has massive (parabolic) valence and conduction bands that touch at the charge neutrality point [26, 27]. For number of

layers of >3, the valence and the conduction bands start overlapping and the electronic structure of graphene approaches to limit of three-dimensional graphite at 10 layers [9, 28].

2.2. Bandgap Formation in Graphene

Si-based technology is approaching its limits in terms of miniaturization; therefore alternative technologies beyond complementary metal-oxide-semiconductor (CMOS) technology are investigated [29]. Carbon-based materials such as carbon nanotubes and graphene are promising candidates for future electronic applications, at which they might be replaced with Si. However, the lack of a bandgap in single layer graphene limits its use in electronic devices due to low on/off switching ratios.

A band gap can be created in graphene when the equivalence of the A and B sublattices is broken. A possible way to produce this effect is to choose a specific substrate that generates an electrostatic potential that is different in different sub-lattices. So that the sub-lattice symmetry is broken and a gap opens in the spectrum [29]. Another approach to bandgap creation is to make graphene nanoribbons [30], which are elongated strips of graphene with a finite width (about <10nm) and expected to have a bandgap that scales inversely with width. Graphene nanoribbons can be fabricated via lithographical patterning [31], chemical routes [32] and unzipping carbon nanotubes [33]. Chemical modification of graphene also offers a promising route for bandgap engineering, with advantage of being scalable and inexpensive [26]. Graphene shows a semiconductor behavior when it is chemically reacted with hydrogen atoms. Hydrogenation causes formation of sp^3 C-H functionality on the basal plane of graphene [34]. This material is called as graphane, which exhibits a semiconductor character with a bandgap of 3.5 eV and is stable at room temperature [35]. Graphane can be reverted to graphene by thermally desorbing bound hydrogen atoms [34].

Despite being a zero-gap semiconductor similar to single layer graphene, a bandgap is opened when an electric field is applied perpendicular to bilayer graphene and this bandgap could be tuned with a controlled electric field [36].

2.3. Potential Applications of Graphene-based Materials

Graphene is an attractive material for a wide variety of application fields such as electronics, photonics, energy storage, sensors, composites, conductive inks, coatings and bio-applications [37].

Graphene is a good candidate for electronic applications such as high frequency transistors [38] due to its high carrier mobility, atomic thickness and stability; however, the absence of a bandgap limits its use as a digital switch where high on/off ratios are required [20]. Another promising application field of graphene is flexible electronics (transparent conductive coatings) such as touch screen displays and organic light emitting diodes (OLEDs), which require a low sheet resistance (<90 Ω/□) with high transmittance (>90%) [39]. Flexible electronics are expected to be one of the first commercial graphene products in the market [40].

The excellent heat-conduction properties of graphene are beneficial for all the proposed electronic devices for thermal dissipation. The transparent few-layer graphene electrodes can perform the additional function of removing heat and improving the efficiency of photovoltaic solar cells through the reduction of its temperature under illumination [23]. Similarly, few-layer graphene serving as interconnects in 3D electronics can simultaneously act as lateral heat spreaders [41]. The thermal conductivity enhancement of composites by addition of small volume fractions of liquid-phase exfoliated graphene is promising for thermal interface material (TIM) applications [23]. Polymer and ceramic matrix nanocomposites with multifunctional properties are promising and realistic applications of graphene due to combination of its unique electrical, thermal and mechanical properties, as well as its two-dimensional nature and high specific surface area.

Chemical and biological sensors are also promising applications of graphene. It has been shown that electrical properties of graphene changes when gas molecules from the surrounding environment are absorbed on the graphene surface resulting in doping of graphene with electrons or holes depending on the nature of the gas. Thus, certain gases in the environment can be detected very sensitively by measuring the changes in electrical resistivity of graphene [42].

Graphene is also widely investigated for energy storage applications such as supercapacitors and batteries. It has been studied as cathodes due to its high electrical conductivity [43] or as anodes to increase the battery charge capacity [44] in lithium ion batteries. Chemically modified graphene with a high specific surface area and good electrical conductivity has been shown to have a great potential for high-performance, electrochemical double-layer supercapacitors [45].

Since different applications require different grades of graphene-based materials [37], it is critical to use the correct material (in terms of quality, number of layers, lateral size, cost, scalability, etc.) for a specific application. While electronic applications require the highest quality graphene with low defects and large-area on dielectric substrates where graphene can be patterned via lithographical methods; lower grade, costly effective and scalable graphene-based materials produced by liquid phase exfoliation can find place in nanocomposites as a filler, conductive inks, transparent conductive films and energy storage applications (e.g., dye solar cells, capacitors and batteries). For optical applications, the presence of un-exfoliated graphitic particles and amorphous carbon result in scattering, and the purity of graphene is one of the primary concerns [46]. Thus, the choice of correct grade of graphene-based material and its production at large-scale accelerates the potential applications of graphene take their place in the commercial market.

2.4. Production of Graphene-based Materials

Graphene-based materials are commonly produced by either top-down approaches such as mechanical exfoliation and chemical exfoliation or bottom-up techniques such as epitaxial growth on SiC and chemical vapor deposition.

2.4.1. Mechanical Exfoliation

Novoselov et al. [3] successfully fabricated, isolated and characterized remarkably high quality a few atoms thick graphitic sheets including single-layer graphene, which are stable under ambient conditions, using mechanical

exfoliation method in 2004. This method is based on repeated peeling of commercially available 1 mm thick highly oriented pyrolytic graphite (HOPG) platelet using scotch tape. After repeated peeling process, the tape is stuck onto a substrate such as Si wafer with a SiO_2 layer (typically 300 nm) on top of it to transfer the exfoliated flakes from the tape onto the substrate. The graphene flakes on the SiO_2 surface with a certain thickness become visible in optical microscope due to added optical path that change the interference colors [3]. This method enables production of the highest quality graphene flakes (among the current graphene production methods) in an easy way; however, it has many challenges such as extremely low yield preventing its use for bulk applications, difficulties in identification and counting of graphene layers, and low yield of single layer graphene.

2.4.2. Chemical Exfoliation

Chemical exfoliation methods are promising for large-scale production of graphene-based materials. Graphite oxide route and liquid phase exfoliation are the most popular chemical exfoliation methods. These are cost effective routes since inexpensive graphite powders are utilized as starting materials. The graphene-based materials produced by these techniques can be directly incorporated into polymer or ceramic matrix nanocomposites, since these processes eliminate the need of using a substrate; consequently, there is no need for an additional transfer step [47].

Graphite oxide route enables production of graphene oxide (GO) and reduced-graphene oxide (r-GO) from graphite powders. This method is based on oxidation of graphite using oxidizing agents (acids) and exfoliating prepared graphite oxide into individual hydrophilic GO sheets in water or in an appropriate solvent via sonication. The oxidation process creates hydroxyl and carbonyl groups on the surface of graphene oxide providing electrostatic repulsion between graphene oxide sheets in solutions (Fig. 2.3(a)). Following the sonication, chemical or thermal reduction is applied to obtain conductive r-GO from insulating GO (Fig. 2.3(b)). The graphene-based material obtained by this method is also called as chemically modified graphene. Origin of this technique traces to

1859 when Brodie oxidized graphite using fuming nitric acid and potassium chlorate [48]. Then, Hummers and Offeman developed the well-known Hummers method at which sodium nitrate, potassium permanganate and sulfuric acid was used as oxidizing agents [49]. Over time, Hummers method has been improved so as to reduce the evolution of toxic gases and to increase the oxidation level, and referred to as modified Hummers method [50]. Despite its high yield and dispersibility in aqueous solutions, graphite oxide route has also some drawbacks such as residual oxygen functional groups remaining after reduction, and topological defects which deteriorate the electrical properties of r-GO in comparison to pristine graphene. The process also has the risk of explosion due to the chemicals used.

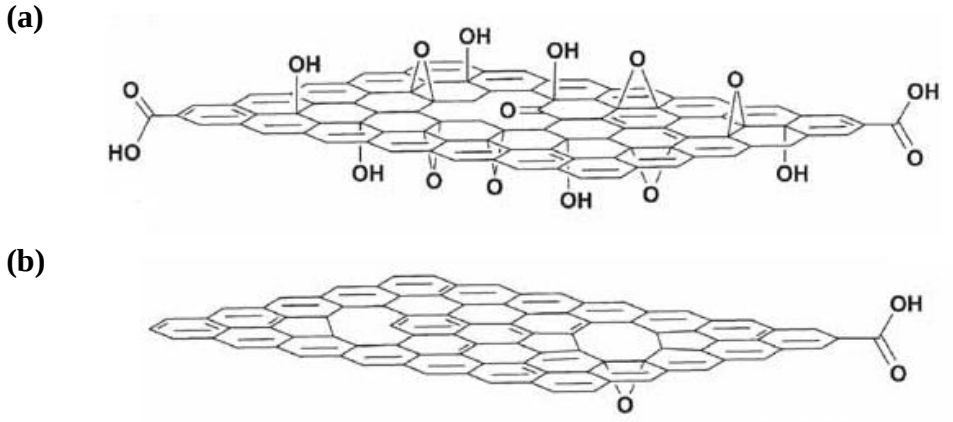

Figure 2.3. Structural models of **(a)** graphene oxide showing hydroxyl and carbonyl functionalities and **(b)** reduced-graphene oxide [51].

On the other hand, liquid phase exfoliation is based on direct exfoliation of graphite into single-, few (3-5 layers)- or multilayer (<10 layers)-graphene in organic solvents [14] or aqueous surfactant solutions [52] through ultrasonication followed by centrifugation to remove large, un-exfoliated flakes. Figure 2.4 shows a schematic representation of this process [53]. It is known that graphite can be exfoliated into high-quality graphene sheets (with <5 layers) in certain organic solvents such as 1-methyl-2-pyrrolidone (NMP) due to well matched surface energy between graphene and the solvent [14]. However, the high boiling point of NMP makes it difficult to be completely removed from the system. In contrast to

graphite oxide route, graphene samples prepared by liquid phase exfoliation are free from residual oxygen and they contain much lower structural defects. Therefore, this simple and cost-effective technique is one of the most promising methods for mass production of high quality graphene samples. The main drawbacks of this method are low graphene concentrations and relatively small lateral sizes (about several hundred nm) of graphene flakes due to cutting of initially large crystallites into smaller flakes as a result of sonication [54]. Prolonged sonication times (>400 h) were shown to increase graphene concentration [55]; however, this also leads to further decrease in size of graphene flakes and also not practical for industrial applications. Therefore, this method has to be further investigated to obtain high concentration graphene dispersions within short process times, preferably in low boiling point solvents. Detailed information about liquid phase exfoliation method is given in Chapter 3.

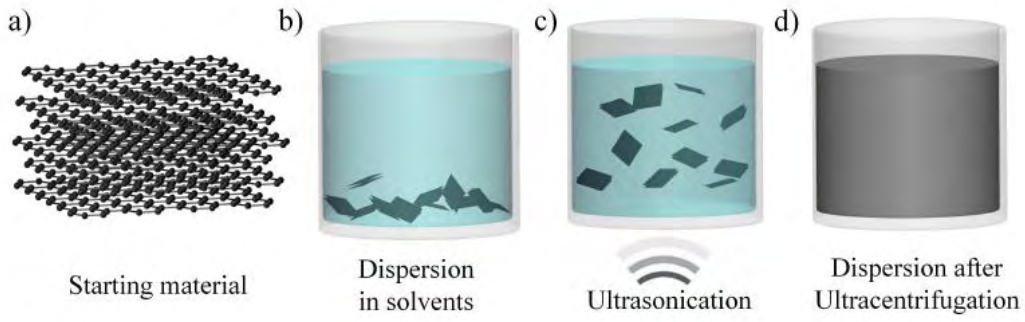

Figure 2.4. Schematic representation of liquid phase exfoliation process. **(a)** Starting material (graphite). **(b),(c)** Dispersion of graphite in an appropriate solvent by sonication, and **(d)** Final dispersion after centrifugation [53].

2.4.3. Epitaxial Growth on SiC

In epitaxial growth, graphene is directly grown on large area insulating or semiconducting substrates. After growth, the films are lithographically patterned and metal contacts are applied to make electronic devices [12]. SiC is currently the primary substrate for growing epitaxial graphene. The basic mechanism for growing epitaxial graphene on SiC is simply to heat the substrate (in ultra-high vacuum or inert atmosphere) to temperatures typically in the range of 1200°C to

1800°C. At these temperatures, Si atoms desorb from the surface and the remaining carbon atoms rearrange to form sheets of graphene [56]. SiC has two polar faces perpendicular to the c-axis, and morphology and electronic properties of epitaxial graphene depend on over which of the two polar faces they are grown (Fig. 2.5(a)) [12]. Although this method was first applied by Forbeaux et al. [57] in 1998, the transport measurements on ultrathin carbon films were reported for the first time by Berger et al. [58] in 2004. This technique enables direct growth of high quality graphene on a single crystal semiconductor; so that the grown material can be directly used in device fabrication without transferring it onto another substrate. However, this could be also a limitation, if the graphene sheets are desired to be transferred onto alternative substrates, e.g., for integration with CMOS technology. Another drawback of this method is its high cost due to requirement of a high quality substrate, high temperature and ultra-high vacuum conditions. Moreover, the steps and terraces present on the surface lead to non-uniformity in the number of layers, especially at the terrace edges (Fig. 2.5(b)) [59], deteriorating the electrical properties of the grown films; therefore the process needs to be optimized to control the thickness of the graphene sheets and to improve their quality.

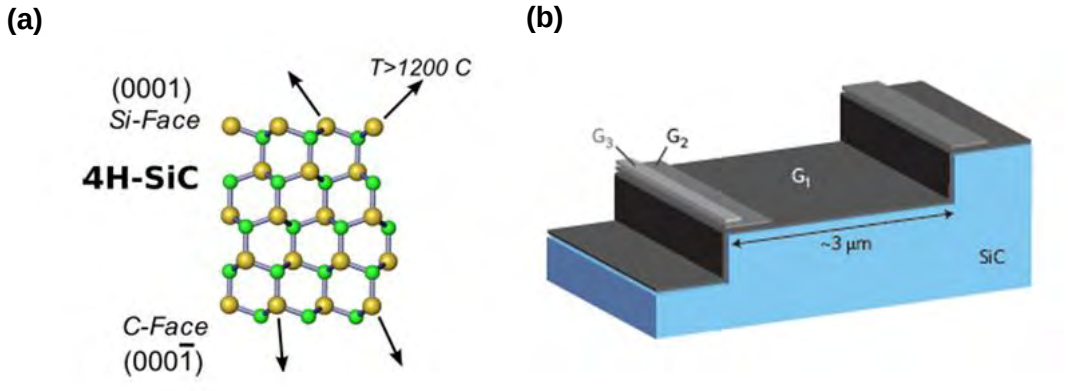

Figure 2.5. **(a)** At a typical growth temperature, few graphene layers are formed on the Si-terminated face (top), with substantially more on the C-terminated face (bottom) [56]. **(b)** Morphology of SiC obtained in high-pressure argon. The surface termination is predominantly monolayer graphene. Multilayer regions are present at the terrace edges [59].

2.4.4. Chemical Vapor Deposition

Chemical vapor deposition (CVD) is a promising method for graphene production since it has a capability of scalable and large-area synthesis of high quality graphene with low defects, good uniformity and controlled number of layers. In this method, a metal substrate is placed into a tube furnace, a hydrocarbon gas (such as methane (CH_4) or acetylene (C_2H_2)) that act as a carbon source is fed into the system at high temperatures (~900–1100°C) and graphene films is deposited on the metal substrate. Figure 2.6 shows a schematic representation of a typical tube-furnace CVD unit for graphene growth [60].

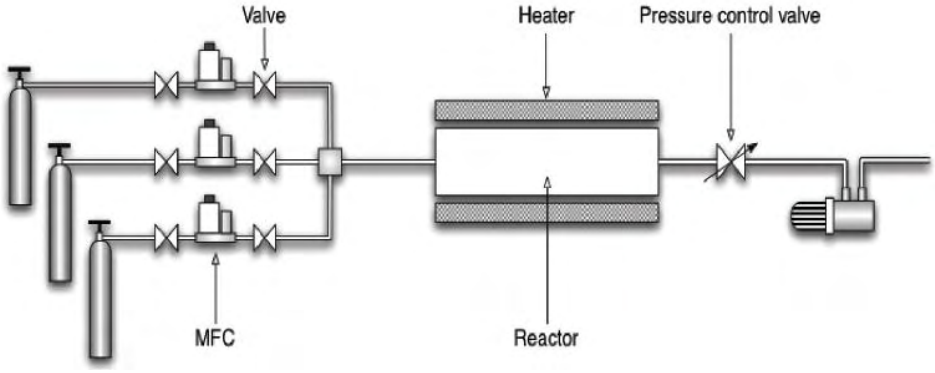

Figure 2.6. Schematic representation of a typical CVD unit. The system consists of a gas delivery system, a quartz reactor and a gas removal system. Reactive gases are fed into the reactor, where the chemical reactions take place and the solid films are deposited on substrates, by the gas delivery system composed of valves, mass flow controllers (MFC) and a gas mixing unit. The heaters, which provide high temperatures required for the reaction, are located around the reactor. The exhaust gases are removed from the system via vacuum pumps [60].

Following the graphene growth, metal substrate is removed and the graphene film is transferred onto another substrate of interest for further applications. Single crystal or polycrystalline transition metals are used as catalyst materials. Although single crystal transition metals [61-63] has shown to lead high quality graphene, using polycrystalline metal films or foils reduces production cost. Nickel (Ni) and copper (Cu) are the most widely used catalysts for graphene

growth due to their relatively low cost, finite carbon solubility and etchability. However, carbon solubility in Cu is much lower than that in Ni; therefore, Cu has shown to be a superior catalyst in terms of controlling the number of layers and more promising for growing single layer graphene. In 2009, Reina et al. [11] synthesized graphene films composed of mostly one or two layers by controlled carbon precipitation on the surface of polycrystalline Ni thin films during atmospheric CVD. Li et al. [64] demonstrated the growth of centimeter-scale graphene films on commercially available Cu foils by low pressure CVD of methane. It was observed that the films are predominantly single layer graphene, with a small percentage (< 5%) of the area having 2-3 layers, and are continuous across Cu surface steps and grain boundaries [64]. Bae et al. [40] have adapted this approach [64] to produce larger graphene sheets and synthesized graphene films on a roll of Cu foil with dimensions as large as 30 inches (76 cm) in the diagonal direction (Fig. 2.7). The size of graphene films that can be produced by CVD method is limited by size of the substrate used and size of the CVD chamber. Graphene growth on Cu foils has shown great promise for large-area, single layer graphene; however, it has also some challenges such as high growth temperatures. Moreover, the graphene films usually contain some disorders, defects and impurities arising from both growth and transfer steps. The impurities of Cu foils may act as seeds for graphene growth; therefore, affect not only the quality, but also the uniformity of graphene films. The transfer step may cause graphene film to be mechanically damaged (cracks can be formed) or contaminated due to use of polymers, solvents and acids. Therefore, both CVD and transfer processes have to be optimized for making CVD-grown graphene viable for industrial applications. Detailed information about this method is given in Chapter 5.

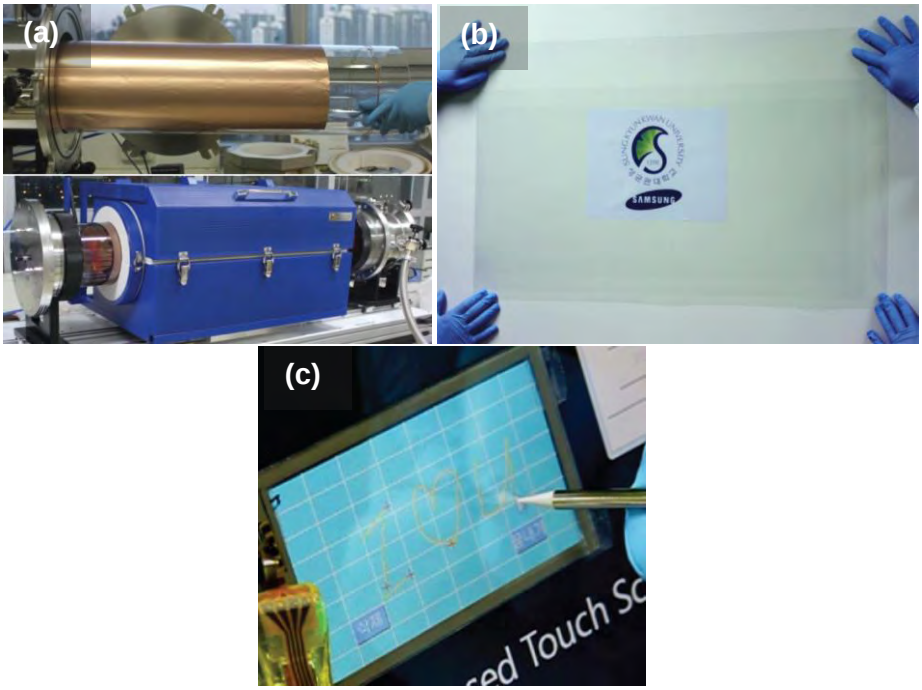

Figure 2.7. (a) Copper foil wrapping around a 7.5-inch quartz tube to be inserted into an 8-inch quartz reactor. The lower image shows the stage in which the copper foil reacts with CH_4 and H_2 gases at high temperatures, **(b)** A transparent ultra large-area graphene film transferred on a 35-inch PET sheet, **(c)** A graphene-based touch-screen panel connected to a computer with control software [40].

In conclusion, structure and properties of graphene-based materials are determined by the production methods and each potential application field of graphene has specific requirements of graphene characteristics. Therefore, it is critical to produce graphene-based materials using an appropriate method for a certain application where they can exhibit the maximum performance and enable bulk applications. Table 2.1 gives a comparison of widely used graphene production methods described above, in terms of their cost, throughput, quality, advantages and disadvantages. Among these methods, liquid phase exfoliation and CVD are the most promising methods for mass production of high quality graphene-based materials at a large-scale for the relevant applications, such as nanocomposites and electronic devices, respectively. These two graphene production methods were further investigated in this thesis study to overcome their current challenges and to obtain high quality graphene-based materials with a high yield for high performance applications.

Table 2.1. Comparison of widely used methods for graphene-based material production [37, 65, 66]

Method	Precursor	Quality	Throughput	Cost	Advantages	Challenges	Applications/Status of the technology
Mechanical Exfoliation	Graphite	Very high	Very low	High	Simple High quality	Extremely low yield Difficult to identify Monolayers are in minority	Fundamental research
Liquid-Phase Exfoliation	Graphite	High	High	Low	Simple Potentially scalable Non-oxidative	Low graphene concentration Small flake size Dispersibility in low boiling point solvents	Composites, conductive ink/paint, transparent conductive films, coatings, energy storage, bio-applications
Graphite oxide route	Graphite	Low	High	Low	No special instrument High yield Dispersibility in aqueous solutions	Potentially explosive process Residual oxygen Significant number of defects	Composites, conductive ink/paint, transparent conductive films, coatings, energy storage, bio-applications
CVD	Hydrocarbons	High	Limited by chamber and substrate size	High	Large-area graphene production Compatible to chip fabrication	High growth temperature Need for transfer to arbitrary substrates Presence of disorders and impurities	Electronic devices, photonics, transparent conductive films, sensors
Epitaxial Growth on SiC	Single crystal SiC	High	Low	High	High quality graphene Direct growth on a semiconductor	High cost Low yield Thickness variations in graphene	Electronic devices

3. PRODUCTION OF FEW-LAYER GRAPHENE SHEETS BY LIQUID PHASE EXFOLIATION IN A LOW BOILING POINT SOLVENT

3.1. Introduction

Graphite is a readily available and the least expensive source for production of graphene-based materials (single layer, few-layer or multi-layer graphene sheets, graphene oxide, reduced-graphene oxide, etc.). The main challenge of graphene production from graphite is to overcome van der Walls forces which hold graphene sheets together [67]. Liquid phase exfoliation is a promising method to exfoliate graphite into thin flakes, dispersed as a colloidal suspension in a solvent with or without surfactant [68]. This process eliminates the need of using a substrate. Since there is no graphene transfer step, the produced graphene-based materials can be readily incorporated into other materials such as polymers or ceramics to form composites. The critical point in liquid phase exfoliation is to be able to increase graphene concentration as much as possible while maintaining the quality of the flakes.

The recent progress made on exfoliation of graphite powders into single- and few-layered graphene sheets in various liquids, including organic solvents, ionic liquids, and water/surfactant solutions has been reviewed by Du et al. [69] The qualities, yields and electrical properties of exfoliated graphene samples are also reviewed in this paper [69]. Zhong et al. [66] have recently reviewed wet chemical graphite exfoliation routes highlighting their progress and challenges in terms of graphene commercialization. There have been several attempts to produce graphene-based materials at a large-scale (Table 3.1). Exfoliation of graphite in aqueous solutions with aid of surfactants yielded graphene concentrations of mostly <1 mg/ml [52]. Concentration was further increased up to 15 mg/ml by continuous addition of surfactant throughout the sonication process [70]. However, using high amount of surfactants brings additional cost; moreover, most surfactants are insulators that should be removed from the system by an additional washing step for further applications [66].

Table 3.1. Comparison of different liquid phase exfoliation routes reported in the literature to prepare graphene-based materials.

Starting material	**Dispersing medium**	**Type and time of sonication**	**Graphene concentration (mg/ml)**	**Electrical conductivity (S/m)**	**Ref.**
Natural graphite	Nonionic surfactants	Bath/2-5 h	< 1	1160	[52]
Synthetic and natural graphite	Cationic, anionic, nonionic surfactants	Bath/continuous surfactant addition during sonication	15	-	[70]
Microcrystalline graphite	Chlorosulphonic acid	Spontaneous dissolution	2	110000 (8 μm thick film on Teflon)	[71]
Graphite powder (sieved natural graphite)	NMP	Bath/30 min	0.01	~ 5 (before annealing) 6500 (annealed)	[14]
Natural graphite	NMP	Bath/460 h	1.2	$1.8 \pm 0.1 \times 10^{4}$	[55]
Graphite powder	NMP	Tip/6 h	2	–	[72]
Graphite intercalation compound KC_8	NMP	Spontaneous dissolution / 24 h stirring to speed-up	0.7	$25\text{-}30 \times 10^{-4}$	[73]
Natural graphite	IPA	Bath/48 h (centrifugation at 500 rpm)	0.5	–	[74]
Graphite oxide* (chemically modified)	Water+KOH	Stirring at 35°C for 6 h	7	$6.87 \pm 0.07 \times 10^{2}$	[75]

* Chemically modified graphene produced by graphite oxide route was given for comparison.

Chlorosulphonic acid was also reported as a highly efficient solvent for graphene production with concentration values up to 2 mg/ml [71]; however, it is toxic, highly corrosive and reactive which prevents its use for further processing. Graphite can also be exfoliated into high-quality graphene sheets (with <5 layers) in 1-methyl-2-pyrrolidone (NMP) due to well matched surface energy between graphene and the solvent [14]. Therefore, it is one of the most widely preferred organic solvent for sonication assisted liquid-phase exfoliation of graphene from graphite. However, high boiling point (~204°C at 760 mm Hg) of NMP makes it difficult to be completely removed from the system and the residual solvent can be detrimental for composites. Moreover, this may cause problems during flake deposition onto a substrate, since agglomeration tends to occur during the slow solvent evaporation [74]. Hence, exfoliating graphite in a low boiling point solvent to give graphene-based dispersions with a concentration as high as possible would facilitate applicability of these materials into composites and deposition onto substrates. Initial studies of direct exfoliation of graphene in organic solvents resulted in graphene dispersions at very low concentrations of 0.01 mg/ml [14]. Khan et al. [55] showed that the concentration of graphene dispersed in NMP can be increased dramatically (up to 1.2 mg/ml) by sonicating at low power for very long times (~460 h). Recently, Khan et al. [72] increased graphene concentration up to 2 mg/ml by simply tip sonication of graphite for 6 h in N-methyl-2-pyrrolidone (NMP, C_5H_9NO), followed by centrifugation. The authors further increased graphene concentration up to 63 mg/ml at a yield of 19% (percentage of graphite exfoliated as few-layer graphene) by re-dispersing the exfoliated material after centrifugation [72]. Catheline et al. [73] reported that graphite intercalation compound KC_8 spontaneously dissolves in NMP, yielding solutions of negatively charged graphene layers with a concentration of 0.7 mg/ml after stirring overnight and centrifugation to remove insoluble material. O'Neill et al. [74] recently achieved graphene concentrations of up to 0.5 mg/ml in isopropanol (IPA), the boiling point of which is 82.5°C, by a low power sonication of graphite for 48 h followed by a centrifugation at 500 rpm, showing that it is possible to produce graphene dispersions with a relatively high concentration in low boiling point solvents. However, long process times make

the method impractical for realizing the potential applications. Therefore, this process needs to be improved so as to achieve a higher graphene concentration within a shorter time.

The choice of starting materials, as well as the use of an appropriate solvent, is critical for liquid phase exfoliation process. The most commonly used starting material for the production of graphene-based materials by liquid phase exfoliation is natural graphite powder. The number of studies which use expandable/expanded graphite and nano-graphite powders as precursors is limited [67, 73]. Kozhemyakina et al. [76] has recently published a comprehensive study at which they investigated the dispersibility of several types of graphite with different morphological and structural characteristics in two high boiling point organic solvents (including NMP) and one surfactant-water solution. The authors followed an uncommon way to prepare their dispersions. They stirred graphite in the corresponding solvent over a period of two-days. The carbon uptake of the graphite materials into solvents was determined by absorption measurements on the decanted part after leaving them for 1 day of sedimentation. It was observed that the dispersibility of graphite materials with small grain size is better than that of big grain sized graphite materials, and this depends not only on the nature of the graphite but also on the viscosity of the solvent used. The authors reported that some graphite grades such as natural amorphous or natural flake graphite with small grain size (up to ~40 μm), natural flake expanded graphite and synthetic graphite can be readily dispersed into the liquid phase [76].

The objective of this study was to investigate three different graphite materials (expandable graphite, nano-graphite powder derived from natural graphite and nano-graphite powder derived from synthetic graphite) as starting powders for liquid phase exfoliation in a low boiling point solvent (IPA) in order to produce good quality graphene-based materials at a large-scale within relatively short sonication times (<120 min). The prepared graphene-based dispersions were characterized and compared in terms of their concentration and stability, and number of layers, quality and electrical conductivity of the graphene-based materials.

3.2. Experimental Procedure

3.2.1. Starting materials

Three different graphite-based materials, expandable graphite, surface enhanced flake graphite (SEFG) and primary artificial (PA) were used as starting powders for the exfoliation studies. The expandable graphite (Expansion ratio: 307, Grade 3772), SEFG (Grade 3725) and PA (Grade TC307) were kindly provided by Asbury Carbons Inc. The SEFG, which was derived from natural flake graphite and the PA, which was derived from synthetic graphite are nano-graphite powders, the specific surface area of which are 175 and 350 m^2/g, respectively. These two powders were used as-received for further exfoliation studies, while expandable graphite was subjected to an abrupt heating in a preheated furnace at 900°C for 2 min to prepare expanded graphite (EG). Before thermal expansion, the expandable graphite was first dried in a vacuum oven at 60°C and 35 hPa, and then a small amount of dried powder was put at the bottom of an alumina crucible and placed in the furnace.

3.2.2. Exfoliation process

SEFG and PA powders were dispersed in isopropyl alcohol (IPA, Merck-Emsure) and also in 1-methyl-2-pyrrolidone (NMP, Merck-Emplura) at an initial concentration of 3 mg/ml by sonicating in an ultrasonic bath (Kudos, 100 W) for 10-120 min. The EG was dispersed in IPA at an initial concentration of 0.2 mg/ml by bath sonication (100 W) as well as using tip sonication (Cole Parmer, CP750, running at 250 W) in order to observe the effect of sonication power on the graphene concentration. Large graphitic flakes were removed from the dispersions of the SEFG and PA by a subsequent centrifugation at 500 rpm for 45 min unless otherwise stated. The dispersions prepared from the EG powder were centrifugated at 900 rpm for 45 min. After centrifugation, the top ~90% of the supernatant was removed by pipetting for further use. Prepared dispersions were denoted as ‘Precursor-Solvent-Sonication time’. This is valid for the dispersions which were prepared in ultrasonic bath and centrifuged at 500 rpm for 45 min. For

the tip sonicated samples, the abbreviation ‘TS’ was added at the end; likewise, for the samples centrifugated at 900 rpm for 45 min, the term of ‘900rpm’ was added at the end.

3.2.3. Characterization of the starting powders and the exfoliated materials

Thermo-gravimetric analysis (TGA) of expandable graphite was carried out to observe its expansion behavior using Netzsch STA 409 PG instrument in air up to 1000°C with a heating rate of 10°C/min. Phase analyses of the expandable and the expanded graphite samples were performed by X-ray diffractometer (XRD, Rigaku Rint 2200, Tokyo, Japan) with CuKα radiation.

Field emission gun-scanning electron microscopy (FEG-SEM) analyses of the precursor powders and the prepared graphene-based materials were performed using Zeiss Supra 50VP. FEG-SEM samples of the exfoliated materials were prepared by dropping some dispersion onto a Si substrate with an oxide layer thickness of 300 nm and subsequently drying in an oven. Lateral size distribution of exfoliated graphene/graphite flakes and zeta potential of dispersions were measured by dynamic light scattering (DLS) and electrophoretic light scattering (ELS), respectively, using Malvern Zetasizer Nano ZS system with a 633 nm laser.

The stability of the prepared graphene-based dispersions was investigated by observing their sedimentation behavior. The sedimentation study was performed by allowing the dispersions to sediment for 8 weeks and measuring the optical absorbance (at 660 nm) of the supernatant at 1-3 weeks of intervals.

UV-VIS absorbance spectra of the graphene-based dispersions and the pure solvents were recorded in 200-800 nm wavelength range using Varian Cary100Bio spectrometer with 1 cm cuvettes. The concentration of graphene remaining after centrifugation was determined by measuring the absorbance at 660 nm. The absorbance value was transformed into concentration using Lambert-Beer Law [77], Eqn. (3.1):

$$A = \alpha'.l.C \tag{3.1}$$

Accordingly, absorbance (A) of the suspension is proportional to the concentration (C), the cell length (l) and the absorption coefficient (α′), which was taken as 2460 ml mg^{-1} m^{-1} [14]. For comparison with the literature, 'α′' was also determined experimentally for one of the dispersions (SEFG-IPA-90m). For this purpose, large volume of dispersions (~350-400 ml) were prepared and filtered through a pre-weighted PVDF membrane by vacuum filtration using a Buchner Funnel. After filtration, the membranes were dried in an oven at ~80°C overnight. The dried membranes were weighed again and the mass of the graphitic material on the membrane was determined. Finally, the absorption coefficient (α) was determined using the Lambert-Beer Law. Accordingly, for the SEFG-IPA-90min dispersion 'α′' was calculated as ~2468 ml mg^{-1} m^{-1} (the average of three measurements). This value is almost the same of the one estimated by Hernandez et al. [14] as 2460 ml mg^{-1} m^{-1}, although the same group was later determined the 'α' as 3620 ml mg^{-1} m^{-1} for these type of systems [55].

Raman analysis and electrical characterization of the samples were performed on thin films with thicknesses of ~43-86 nm. Sheet resistance measurements were carried out by four-point probe technique using Lucas Labs Pro4 Resistivity System. The conductivity values of the thin films were calculated from the measured sheet resistances using Eqn. (3.2)

$$\sigma_{el} = R_s^{-1} t^{-1} \tag{3.2}$$

where σ_{el} is the electrical conductivity; R_s is the sheet resistance and t is the thickness of the film.

Micro-Raman analyses of the starting materials and the exfoliated samples were performed on a Renishaw Invia spectrometer using 532 nm laser (2.33 eV) excitation and 100x objective lens. The laser power was kept below 1 mW in order to prevent sample damage. 50 spectra were recorded (each one at a different location) for each sample to create statistical histogram of the I_D/I_G ratio.

Transmission Electron Microscopy (TEM) analyses (both low magnification and high resolution) were performed with a Jeol JEM 2100F at 'service commun TEMSCAN' in Université Paul-Sabatier. TEM samples were prepared by drop casting the graphene-based dispersions onto holey carbon coated copper grids

(200 mesh). In order to investigate the effect of high temperature annealing on the quality of graphene-based materials, one of the exfoliated samples (SEFG-IPA-90m) was annealed at 2600°C in Ar atmosphere for 4 h, and further characterized by Raman spectrometer and TEM.

3.2.3.1. Thin film preparation

Thin films were prepared by vacuum filtration of the graphene-based dispersions through porous alumina membranes (Whatman Anodisc 47 mm, 0.02 μm pore size). After vacuum filtration, the thin films prepared from IPA-based dispersions were dried in air at room temperature, while the thin films prepared from NMP-based dispersions were dried in vacuum oven at 25 hPa and 50°C for overnight. The thickness of the films was calculated using Eqn. (3.3):

$$\frac{\pi D^2}{4} t\rho = VC \tag{3.3}$$

where D is the diameter of the film (~ 4 cm); t is the thickness of the film; ρ is the density of graphene (taken as 2.2 g/cm^3); V is the volume of the dispersion and C is the concentration of graphene in dispersion (mg/ml) [78]. This equation was previously used by Yu et al. [78] for the calculation of the thickness of carbon nanotube films; here it was adapted for graphene-based films. Accordingly, it was found that the thickness values of the graphene-based thin films range from 43 to 86 nm depending on the volume and the concentration of the dispersions used. Figure 3.1 shows photos of an alumina membrane before and after vacuum filtration of the graphene-based dispersion.

Figure 3.1. Anodisc alumina membrane (47 mm diameter, with a polymer ring) (on the left). Graphene thin film with a thickness of ~55 nm over the alumina membrane (on the right) .

3.3. Results and Discussion

3.3.1. Exfoliation of expandable graphite

3.3.1.1. Preparation of expanded graphite from expandable graphite

Expandable graphite is a form of intercalated graphite, i.e., an intercalant material is inserted between the graphene layers of a graphite crystal. The expanded graphite material used in the present study is manufactured by treating highly crystalline natural flake graphite with a mixture of sulfuric acid and certain other oxidizing agents like potassium permanganate and/or nitric acid which aid in catalysis of the sulfate intercalation [79]. This type of intercalation is called 'sulfate' intercalation and the intercalation compound is sometimes referred to as 'graphite bisulfate'. The primary reason for bisulfate intercalation is to impart the ability of the treated flake graphite to exfoliate or expand when heated. Heating of the treated graphite causes the expansion agent to gasify. Gas formation results in an increase in volume of the intercalant of approximately 1000 fold. The pressure generated by this volume increase pushes adjacent graphene layers apart. As a result, crystallographic delamination occurs as parallel to the 'c' crystallographic axis of the graphite flake resulting in the accordion-like morphology [79]. This material is called-as expanded graphite (EG). FEG-SEM micrographs of the as received expandable graphite reveal the lamellar structure of the flakes with an average size of ~450 μm and a thickness of mostly <50 μm (Figs. 3.2(a) and (b)). There are also small amount of thicker flakes up to 180 μm in thickness.

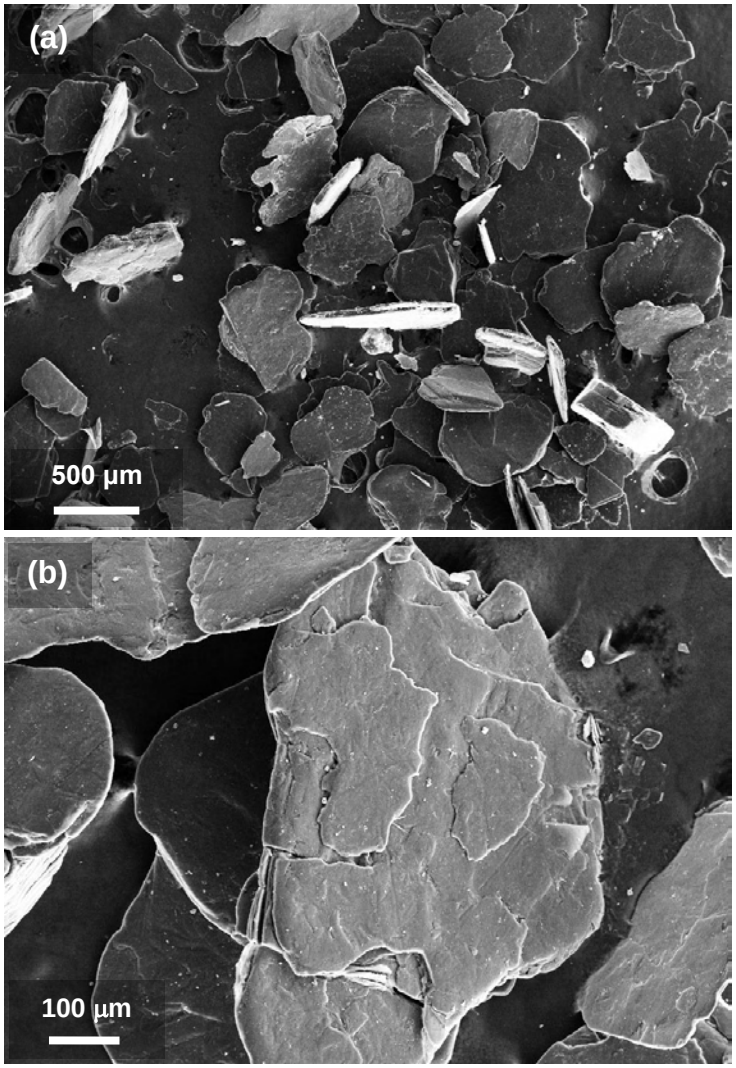

Figure 3.2. FEG-SEM micrographs of expandable graphite flakes. **(a)** The general view of the flakes. **(b)** A higher magnification image of a flake revealing its layered morphology.

Although the extent of thermal expansion depends on the type of graphite used and how the intercalation is carried out, expansion temperature and time also play a critical role on obtaining the optimum expansion degree. To be able to determine the expansion temperature, TGA analysis of the expandable graphite was performed. Figure 3.3 shows the thermal behavior of expandable graphite, which exhibits a two-step weight loss. The sample starts to degrade at ~170°C as in agreement with Chiang and Hsu [80] who reported that expandable graphite starts to decompose at 170-250°C. The great mass drop in the sample is mostly related to the release of gaseous intercalation species from the expandable

graphite interlayers due to decomposition of the intercalating acid. It was also reported that pristine graphite starts to lose weight at 650°C due to combustion to carbon dioxide [81], which explains the weight loss observed at ~600–1000°C. Accordingly, the expansion temperature was determined as 900°C and the degree of expansion was investigated depending on the expansion time by varying it from 10 s to 2 min.

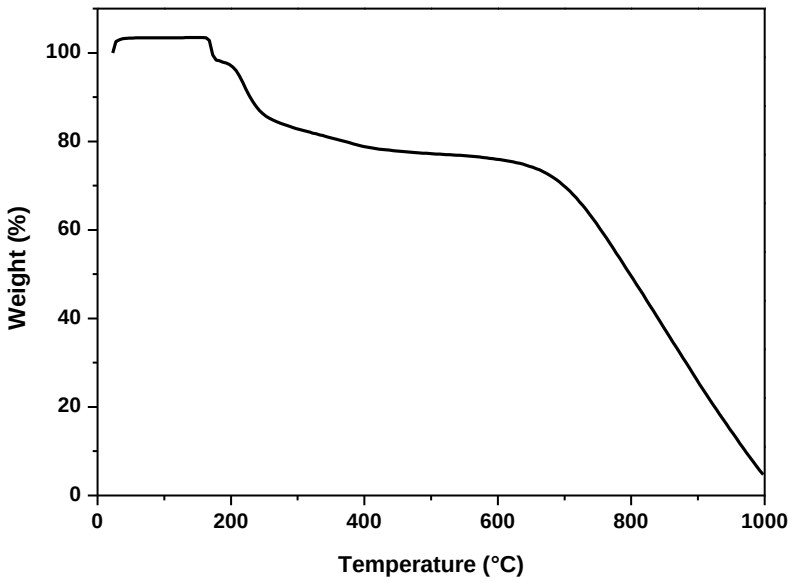

Figure 3.3. TGA plot of expandable graphite in air.

Abrupt heating of the expandable graphite at 900°C for 10 s did not lead to considerable volume increase due to remaining un-expanded flakes. When the expansion time increased to 1 min, a significant volume increase was observed. However, the highest volume increase, accompanied by the highest level of mass loss, occurred when the sample heated for 2 min.

XRD analysis was performed to investigate the expansion degree of EG samples depending on the expansion time. XRD patterns of expandable and EG samples are presented in Fig. 3.4. The expandable graphite exhibits peaks at 26.7° and 54.9° 2θ values corresponding to (002) and (004) basal planes of graphite layers, respectively (Fig. 3.4(a)). These peaks are not very narrow and symmetrical compared to natural flake graphite which shows a sharp, narrow and symmetrical peak with a d-spacing of 3.3539 Å, due to its high crystallinity [82].

The intercalation increases the interlayer spacing (c-axis) and may create crystal defects and decrease the crystallinity. The rapid thermal expansion of expandable graphite causes decomposition of intercalates which were trapped between graphite layers and to separate the graphite layers randomly due to generated pressure during heating. Therefore, the expansion process causes destruction of graphite crystal structure while increasing the volume and thickness in the c-direction enormously [83]. The XRD patterns of the EG samples reveal a significant decrease at the intensity of the diffraction peaks, although they did not disappear completely (Figs. 3.4(b), (c) and (d)). The presence of (002) peak in the XRD pattern shows that there are still some un-expanded graphite flakes in the sample. The inset shows obviously that the intensity of the (002) peak decreases as the expansion time increases from 10 seconds to 2 minutes. This result indicates that heating at 900°C for 2 minutes provides more efficient expansion.

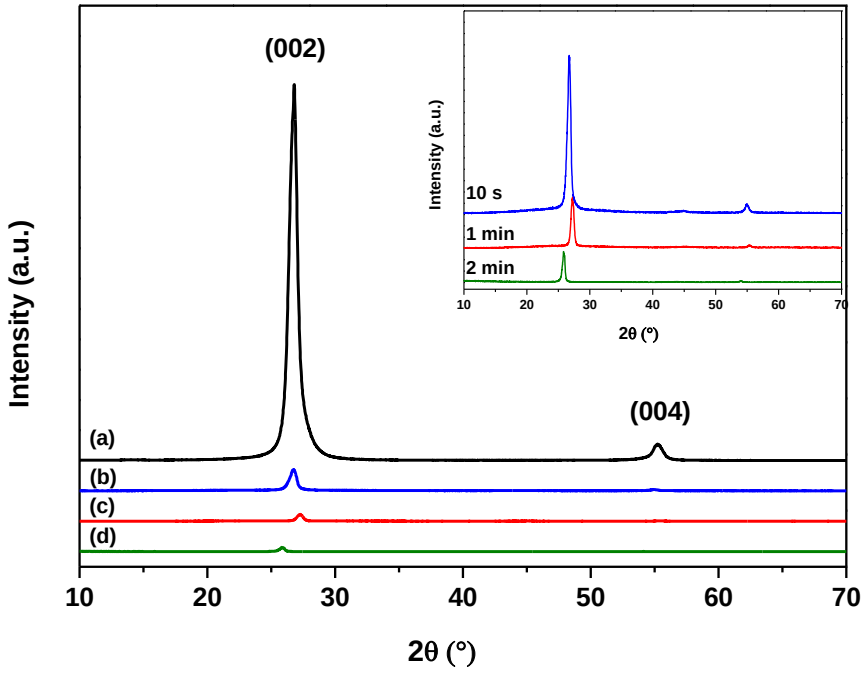

Figure 3.4. XRD patterns of **(a)** expandable graphite, and EG powders prepared by heating at 900°C for **(b)** 10 s, **(c)** 1 min and **(d)** 2 min. Inset reveals the difference between intensity of the (002) planes of expanded graphite powders more clearly.

Figure 3.5 shows the FEG-SEM micrographs of EG powders obtained by heating the expandable graphite at 900°C for 10 s, 1 min and 2 min. Although a characteristic loose and porous worm-like (vermicular) structure was achieved to some extent after exposing the expandable graphite to 900°C for 10 s, some of the graphite flakes remained un-expanded, as indicated by white arrows (Fig. 3.5(a)). The higher magnification image of the worm-like graphite revealed the formation of bubbles on the surface of layers indicating that the gas release arising from thermal decomposition of the intercalant could not be completed just after 10 s (Fig. 3.5(b)). This is not in agreement with Gu et al. [84] who carried out the expansion process successfully at 900°C for 10 s and obtained single layer and few-layer graphene sheets by liquid phase exfoliation using this powder. This could arise from the characteristics of the starting graphite powder such as particle size which affects the magnitude of the expansion ratio, and also from the type of intercalation. The SEM micrographs of EG heated at 900°C for 1 min reveal the vermicular structure with many large pores formed due to separation of graphite layers and attaching together at their edges in some parts by weak van der Waals forces (Figs. 3.5(c) and (d)). The pore size and pore shape of EG may give information about the degree of expansion. In comparison to expansion for 1 min, the EG exhibited smaller and less amount of pores when heated for 2 min (Figs. 3.5(e) and (f)), indicating a better expansion, as in agreement the XRD results. Therefore, the EG powder which was prepared by heating the expandable graphite at 900°C for 2 min was selected to be utilized for further exfoliation studies.

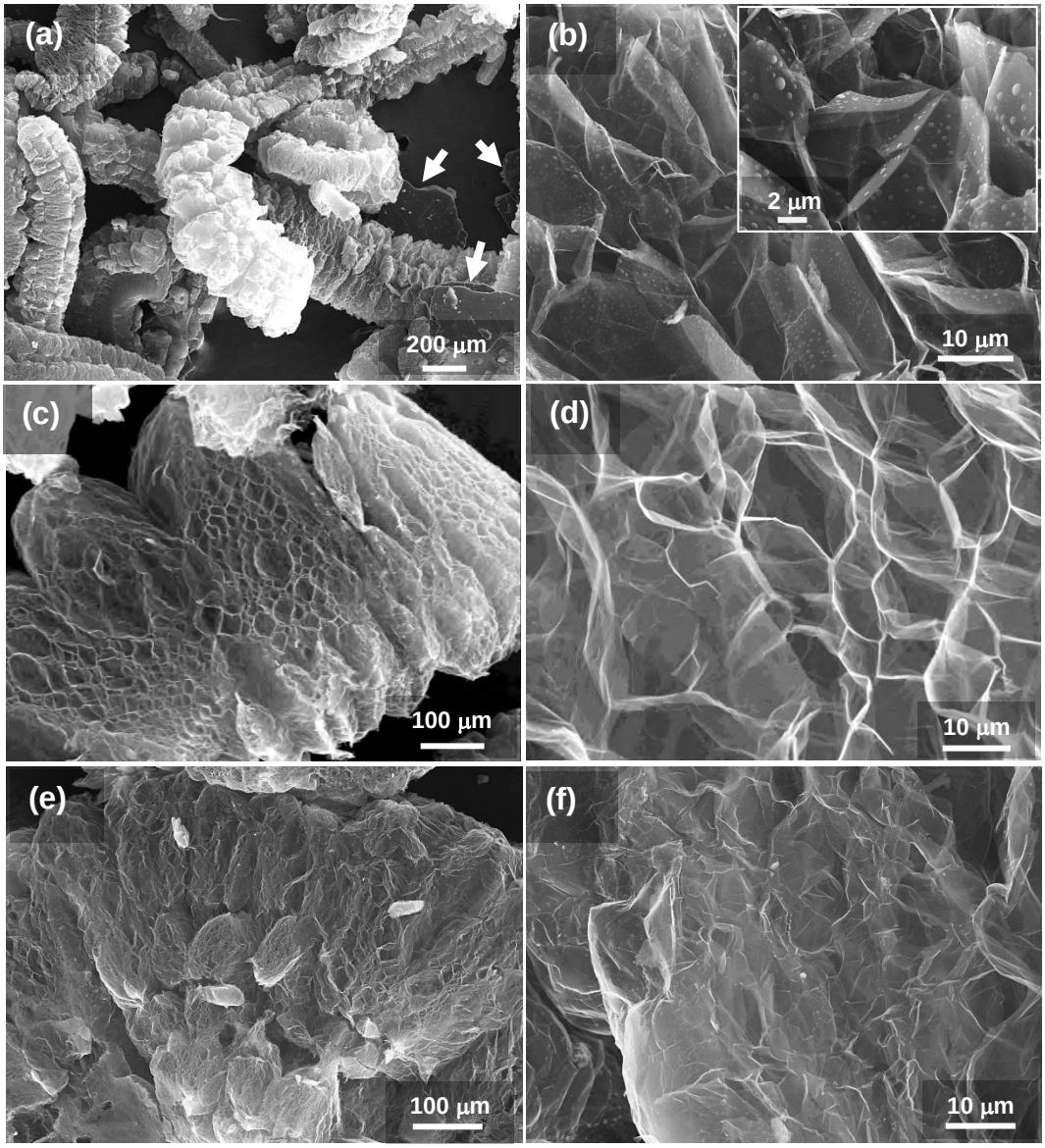

Figure 3.5. FEG-SEM micrographs of EG powders prepared by abrupt heating of expandable graphite at ~900°C for **(a), (b)** 10 s, **(c), (d)** 1min, and **(e), (f)** 2 min. Arrows in (a) indicate the un-expanded flakes. Inset in (b) shows a higher magnification image revealing the incomplete gas release after 10 s.

3.3.1.2. Exfoliation of expanded graphite (EG)

As explained in the previous section (3.3.1.1), the EG has a vermicular structure, at which graphene layers are separated each other to some extent such that still attaching together at some points by weak van der Waals forces. For a full separation of these graphene sheets, an external force such as sonication is required. The dispersibility of EG in IPA was examined using the relationship between the absorbance and the concentration (Lambert-Beer Law) [77]. Here, the dispersibility can be defined as the concentration of graphene-based material remaining after centrifugation [85]. Figure 3.6(a) shows UV-VIS absorption spectra of the pure IPA and the EG-IPA-90min and EG-IPA-TS-90min dispersions. The spectra of the dispersions are flat and featureless [14] except the peak at ~264 nm which is characteristic to graphene and can be attributed to the $\pi \rightarrow \pi^*$ transitions of aromatic C=C bonds [86]. The absorbance values at 660 nm were measured for the calculation of graphene concentrations. The concentration showed an increasing trend with increasing sonication time up to 90 min for both bath and tip sonication (Fig. 3.6(b)). 90 and 120 min sonication time led to similar concentration values in the case of bath sonication; while 120 min tip sonication resulted in a slightly higher concentration in comparison to 90 min. Although tip sonication provided a higher concentration than that of sonic bath (e.g., 0.06 and 0.04 mg/ml for tip and bath sonication for 120 min, respectively), these values are much below the requirements for the large-scale production of graphene.

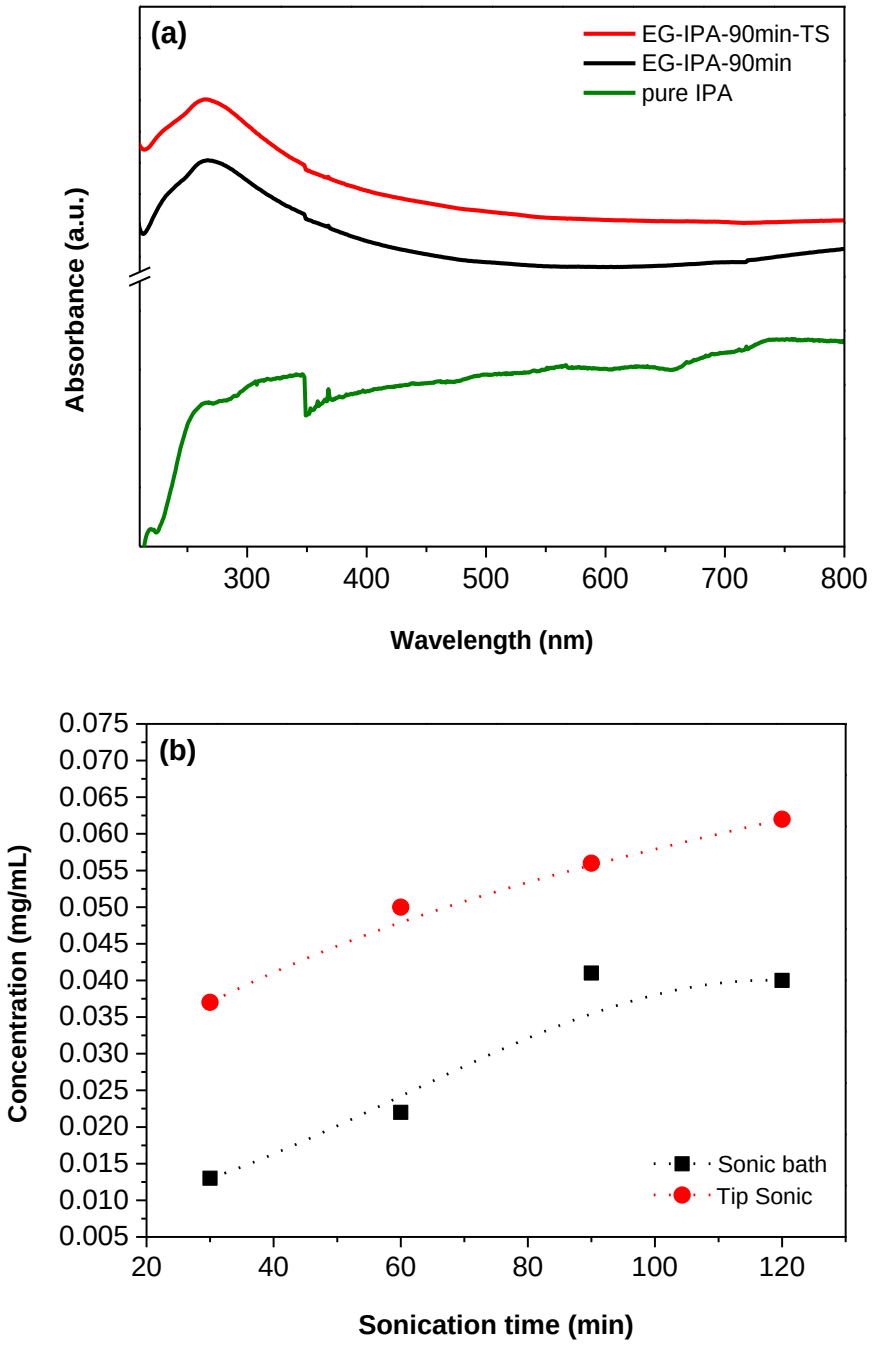

Figure 3.6. **(a)** Absorption spectra of EG -IPA dispersions prepared by sonication using either bath sonication or tip sonication for 90 min and a subsequent centrifugation at 900 rpm for 45 min. **(b)** Concentration of graphene remaining after centrifugation as a function of sonication time in both bath and tip sonicated EG-IPA dispersions.

Figure 3.7 shows FEG-SEM micrographs the EG-IPA-90m and EG-IPA-90min-TS samples. It was revealed that exfoliation of EG in ultrasonic bath for 90 min followed by a centrifugation resulted in thin, transparent flakes with lateral sizes of ~1 to 5 μm (Figs. 3.7(a) and (b)). The FEG-SEM micrographs of the EG-IPA-90min-TS sample look similar to that of the bath sonicated sample in terms of lateral sizes of the exfoliated flakes after centrifugation (Figs. 3.7(c) and (d)).

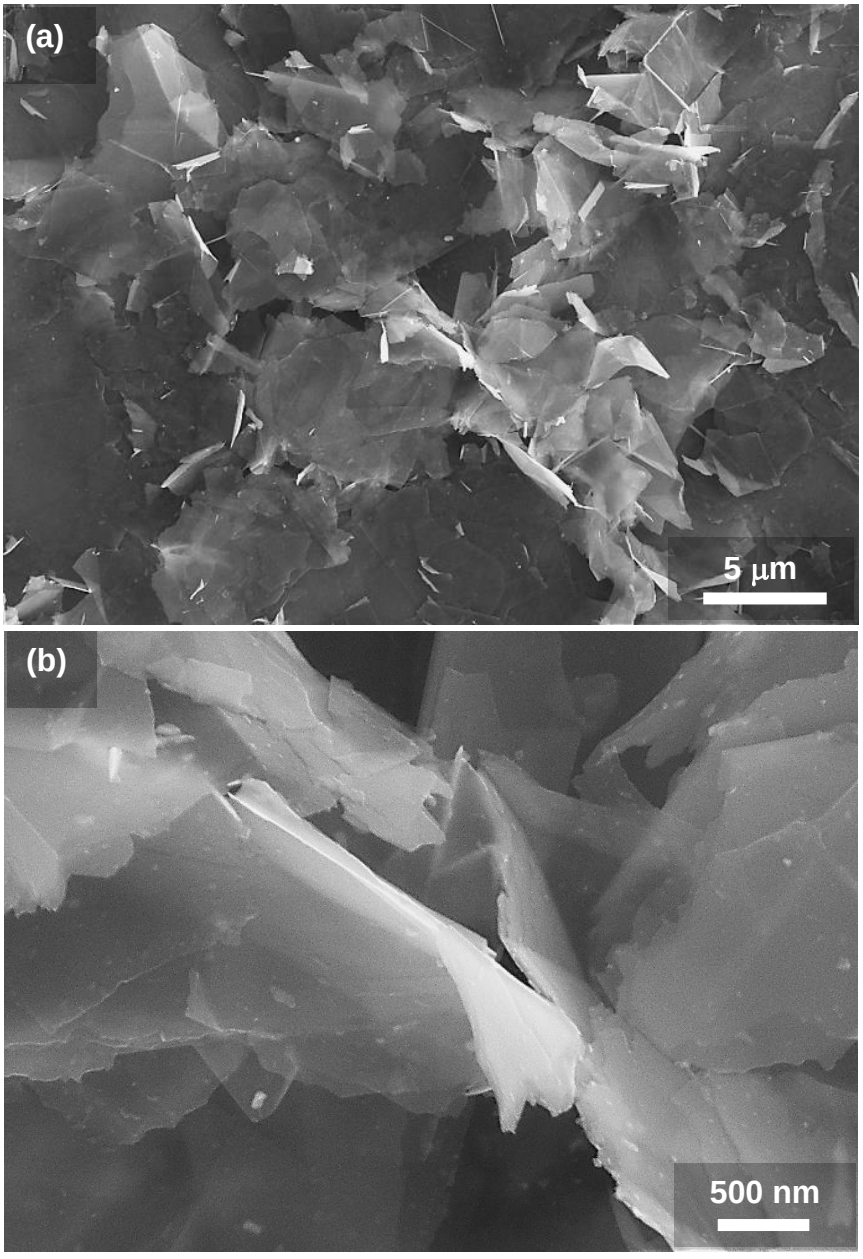

Figure 3.7. FEG-SEM micrographs of **(a),(b)** EG-IPA-90min, **(c),(d)** EG-IPA-90min-TS.

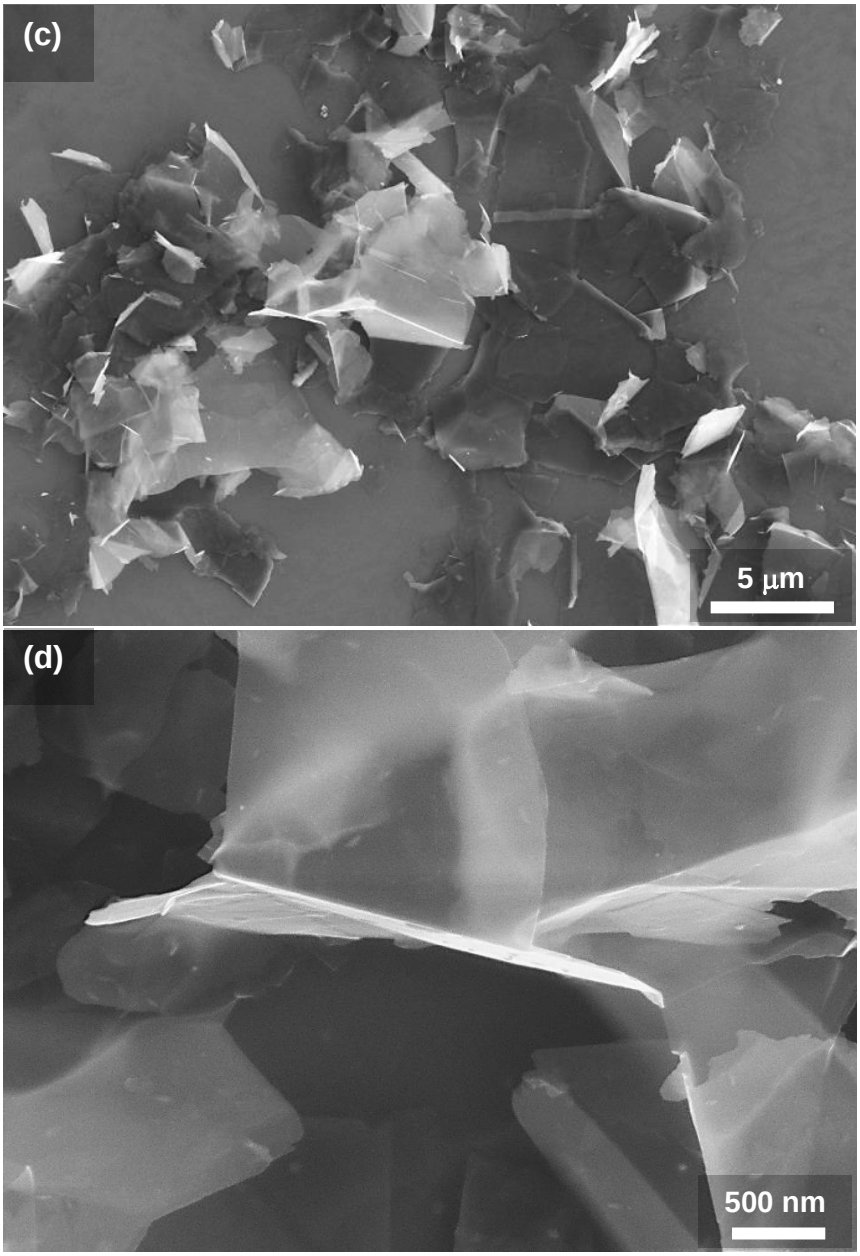

Figure 3.7. (Continued) FEG-SEM micrographs of **(a), (b)** EG-IPA-90min, and **(c), (d)** EG-IPA-90min-TS.

3.3.2. Exfoliation of nano-graphite powders

SEFG and PA nano-graphite powders are composed of primary graphene flakes which are much smaller than that of the EG powder. The dispersibility of these nano-graphite powders was investigated in two different solvents (NMP, which is known as a good solvent and IPA, which is known as a poor solvent) by taking into account the centrifugation speed and the sonication power. The SEFG-IPA dispersion was divided into two parts; one part was centrifuged at 500 rpm for 45 min, while the other part was centrifuged at 900 rpm for 45 min in order to observe the effect of centrifugation speed on the concentration, lateral size and number of layers of the prepared graphene-based materials. Figure 3.8 shows UV-VIS absorption spectra of the SEFG-IPA-90min, SEFG-IPA-90min-900rpm, SEFG-NMP-90min, PA-IPA-90min and PA-NMP-90min dispersions. The absorbance spectrum of the EG-IPA-90min was also shown in the plot, for comparison. Similar to the absorption spectra of the EG-IPA-90min and EG-IPA-90min-TS dispersions (Fig. 3.6(a)), the spectra of the dispersions of SEFG and IPA are also flat and featureless [14] except the characteristic peak of graphene at ~266 nm for the dispersions prepared in IPA, which can be attributed to the $\pi \rightarrow \pi^*$ transitions of aromatic C=C bonds [86] (Fig. 3.8). This peak was shifted to ~281 nm for the dispersions prepared in NMP. The EG-IPA-90min dispersion shows the lowest absorbance among the prepared dispersions.

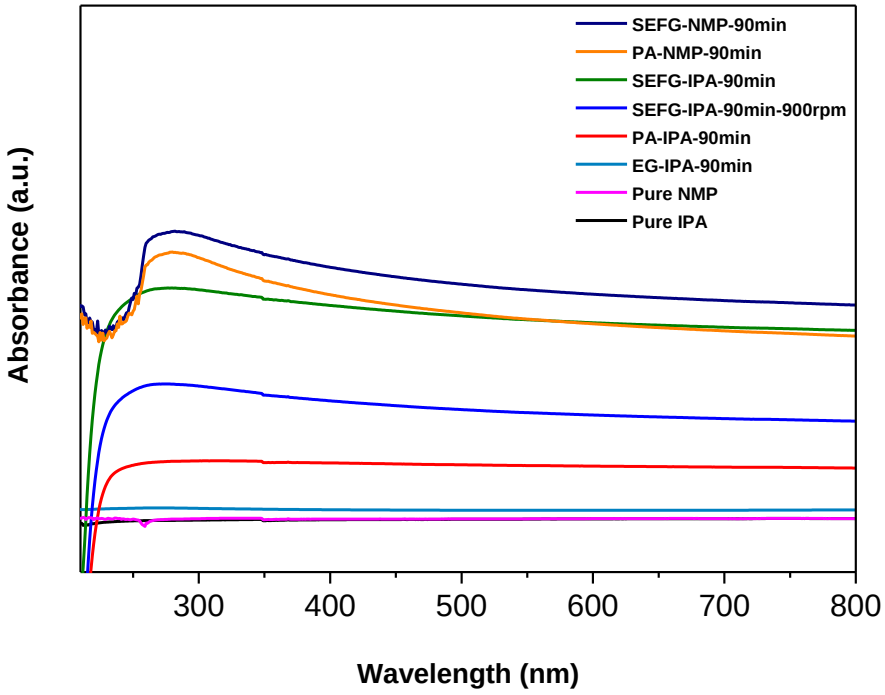

Figure 3.8. Absorption spectra of the dispersions prepared by bath sonication of SEFG and PA in either IPA or NMP for 90 min and by a subsequent centrifugation at 500 rpm for 45 min. SEFG-IPA dispersion also centrifugated at 900 rpm for 45 min. The absorption spectra of the EG-IPA-90min and the pure solvents were also shown in the plot for comparison. The sequence of the legends follows the order of plots from top to bottom.

The concentration of graphene-based material remaining after centrifugation was determined by measuring the absorbance of the dispersions at 660 nm. Figure 3.9(a) shows that SEFG-IPA and SEFG-NMP dispersions resulted in higher concentration values than PA-IPA and PA-NMP dispersions, respectively. Especially, the concentration difference between SEFG-IPA and PA-IPA dispersions is significant. The dispersibility of SEFG and PA powders in NMP is higher than the dispersibility of these powders in IPA, as expected (Fig. 3.9(a)). It is well known that NMP is an efficient solvent in exfoliation of graphene since the surface energy of NMP is well matched to that of graphene; therefore, the energy required to exfoliate graphene is balanced by the solvent-graphene interaction [14]. SEFG-NMP-120min dispersion provided the maximum concentration of graphene-based material achieved (~1.22 mg/ml) in this study. However, the

SEFG-IPA-120min dispersion also resulted in a relatively high concentration (~1.16 mg/ml), although IPA is assumed as a poor solvent. This concentration value is much higher than that of the concentration (0.5 mg/ml) reported by O'Neill et al. [74] who dispersed graphite powder in IPA for 48 h and subsequently centrifuged at 500 rpm.

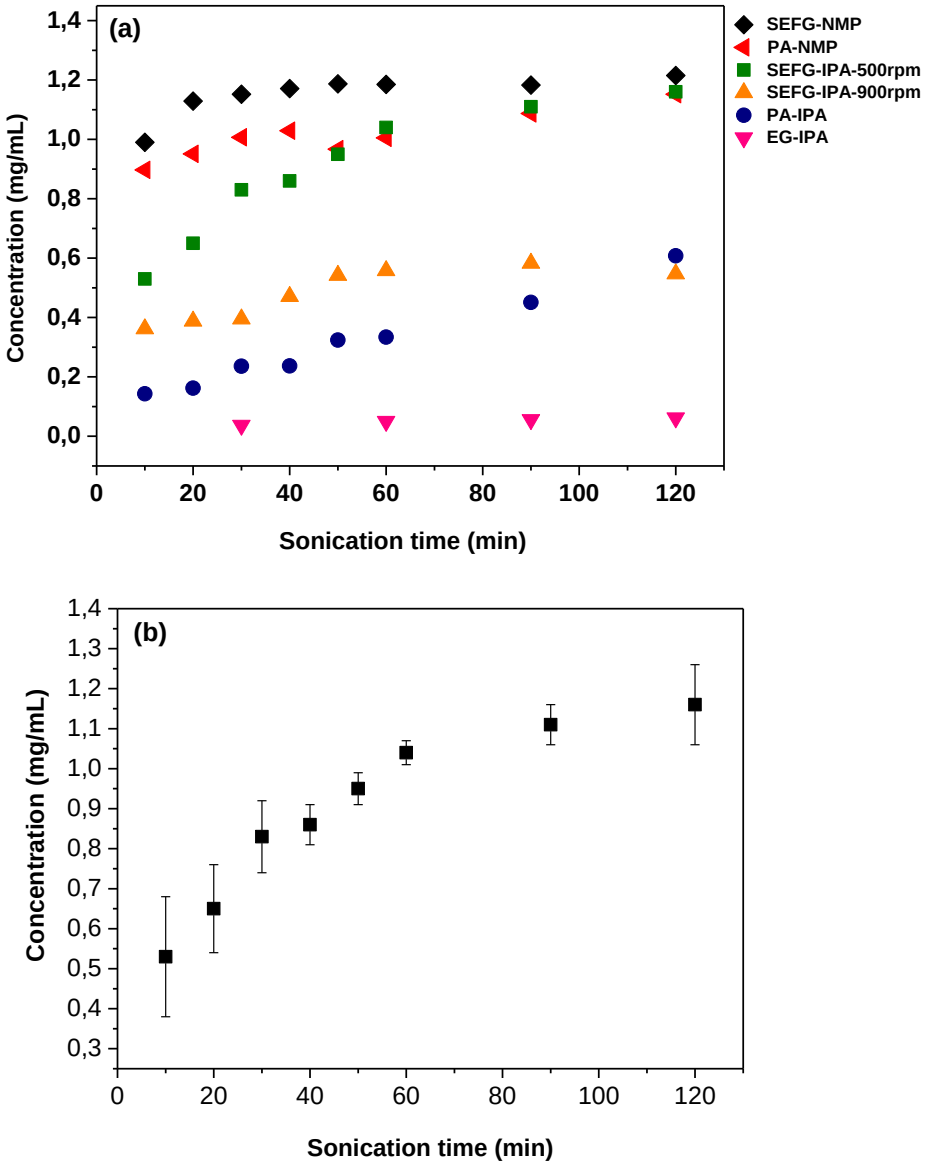

Figure 3.9. Concentration of graphene-based material remaining after centrifugation at 500 rpm for 45 min as a function of sonication time **(a)** for the IPA- and NMP-based dispersions prepared by bath sonication of SEFG and PA powders and a following centrifugation at 500 rpm for 45 min (the results for the SEFG-IPA dispersions which were centrifugated at 900 rpm for 45 min and the EG-IPA dispersions were also shown in the plot, for comparison), and **(b)** for the SEFG-IPA dispersions.

It should be noted here that the concentration values achieved at any sonication time show some variations depending on the equipment related variability, as in agreement with Khan et al. [55]. Figure 3.9(b) shows the concentration vs. sonication time plot of the SEFG-IPA dispersions (centrifuged at 500 rpm) where the error bars represent the standard deviation calculated from at least three measurements. Khan et al. [55] reported that the sonic energy input to the sample is sensitive to the water level, the exact position in the bath, the volume of dispersion and vessel shape; moreover, sonic baths often have power outputs different to the rated power output. Consequently, this may cause variations in the concentration values attained at any sonication time, even if nominally identical baths are used [55]. In the present study, in order to minimize the variations arising from the ultrasonic bath, all the dispersions were prepared in the same volume (in 20 ml vials by dispersing the powders in 10 ml solvent), and the vials (4 vials at the same time) were placed at a certain position of the sonic bath up to a certain level of water in each time. The water level of the sonic bath was followed carefully since water evaporation occurs due to temperature increase in water during sonication, and the level of water was kept at a certain level.

The absorbance measurements and the concentration calculations revealed that high concentration graphene-based dispersions (~1.11 mg/ml) can be prepared in a low boiling point solvent, IPA, in a very short sonication time (~90 min) by using SEFG powder (SEFG-IPA-90min sample). It should be also noted that this concentration value was further increased up to ~1.3 mg/ml, when the sonication was performed in vials of 50 ml (instead of 20 ml). Although long sonication times may provide a higher degree of exfoliation depending on the characteristics of the graphite-based precursor, it may also cause cutting of the graphene sheets into much smaller pieces and may introduce defects into them [54]. Therefore, determination of the optimum sonication time as well as the concentration of graphene is critical to be able to maintain the graphene quality while increasing its concentration. In this study, the optimum sonication time was determined as 90 min for further characterization and comparison of the dispersions prepared from different graphite-based precursors.

Table 3.2 summarizes the concentration values of graphene-based materials in IPA- and NMP-based dispersions prepared from EG, SEFG or PA powders by sonication for 90 min and a following centrifugation. Although tip sonication was successfully applied to exfoliate EG and higher concentration values were obtained in comparison to that of the bath sonication, it was not very efficient at exfoliating SEFG and PA powders. For the SEFG powder, the concentration of graphene-based material remaining in the dispersion after 90 min sonication followed by centrifugation at 500 rpm decreased from 1.11 to 0.83 mg/ml, when tip sonication was used instead of bath sonication. For the PA powder, tip sonication and bath sonication provided similar concentration values (Table 3.2). Table 3.2 also shows the concentration value measured for the SEFG-IPA-90min dispersion which was centrifuged at 900 rpm in order to investigate the effect of centrifugation speed on the concentration of the graphene-based materials. As the centrifugation speed increased to 900 rpm, concentration value decreased from 1.11 mg/ml to 0.58 mg/ml, as expected. It is reported in the literature that centrifugation at 500 rpm is usually enough to remove un-exfoliated graphitic crystallites [14, 55, 68]. At higher centrifugation speeds, it is expected that smaller and thinner flakes are kept in the dispersion [55].

Table 3.2. Concentration of graphene in IPA- and NMP-based dispersions prepared from EG, SEFG or PA powders by 90 min of sonication and a following centrifugation.

	Concentration (mg/ml)
EG-IPA-90min	0.04 ± 0.01
EG-IPA-90min-TS	0.06
SEFG-IPA-90min	1.11 ± 0.05
SEFG-IPA-90min-TS	0.83 ± 0.14
SEFG-IPA-90min-900rpm	0.58
SEFG-NMP-90min	1.18 ± 0.04
PA-IPA-90min	0.45 ± 0.13
PA-IPA-90min-TS	0.52
PA-NMP-90min	1.09

Figure 3.10 shows FEG-SEM micrographs of the SEFG powder before and after exfoliation in IPA and in NMP for 90min followed by a centrifugation. The SEM micrographs of the as-received SEFG powder show agglomerates with lateral dimensions of ~1-4 μm (Figs. 3.10(a) and (b)). These agglomerates are mostly composed of graphene/graphite flakes which are 100-500 nm across, as well as small amount of larger flakes up to a few μm. Although sonication for 90 min in IPA provided dispersion of these agglomerates into smaller and thinner flakes to some extent, the agglomerated structure could not be prevented completely due to van der Waals forces between individual flakes (Figs. 3.10 (c) and (d)). It was also revealed that sonication of SEFG in NMP provided somewhat a higher degree of this dispersion compared to dispersion in IPA, in agreement with the concentration values (Figs. 3.10 (e) and (f)).

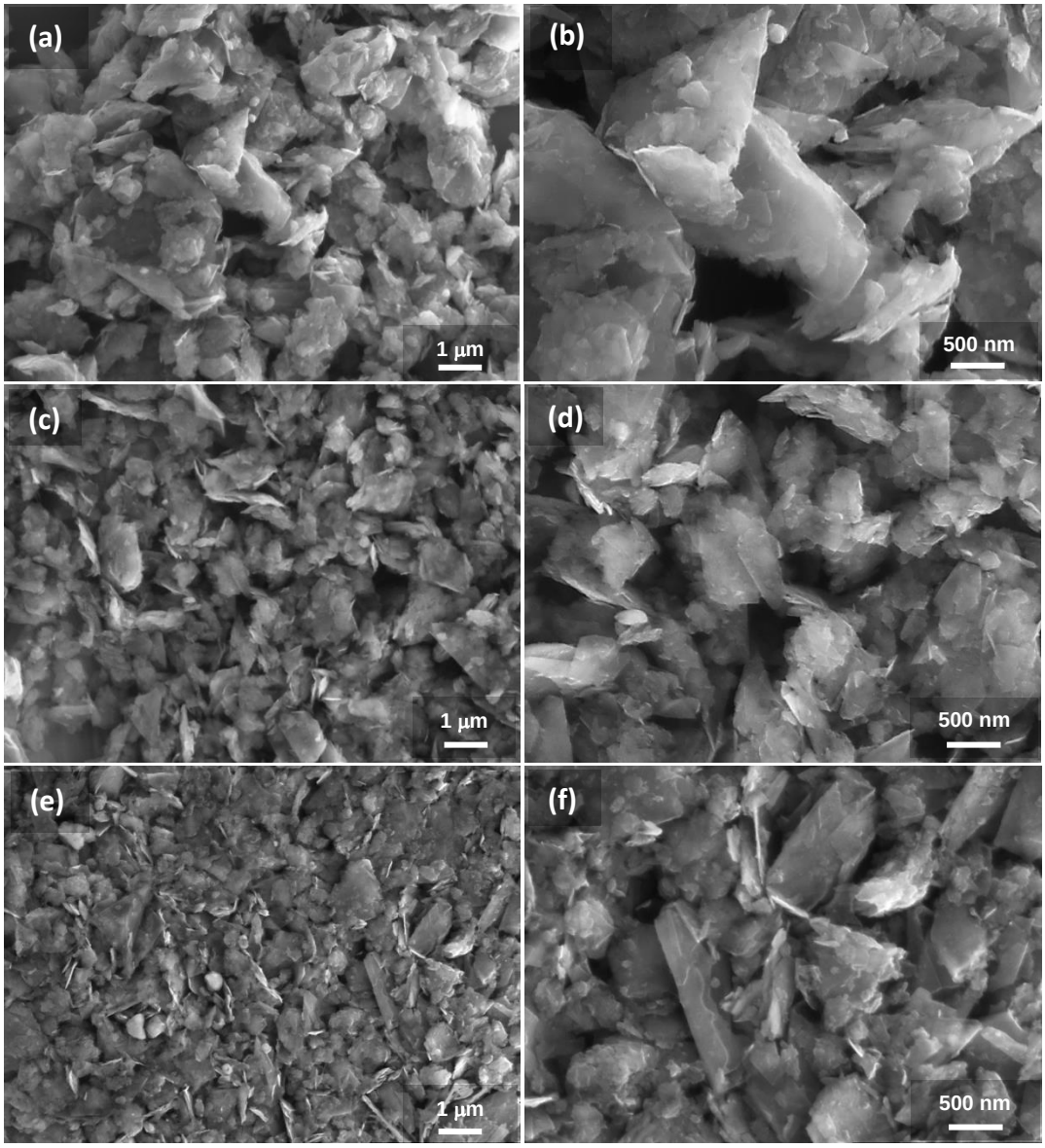

Figure 3.10. FEG-SEM micrographs of **(a,b)** SEFG, **(c,d)** SEFG-IPA-90min, and **(e,f)** SEFG-NMP-90min.

The FEG-SEM micrographs of the as-received PA powder (Figs. 3.11(a) and (b)) show much larger and thicker agglomerates in comparison to the SEFG powder. This is due to specific surface area of the PA powder which is twice that of the SEFG. Due to smaller primary particle sizes, van der Waals forces between graphene layers are higher; therefore, the degree of agglomeration is expected to be higher than that of the SEFG. Sonication of the PA powder in IPA for 90 min successfully dispersed these agglomerates into smaller and thinner pieces (Figs.

3.11(c) and (d)). Moreover, sonication in NMP for 90 min resulted in a much higher degree of exfoliation than that in IPA, as it is seen in Figs. 3.11(e) and (f). However, it should be noted that the dispersed materials are still in the agglomerated form since the van der Waals forces between nano-flakes cannot be overcome completely.

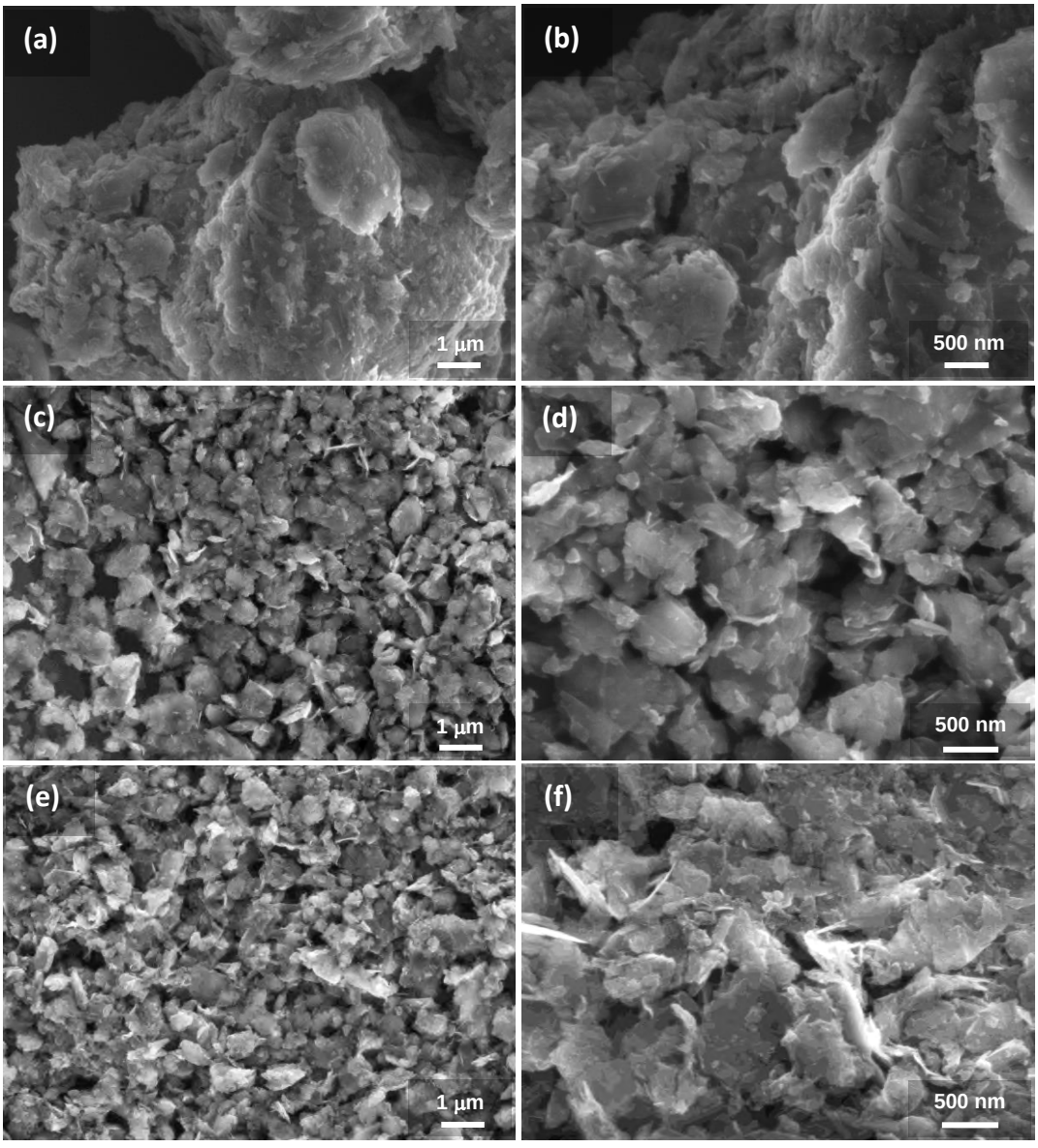

Figure 3.11. FEG-SEM micrographs of **(a,b)** PA, **(c,d)** PA-IPA-90min, and **(e,f)** PA-NMP-90min.

3.3.3. Size distribution and zeta potential measurements

Dynamic light scattering (DLS) analyses of the IPA- and NMP-based dispersions of the SEFG and PA powders exhibited a monomodal size distribution (Fig. 3.12). The dispersions prepared from the SEFG powder have broader size distributions and smaller mean particle sizes than the dispersions prepared from the PA powder (Figs. 3.12(a), (c), and (d), (e)). Table 3.3 gives the mean particle size values of the dispersions. The lateral size (hydrodynamic diameter) of the graphene sheets in the SEFG-IPA-90min and the SEFG-NMP-90min dispersions ranges between 200 to 800 nm with similar average sizes of 403 and 397 nm, respectively (Fig. 3.12(a), (d) and Table 3.3). Increasing the centrifugation speed to 900 rpm (for the SEFG-IPA dispersion) resulted in graphene sheets with a narrower size distribution (between 200 to 600 nm) and a smaller average lateral size, 335 nm, as expected. The IPA- and NMP-based dispersions of the PA gave graphene sheets with similar average lateral sizes of 299 and 303 nm for the PA-IPA-90min and PA-NMP-90min samples, respectively (Fig. 3.12(c), (e) and Table 3.3). The DLS measurements of the dispersions of EG powder could not be performed, since the polydispersity index of the dispersions is very high. This means that these dispersions have a very broad size distribution and may contain large particles or agglomerates; therefore, may not be suitable for DLS measurements.

Zeta potential measurements of the graphene sheets were performed at the natural pH of the dispersions at 25°C. It should be noted that these measurements were done a few months later than the dispersions were prepared. They were diluted and mildly sonicated for ~30 s just before the measurements. Table 3.3 shows the zeta potential values measured for the IPA-based dispersions of the EG, SEFG and PA precursors. SEFG and PA dispersions showed zeta potential values between -30 mV and -40 mV indicating moderate stability according to ASTM [87]. The zeta potential value of the dispersions prepared from the EG precursor is ~25 mV, which shows a relatively lower stability in comparison to the SEFG and PA dispersions.

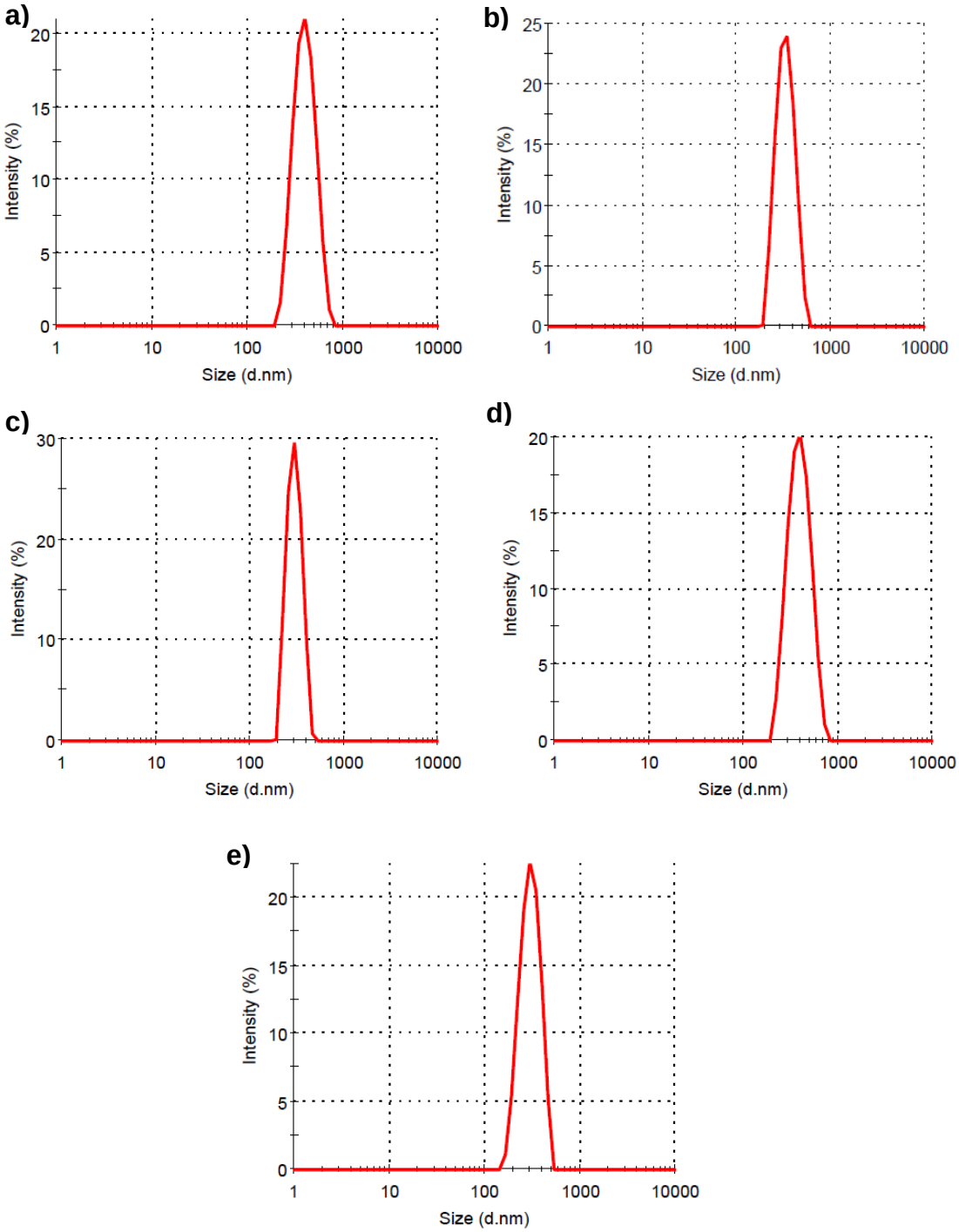

Figure 3.12. Particle size distributions of **(a)** SEFG-IPA-90min, **(b)** SEFG-IPA-90min-900rpm, **(c)** PA-IPA-90min, **(d)** SEFG-NMP-90min, **(e)** PA-NMP-90min

Table 3.3. Mean particle size values of IPA- and NMP-based graphene dispersions and zeta potential measurements of IPA-based graphene dispersions.

	Mean particle size (D_{50}) (nm)	**Zeta Potential (mV)**
EG-IPA-90min	-	-24.4
EG-IPA-TS-90min	-	-25.9
SEFG-IPA-90min	403	-33.8
SEFG-IPA-90min-900rpm	335	-30.3
SEFG-NMP-90min	397	-
PA-IPA-90min	299	-36.2
PA-NMP-90min	303	-

3.3.4. Sedimentation measurements

Figure 3.13 shows the sedimentation data for the dispersions prepared by bath sonication of the SEFG and PA powders in NMP and IPA solvents for 90 min followed by centrifugation. The SEFG-IPA-90min-900rpm dispersion exhibits the most stable behavior with only 17 and 39% sedimentation after 1 and 8 weeks, respectively. The experimental sedimentation curves can be best fit with a bi-exponential (Fig. 3.13), indicating the presence of two sedimenting phases and one stably dispersed (non-sedimenting) component [14, 88]. The corresponding fitting parameters (y_0, A_1, A_2, τ_1 and τ_2) are shown in Table 3.4. Here, y_0 represents the partial amount of non-sedimenting stable phase, A_1 and A_2 are the partial amounts of the sedimenting phases, and τ_1 and τ_2 are the time constants. Some sedimentation occurs in all the dispersions; however, the rate of sedimentation and the amount of sedimented material is different. The first sedimenting phase has a shorter time constant ($\tau_1 < \tau_2$) for all dispersions and can be attributed to large graphitic flakes which remain in the dispersion after centrifugation. From the fittings it can be estimated that this phase comprises 14% of total mass of the dispersed material for the SEFG-IPA-90m-900rpm, while this amount is 48% for the SEFG-IPA-90m which was centrifugated at 500 rpm. This

indicates that centrifugation at 500 rpm is not as effective as the centrifugation at 900 rpm in removing large flakes from the dispersion.

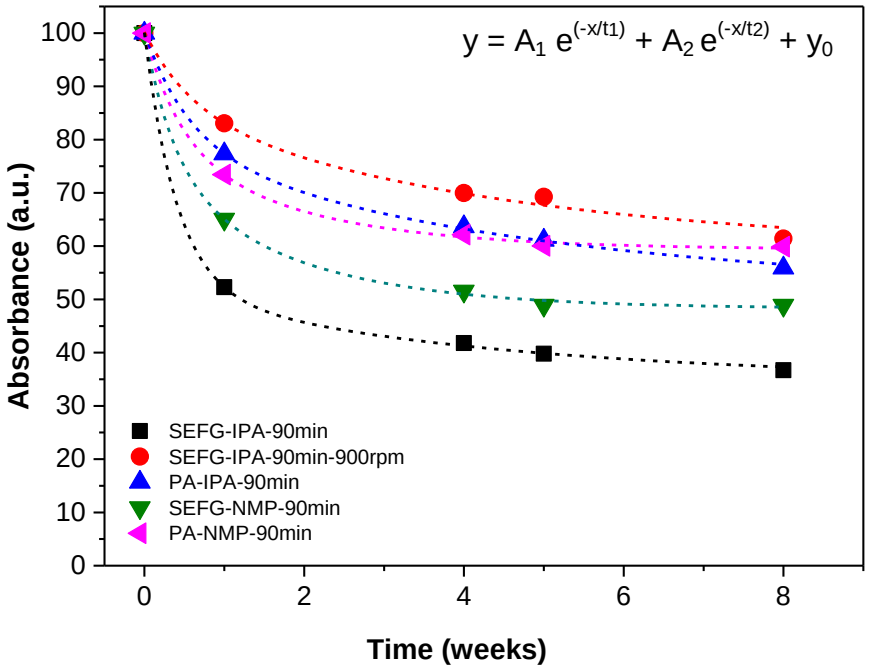

Figure 3.13. Sedimentation data for the dispersions of SEFG and PA powders in IPA and NMP solvents. Dispersions were prepared by 90 min bath sonication followed by centrifugation at 500 rpm for 45 min. The SEFG-IPA dispersion was also centrifugated at 900 rpm for 45 min after sonication in order to observe the effect of centrifugation speed. The absorbance of the dispersions was measured at 660 nm. The dashed lines show the bi-exponential fits.

Table 3.4. Fit constants obtained from bi-exponential fittings of the sedimentation curves shown in Fig. 3.12.

	R^2	y_0	A_1	τ_1 (weeks)	A_2	τ_2 (weeks)
SEFG-IPA-90m	0.999	35.0	48.0	0.4±0.03	17.1±0.58	4.0±0.26
SEFG-IPA-90m-900rpm	0.985	59.4	14.0	0.6±0.31	26.8±1.84	4.3±0.55
PA-IPA-90m	0.999	51.9	21.0	0.6±0.06	27.2±0.59	4.6±0.19
SEFG-NMP-90m	0.997	48.3	25.0	0.4±0.19	26.7±1.77	1.7±0.52
PA-NMP-90m	0.997	59.4	20.4	0.5±0.16	20.2±1.39	1.9±0.53

The second sedimenting phase has a much longer time constant (~4.3 weeks for the IPA-based dispersions) indicating the sedimentation of smaller particles. Therefore, this phase is supposed to be large multilayer graphene flakes [14] or agglomerates of few-layer graphene sheets. The SEFG-IPA-90m-900rpm dispersion exhibits a very stable behavior with a non-sedimenting component consisting of 59.4% of the sample mass after 8 weeks. This stable phase can be attributed to few-layer (<5 layers) graphene sheets. However, it should be noted that the non-sedimenting graphene concentration (0.39 mg/ml) of the SEFG-IPA-90min is still higher than that of the SEFG-IPA-90m-900rpm dispersion (0.34 mg/ml), when the initial concentration of the dispersions was taken into account. It was observed that the dispersions prepared from the PA powder show relatively high stability due to narrower size distribution and smaller mean particle size of the PA starting powder in comparison to the SEFG powder. There is not a significant difference between the stability of the dispersions prepared from the PA powder in IPA and in NMP; however, for the dispersions prepared from the SEFG powder, NMP provides slightly higher stability than IPA. The dispersions prepared from the EG powder precipitated completely within 2 days, indicating a very poor stability as in good agreement with the DLS particle size analysis results, which revealed a high polydispersity index for these dispersions. High polydispersity index indicates that the dispersions prepared from the EG powder have a very broad size distribution and may contain large particles or agglomerates.

3.3.5. Raman analyses of the starting powders and the exfoliated materials

Raman spectroscopy, which provides a fast, high-throughput and nondestructive identification of graphene layers [89] was used to evaluate the number of layers and the quality of the prepared graphene-based materials. Raman analyses were performed on the starting materials and their dispersions in IPA.

Figure 3.14 shows the representative Raman spectra of the expandable graphite, expanded graphite (EG) and the exfoliated EG (EG-IPA-90min-TS). Table 3.5 gives a summary of the corresponding Raman characteristics. Raman spectra of all the samples shown in Fig. 3.14 include a strong G-band at 1582 cm^{-1}, which arises from the in-plane C-C bond stretching in graphitic materials and is common to all sp^2-bonded carbon systems [90], and a second order G'-band, also named 2D-band, at ~2720 cm^{-1}. The spectra of the expandable graphite and the EG-IPA-90m-TS samples also include disorder induced D-band at ~1350 cm^{-1} and D'-band at ~1620 cm^{-1}.

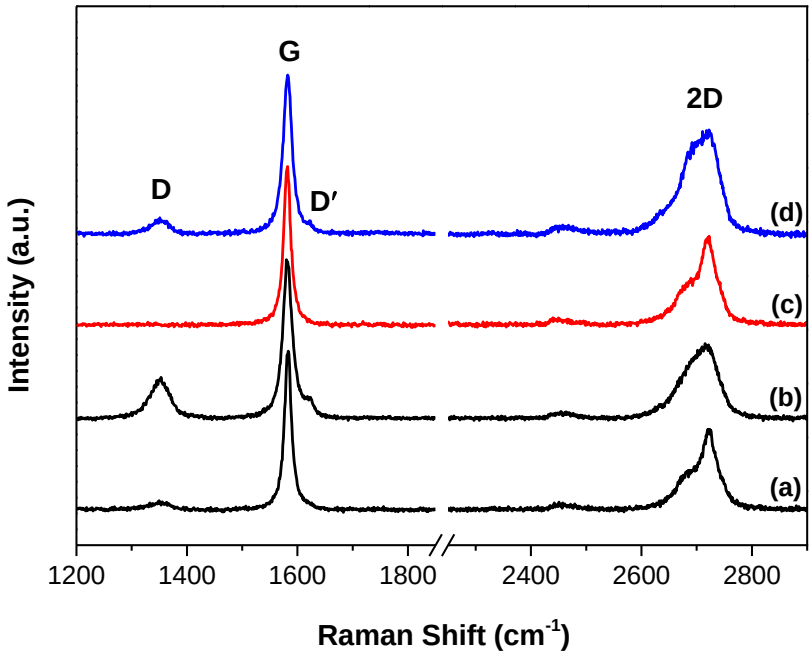

Figure 3.14. Representative Raman spectra (normalized to the G-band) of **(a), (b)** expandable graphite ((a) and (b) show the Raman spectra recorded at different locations of the laser spot over the thin film), **(c)** expanded graphite **(**EG), and of **(d)** exfoliated EG-IPA-90min-TS sample on SiO_2/Si substrate.

Table 3.5. Raman features of the starting powders (EG, SEFG and PA) and of the thin films prepared from IPA-based dispersions of these powders[†]

	D-band	G-band		2D-band				
	Position (ω) (cm^{-1})	**FWHM (cm^{-1})**	**Position (ω) (cm^{-1})**	**FWHM (cm^{-1})**	**Position (ω) (cm^{-1})**	**I_D/I_G**	**I_{2D}/I_G**	**Estimated Number of Layers**
Expandable Graphite (1)	1351	17	1582	53	-	0.08	-	-
Expandable Graphite (2)	1353	21	1582	71	2717	0.19	0.46	-
EG	1350	17	1582	56	-	0.01	-	-
EG-IPA-90min-TS (1)	1353	18	1582	68	2720	0.07	0.60	Few-layer (3-5 layers)
EG-IPA-90min-TS (2)	1353	17	1582	54	-	0.03	0.60	(> 10 layers)
SEFG[*]	1345	24	1574	77	2696	0.26	0.37	Agglomerates of few-layers
SEFG-IPA-90min	1346	23	1573	75	2697	0.24	0,38	Few-layer (3-5 layers)
SEFG-IPA-90min-900rpm	1346	24	1573	74	2693	0.25	0.39	Few-layer (3-5 layers)
SEFG-IPA-90min-2600°C	1344	23	1572	75	2692	0.07	0.43	Few-layer (3-5 layers)
PA[**]	1344	30	1575	78	2692	0.39	0.43	Agglomerates of few-layers
PA-IPA-90min	1343	28	1571	76	2685	0.30	0.43	Few-layer (3-5 layers)

[†] The values shown in the Table are the average of ~50 spectra for each sample. The numbers in parenthesis next to the sample names indicate different 2D-band line-shapes of the same sample.

[*] Surface Enhanced Flake Graphite [**] Primary Artificial

The 2D-band is a second-order process related to a phonon near the K point in graphene, activated by double resonance process, which is responsible for its dispersive nature and cause a strong dependence on any perturbation on the electronic and/or phonon structure of graphene [90]. Therefore, the 2D-band changes in line-shape, line-width and peak position when the number of graphene layers increases in a Bernal stacked graphene [91]. It should be also noted that this two-phonon band is allowed in the second order Raman spectra of graphene without any kind of disorder or defects [92]. Raman measurements which were performed on different regions of expandable graphite revealed variations in the line-shape of the 2D-band (Fig. 3.14). Figure 3.15 and Table 3.6 show the curve fittings and the fitting parameters of the 2D-bands of expandable graphite, EG and EG-IPA-90min-TS samples, respectively. Although the 2D-band of expandable graphite could be generally fit using two Lorentzian peaks revealing a graphite structure (Fig. 3.14(a), Fig. 3.15(a) and Table 3.6), some spectra needed three Lorentzian peaks to fit the 2D-band of expandable graphite (Figs. 3.14(b), 3.15(b) and Table 3.6). The latter one (indicated as Expandable Graphite–2 in Tables 3.5 and 3.6) was accompanied by a relatively higher intensity D-band at ~1350 cm^{-1} and the appearance of the D'-band at ~1620 cm^{-1} compared to the former and supposed to be recorded from flake edges rather than basal plane of the expandable graphite (Fig. 3.14). D-band arises from breathing modes of sp^2 atoms in rings and requires a defect for its activation [14, 90]. Hence, it is observed in case of a disordered sample and/or at the edge of the sample [92]. The presence of disorder/defect induced D- and D′-bands in the Raman spectrum of expandable graphite can be generally attributed to lattice deformation since the acid intercalation causes symmetry changes at a graphitic layer adjacent to an intercalant layer [84, 93], as well as to edge distortion.

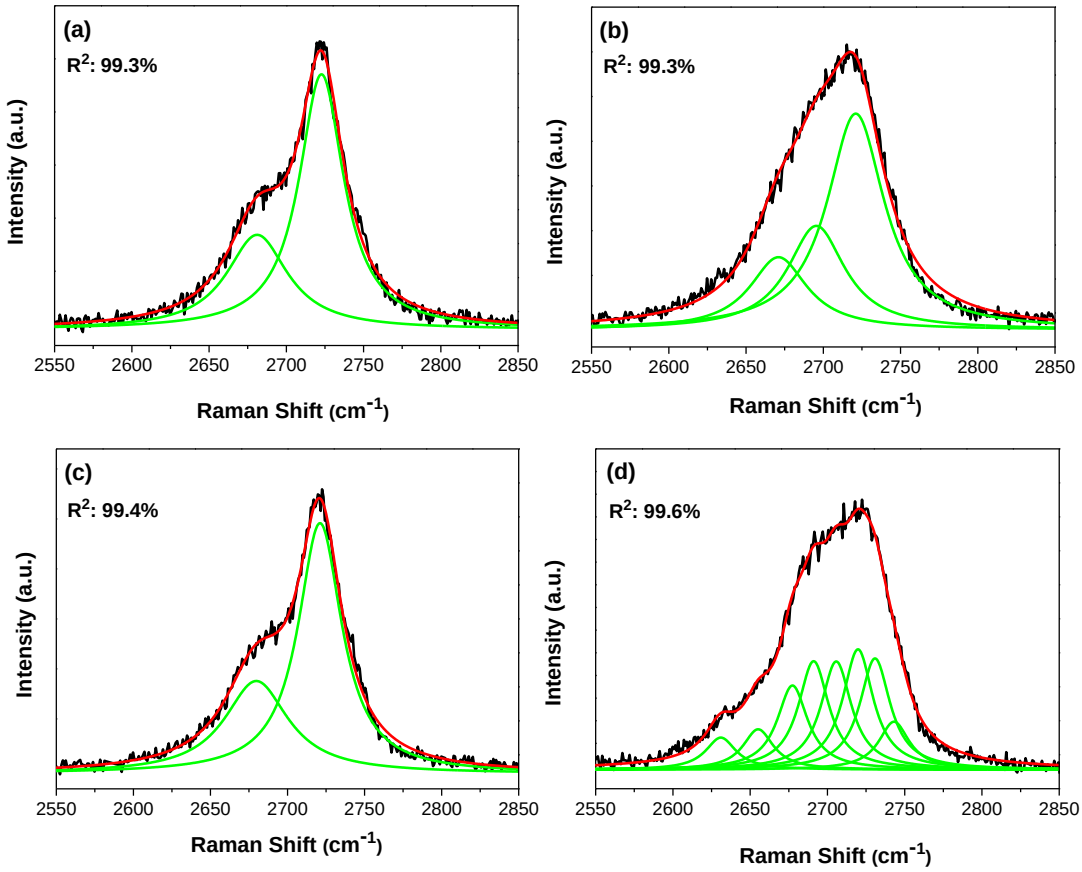

Figure 3.15. The enlarged 2D-band regions (of Fig. 1) with Lorentzian curve fittings of **(a), (b)** expandable graphite, **(c)** expanded graphite (EG), and **(d)** exfoliated sample (EG-IPA-90min-TS). The black, green and the red curves represent the spectra, fit peaks and the cumulative fit peak, respectively.

Table 3.6. Fitting components of the 2D-bands of the corresponding spectra shown in Fig. 3.15. The value in parentheses is the FWHM (cm^{-1}) of the corresponding fit peak.

	Peak 1 (cm^{-1})	**Peak 2 (cm^{-1})**	**Peak 3 (cm^{-1})**	**Peak 4 (cm^{-1})**	**Peak 5 (cm^{-1})**	**Peak 6 (cm^{-1})**	**Peak 7 (cm^{-1})**	**Peak 8 (cm^{-1})**
Expandable Graphite -1 (a)	-	-	2681 (35)	-	-	2723 (48)	-	-
Expandable Graphite-2 (b)	-	-	2671 (45)	2696 (45)	-	2721 (45)	-	-
EG	-	-	2680 (35)	-	-	2721 (50)	-	-
EG-IPA-90min-TS	2631 (24)	2655 (24)	2677 (24)	2691 (24)	2706 (24)	2720 (24)	2731 (24)	2743 (24)

The intensity ratio of the D-band to that of the G-band (I_D/I_G) is generally used to characterize defect content [90]. Figure 3.16 shows the statistical histograms of the I_D/I_G ratio for the expandable graphite, EG powder and EG-IPA-90min-TS samples. The I_D/I_G ratio of the expandable graphite ranged from ~0.01 to ~0.45 with a mean value of ~0.13 (Fig. 3.16(a)). When expandable graphite was subjected to a thermal expansion, the D-band almost disappeared and an extremely low I_D/I_G ratio (~0.01 in average) was found for EG, indicating removal of the defects (Fig. 3.16(b)). The 2D-band of the EG exhibited two-peaks profile, typical to graphite (Fig.3.15(c) and Table 3.6). The I_D/I_G ratio of the EG-IPA-90min-TS (~0.06 in average) showed a slight increase in comparison to that of the EG powder, indicating that exfoliation process introduced some defects to the graphene/graphite flakes (Fig. 3.16(c)). These defects may be either point defects in the basal planes or may arise from the flake edges [54, 55, 74]. For solvent exfoliated graphene flakes, the defects are generally attributed to the new edges which are created as a result of cutting initially large crystallites into smaller flakes by sonication and act as defects [14, 54, 68]. However, this I_D/I_G ratio is still significantly low, revealing a very high quality of the exfoliated flakes. The line-shape of the 2D-bands recorded from different locations of the EG-IPA-90min-TS sample showed variations, indicating that the exfoliated sample is composed of few- or multi-layer graphene sheets as well as graphite flakes (Raman spectrum belonging to the graphite flakes were not shown, but the corresponding Raman features are presented in Tables 3.5 and 3.6). This result is consistent with the DLS particle size analysis and the sedimentation results, which revealed a polydisperse character for this sample. This may indicate that some of the expanded graphite remained in the dispersion without exfoliation or re-agglomerated during sample preparation. The line-shape of the 2D-band shown in Fig. 3.14(d) is asymmetric; however, different from that of graphite. This peak was best fit with eight Lorentzian components with a fixed FWHM of 24 cm^{-1} (Fig. 3.15(d)) and could be attributed to few-layer (3–5 layers) graphene. The corresponding curve fitting parameters are shown in Table 3.6. The π electronic structure of graphene splits when a second layer is added. With an increase in the number of layers, the number of double resonance scattering processes increases,

and eventually the line-shape converges to graphite, where only two peaks are observed [90]. Raman spectrum becomes hardly distinguishable from that of bulk graphite for more than five layers [89]. Malard et al. [92] reported that to correctly identify the line-shape of 2D-band for trilayer graphene, one should model the double resonance process by considering 15 different transitions. However, the energy separations of many of these fifteen different processes can be very close to each other from an experimental point of view. The authors reported that minimum number of peaks with a FWHM of ~24 cm^{-1} is necessary to correctly fit the 2D-band, and splitting of 2D-band of tri-layer graphene needs at least six peaks with a FWHM of ~24 cm^{-1} for laser energies ≤2.41 eV.

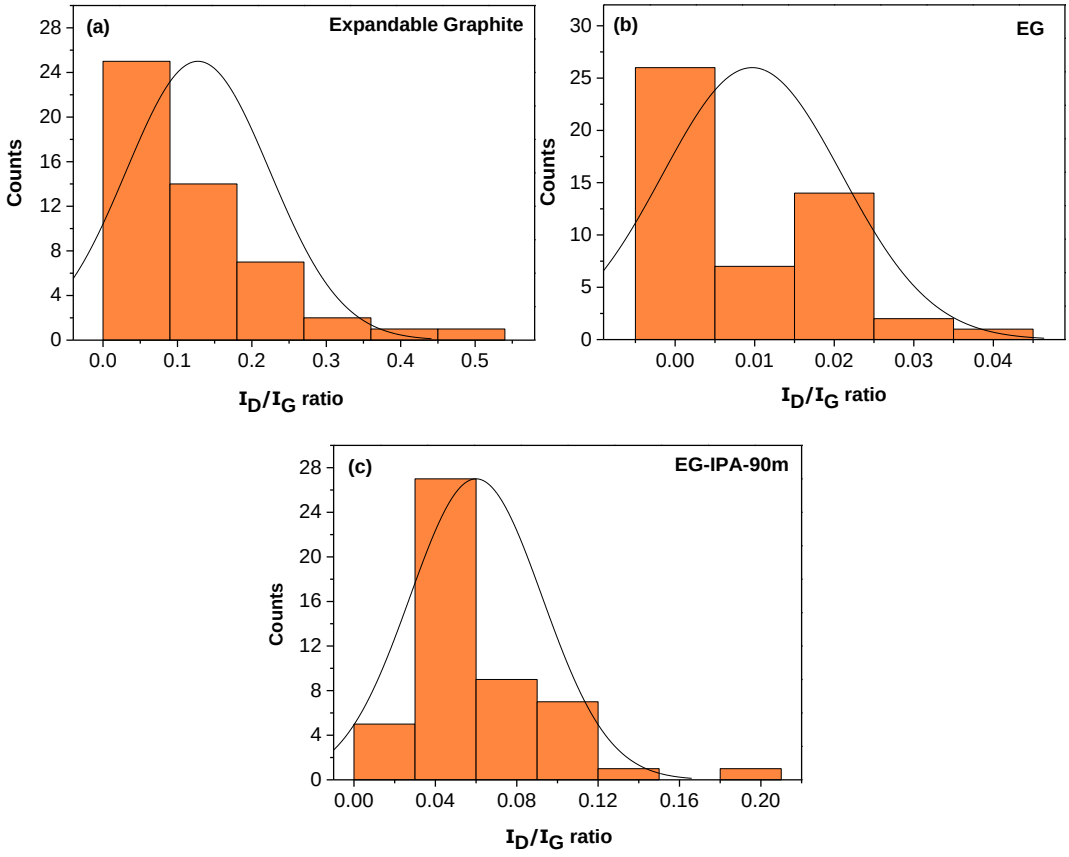

Figure 3.16. Statistical histogram of the $\langle \frac{I_D}{I_G} \rangle$ ratios derived from 50 Raman spectra recorded at different locations. **(a)** Expandable graphite, **(b)** EG, and **(c)** EG-IPA-90min sample. The distribution curves indicate the mean of the data.

Figure 3.17 shows the Raman spectra (normalized to the G-band) of the thin films prepared from the SEFG starting powder and its IPA-based dispersions (SEFG-IPA-90m and SEFG-IPA-90m-900rpm). The spectrum of the SEFG-IPA-90m sample annealed at 2600°C in Ar atmosphere is also presented in Fig. 3.17. The corresponding Raman characteristics are given in Table 3.5. A red-shift was observed in all the band-positions of these samples compared to that of the EG-based samples accompanied by a broadening of the FWHM (Table 3.5). The 2D-band line-shapes of all the samples, including the SEFG starting powder, are distinctly different from that of graphite and were best fit with eight Lorentzian peaks, each with a FWHM of ~24 cm^{-1} (similar to the case observed for the EG-IPA-90min sample as discussed previously), indicating that the number of layers of individual flakes are mostly 3-5. The representative fitting curve of the 2D-band of the SEFG-IPA-90min sample and the corresponding fitting parameters are shown in the inset of Fig. 3.17 and Table 3.7, respectively. These fitting results could be interpreted as the SEFG starting material, which is a nano-graphite powder produced by subjecting natural graphite to many processing steps in order to increase its SSA to ~175 m^2/g, is composed of agglomerates of individual few-layer graphene sheets mostly, while the exfoliation process helps to disperse these agglomerates. The statistical histograms shown in Figs. 3.18(a)-(c) exhibited distributions of I_D/I_G ratio in the range between 0.05 – 0.53 with a mean value of 0.26, 0.08 – 0.60 with a mean value of 0.24 and 0.06 – 0.51 with a mean value of 0.25 for the SEFG starting powder, SEFG-IPA-90min and SEFG-IPA-90min-900rpm samples, respectively. The I_D/I_G ratio obtained for the SEFG-IPA-90min (0.24 in average) is comparable to those reported in the literature for liquid phase exfoliated graphite (<0.5) [55, 74, 94]. The similar I_D/I_G ratio observed for the starting powder and the exfoliated samples may indicate that the defects in the exfoliated samples originate from the starting powder, rather than introduction of new defects (such as flake edges) into the sample during exfoliation process. Annealing of the SEFG-IPA-90min sample at 2600°C in Ar atmosphere for 4 h resulted in a significant decrease in the I_D/I_G ratio, which ranged from 0 to 0.26 with a mean value of 0.07, as shown by the corresponding statistical histogram (Fig. 3.18(d)), and also in disappearance of the D′-band (Fig.

3.17(d)). These could be attributed to elimination of most of the defects/disorders in the SEFG-IPA-90min sample and recovery of it as a result of annealing, indicating that the defects are mainly structural imperfections which most probably originate from the starting powder. These defects/disorders could be introduced into the SEFG powder during its production process as the point defects in the basal planes and/or the chemical residues.

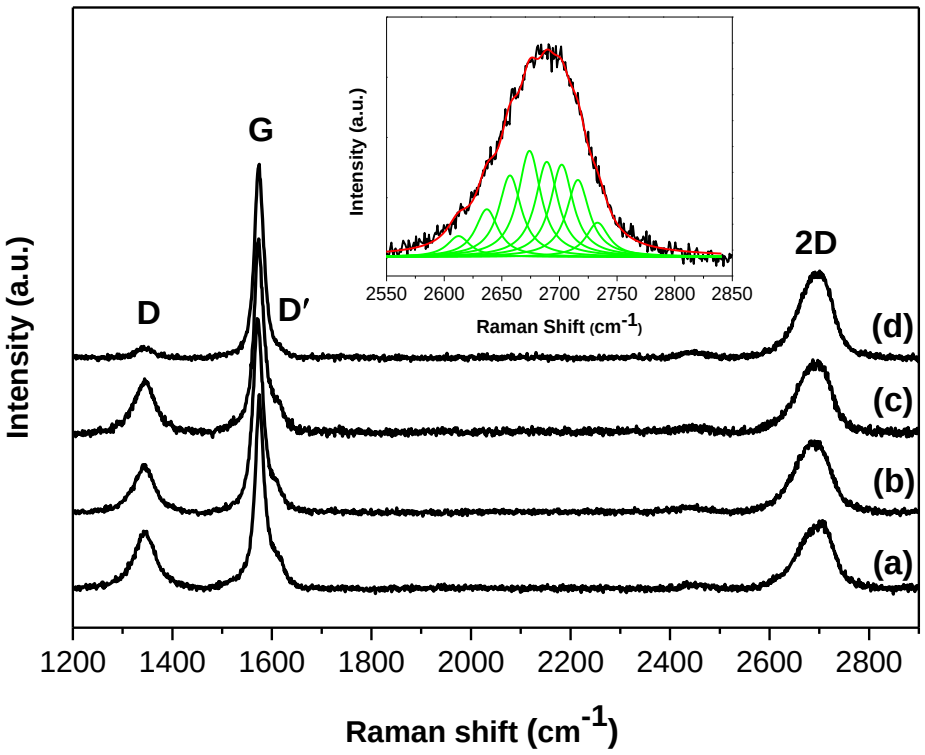

Figure 3.17. Representative Raman spectra (normalized to the G-band) of the thin films prepared from **(a)** SEFG starting powder, **(b)** SEFG-IPA-90min, **(c)** SEFG-IPA-90min-900rpm, and **(d)** SEFG-IPA-90min sample annealed at 2600°C in Ar atmosphere (SEFG-IPA-90min-2600°C). Inset shows the curve fitting of 2D-band of SEFG-IPA-90min with eight Lorentzians, the FWHM of which are 24 cm^{-1}.

Table 3.7. Fitting components of the 2D-bands shown in the insets of Figs. 3.16 and 3.18. The value in parentheses is the FWHM (cm^{-1}) of the corresponding fit peak.

	Peak 1 (cm^{-1})	**Peak 2 (cm^{-1})**	**Peak 3 (cm^{-1})**	**Peak 4 (cm^{-1})**	**Peak 5 (cm^{-1})**	**Peak 6 (cm^{-1})**	**Peak 7 (cm^{-1})**	**Peak 8 (cm^{-1})**
SEFG	2615 (24)	2642 (24)	2660 (24)	2675 (24)	2690 (24)	2706 (24)	2721 (24)	2736 (24)
SEFG-IPA-90min	2613 (24)	2637 (24)	2657 (24)	2674 (24)	2689 (24)	2702 (24)	2716 (24)	2733 (24)
PA	2617 (24)	2642 (24)	2662 (24)	2677 (24)	2691 (24)	2706 (24)	2721 (24)	2740 (24)
PA-IPA-90min	2605 (24)	2628 (24)	2648 (24)	2665 (24)	2682 (24)	2698 (24)	2715 (24)	2735 (24)

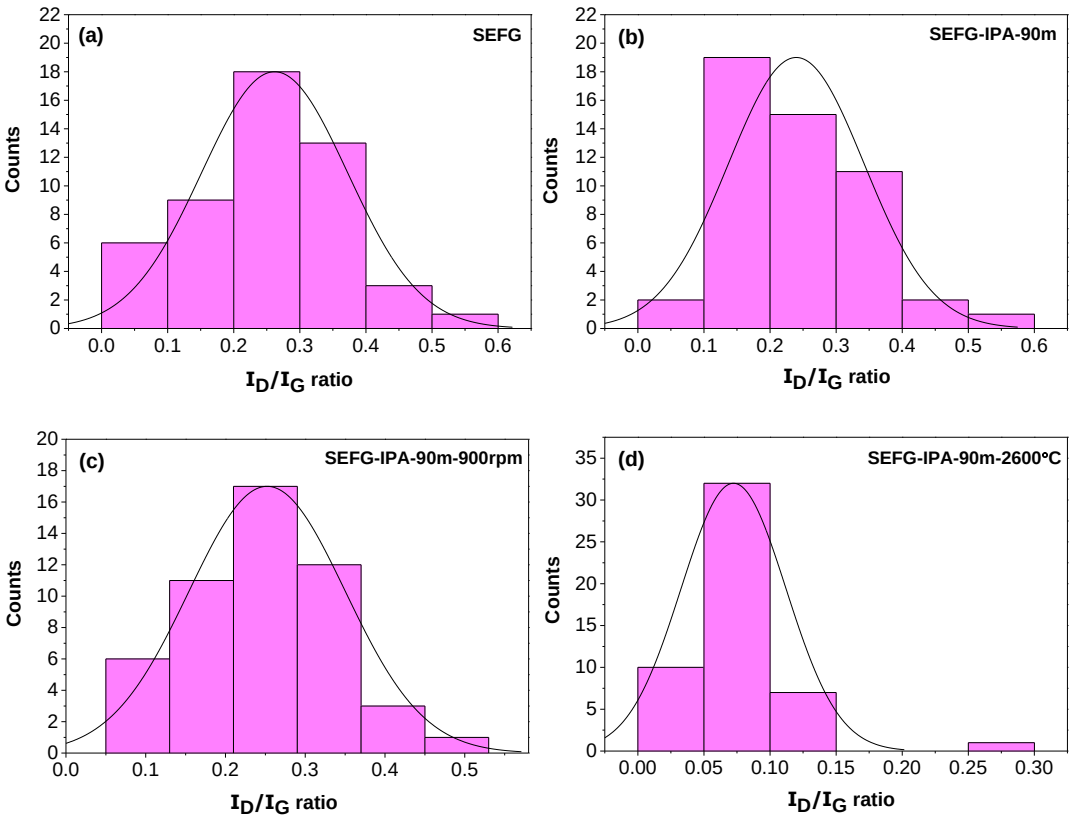

Figure 3.18. Statistical histogram of the $\langle \frac{I_D}{I_G} \rangle$ ratios derived from 50 Raman spectra recorded at different locations. **(a)** SEFG, **(b)** SEFG-IPA-90m, **(c)** SEFG-IPA-90m-900rpm, and **(d)** SEFG-IPA-90m sample annealed at 2600°C in Ar atmosphere for 4 h. The distribution curves indicate the mean of the data.

Figure 3.19 shows the Raman spectra of the thin films of the PA starting powder and the PA-IPA-90min dispersion. Raman features of these samples are summarized in Table 3.5. 2D-bands of both PA and PA-IPA-90min were best fit with eight Lorentzians with a FWHM of 24 cm^{-1}, similar to those observed for the SEFG and its related dispersions, indicating the presence of few-layer (3-5 layers) graphene flakes in the samples. The fitting components are given in Table 3.7 and the inset in Fig. 3.19 shows the 2D-band fitting of the PA-IPA-90min sample. Figure 3.20 shows the statistical histograms of the I_D/I_G ratio for the PA starting powder and the PA-IPA-90min sample. The I_D/I_G ratio of the PA powder ranged from 0.15 – 1.0 with a mean value of 0.39, while the I_D/I_G ratio of the PA-IPA-90min is in the range of 0.12 – 0.58 with a mean value of 0.30. These defect contents are higher than that of the SEFG powder and its dispersions. Narrower I_D/I_G ratio distribution and a lower average I_D/I_G ratio observed for the PA-IPA-90m sample with respect to the PA powder indicates that the defect content of the starting powder is much higher than that of the exfoliated sample. Both basal plane defects and/or flake edges could be responsible for this defect content. The PA is a nano-graphite powder with a very high SSA (350 m^2/g), about twice that of the SEFG powder, resulting in a higher degree of agglomeration of the graphene/graphite flakes compared to the SEFG powder. Due to this agglomeration, more flake edges could have encountered with the laser spot during Raman analysis, giving rise to D and D′-bands. In addition, the imperfections such as the point defects in the basal planes and/or the chemical residues could have been introduced into the PA powder during its production from synthetic graphite. The reason of decreasing defect amount with exfoliation could be the dispersion of the agglomerates, therefore, decreasing the flake concentration in the area of the laser spot and/or removal of some of the defected flakes or impurities, originated from the starting powder, by centrifugation.

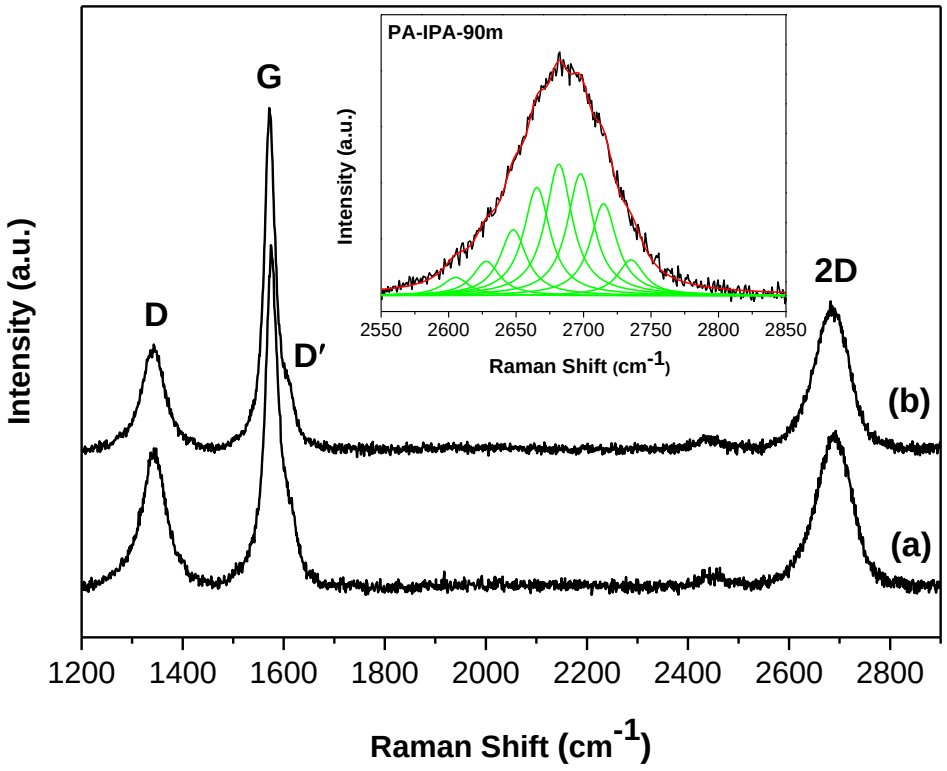

Figure 3.19. Representative Raman spectra (normalized to the G-band) of the thin films prepared from **(a)** PA starting powder and **(b)** PA-IPA-90min dispersion. Inset shows the curve fitting of 2D-band of PA-IPA-90min with eight Lorentzians, the FWHM of which are 24 cm^{-1}.

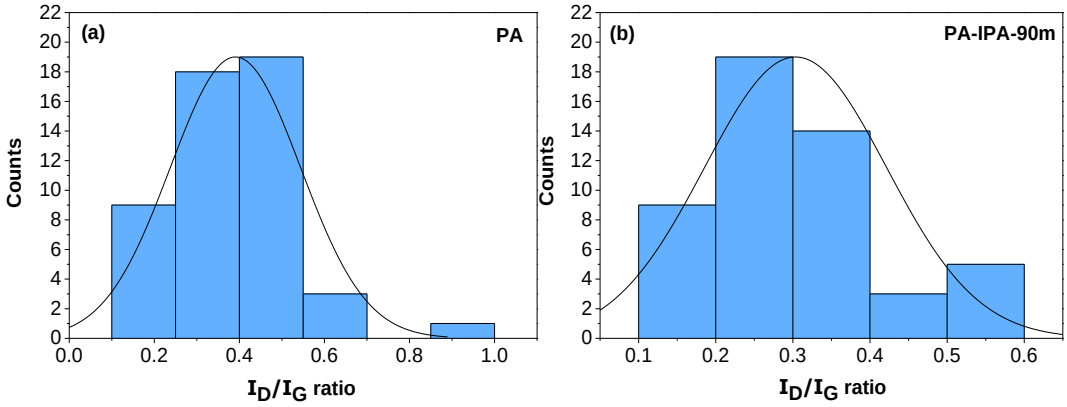

Figure 3.20. Statistical histogram of the $\langle \frac{I_D}{I_G} \rangle$ ratios derived from 50 Raman spectra. **(a)** PA, **(b)** PA-IPA-90min. The distribution curves indicate the mean of the data.

3.3.6. TEM analyses of the starting powders and the exfoliated materials

Electron microscopy enables one to determine the stacking order and the orientation of the graphene layers with respect to each other, as well as determining the number of layers [95].

Figure 3.21 shows a representative low magnification TEM image of the graphene flakes in the EG-IPA-90min-TS sample. The lateral sizes of the flakes are relatively large, which are mostly a few micrometers. Folded and wrinkled regions are observed in most of the flakes (yellow arrows point out the folded regions, white arrows point out the wrinkles). The color contrast in the region shown by the dashed rectangle in Fig. 3.21 reveals single- or bi-layer graphene at the bottom and many other layers which are piled disorderedly on top of it.

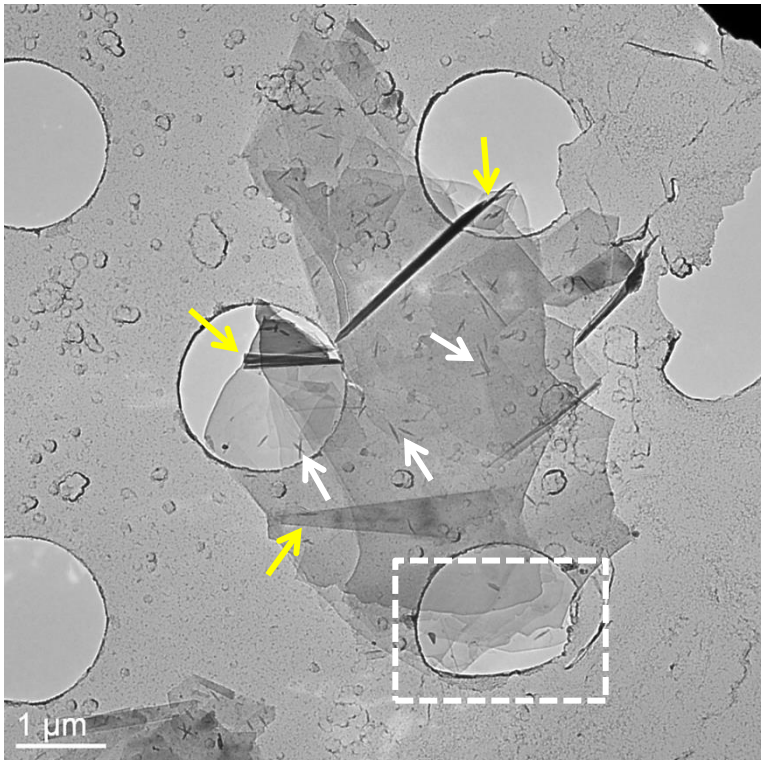

Figure 3.21. TEM image of graphene flakes deposited from EG-IPA-90min-TS dispersion. Yellow arrows show the folded regions, white arrows show the wrinkles and dashed box indicates the graphene layers on top of each other.

Figure 3.22 shows high resolution TEM (HRTEM) images of graphene sheets in EG-IPA-90min-TS sample, revealing the highly crystalline structure of the graphene-based materials obtained by exfoliation of expanded graphite. Corresponding fast Fourier transforms (FFTs) (at the insets in Fig. 3.22) show hexagonal spot patterns indicating the six-fold symmetry feature of graphene. Diffraction patterns and FFTs are also utilized to identify and observe misoriented (turbostratic) graphene sheets [95]. HRTEM analyses of the EG-IPA-90min-TS sample revealed turbostratic graphene (Fig. 3.23), as well as ordered (Bernal stacked) graphene sheets as shown in Fig. 3.22. Figure 3.23(a) shows a Moiré pattern which indicates that graphene layers are misoriented. To be able to see the Moiré pattern more clearly, the region shown by the dashed rectangle in Fig. 3.23(a) was magnified and presented in Fig. 3.23(b). The misalignment in between layers might be a result of restacking of layers with different orientations on top of each other during exfoliation or folding of layers [95]. When graphene layers are rotated with respect to each other, it gives rise to Moiré patterns and changes the periodicity in the graphene lattice [95]. The misorientation (rotation angle) between the top and underlying graphene layers can be calculated using the Moiré rotation-pattern assumption [96]:

$$D_{\text{Moiré}} = \frac{d}{2\sin(\frac{\theta}{2})} \tag{3.4}$$

where, '$D_{\text{Moiré}}$' is the periodicity of the Moiré pattern, 'θ' is the rotation angle between the two layers of the hexagonal lattice and 'd' is the lattice constant (0.246 nm for HOPG).

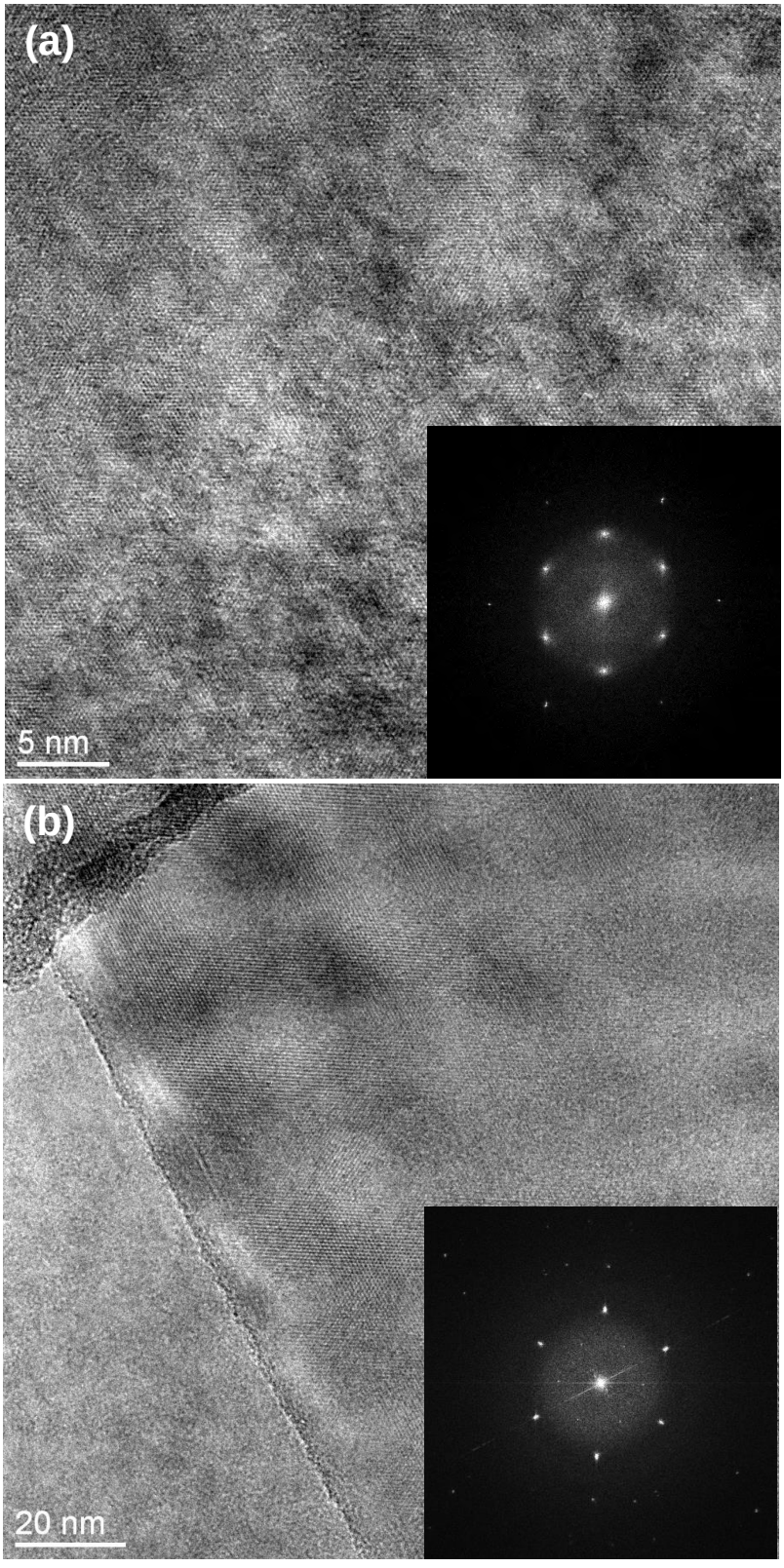

Figure 3.22. (a), (b) HRTEM images of graphene sheets obtained by exfoliation of expandable graphite (EG-IPA-90min sample). Insets show FFT of the corresponding HRTEM images.

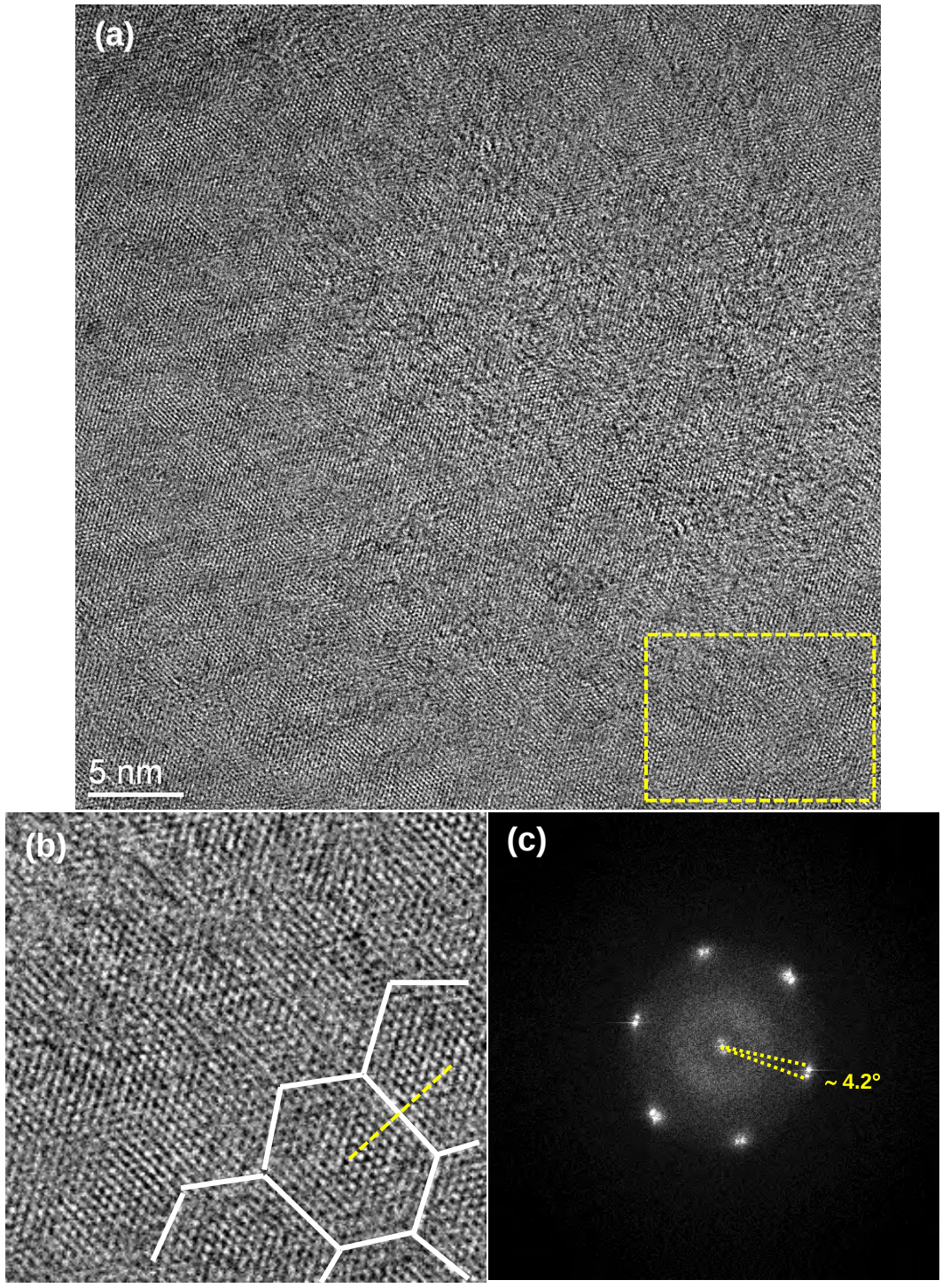

Figure 3.23. (a) HRTEM image of a turbostratic graphene deposited from EG-IPA-90m dispersion revealing a Moiré pattern. **(b)** A magnified image of the region shown by a dashed rectangle in (a). The Moiré pattern with a periodicity of ~3.3 nm (the dashed line) is seen. **(c)** A FFT of the pattern in (a), showing misorientation of layers with a rotation angle of ~4.2°. **(d)** A HRTEM image showing an amorphous layer covering the surface. It's FFT (inset) indicates a rotation angle of 10.5°.

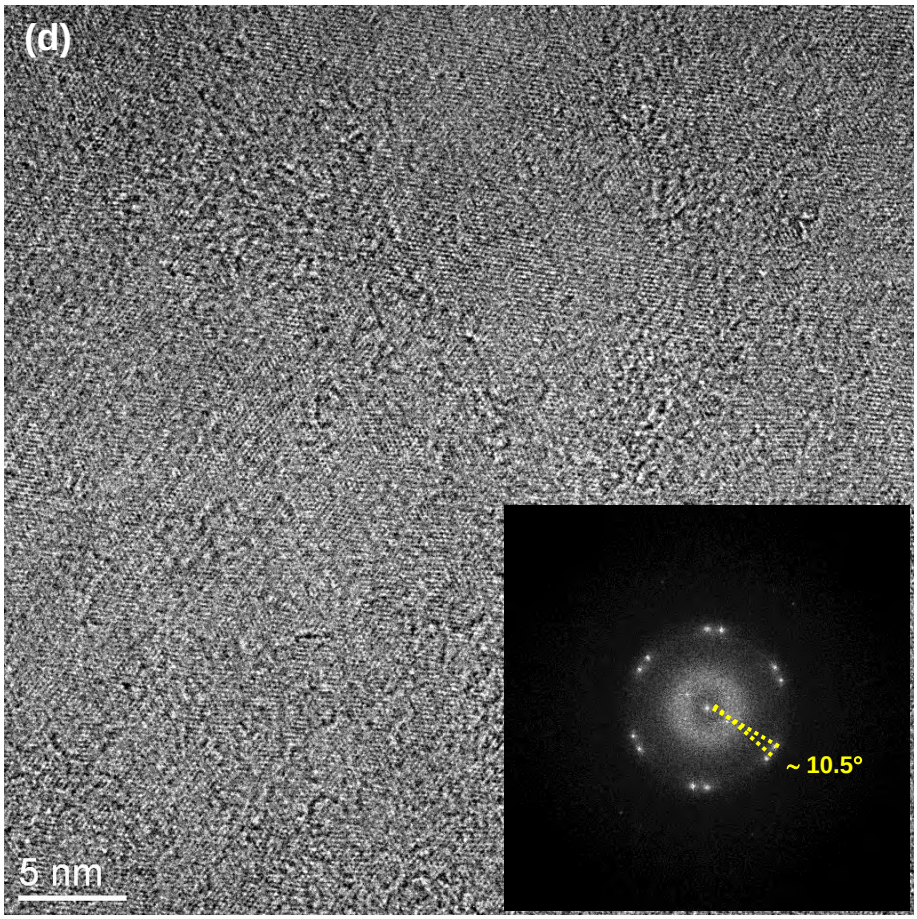

Figure 3.23. (Continued) (a) HRTEM image of a turbostratic graphene deposited from EG-IPA-90m dispersion revealing a Moiré pattern. **(b)** A magnified image of the region shown by a dashed rectangle in (a). The Moiré pattern with a periodicity of ~3.3 nm (the dashed line) is seen. **(c)** A FFT of the pattern in (a), showing misorientation of layers with a rotation angle of ~4.2°. **(d)** A HRTEM image showing an amorphous layer covering the surface. It's FFT (inset) indicates a rotation angle of 10.5°.

The periodicity of the observed Moiré pattern is directly related to the angle of rotation, which can be determined by measuring the angle between neighboring diffraction spots in the same ring of the diffraction pattern [95]. The periodicity of the Moiré pattern shown in Fig. 3.23(b) is ~ 3.3 nm. This periodicity corresponds to a rotation angle of ~4.2° (calculated using Eqn. (3.4)) between graphene layers, which is in good agreement with the value measured between the neighboring spots in the corresponding FFT (Fig. 3.23(c)). Turbostratic graphene reveals itself

in the diffraction pattern or in the FFT by multiple diffraction spots [97]. Rather than having only 6 spots in each ring of the pattern as in the case for single and AB-stacked few layer graphene, several orders of 6 spots (6, 12, 18 etc.) appear for misoriented layers [95]. Figure 3.23(d) shows a HRTEM image of another turbostratic graphene sheet with a higher degree of rotation (~10.5°) as confirmed by its FFT in the inset. A higher rotation angle indicates a smaller Moiré periodicity [95]. It should be also noted that the HRTEM image in Fig. 3.23(d) indicates that the flake surface is not uniform and an amorphous layer is present on the top. This could be due to residual solvent (IPA). HRTEM results also revealed a small amount of graphite flakes (>10 layers) (not shown), as well as single layer, bilayer and turbostratic graphene sheets.

Low magnification TEM micrographs of the starting SEFG powder showed agglomerates/aggregates of graphene/graphite flakes with some impurities on their surface and vicinity (Fig. 3.24(a)). The exfoliation of this powder dispersed these agglomerates to some extent and provided mostly few-layer graphene flakes with a lateral size of a few hundred nanometers. These flakes are mostly folded, scrolled and entangled each other (Fig. 3.24(b)). Wang et al. [98] reported that corrugation and scrolling are part of the intrinsic nature of graphene nanosheets, which result from the fact that the 2D membrane structure becomes thermodynamically stable via bending.

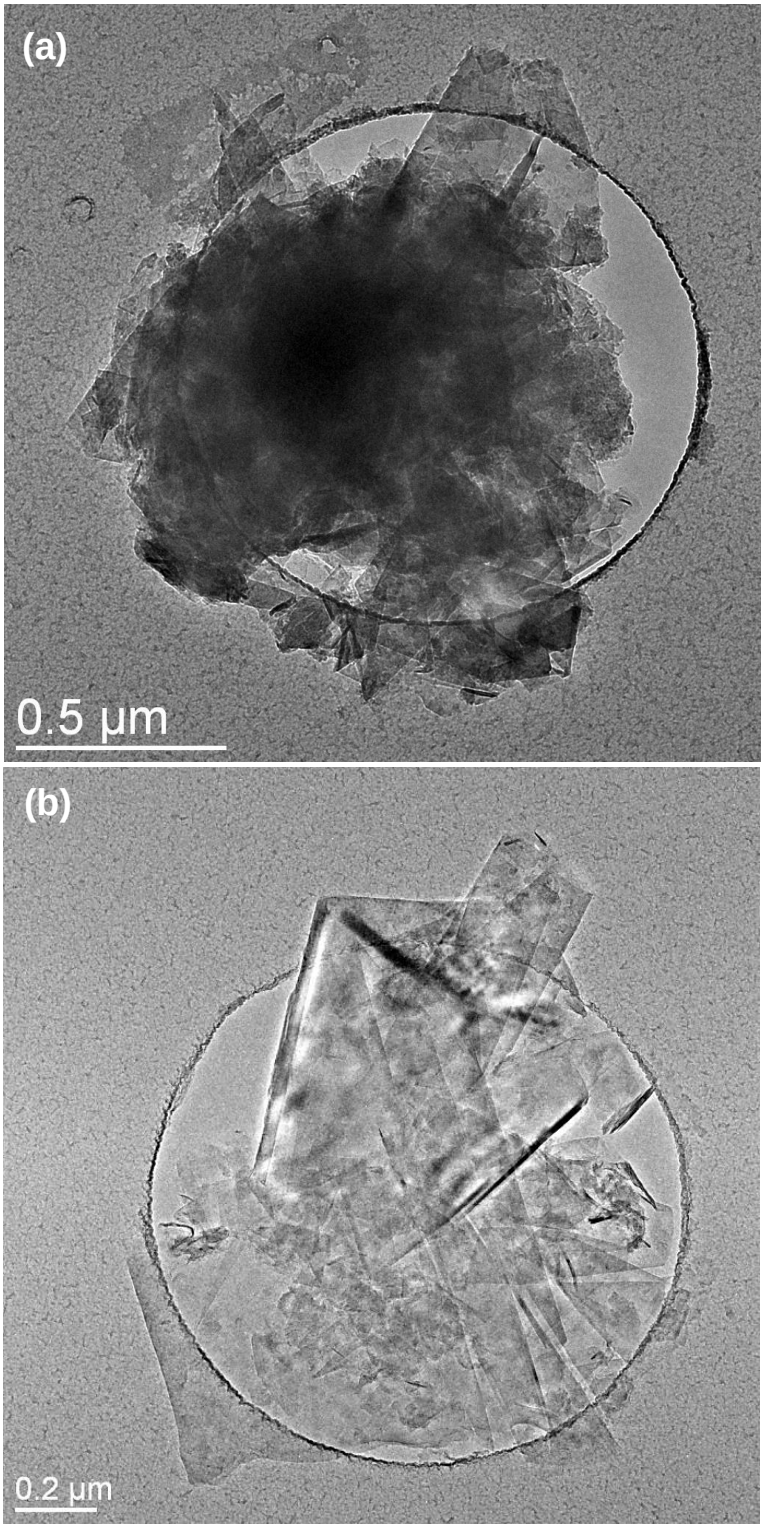

Figure 3.24. TEM images of **(a)** Surface enhanced flake graphite (SEFG) powder and **(b)** Few-layer (<5 layers) graphene sheets achieved after sonication of SEFG in IPA for 90 min followed by centrifugation (SEFG-IPA-90min sample).

Figure 3.25 shows the representative HRTEM micrographs of the flakes deposited from the SEFG-IPA-90m dispersion. FFT images of these micrographs are shown in the insets. HRTEM micrographs revealed mostly few-layer graphene flakes as in agreement with Raman analyses, although sheets with greater than 10 layers were also observed rarely (Figs. 3.25(a) and (b)). Figure 3.25(a) shows a bilayer graphene, the edge of which was folded back allowing for a cross-sectional view. The FFT of this image shows one set of hexagonal spots confirming the six-fold symmetry of graphene and indicating that the fold back part has the same orientation as the original one [99]. Figure 3.25(b) shows several few-layer graphene flakes as well as large, bended and folded graphite flakes which are randomly oriented with respect to each other, as confirmed by the multiple diffraction spots in the FFT (inset in Fig. 3.25(b)). HRTEM analyses also revealed an amorphous layer covering the surface of some flakes (Fig. 3.25(c)). This can be attributed to residual solvent (IPA) or to impurities originating from the starting powder, in agreement with the Raman analyses which revealed a relatively high amount of defects for the SEFG powder.

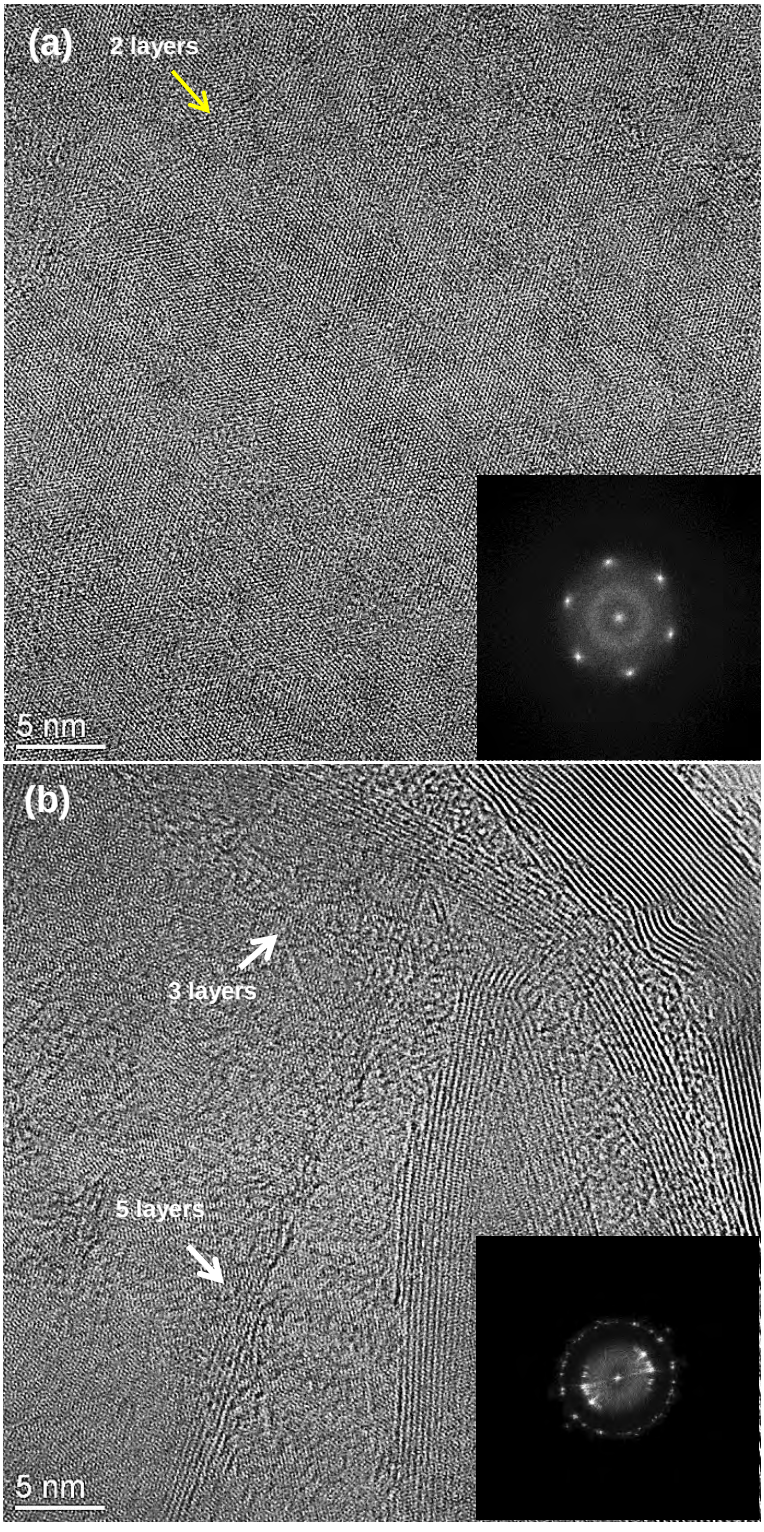

Figure 3.25. HRTEM images of SEFG-IPA-90m sample showing **(a)** a bilayer graphene, **(b)** few-layer (<5 layers) graphene sheets and graphite flakes, **(c)** the presence of an amorphous layer covering the surface. Insets show the FFTs of the corresponding HRTEM micrographs.

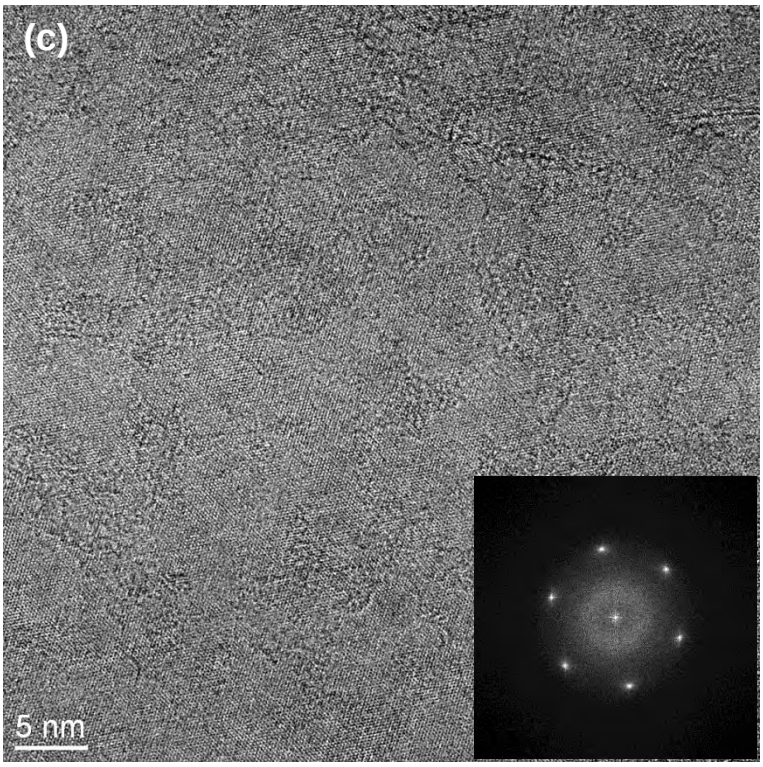

Figure 3.25. (Continued) HRTEM images of SEFG-IPA-90m sample showing **(a)** a bilayer graphene, **(b)** few-layer graphene (<5 layers) and graphite flakes, **(c)** the presence of an amorphous layer covering the surface. Insets show the FFTs of the corresponding HRTEM micrographs.

The HRTEM micrographs and their corresponding FFT images revealed that the SEFG-IPA-90min sample preserves its highly crystalline structure even after annealing at 2600°C in Ar atmosphere for 4 h, confirming the Raman analyses results which indicated that the defects/disorders and impurities in the exfoliated sample mainly arise from the SEFG starting powder and are eliminated and/or recovered by annealing (Fig. 3.26).

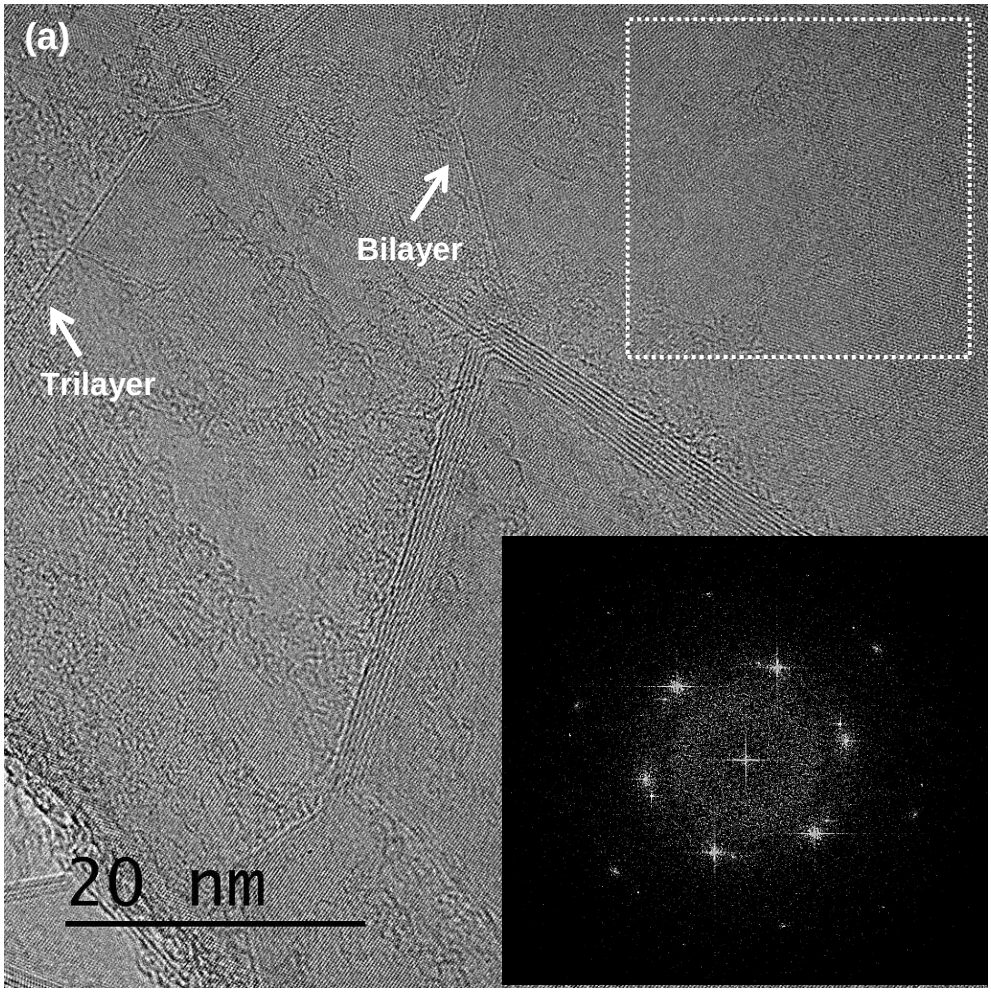

Figure 3.26. HRTEM images of SEFG-IPA-90m sample annealed at 2600°C in Ar atmosphere for 4 h revealing bi-layer and few-layer (<5 layers) graphene sheets **(a), (b)**. Inset in (a) show the corresponding FFT image of the region indicated by the dashed rectangle and inset in (b) is the corresponding FFT image of the micrograph shown in (b).

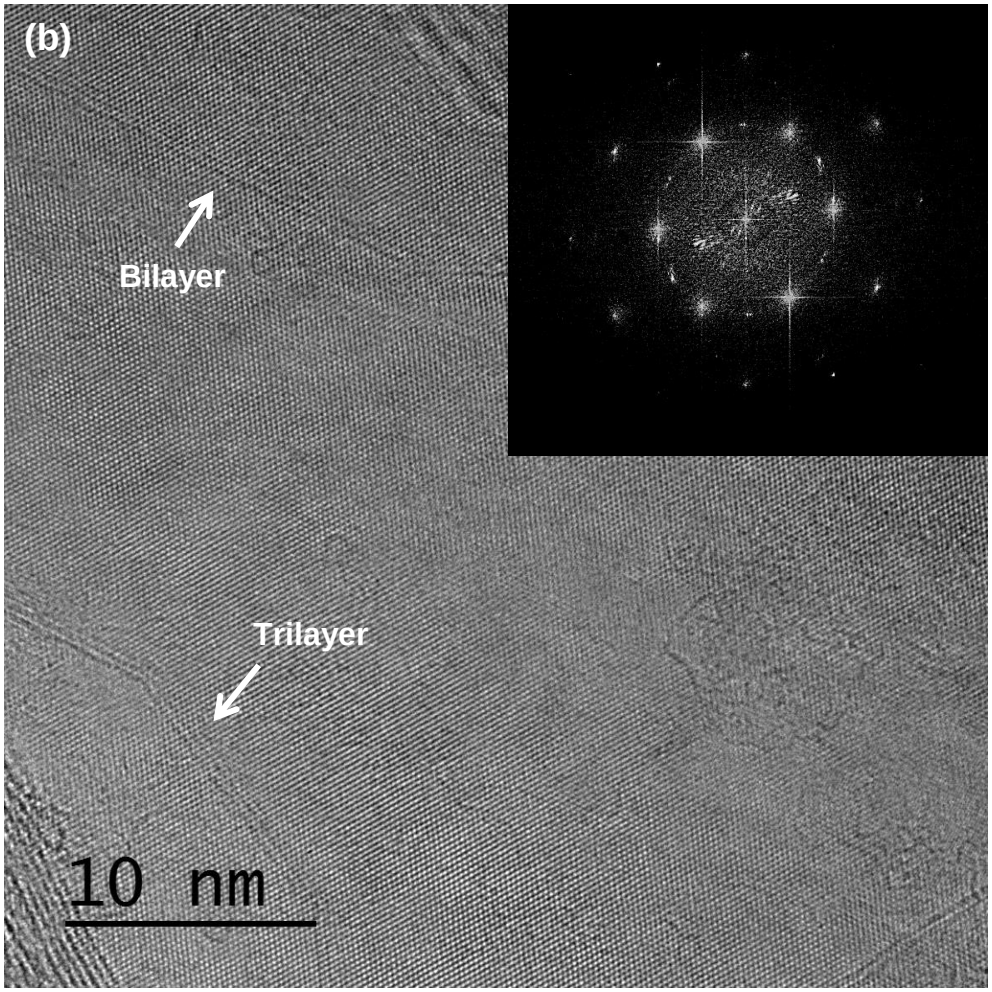

Figure 3.26. (Continued) HRTEM images of SEFG-IPA-90m sample annealed at 2600°C in Ar atmosphere for 4 h revealing bi-layer and few-layer (<5 layers) graphene sheets **(a), (b)**. Inset in (a) show the corresponding FFT image of the region indicated by the dashed rectangle and inset in (b) is the corresponding FFT image of the micrograph shown in (b).

Figure 3.27(a) shows the low magnification TEM micrograph of the PA starting powder. This nano-graphite powder exhibited agglomerates/aggregates of graphite/graphene flakes. Exfoliation process dispersed these agglomerates to some extent similar to the exfoliation of SEFG and revealed graphene-like sheets with a smaller lateral size in comparison to those derived from the SEFG (Fig. 3.27(b)), as in agreement with the DLS analyses. However, large agglomerates were still observed after exfoliation of the PA powder due to relatively high SSA (350 m^2/g) of the PA powder that leads to higher van der Waals forces (Fig. 3.27(c)).

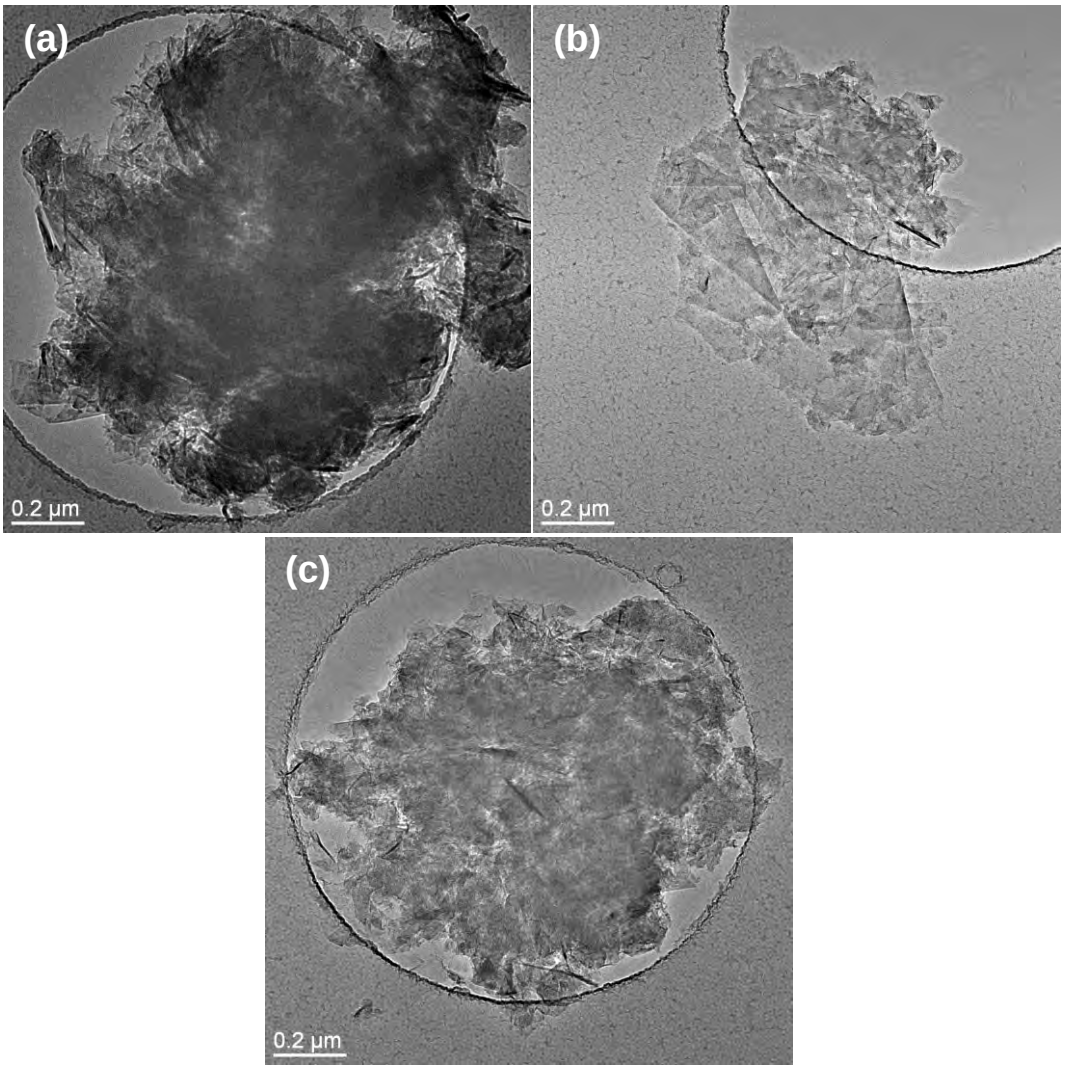

Figure 3.27. Low magnification TEM micrographs of **(a)** Primary artificial (PA) starting powder and **(b), (c)** Exfoliated sample deposited from PA-IPA-90m dispersion.

HRTEM micrographs revealed the edge details of the exfoliated flakes indicating mostly few-layer graphene sheets (<5 layers) confirming the Raman analyses, as well as very few amount of graphite flakes with more than 10 layers (Figs. 3.28(a) and (b)). As shown by the low magnification TEM images, the exfoliated graphene sheets are re-aglomerated and entangled each other. The inset in Fig. 3.28(a) shows the FFT of the corresponding HRTEM micrograph and reveals multiple spots indicating misoriented layers. Traces of the exfoliation process can be realized by observation of a flake with different numbers of layers along its edge as indicated by a dashed circle in Fig. 3.28(b). A non-uniformity over some flake surfaces was also observed during HRTEM analysis (Fig. 3.28(b)). The respective FFT pattern of the region enclosed by a dashed square exhibited a strong contribution of an amorphous phase, which most probably originates from the PA starting powder as in aggrement with the Raman analyses.

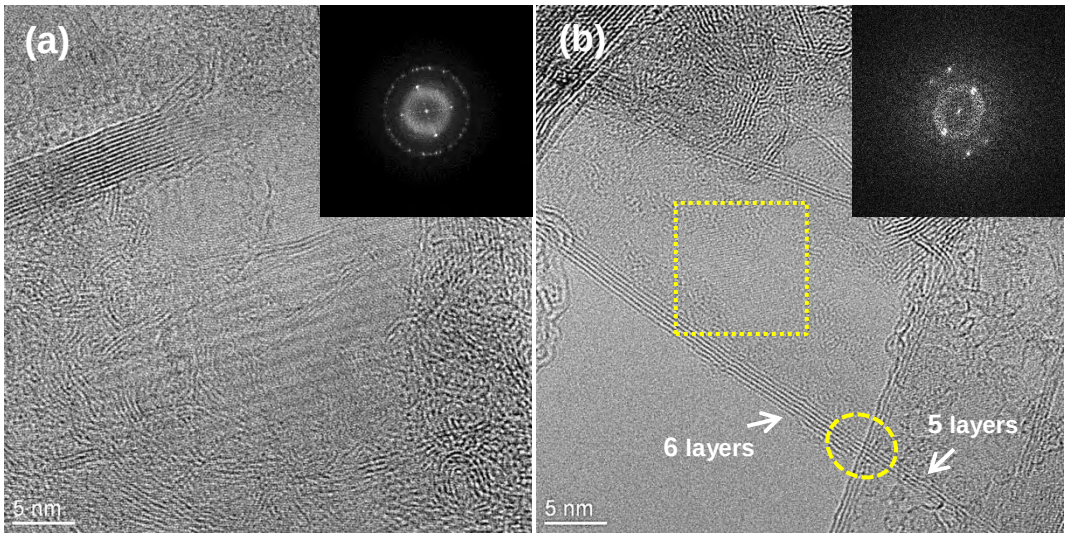

Figure 3.28. HRTEM micrographs of flakes deposited from the PA-IPA-90m dispersion. **(a)** Turbostratic flakes with edge details which allow evaluating the number of layers. **(b)** Few-layer graphene sheets with an amorphous coating on their surface.

3.3.7. Electrical Conductivity Measurements

Four-point probe measurements were performed on thin films on alumina membranes since it is not possible to remove these films from the membranes. The thickness, sheet resistance and conductivity values of the thin films are shown in Table 3.8. The sheet resistances of the thin films prepared from the EG-IPA-90min and the EG-IPA-90min-TS dispersions are 22.9 and 7.3 kΩ/□, respectively, and the conductivity values of these thin films are 1006 and 2104 S/m, respectively. The thin films prepared from the IPA- and NMP-based dispersions of the SEFG and PA precursors resulted in much higher sheets resistances (~226-858 kΩ/□); consequently, much lower conductivity values (~15-52 S/m) than that of the samples prepared from the EG powder. It should be noted that the NMP-based dispersions led to a slightly higher conductivity compared to IPA-based dispersions due to a better exfoliation. These values are higher than those reported by Hernandez et al. [14] who obtained sheet resistance and conductivity values of 7.2 MΩ/□ and 5 S/m, respectively, for their thin graphene films prepared from dispersions of graphite in NMP. However, the authors improved the conductivity of the films to 6500 S/m by annealing them in Ar/H_2 (90%-10%) atmosphere at 250°C for 2 h [14]. The relatively low conductivity values of the graphene-based materials obtained from the SEFG and PA starting powders can be attributed to their small flake sizes. It is known that smaller flakes result in more junctions and consequently in lower conductivity due to effect of inter-flake junction resistances [39, 68]. Moreover, the defects/disorders originating from the starting powder and the residual solvent that were revealed by the Raman and HRTEM analyses may act as scattering regions in these samples. Therefore, the thin films were annealed at 400°C in Ar/H_2 (95:5%) atmosphere for 4 h, which resulted in a decrease in the resistance values (Table 3.8). Especially, the conductivity of the EG-IPA-90min-TS sample improved significantly reaching up to 19200 S/m (corresponding Rs: 0.8 kΩ/□), which is much better than many values reported in the literature [14, 52, 55]. However, the conductivity values of the graphene-based materials obtained from the SEFG and the PA starting powders are still too low for applications such as

transparent electrodes, for which industry specifications require transparencies and sheet resistances better than 90% and less than ~90 Ω/□, respectively [39]. For this purpose, the corresponding film conductivity that meets these requirements should be higher than 7×10^5 S/m [39]. However, the electrical conductivity values achieved in the present study are sufficiently enough to be incorporated into composites to improve the electrical properties of the ceramic or polymer matrix materials.

Table 3.8. Sheet resistance of graphene-based thin films measured by four-point probe technique and the corresponding conductivity values.

	t (nm)	**R_s (kΩ/□)**	**σ_{el} (S/m)**	**R_s (Annealed*) (kΩ/□)**	**σ_{el} (Annealed) (S/m)**
EG-IPA-90min	43	22.9	1006	-	-
EG-IPA-90min-TS	65	7.3	2104	0.8	19200
SEFG-IPA-90min	80	807.8	15	144.8	86
SEFG-IPA-90min-900rpm	71	485.1	29	-	-
SEFG-NMP-90min	86	225.6	52	58.5	199
PA-IPA-90min	76	858.3	15	173.8	76
PA-NMP-90min	79	509.3	25	-	-

t: Thin film thickness
R_s: Sheet resistance
σ_{el}: Electrical conductivity
* Annealing was performed at 400°C in Ar/H_2 (95:5%) atmosphere for 4 h.

3.4. Conclusions

Three different graphite-based materials (expanded graphite (EG) prepared from expandable graphite and two different nano-graphite powders (SEFG and PA)) were investigated as starting powders for the liquid phase exfoliation in a low boiling point solvent, isopropyl alcohol (IPA), within relatively short sonication times (<120 min). Accordingly, using nano-graphite powders as starting materials in LPE process was found to be advantageous for obtaining high-concentration graphene-based dispersions (up to ~1.1 mg/ml). However, the lateral size of the few-layer graphene flakes obtained from the nano-graphite powders was relatively low, leading to a relatively low electrical conductivity, and the dispersibility of the nano-graphite powders decreased with increasing SSA. Expanded graphite enabled production of highly conductive graphene-based materials; however, with a relatively low yield (~0.06 mg/ml). The comparison of the prepared dispersions in terms of concentration, stability, number of layers and quality of the prepared graphene-based materials are summarized below:

- Good quality graphene-based dispersions (I_D/I_G < 0.3) with a relatively high concentration (~1.1 mg/ml) have been successfully prepared in IPA within 90 min of bath sonication by utilizing a surface enhanced (SSA: ~175 m^2/g) nano-graphite powder (SEFG), which was derived from natural graphite. Sheet resistance measurements revealed a relatively high resistance (807.8 kΩ/□) and a low electrical conductivity value (~15 S/m) for the thin film (~80 nm in thickness) prepared from this dispersion (SEFG-IPA-90min). Annealing of this thin film at 400°C in Ar/H_2 atmosphere for 4 h decreased sheet resistance to 144.8 kΩ/□ and resulted in a conductivity value of 86 S/m. Although this electrical conductivity value is too low for transparent conductive electrode applications, it is sufficiently enough for composite applications. The relatively low electrical conductivity of this sample can be attributed to small lateral sizes (D_{50}: 403 nm) of the flakes as well as the impurities/defects originating from the starting powder and the presence of residual solvent. TEM and HRTEM analyses of this sample revealed mostly folded and scrolled few-layer graphene sheets (3-5 layers) entangled each other as in agreement with Raman spectra,

as well as bilayer graphene sheets and very few amount of thicker (>10 layers) graphite flakes. The sedimentation measurements of this dispersion which exhibited the highest concentration among the prepared dispersions revealed a moderate stability with 35% non-sedimenting few-layer graphene sheets remaining in the dispersion after 8 weeks.

- On the other hand, exfoliation of EG in IPA for 90 min by tip sonication enabled production of graphene-based materials with a relatively large lateral sizes (~a few μm), very high quality (I_D/I_G <0.09) and high electrical conductivity (~3167 S/m with the corresponding sheet resistance of 7.3 kΩ/□), especially when annealed (~19200 S/m, 0.8 kΩ/□). However, graphene-based material concentration of the prepared dispersion was relatively low (~0.06 mg/ml) and it exhibited a polydisperse character. HRTEM analyses of these dispersions revealed few-layer (<5 layers) graphene sheets, as well as large graphite flakes. The FFT images of the HRTEM micrographs indicated the presence of turbostratic (misaligned) graphene in this sample. Raman analyses also confirmed the presence of few-layer graphene, as well as graphite flakes. Optimization studies could be performed as a future work to increase concentration and to obtain more uniform dispersions in terms of flake thicknesses.
- HRTEM analyses revealed highly crystalline structures of the graphene-based materials obtained by exfoliation of EG and SEFG powders, but with some non-uniformity on the flake surfaces. However, a very strong contribution of an amorphous phase was observed for the exfoliated sample obtained from PA powder, which is a high surface area (~175 m^2/g) nano-graphite powder derived from synthetic graphite. Although the dispersions prepared from the PA powder in IPA exhibited a relatively high stability, their concentration was much lower (~0.45 mg/ml in case of 90 min sonication) than that of the dispersions prepared from the SEFG powder.
- Consequently, SEFG powder was found to be a promising starting material for an environmentally friendly, time and cost effective, and a high yield liquid phase exfoliation process, which may enable mass production of readily applicable graphene-based materials for the applications such as composites. In

Chapter 4, the applicability of the SEFG-IPA-90m sample into ceramic matrix nanocomposites to improve mechanical, electrical and thermal properties of the matrix material was investigated.

4. ANISOTROPIC MECHANICAL AND FUNCTIONAL PROPERTIES OF GRAPHENE-BASED Al_2O_3 MATRIX NANOCOMPOSITES

4.1. Introduction

Nanocomposites, which exhibit superior mechanical and physical properties compared to their respective matrix materials, are among the most technologically promising materials to meet the worldwide demand for high performance applications in many fields. In that respect, development of novel nanocomposites with improved properties plays a critical role to extend their use in industry.

Nanocomposite is defined as a composite in which nanoparticles are dispersed in a continuous matrix. Generally accepted length scale for the nanophase is <100 nm in at least one dimension. Continuous phase in such composite structures can be ceramic, metallic or polymeric materials, either in bulk or thin film forms [100]. Nanocomposites differ from conventional composites in terms of higher chemical reactivity of grain boundaries due to small size of the reinforcing phases. Each crystalline particle consists of inner ordered lattice atoms and outer disordered grain boundary atoms. In nanoparticles and bulk nanocrystalline materials, the grain boundary (i.e., surface) atoms have much higher volume fraction than conventional materials. These grain boundary atoms are electronically unsaturated and chemically active that may result in some unusual electromagnetic behaviors which sometimes cannot be predicted by simple rule of mixtures. For example, the strengths of Al_2O_3 and SiC are 800 MPa and 500 MPa, respectively; however, a nanocomposite, composed of Al_2O_3 and SiC, shows 1500 MPa strength [100, 101], where grain boundary interaction plays an important role on the strength improvement [100].

Carbon-based fillers, especially carbon nanotubes (CNTs), have been widely utilized in nanocomposite research in order to improve structural and functional properties of various host materials [102-107]. However, dispersing CNTs homogeneously throughout a matrix is a big challenge since they show high tendency to agglomeration and bundle formation. Graphene-based materials are promising candidates as filler materials in nanocomposites due to their unique combination of outstanding mechanical properties and exceptionally high thermal

and electrical conductivities. Furthermore, their two dimensional nature and high aspect ratio may enable dispersion of graphene-based materials easier with respect to CNTs during nanocomposite production [108, 109].

Studies on nanocomposites containing graphene-based materials have been mainly focused on polymer matrices and it has been shown that significant multifunctional property enhancements are possible even at low filler contents. Recent achievements and advances in graphene-based polymer matrix composites have been reviewed by many authors [110-112]. In addition, potential of graphene-based fillers in ceramic matrix nanocomposites has been realized in recent years. High mechanical strength, thermal resistance and good chemical stability of monolithic ceramics make them promising materials for high technology applications such as electronics, defense, aerospace and transportation. However, they tend to be brittle and are poor electrical conductors, which limit their use in many potential applications [109]. Wear resistant materials and structural materials for extreme environments, such as high temperature/pressure, nuclear radiation, and chemicals, are required to be both strong and tough [113]. It is also challenging to shape these materials into complex geometries due to their brittle nature. Manufacturing of complex-shaped ceramic parts is possible by electro discharge machining (EDM), if the material has a certain level of electrical conductivity (>0.3 – 1 Sm^{-1}) [114]. Therefore, it is essential to improve mechanical and electrical properties of ceramic materials, which can be provided by nanocomposite formation. Porwal et al. [109] have also recently reviewed the state of the art of graphene-based ceramic matrix nanocomposites. Although, significant improvements of mechanical and electrical properties of monolithic ceramics have been reported with incorporation of graphene-based materials, there is very limited number of study where thermal properties of graphene-based ceramic matrix nanocomposites were investigated [115]. Table 4.1 gives a summary of the mechanical and functional properties reported for graphene-based ceramic matrix nanocomposites in the literature.

Table 4.1. Mechanical and functional properties of graphene-based ceramic matrix composites reported in the literature† The results for carbon nanotube reinforced ceramics were also included for comparison.

Mechanical Properties						
Matrix material	**Filler type††**	**Filler Content**	**Processing route /sintering method**	**Orientation dependent measurement**	**Investigated property (maximum value measured - % improvement compared to monolith)**	**Ref.**
Si_3N_4	Reduced -graphite oxide (thermally)	1.5 vol.%	Colloidal/SPS 99.6% RD	No	HV: 15.7 GPa $K_{Ic(m)}$: 2.8 MPa $m^{1/2}$ (by Vickers indentation) $K_{Ic(c)}$: 6.6 MPa $m^{1/2}$ **(235% increase)**	[116]
Al_2O_3	Reduced-graphene oxide (chemically)	2 wt.%	Colloidal/SPS	No	$K_{Ic(m)}$: 3.40 MPa $m^{1/2}$ (by SENB) $K_{Ic(c)}$: 5.21 MPa $m^{1/2}$ **(53% increase)**	[117]
Al_2O_3	Exfoliated expanded graphite (commercial)	0.38 vol.%	Powder/SPS	No	$K_{Ic(m)}$: 3.53 MPa $m^{1/2}$ (by SENB) $K_{Ic(c)}$: 4.49 MPa $m^{1/2}$ **(27.2% increase)** $G_{f(c)}$: 523 MPa **(30.8% increase)** $Hardness_{(c)}$: 17.66 GPa	[118]
ZrO_2-toughened Al_2O_3	Exfoliated expanded graphite (commercial)	0.81 vol.%	Powder/SPS	No	$K_{Ic(m)}$: 6.46 MPa $m^{1/2}$ (by SENB) $K_{Ic(c)}$: 9.05 MPa $m^{1/2}$ **(40% increase)**	[119]
Si_3N_4 + ($AlN+Al_2O_3+Y_2O_3$)	Exfoliated graphite	3 wt.%	Powder/HIP and SPS	No	$K_{Ic(c)\ (HIP)}$: 4.29, $K_{Ic(c)\ (SPS)}$: 3.24 $MPam^{1/2}$ $HV_{(HIP)}$: 12.6 GPa, $HV_{(SPS)}$: 17.37 GPa $E_{(HIP)}$: 214 GPa, $E_{(SPS)}$: 227 GPa	[120]
Si_3N_4 + (4 wt% Al_2O_3+ 6 wt% Y_2O_3)	Milled multilayer graphene*****, Exfoliated graphite nanoplatelet and graphene platelet (commercial)	3 vol.%	Powder/HIP	No	HV: 16.4 GPa (by Vickers indentation) $K_{Ic(m)}$: 6.9 MPa $m^{1/2}$ $K_{Ic(c)}$: 9.9 MPa $m^{1/2}$ **(43.5% increase)**	[121]
Al_2O_3	Chemically exfoliated graphene*****, graphene oxide, reduced-graphene oxide	0.5 vol.%	Colloidal/Pressureless sintering (solid state and liquid phase) RD >95%	No	$K_{Ic(m)}$: 3.28 MPa $m^{1/2}$ (by SENB) $K_{Ic(c)}$: 5.6 MPa $m^{1/2}$ **(75% increase)** $G_{f(c)}$: 430 MPa **(25% increase)**	[113]

Table 4.1. (Continued) Mechanical and functional properties of graphene-based ceramic matrix composites reported in the literature[†] The results for carbon nanotube reinforced ceramics were also included for comparison.

Mechanical Properties						
Matrix material	**Filler type[††]**	**Filler Content**	**Processing route /sintering method**	**Orientation dependent measurement**	**Investigated property (maximum value measured - % improvement compared to monolith)**	**Ref.**
Al_2O_3	Few-layer graphene (simultaneously reduced graphene oxide during SPS)	0.6-1.2 vol.%	Colloidal/SPS RD >98.2%	No	Hardness: 25.4 for Al_2O_3 (by nanoindentation) Similar or lower hardness for nanocomposites 'E' decrease with graphene addition	[122]
Al_2O_3	Graphene oxide (simultaneous reduction during SPS)	0.22 wt%	Colloidal/SPS 99% RD	**Yes**	$K_{Ic(m)}$: 3.4 MPa $m^{1/2}$ (by Vickers indentation) $K_{Ic(c)}$: 5.1 MPa $m^{1/2}$ **(50% increase in through-thickness direction)** $K_{Ic(c)}$: 3.2 MPa $m^{1/2}$ (in-plane)	[123]
Al_2O_3	Multi-wall carbon nanotubes (MWNTs)	0.9 vol.%	Precursor method/SPS	No	$K_{Ic(c)}$: 5.9 MPa $m^{1/2}$ **(25% increase)** (by SENB)	[124]
Al_2O_3	Single-wall carbon nanotubes (SWNTs)	10 vol.%	SPS	No	$K_{Ic(m)}$: 3.7 MPa $m^{1/2}$ $K_{Ic(c)}$: 9.7 MPa $m^{1/2}$ **(162% increase)**	[125]
Functional Properties						
Matrix Material	**Filler Type**	**Filler Content**	**Processing route/sintering method**	**Orientation dependent measurement**	**Investigated property (maximum value measured)**	**Ref.**
Al_2O_3	Graphene oxide (simultaneous reduction during SPS)	0.22 wt%	Colloidal/SPS (RD >97%)	**Yes**	$\rho_{el(m)}$: 10^9 Ω.cm $\rho_{el(c)}$: 15 Ω.cm (through-thickness direction) $\rho_{el(c)}$: 75 Ω.cm (in-plane direction)	[123]
Al_2O_3	Milled expanded graphite	0.8-15 vol.%	Powder/SPS	No	σ: 5709 S/m (for 15 vol.% filler content) Percolation threshold: 3 vol.%	[108]
Al_2O_3	Reduced-graphene oxide (chemically)	2 wt.%	Colloidal/SPS	No	σ: 172 S/m (10^{13} times higher than monolithic Al_2O_3)	[117]

Table 4.1. (Continued) Mechanical and functional properties of graphene-based ceramic matrix composites reported in the literature[†] The results for carbon nanotube reinforced ceramics were also included for comparison.

Functional Properties						
Matrix Material	**Filler Type**	**Filler Content**	**Processing route/sintering method**	**Orientation dependent measurement**	**Investigated property (maximum value measured)**	**Ref.**
Si_3N_4 + (2 wt% Al_2O_3+ 5 wt% Y_2O_3)	Graphene platelets (commercially available) - exfoliated before processing	4-24 vol.%	Powder/SPS (99% RD)	**Yes**	σ: 4000 S/m (in-plane direction-for 24 vol.% filler content) Percolation threshold:7-9 vol.% (depending on measuring direction)	[126]
Al_2O_3	Few-layer graphene (simultaneously reduced graphene oxide during SPS)	0-2.35 vol.%	Colloidal/SPS	No	0.38 vol.% percolation threshold, σ: 1038.2 S/m for 2.35 vol.% filler content	[127]
Si_3N_4 + (2 wt% Al_2O_3+ 5 wt% Y_2O_3)	Graphene platelets (commercially available)	4.3-24.4 vol.%	Powder/SPS	**Yes**	Thermal conductivity: 40 $W.m^{-1}.K^{-1}$ in-plane direction – twice that of the Si_3N_4 matrix	[115]
$MgAl_2O_4$	SWNTs	0.23-24.5 vol.%	In-situ growth by CCVD	No	σ_{el}: 0.4-850 S/m	[104]
Al_2O_3	SWNTs	15 vol.%	SPS	No	σ_{el}: 3345 S/m	[128]

[†] Adapted from Ref.[109].

[††] The filler type shows the detailed description of the graphene-based material used in the corresponding reference rather than the short denominations that the authors used.

* indicates the filler type for which the properties in the table are reported for.

RD: relative density

$K_{ic(m)}$: fracture toughness of monolithic material, **$K_{ic(c)}$:** fracture toughness of nanocomposite

HV: Vickers Hardness, **SENB:** single edge notch beam, **$G_{f(c)}$:** flexural strength of nanocomposite, **E:** Elastic modulus

$\rho_{el(m)}$: electrical resistivity of monolithic material, **$\rho_{el(c)}$:** resistivity of nanocomposite

σ_{el}: electrical conductivity of nanocomposite at room temperature

SPS: spark plasma sintering, **HIP:** hot isostatic pressing, **CCVD:** catalytic chemical vapor deposition

The filler types in Table 4.1 show mostly detailed description of the graphene-based material rather than the general denominations (such as graphene nanosheets, graphene nanoplatelets, etc.) that the authors used in the corresponding references, in order to clarify the possible effects of different types of graphene-based materials on the measured properties. It should be noted here that there is an inconsistency in naming of different derivatives of graphene-based materials which sometimes causes confusions in the literature. Generally, different types of graphene materials (e.g., few-layer graphene, multi-layer graphene, graphite nanosheet/nanoplatelet, graphene platelet and graphene nanosheet/nanoplatelet) are not clearly distinguished. The terms of 'graphene nanoplatelets' or 'graphene nanosheets' are widely used to describe flakes with 0.05-10 μm in length and width, and 1–10 nm in thickness [121]. However, it is recommended to use prefix 'nano' together with 'graphene' to describe the lateral dimensions since the presence of the word 'graphene' itself implies a two-dimensional material whose thickness is always less than 100 nm; therefore, there is no need to include 'nano' to describe the thickness of a material [129]. On the other hand, the prefix 'nano' can be used to distinguish ultrafine graphite forms (thickness <100 nm) from thicker flakes [129]. Recently, editorial team of *Carbon* journal has reported a recommended nomenclature, where they refer two-dimensional graphite materials having a thickness and/or lateral dimension less than 100 nm to 'graphite nanoplatelets (GNPs)' or 'graphite nanosheets (GNSs)' [129]. On the other hand, Shahil and Balandin [130] proposed that it is reasonable to consider the material to be multilayer graphene (MLG) as opposed to graphite as long as its Raman spectrum is distinctively different from that of bulk graphite. The authors also assume that MLG has much larger lateral dimensions than their thickness, while the lateral dimensions of GNPs can be of the same order of magnitude as the thickness, i.e., the aspect ratio can be close to one, which lead to differences in thermal properties between MLG and GNPs [130]. Therefore, the graphene-based material, which generally has higher thickness compared to few-layer (2-5 layers) and multilayer (2-10 layers) graphene due to agglomeration and/or overlapping of individual sheets, but has a Raman spectrum different from that of bulk graphite, as in the case of the exfoliated materials used in the present

study, will be further referred to ‘graphene platelets (GPLs)’ in order to prevent any confusion from characterization point of view.

One of the main challenges of graphene-based nanocomposite manufacturing is the mass production of high quality graphene-based materials with a reasonable lateral size. Liquid phase exfoliation routes are promising to produce graphene-based materials in a large scale. These techniques utilize inexpensive graphite powder as a starting material and exfoliate it down to thin flakes dispersed as a colloidal suspension in a solvent with or without surfactant [68], as described in detail in Chapter 3. The critical point in these methods is to be able to increase graphene-based material concentration as much as possible while maintaining high quality of the flakes. GPLs are attractive fillers in nanocomposites since they can be easily produced at large scales by liquid phase exfoliation, as well as their outstanding properties. Therefore, they are also expected to be also the low cost alternatives to CNTs.

GPLs may enable one to develop multifunctional nanocomposites with anisotropic properties for a wide range of applications due to their unique two-dimensional geometry, high aspect ratio and stiffness. It has been shown that GPLs can be preferentially oriented in the matrix during spark plasma sintering (SPS). However, the number of studies where anisotropy in graphene-based ceramic matrix nanocomposites was investigated is very limited. Centeno et al. [123] investigated effect of orientation of reduced graphene oxide sheets on mechanical properties of Al_2O_3 matrix nanocomposites, but only for one composition. Ramirez et al. [126] examined anisotropic electrical conductivity of GPLs–containing Si_3N_4 nanocomposites as a function of orientation of the GPLs. Miranzo et al. [115] investigated anisotropic thermal conductivity of Si_3N_4 ceramics containing GPLs. Although Al_2O_3 has been one of the most widely utilized matrix materials, thermal conductivity of graphene-based materials/Al_2O_3 nanocomposites has not been investigated to date. Accordingly, the objective of this study was to produce Al_2O_3 matrix nanocomposites using the GPLs that were produced by liquid phase exfoliation (as described in Chapter 3) as a filler, and to investigate effects of preferential orientation of GPLs in the matrix on their

mechanical, thermal and electrical properties all together for the first time in the literature.

4.2. Experimental Procedure

4.2.1. GPLs/Al_2O_3 Nanocomposite Production

High concentration (~1.3 mg/ml) graphene-based dispersions were prepared by exfoliation a high surface area nano-graphite powder in isopropyl alcohol (IPA) within a short bath sonication time (90 min). The dispersion preparation process and the characterization of the obtained GPLs (*SEFG-IPA-90min sample*) are given in detail in 'Chapter 3' of this thesis. α-Al_2O_3 powder (TM-DAR, Taimei Chemicals Co., Japan – 99.99% purity and ~0.1 μm average particle size) was dispersed separately in IPA by magnetic stirring for ~1 h in combination with bath sonication for ~5 min in every 15 min. The graphene-based dispersion was then incorporated into the Al_2O_3 suspension during magnetic stirring in required amounts as to provide 3, 5, 7, 9, 10 and 15 vol.% GPLs and stirred for ~45 min. The resulting GPLs/Al_2O_3 mixtures were ball milled in IPA at 200 rpm for 3 h using yitria-stabilized ZrO_2 balls. The milled slurry was dried by rotary evaporator and then ground in an agate mortar. Well dispersed GPLs/Al_2O_3 powder was then loaded into a 14 mm inner diameter graphite die and sintered by spark plasma sintering (SPS, FCT System GmbH - Anlagenbau, Germany) at 1250-1600°C (depending on the graphene content) for 5 min under a uniaxial pressure of 50 MPa. The dimensions of the sintered samples were ~14 mm in diameter and ~8 mm in thickness. SPS method enables rapid heating rates and applying pressure simultaneously; therefore, it limits thermally induced structural damage to the graphene by avoiding long processing times at high temperatures [116]. As a result of the applied pressure during SPS, GPLs are preferentially oriented in the matrix with their basal planes perpendicular to the SPS pressing axis, as shown in Fig. 4.1. The direction parallel to the SPS pressing axis will be referred to as through-thickness and the direction perpendicular to the SPS pressing axis will be referred to as in-plane direction, from now on. Mechanical, thermal and electrical

characterizations of the nanocomposites were performed by taking this anisotropy into consideration. Samples with ~8 mm × 8 mm × 1-2 mm were cut along both the in-plane and through-thickness directions for further characterization.

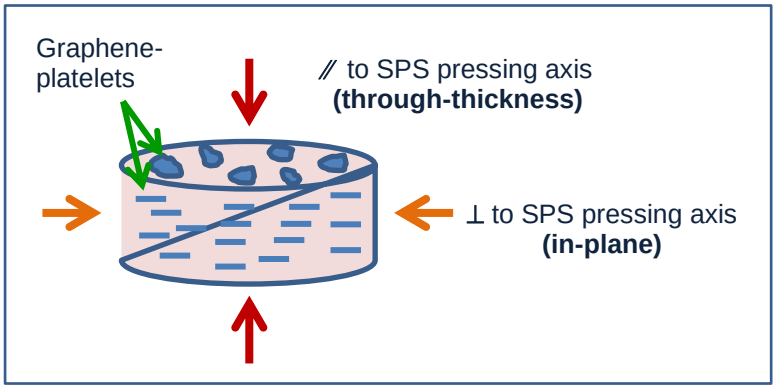

Figure 4.1. Schematic representation of orientation of GPLs in the matrix with the help of applied pressure during SPS process.

Density of the nanocomposites was measured by Archimedes method with water immersion. In order to determine their relative density, the theoretical density of the nanocomposites was calculated by the volume-based rule of mixtures assuming densities of 3.96 g/cm^3 and 2.2 g/cm^3 for Al_2O_3 and GPLs, respectively. The microstructure of the samples was characterized by field emission gun – scanning electron microscope (FEG-SEM, Supra 50 VP). Micro-Raman analyses of the initial GPLs, the as-prepared 10 vol.% GPLs containing Al_2O_3 powder and of the 10 vol.% GPLs/Al_2O_3 nanocomposites (on both through-thickness and in-plane directions) were performed on a Renishaw Invia spectrometer using 532 nm laser excitation and 100x objective lens. The laser power was kept below 1 mW in order to prevent sample damage. 50 spectra were recorded (each one at a different location) for these samples to create statistical histogram of the I_D/I_G ratio.

4.2.2. Mechanical Characterization

Vickers hardness tests were performed by applying a force of 2 kg on the polished sample surfaces. Hardness and fracture toughness values of the monolithic Al_2O_3 and the nanocomposites were determined from Vickers indentations and the corresponding crack-length measurements using Eqn. (4.1) and Eqn. (4.2) [131], respectively.

$$HV = \frac{1.8P}{a^2} \tag{4.1}$$

$$K_{IC} = 0.16HV(a^{1/2})(\frac{c}{a})^{-3/2} \tag{4.2}$$

where HV is the Vickers hardness, K_{IC} is the fracture toughness, P is the indentation load, 'a' is the length of indentation half diagonal and 'c' is the average crack length measured at the tips of the crack trace (Fig. 4.2).

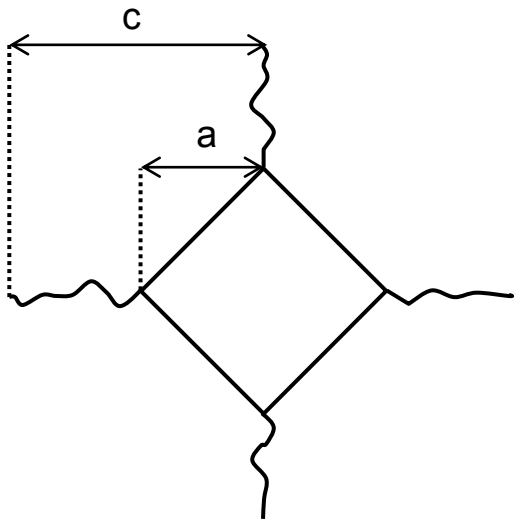

Figure 4.2. Schematic representation of cracking around Vickers indentation mark.

4.2.3. Electrical Characterization

Electrical measurements were also performed along both in-plane and through-thickness directions. The resistance of the samples was first measured by Signatone semi-automatic probe station connected to Keithley 4200 semiconductor characterization system. Au-Pd coating was applied to the surfaces of interest by sputtering. Monolithic Al_2O_3 and nanocomposites with 3, 5 and 7 vol.% GPLs exhibited high resistance, while nanocomposites with higher GPLs contents showed conductive behavior. In order to eliminate the possible effect of sample thickness on the orientation dependent conductivity measurements, cubic samples (~ 5 mm × 5 mm × 5 mm) were cut from the sintered nanocomposites with 9, 10 and 15 vol.% GPLs. The corresponding surfaces of the cubic samples were coated with Au-Pd before each measurement. The resistance values were measured by Agilent 4294 Precision Impedance Analyzer in through-thickness and in-plane directions. The corresponding conductivity values were then calculated by using the following equations:

$$\rho_{el} = R\frac{S}{l} \tag{4.4}$$

$$\sigma_{el} = \frac{1}{\rho_{el}} \tag{4.5}$$

where R is the resistance, ρ_{el} is the electrical resistivity, S is the cross-sectional area, l is the length and σ_{el} is the electrical conductivity.

4.2.4. Thermal Characterization

In-plane and through-thickness thermal diffusivity measurements were carried out from room temperature up to 600°C at intervals of ~100°C in N_2 atmosphere by laser flash method using Netzsch LFA 457 Microflash (USA) equipment. Three shots were recorded per temperature for each sample and the data were averaged. Specific heat (C_p) measurements of the monolithic Al_2O_3 and the nanocomposites with 3, 7, 10 and 15 vol.% GPLs contents were carried out by a differential scanning calorimeter (Netzsch STA 449F3, USA) in 42-700°C temperature range in N_2 atmosphere using a sapphire crystal as a reference. HSC Chemistry Software 7.0 [132] was also used to estimate the C_p, for comparison. The C_p values of Al_2O_3 (corundum) and graphite were determined by this software as a function of temperature from 25°C to 700°C with intervals of 1°C. The C_p of the GPLs/Al_2O_3 nanocomposites was then calculated using the rule of mixtures by taking weight fractions of the components into consideration. The experimental C_p values were used for further thermal conductivity calculations. The C_p values at room temperature and of the 5 and 15 vol.% GPLs/Al_2O_3 samples were determined by extrapolation and interpolation of the measured data. The corresponding thermal conductivity (k) values were calculated by using the following expression [133]:

$$k = \alpha . \rho . C_p \tag{4.3}$$

where α and ρ represent the thermal diffusivity and density, respectively.

Thermo-gravimetric analysis (TGA) of 15 vol.% GPLs/Al_2O_3 nanocomposite was carried out using Netzsch STA 409 PC/PG in air up to 1000°C with a heating rate of 10°C/min in order to investigate its stability in air.

4.3. Results and Discussion

4.3.1. Microstructure Development

The exfoliated graphite nanoplatelets used in the present study are mostly composed of few-layer (< 5 layers) graphene sheets with a lateral size of <1 μm (~400 nm in average diameter of equivalent spherical particle as determined by dynamic light scattering analysis) as confirmed by high resolution TEM and Raman analyses. However, the individual few-layer graphene sheets are usually folded, scrolled and entangled each other during processing, forming the so-called GPLs in this study. A detailed characterization of this material is given in 'Chapter 3' of this thesis with a denomination as SEFG-IPA-90m.

Figure 4.3 shows the relative density of the nanocomposites sintered at 1300°C as a function of the GPLs content. The density of the nanocomposites decreased significantly with increasing GPLs volume fraction, indicating that GPLs addition hinders densification of Al_2O_3. On the other hand, grain growth would be inevitable, especially for the monolithic Al_2O_3 and the low amount of GPLs containing nanocomposites, if the samples are sintered at a higher temperature (e.g., at 1600°C). Therefore, each nanocomposite was sintered at a specific temperature depending on their GPLs content to ensure that all the nanocomposites exhibit as high densification as possible. As a result, the monolithic Al_2O_3 and the nanocomposites were highly densified with relative densities of ≥98.5%. Table 4.2 shows sintering temperatures of the nanocomposites depending on the GPLs content and the resultant grain size of the nanocomposites. Sintering of each sample at their optimum sintering temperature enables one to investigate the effect of GPLs on the mechanical properties more clearly by eliminating the effect of grain size on these properties.

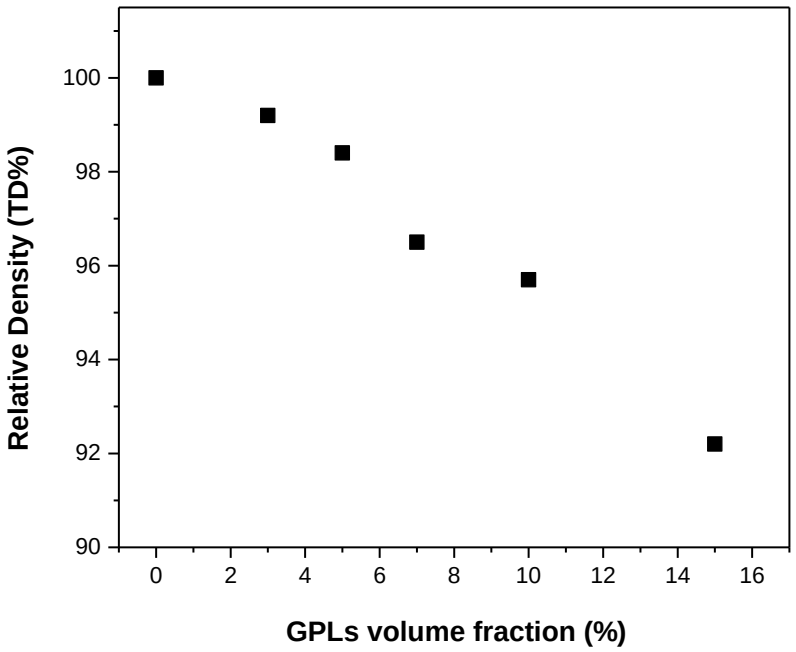

Figure 4.3. Relative density of the nanocomposites sintered at 1300°C as a function of the GPLs content.

Table 4.2. Sintering temperature, relative density and mean grain size for the monolithic Al_2O_3 and the nanocomposites.

Graphene Content (vol.%)	Sintering Temperature (°C)	Relative Density (%TD)	Mean Grain Size (μm)
0	1250	100	2.39
3	1350	99.6	Bimodal (0.7, 1.4)
5	1400	99.4	1.27
7	1450	98.7	1.31
9	1500	99.2	1.31
10	1525	98.7	1.36
15	1600	98.5	1.33

Figure 4.4 shows the FEG-SEM micrographs of the fracture surfaces of sintered monolithic Al_2O_3 and nanocomposites. The monolithic Al_2O_3 is composed of equiaxed-shaped faceted grains with ~2.4 μm in size in average (determined by ImageJ software) (Fig. 4.4(a)). Addition of GPLs inhibited grain growth of Al_2O_3 resulting in a finer microstructure (Fig. 4.4 and Table 4.2). This could be attributed to distribution of GPLs around the matrix grains and between the grain boundaries, which pinned the movement of grain boundaries. Except for the nanocomposite with 3 vol.% GPLs content, the fracture surfaces of the sintered nanocomposites revealed mostly uniform microstructures indicating the homogeneous distribution of GPLs throughout the matrix (Fig. 4.4). It can be clearly seen from these micrographs that some of the GPLs are agglomerated and overlapped forming flakes with ~50 nm in thickness, while the thinner ones are located around the matrix grains and cannot be easily observed. The thick GPLs are aligned in the matrix with their basal planes perpendicular to the SPS pressing axis, leading to an anisotropic microstructure (Figs. 4.4(b)-(f)); consequently, orientation dependent mechanical properties, such as fracture toughness, were observed. 3 vol.% GPLs containing nanocomposite exhibited a bimodal microstructure with some very fine (~0.7 μm in diameter), faceted and equiaxed matrix grains, as well as relatively larger grains (~1.4 μm in average) (Fig. 4.4(b)). This indicates that 3 vol.% is not a sufficient amount for GPLs to be distributed around most of the Al_2O_3 grains in the matrix; therefore, different grain growth rates were observed in the microstructure. Higher GPLs loadings resulted in much more uniform microstructures.

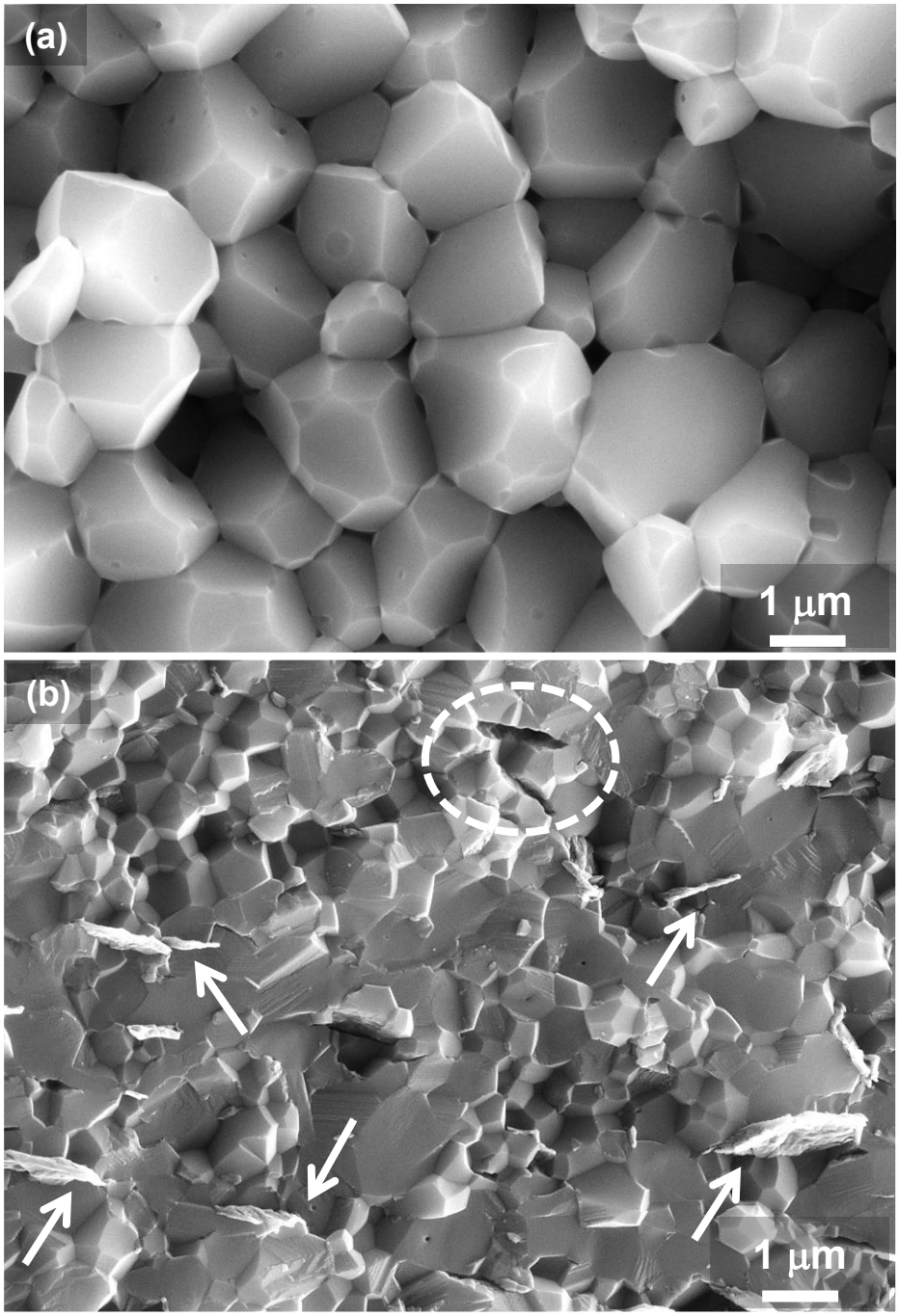

Figure 4.4. FEG-SEM micrographs of fracture surfaces of **(a)** monolithic Al_2O_3 and of nanocomposites with GPLs contents of **(b)** 3 vol.%, **(c)** 5 vol.%, **(d)** 7 vol.%, **(e)** 10 vol.% and **(f)** 15 vol.%. White arrows indicate the aligned protruded and pulled-out GPLs; dashed circle shows the pulled-out GPLs.

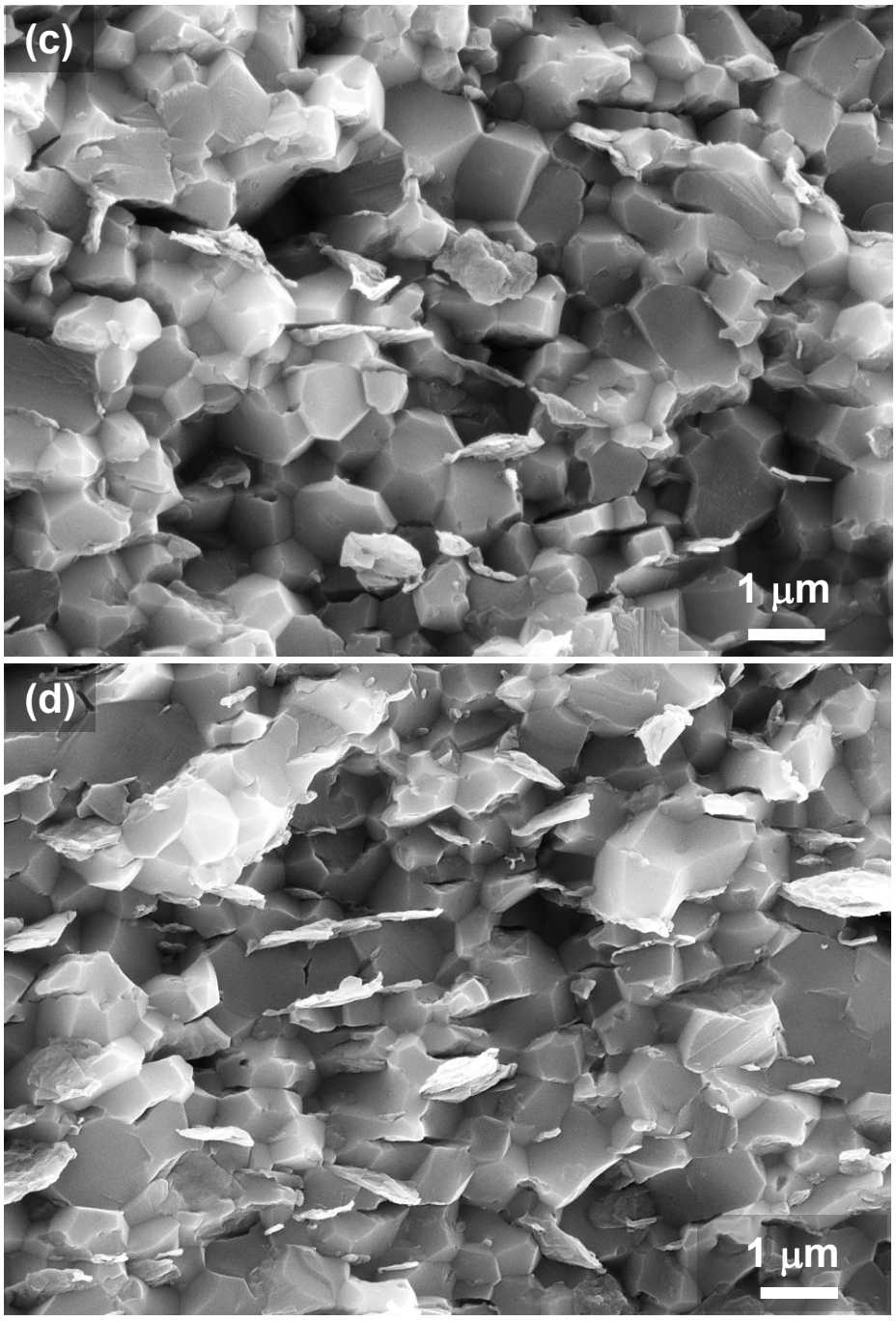

Figure 4.4. (Continued) FEG-SEM micrographs of fracture surfaces of **(a)** monolithic Al_2O_3 and of nanocomposites with GPLs contents of **(b)** 3 vol.%, **(c)** 5 vol.%, **(d)** 7 vol.%, **(e)** 10 vol.% and **(f)** 15 vol.%. White arrows indicate the aligned protruded and pulled-out GPLs; dashed circle shows the pulled-out GPLs.

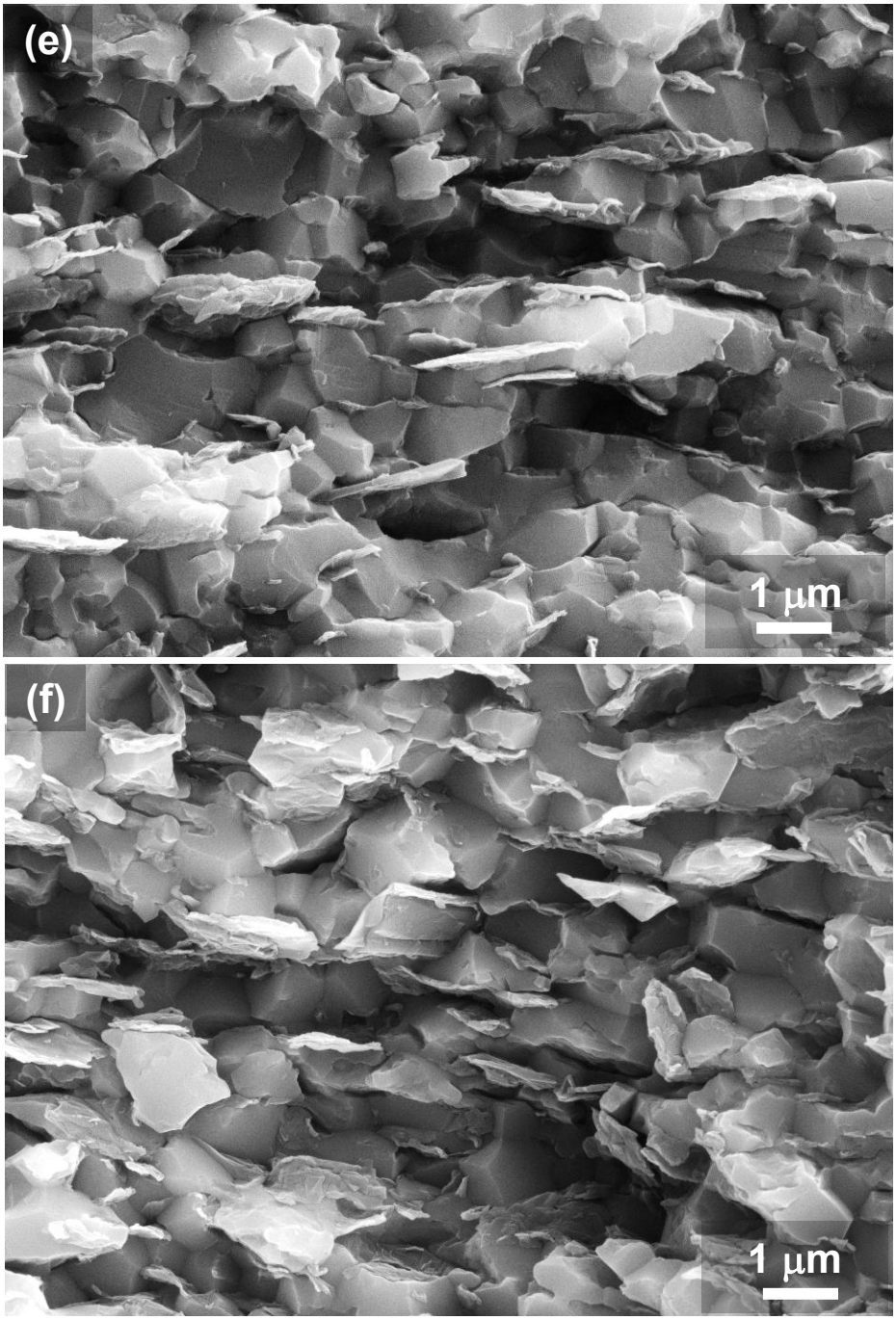

Figure 4.4. (Continued) FEG-SEM micrographs of fracture surfaces of **(a)** monolithic Al_2O_3 and of nanocomposites with GPLs contents of **(b)** 3 vol.%, **(c)** 5 vol.%, **(d)** 7 vol.%, **(e)** 10 vol.% and **(f)** 15 vol.%. White arrows indicate the aligned protruded and pulled-out GPLs; dashed circle shows the pulled-out GPLs.

4.3.2. Mechanical Properties

The fracture surface of monolithic Al_2O_3 revealed intergranular fracture mode, while the GPLs/Al_2O_3 nanocomposites exhibited a combination of transgranular and intergranular fractures (Fig. 4.4). The trend of the Al_2O_3 grains to fracture transgranularly in the nanocomposites indicates the improved interfacial strength, relative to the grain strength. The fracture mode and the mechanical properties of ceramic nanocomposites strongly depend on the strength of grain boundaries. The strong boundary may force the cracks to deflect into the matrix grain, resulting in a transgranular fracture [134]. Fan et al. [108] reported that the phenomena of transgranular fracture increases in milled expanded graphite containing Al_2O_3 nanocomposites compared to monolithic Al_2O_3, suggesting the high strength of the graphene-based material, as in agreement with the present study. Liu et al. [119] observed that the fraction of transgranular mode decreases with increasing graphene platelet (exfoliated expanded graphite) amount in zirconia-toughened alumina composites. The authors suggested that the bonding strength between the graphene platelets and the matrix is less than that between the ZrO_2 and Al_2O_3, and also less than the strength of the Al_2O_3 grains [119]. Wang et al. [117] reported that their reduced graphene oxide-based Al_2O_3 nanocomposite exhibits a predominantly intergranular fracture mode. The authors explained this phenomenon by the existence of residual stress at the Al_2O_3 grain boundaries caused by thermal expansion mismatch which may weaken the interface boundaries. Dusza et al. [121] attributed the observed differences in fracture modes in various studies depending on the interfacial strength to the different characteristics of the graphene-based materials and to the different composite production routes.

Table 4.3 shows the mechanical properties of the monolithic Al_2O_3 and the GPLs/Al_2O_3 nanocomposites. It was observed that hardness values decreased with GPLs content, although the nanocomposites have a much finer microstructure in comparison to the monolithic Al_2O_3. This can be explained by sliding or cleavage of GPLs under the in-plane and out-of plane stresses, as suggested by Fan et al. [122]. The authors also proposed that the graphene addition modifies the faceted

morphology of the Al_2O_3 grains; consequently, deformation can be facilitated since the movement of the rounded surfaces becomes easier [122].

Table 4.3. Mechanical properties of GPLs/alumina composites

Graphene Content (vol.%)	Hardness (GPa)	K_{IC} (Through-thickness) ($MPa.m^{1/2}$)	K_{IC} (in-plane) ($MPa.m^{1/2}$)
0	18.4	2.93	2.95
3	16.2	2.41	3.76
5	15.1	2.59	3.60
7	13.1	2.81	2.98
9	11.8	2.95	3.11
10	11.3	3.18	2.83
15	9.8	3.20	2.58

Fracture toughness of the monolithic Al_2O_3 and the nanocomposites as a function of GPLs content is plotted along both through-thickness and in-plane directions in Fig. 4.5. Preferential orientation of GPLs throughout the matrix resulted in anisotropy in the fracture toughness values. Fracture toughness of monolithic Al_2O_3 was almost same in the in-plane and through-thickness directions (2.95 and 2.93 $MPa.m^{1/2}$, respectively). It increased by ~27.5% in the in-plane direction and decreased by ~17.7% in through thickness direction with the addition of 3 vol.% GPLs into the monolithic Al_2O_3 (Fig. 4.5). The FEG-SEM micrograph of the fracture surface of this nanocomposite revealed the protruded and pulled-out thick GPLs, which are aligned mostly through the in-plane direction (Fig. 4.4(b)). The change of the fracture mode from intergranular to transgranular with the introduction of GPLs into the monolithic Al_2O_3 is a clear indication of improved interfacial strength; however, it is clear that this bonding is weak enough to allow de-bonding at the GPLs-Al_2O_3 interface in the in-plane direction. Delamination of the GPLs themselves may also occur. As a result, energy that would normally cause crack propagation is partially expended by de-bonding and shear, resulting in an increase in fracture toughness [135]. Accordingly, pull-out was supposed to be the main toughening mechanism for the 3 vol.% GPLs containing Al_2O_3 nanocomposite in the in-plane direction. Further

increase in GPLs content started to decrease the in-plane fracture toughness (Fig. 4.5, Table 4.3). The highest GPLs loading (15 vol.%) resulted in a reduction in the fracture toughness by ~12.5% and ~31% compared to the monolithic Al_2O_3 and the 3 vol.% GPLs containing nanocomposite, respectively. The decrease in the fracture toughness could be attributed to weakening of the interface after a certain amount of GPLs loadings (>3 vol.%).

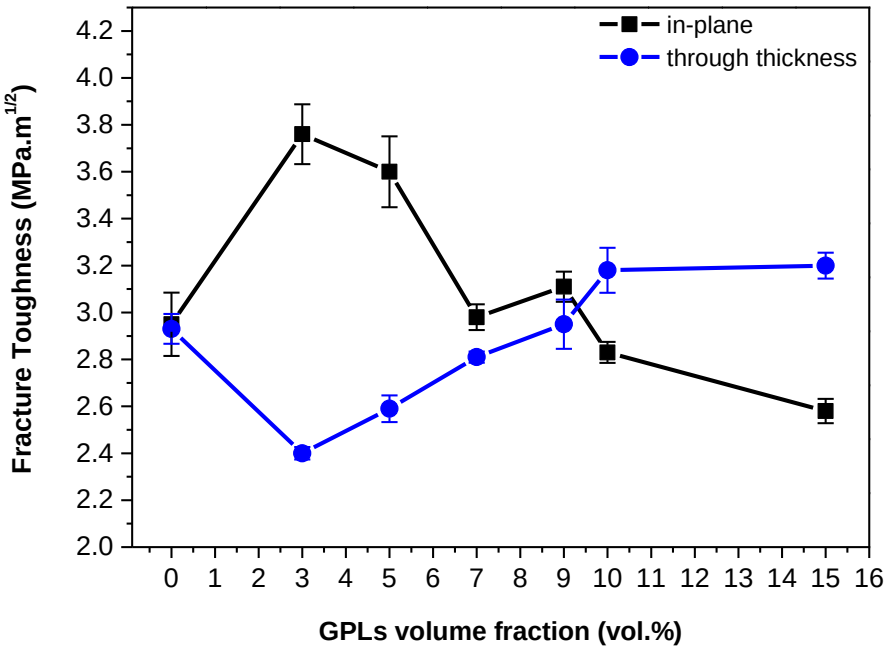

Figure 4.5. Through-thickness and in-plane fracture toughness values of GPLs/Al_2O_3 nanocomposites as a function of GPLs content.

Figure 4.6 shows the in-plane crack paths originating from the Vickers indentations on the monolithic Al_2O_3 and the nanocomposites with 3, 5 and 7 vol.% GPLs contents. The crack paths of the nanocomposites revealed both straight and tortuous regions indicating that the fracture is a mixture of intergranular and transgranular modes, as in agreement with the fracture surfaces. GPLs showed a higher tendency to agglomerate and to overlap at higher loadings. As a result of this agglomeration/overlapping, the amount of large pores between the matrix grains and the thick GPLs increased resulting in weakening of the interfacial bonding in the in-plane direction (Fig. 4.7). This is in agreement with Liu et al. [118] who reported that the large pores are thought to be the origin of

the fractures and weaken the strength of ceramic composites. Dusza et al. [121] prepared Si_3N_4 matrix nanocomposites using various graphene-based materials with different geometry, length/width and thickness. Similarly, they observed that the graphene platelets with larger lateral size and higher thickness, and overlapped graphene platelets are usually connected with porosity, which may result in a weak adhesion bond of graphene platelet/matrix and lower energy dissipation during pull-out [121].

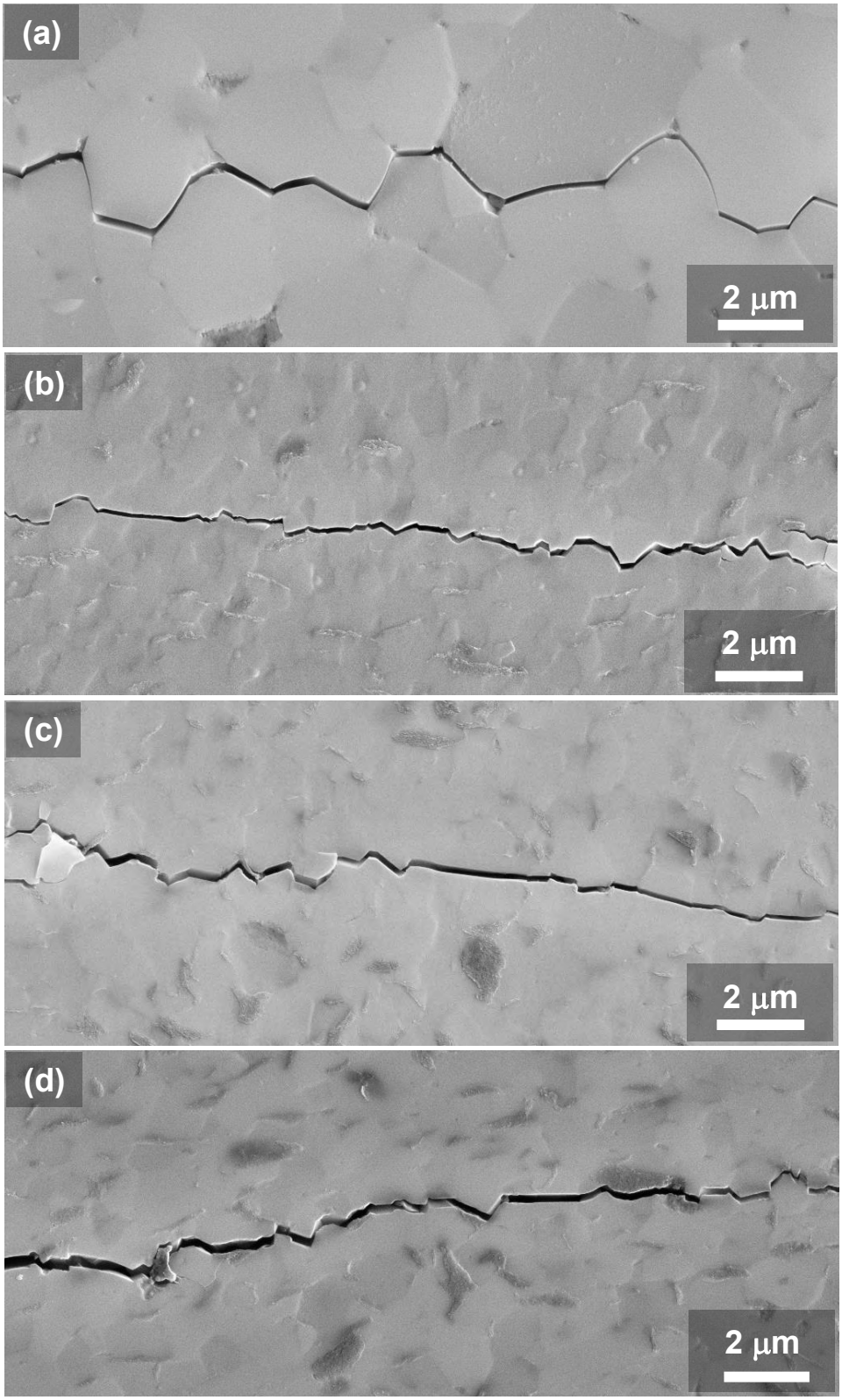

Figure 4.6. FEG-SEM micrographs of in-plane crack paths (created by indentation) of monolithic Al_2O_3 **(a)** and of GPLs/Al_2O_3 nanocomposites with **(b)** 3 vol.%, **(c)** 5 vol.% and **(d)** 7 vol.% GPLs.

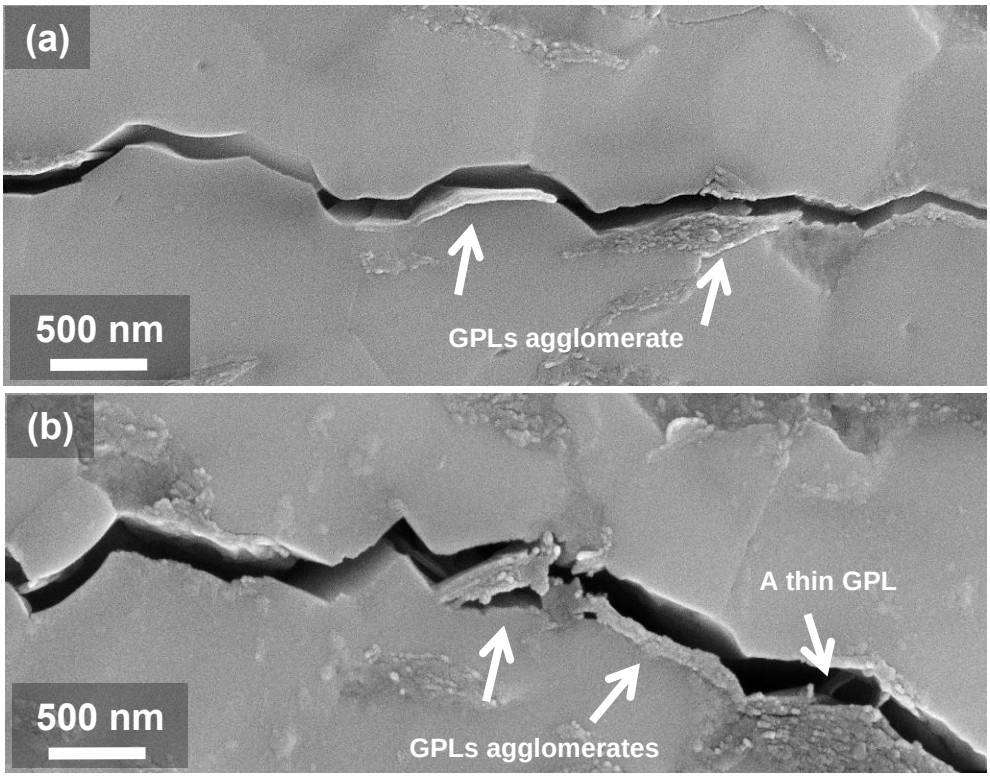

Figure 4.7. High magnification FEG-SEM micrographs of in-plane crack paths (created by indentation) of GPLs /Al_2O_3 nanocomposites with **(a)** 10 vol.% and **(b)** 15 vol.% GPLs.

The decrease in the through-thickness fracture toughness with 3 vol.% GPLs addition could be attributed to the GPLs-Al_2O_3 interface which might be too strong in that direction; therefore, the possible pull-out or bridging mechanisms are prevented and the crack is forced to pass through the GPLs. Further increase in GPLs amount started to increase the fracture toughness in through-thickness direction and the fracture toughness of the nanocomposites got higher than that of the monolithic Al_2O_3 in through-thickness direction at GPLs loadings of ≥ 9 vol.% (Fig. 4.5). Figure 4.8 shows the FEG-SEM micrographs of the through-thickness crack paths originating from the Vickers indentations on the monolithic Al_2O_3 and the nanocomposites with 3, 5, 7, 10 and 15 vol.% GPLs contents. The crack path of the 5 vol.% GPLs/Al_2O_3 nanocomposite, which exhibited a slightly higher fracture toughness than that of the 3 vol.% GPLs/Al_2O_3 nanocomposite, but that is still lower than that of the monolithic alumina, showed a damaged

GPLs induced by crack penetration through it (Fig. 4.8(c)). Crack deflection and crack bridging were observed as the main toughening mechanisms in through-thickness direction especially at relatively low GPLs loadings (~5-7 vol.%) (Figs. 4.8(c),(d)). Increasing GPLs content to ≥9 vol.% led to a much more tortuous and narrower crack path (Figs. 4.8(e)-(f)). Crack branching appeared for the 15 vol.% GPLs containing nanocomposite as a dominant toughening mechanism (Fig. 4.8(f)), resulting in ~9% and ~33% increase in fracture toughness with respect to the monolithic Al_2O_3 and the 3 vol.% GPLs containing nanocomposite, respectively (Fig. 4.5, Table 4.3). These results reveal that the mechanical properties of the GPLs/Al_2O_3 nanocomposites were strongly affected by the orientation of the GPLs throughout the matrix. However, the number of studies which report the effect of anisotropy on the mechanical properties of graphene-based ceramic matrix nanocomposites is very limited. Centeno et al. [123] measured the fracture toughness of one of their reduced-graphene oxide reinforced Al_2O_3 nanocomposites (0.22 wt.% graphene loaded Al_2O_3) along both in-plane and through-thickness directions. The authors reported 50% improvement on the fracture toughness measured in through-thickness direction in comparison to monolithic Al_2O_3 due to graphene bridging effect in that direction [123]. However, they obtained a similar fracture toughness value to that of the monolithic Al_2O_3 in the in-plane direction due to the orientation of the flakes, which induce crack to propagate along the Al_2O_3 grain boundaries in the same way as in the monolithic Al_2O_3 [123].

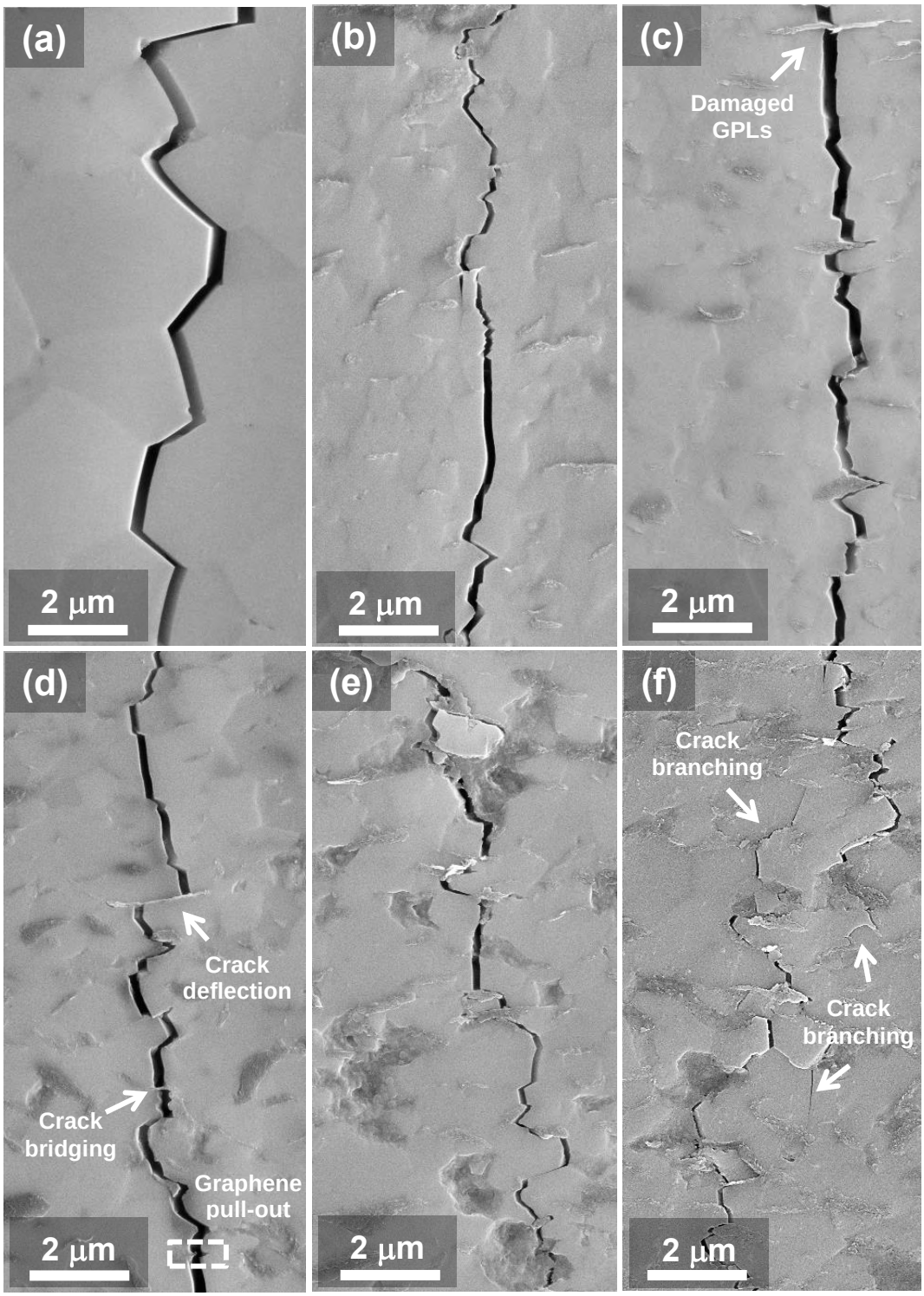

Figure 4.8. FEG-SEM micrographs of through-thickness crack paths (created by indentation) of **(a)** monolithic Al_2O_3 and of GPLs/Al_2O_3 nanocomposites with **(b)** 3 vol.%, **(c)** 5 vol.%, **(d)** 7 vol.%, **(e)** 10 vol.% and **(f)** 15 vol.% GPLs.

Figure 4.9 gives a summary of the GPLs orientation dependent toughening mechanisms observed in the GPLs/Al_2O_3 nanocomposites as a function of GPLs content.

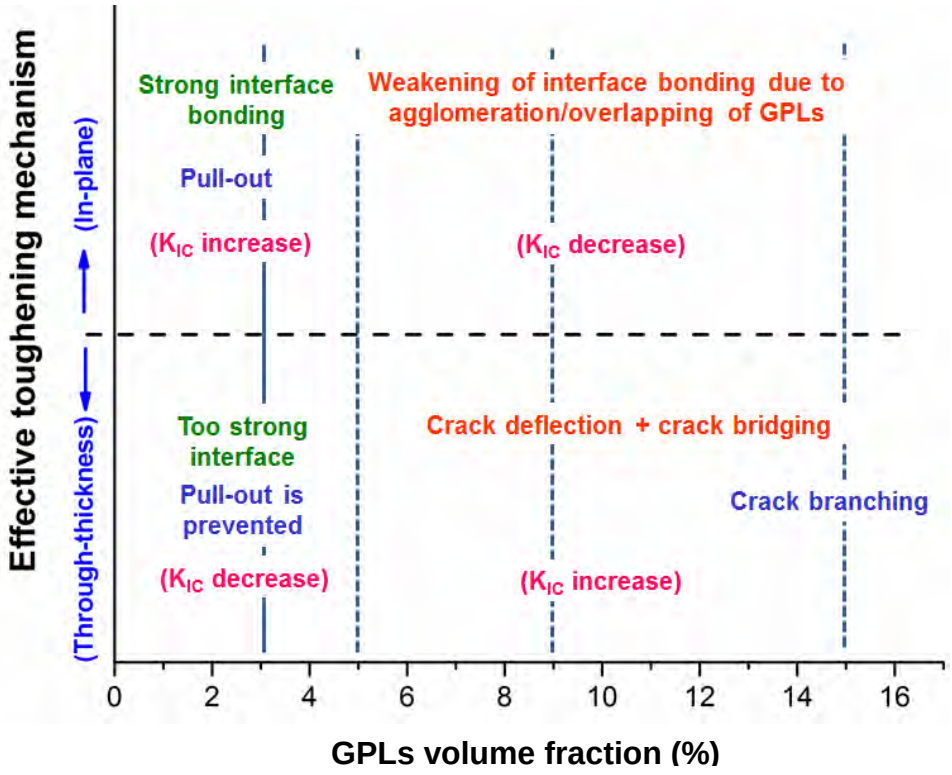

Figure 4.9. Summary of the suggested toughening mechanisms in GPLs/Al_2O_3 nanocomposites depending on GPLs content

It should be noted that the Vickers indentation fracture test is not a recommended method to measure fracture toughness of ceramic materials since it may not give reliable and accurate results [136]. However, it is an easy and quick method with a short sample preparation time [136]; and above all, it is applicable when there is a limited amount of material to test. This technique has been preferred to measure the fracture toughness of CNT-reinforced [137, 138] and graphene-reinforced [113, 116] ceramic matrix composites, for which satisfactory results were reported. This technique was also successfully used in the present study to achieve comparative results depending on the GPLs content and orientation. However, in contrast to relatively high improvements of fracture toughness of ceramic

materials with graphene-based material reinforcing, such as 75% and 135% improvements as reported by Kim et al. [113] and Walker et al. [116], respectively; lower increment could have been achieved in the present study. The relatively low fracture toughness values could arise from the tendency of the GPLs to agglomerate and to overlap especially at relatively high loadings, and from lower aspect ratio of the GPLs used in the present study. The extent of the final toughening strongly depends on the aspect ratio of the graphene-based material and high aspect ratio platelets are generally found to be more beneficial to the mechanical properties of a composite [111]. The intrinsic mechanical properties of the graphene-based fillers also play an important role in their reinforcement efficiency. The strength of the graphene-based materials is affected by their quality (defect content). Kim et al. [113] produced graphene-based alumina nanocomposites by pressureless sintering using different graphene materials (chemically exfoliated graphene, graphene oxide and reduced-graphene oxide) and compared the mechanical properties of these nanocomposites. They reported that the ultra-thin (2-5 nm) un-oxidized platelets (0.5 vol.%), which have the lowest defects, provided the greatest improvement (~75%) in fracture toughness compared to monolithic Al_2O_3 [113]. Graphene oxide and reduced-graphene oxide showed little or less enhancement of fracture toughness (by 14% and 48%, respectively) due to degraded mechanical strength of the reduced-graphene oxide and the structural defects of the graphene oxide composites [113].

The defects may originate intrinsically from the initial GPLs or can be formed during processing of the nanocomposites. Raman spectroscopy was used to evaluate the quality of the GPLs in the nanocomposites before and after SPS process and to compare it with that of the initial GPLs.

4.3.3. Raman Measurements

Figure 4.10 shows the Raman spectra of the initial GPLs, as-prepared 10 vol.% GPLs containing Al_2O_3 powder (before SPS) and of the 10 vol.% GPLs/Al_2O_3 nanocomposite both in through-thickness and in-plane directions, and Table 4.4 gives a summary of the measured Raman characteristics. Each spectra includes a G-band, which is related to the stretching of the C-C bond in

graphitic materials and is common to all sp^2-bonded carbon systems, the so-called disorder/defect-induced D and D′-bands, and the second order 2D-band which is attributed to a second-order process related to a phonon near the K point in graphene and activated by double resonance process [90] (Fig. 4.10). The shape of the 2D-band of all the samples is distinctly different from that of graphite, which consists of two peaks [90]. This indicates the presence of few-layer (2-5 layers) and multi-layer (5-10 layers) graphene flakes both in the initial graphene-based material and in the nanocomposites. It was also observed that the G-band of the as-prepared GPLs/Al_2O_3 powder and the sintered GPLs/Al_2O_3 nanocomposite was blue-shifted with ~7 cm^{-1} and -10 cm^{-1}, respectively, accompanied by a band-width broadening in comparison to that of initial GPLs (Fig. 4.10, Table 4.4). The blue-shift and broadening of the G-band frequency and width, respectively, in the nanocomposites can be attributed to charge doping induced by the Al_2O_3 matrix. It has been shown that the G-band position upshifts for both electron and hole doping [139]. Recently, Fan et al. [127] reported that Hall coefficient of their few-layer graphene/Al_2O_3 nanocomposites reversed its sign from positive to negative with increasing few layer graphene amount, revealing the conversion of major charge carrier. They also confirmed this effect by measuring the thermo-power of composites where the Seebeck coefficient changed from positive to negative with few-layer graphene content [127]. The authors attributed the positive Hall coefficient to doping of the few layer graphene by the Al_2O_3 matrix, since the intrinsic charge carrier type for a graphene film should be electrons due to their semi-metallic character [127]. It is known that the substrate may influence the properties of graphene-based material. When the interaction between graphene-based material and substrate is weak, such as the situation that micromechanical cleaved graphene on different substrates, the influence of substrates is negligible. However, when there is a strong interaction between graphene-based material and substrate, the substrate acts as a buffer layer that causes the subsequent graphene layer performs like isolated but doped graphene [127]. In case of few-layer graphene/Al_2O_3 composites, the interaction between graphene and matrix is strong because of the residual stress that stems from the difference of contraction after cooling caused by the thermal expansion coefficient mismatch [127]. Graphene

has a negative in-plane linear thermal expansion coefficient, while Al_2O_3 has a positive one. Therefore, graphene has a trend of expansion, while Al_2O_3 contracts during cooling. This results in generation of a large pressure which leads to very firm contact between graphene and Al_2O_3. In addition, in an environment of low oxygen partial pressure at high temperature, oxygen vacancies and aluminum interstitials are promoted as main point defects. These positively charged point defects act as electron acceptor to make graphene hole doped. The Hall coefficient changes to a negative value when the thickness of graphene increases with increasing graphene content [127].

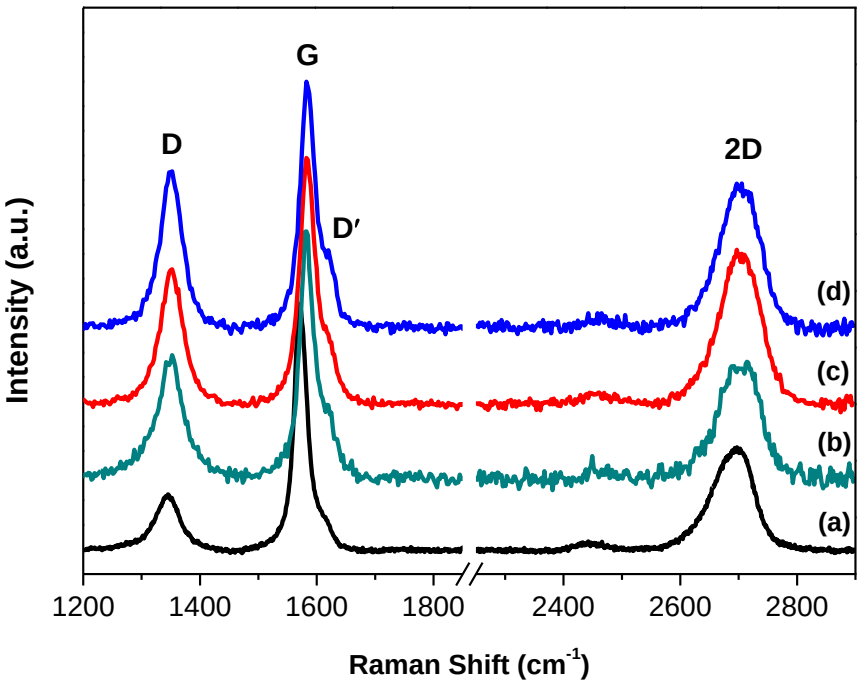

Figure 4.10. Raman spectra of the **(a)** Initial GPLs, **(b)** 10 vol.% GPLs/Al_2O_3 powder (before SPS), **(c)** 10 vol.% GPLs/Al_2O_3 nanocomposite in through-thickness direction, and **(d)** 10 vol.% GPLs/Al_2O_3 nanocomposite in in-plane direction. The spectra are normalized to the G-band.

Table 4.4. Raman features of the GPLs, 10 vol.% GPLs containing Al_2O_3 powder and of the sintered 10 vol.% GPLs/Al_2O_3 nanocomposite recorded for both in-plane (⊥) and through-thickness (//) directions. The data are the average of 50 spectra.

	GPLs (initial)	**10% GPLs/Al_2O_3 (before SPS)**	**10% GPLs/Al_2O_3 (//)**	**10% GPLs/Al_2O_3 (⊥)**
G-band ω (cm^{-1})	1574	1581	1584	1584
G-band FWHM (cm^{-1})	25	28	29	30
I_D/I_G	0.24	0.50	0.52	0.60

The Raman spectra of the as-prepared GPLs/Al_2O_3 powder and of the sintered GPLs/Al_2O_3 nanocomposite revealed an increase in the intensity of the D′-band (at ~1620 cm^{-1}) compared to the initial GPLs indicating an increment in the amount of defects. The intensity ratio of the D-band to G-band (I_D/I_G) is generally used to characterize defect content quantitatively [90]. Figure 4.11 shows the statistical histogram of the I_D/I_G ratio for the initial GPLs, 10 vol.% GPLs containing Al_2O_3 powder before sintering and the sintered 10 vol.% GPLs containing Al_2O_3 nanocomposite both in through-thickness and in-plane directions. While the I_D/I_G ratio of the initial GPLs ranged from ~0.05 to ~0.55 with a mean value of ~0.24, this ratio varied from ~0.2 to ~0.8 with a mean value of ~0.5 for the 10 vol.% GPLs/Al_2O_3 powder (Figs. 4.11(a) and (b)). The significant increase in the I_D/I_G ratio indicates that the powder preparation process (i.e., ball milling) introduced some defects into GPLs. Sintering of this powder did not alter the I_D/I_G ratio much (a mean value of 0.52 in through-thickness direction) revealing that the SPS process does not damage GPLs, as in agreement with Miranzo et al. [115]. However, the I_D/I_G ratio of the nanocomposite was slightly higher for the in-plane direction, which ranged from ~0.3 to ~1 with a mean value of ~0.6, than that of the through-thickness direction (Figs. 4.11(c) and (d)). Higher I_D/I_G ratio in the in-plane direction arises from the presence of more flake edges in that direction, confirming the anisotropic structure of the nanocomposites. Centeno et al. [123] observed a similar orientation influence on the Raman spectra of their reduced graphene oxide/Al_2O_3 nanocomposites; however, the I_D/I_G ratios

of their nanocomposites are much higher (~1.13 for the in-plane direction and ~0.83 for the through-thickness direction). It should be also noted that no correlation was observed between the graphene orientation in the nanocomposites and Raman signal intensity, in contrast to the observations of Centeno et al [123].

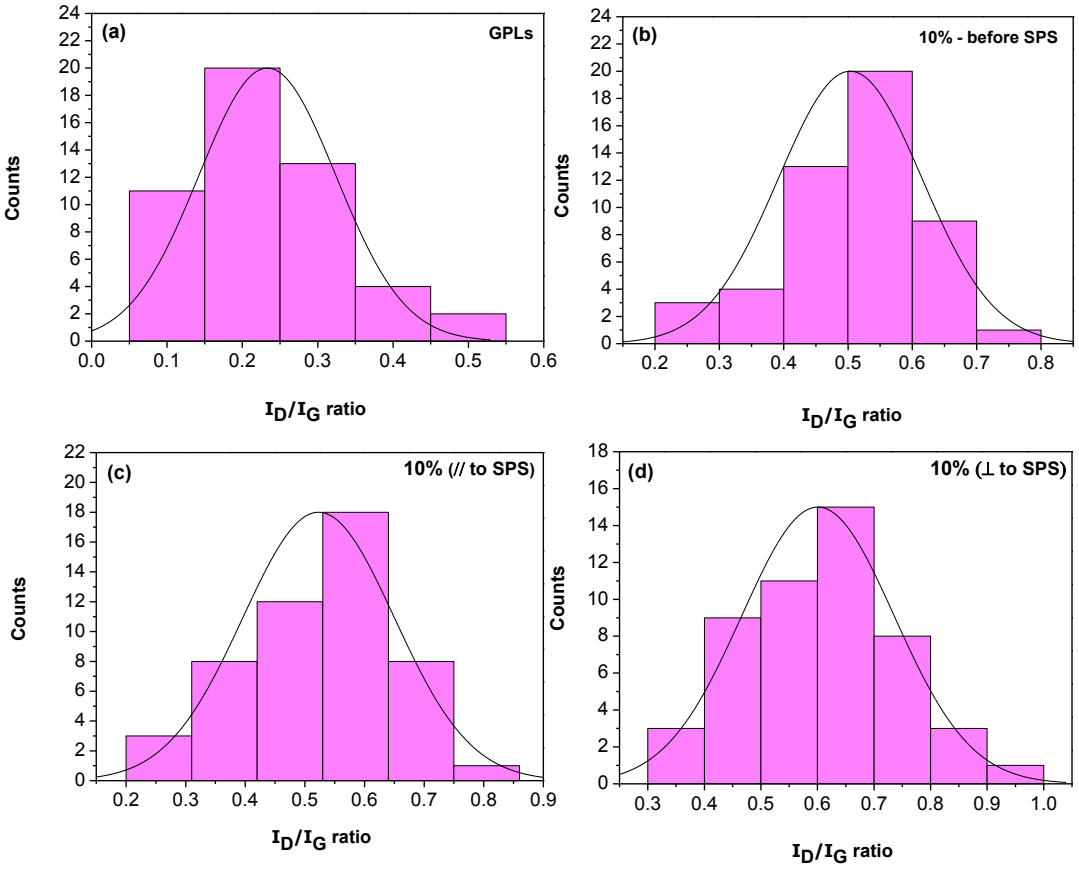

Figure 4.11. Statistical histogram of the D-band intensity to G-band intensity ratios (I_D/I_G) derived from 50 Raman spectra. **(a)** Initial GPLs, **(b)** 10 vol.% GPLs/Al_2O_3 powder (before SPS), **(c)** 10 vol.% GPLs/Al_2O_3 nanocomposite in through-thickness direction, and **(d)** 10 vol.% GPLs/Al_2O_3 nanocomposite in in-plane direction. The distribution curves indicate the mean of the data.

4.3.4. Electrical Properties

The electrical conductivity of composites, which are formed by addition of a conductive filler into an insulating material, follows a power-law near the percolation threshold [140, 141] and can be expressed by the classical percolation theory as:

$$\sigma_{el(c)} = \sigma_0(\phi-\phi_c)^{t_c} \quad \text{for } \phi > \phi_c \tag{4.6}$$

where $\sigma_{el(c)}$ is the conductivity of the composite, σ_0 is a parameter depending on the electrical conductivity of the filler material, t_c is the critical exponent, and ϕ and ϕ_c are the volume fraction and the critical volume fraction (percolation threshold) of the filler material, respectively. The critical exponent is universal, with most widely accepted values of 1.3 and 1.94 for two-dimensional and three-dimensional percolating systems, respectively [141]. It depends only on the type of percolation model and on the dimensionality of the system [142]. ϕ_c depends on the filler geometry, dispersion, and nature of the conduction between particles. Therefore, finding values of t_c and ϕ_c enables one to understand the nature of particle dispersions and percolation processes [143]. These values can be determined by fitting of the experimental data to the percolation model.

Figure 4.12 shows electrical conductivity of the monolithic Al_2O_3 and the GPLs/Al_2O_3 nanocomposites in the in-plane and through thickness directions as a function of the GPLs content. ϕ_c, t_c and σ_0 parameters were determined for both in-plane and through-thickness directions by fitting the experimental data to Eqn.(4.6) (the red solid lines in Fig. 4.12). The fitting parameters are shown in Table 4.5. The log-log plots of σ versus $(\phi-\phi_c)$ shown in the inset of Fig. 4.12 reveal linear relationships indicating a good fit (R^2 is 0.992 and 0.998 for the in-plane and through-thickness directions, respectively). Figure 4.12 shows that the monolithic Al_2O_3 and the nanocomposites with GPLs contents up to 7 vol.% exhibited insulating behavior with electrical conductivities in the range of ~10^{-10}-10^{-8} S/m. When the GPLs amount was increased to 9 vol.%, the electrical conductivity increased sharply by ~9 orders of magnitude compared to the monolithic Al_2O_3 leading to an electrically conductive nanocomposite with 1.42

and 0.74 S/m conductivity values in the in-plane and through-thickness directions, respectively. This increase is attributed to formation of a conductive network by interconnected GPLs resulting in an electrical percolation. The fittings of the experimental data gave percolation threshold (ϕ_c) of ~7.1 ± 1.36 and ~7.5 ± 0.46 vol.% for the in-plane and through-thickness directions, respectively, revealing that preferential orientation of GPLs has not affected the percolation threshold much, as in agreement with Ramirez et al. [126] who reported similar ϕ_c values to those observed in the present study. It should be noted that GPLs loadings higher than the percolation threshold extended the improvement of the electrical conductivity (Fig. 4.12). This phenomenon is in agreement with previous studies [108, 123, 127] and could be attributed to an increase in the number of interconnections between GPLs with increasing GPLs amount.

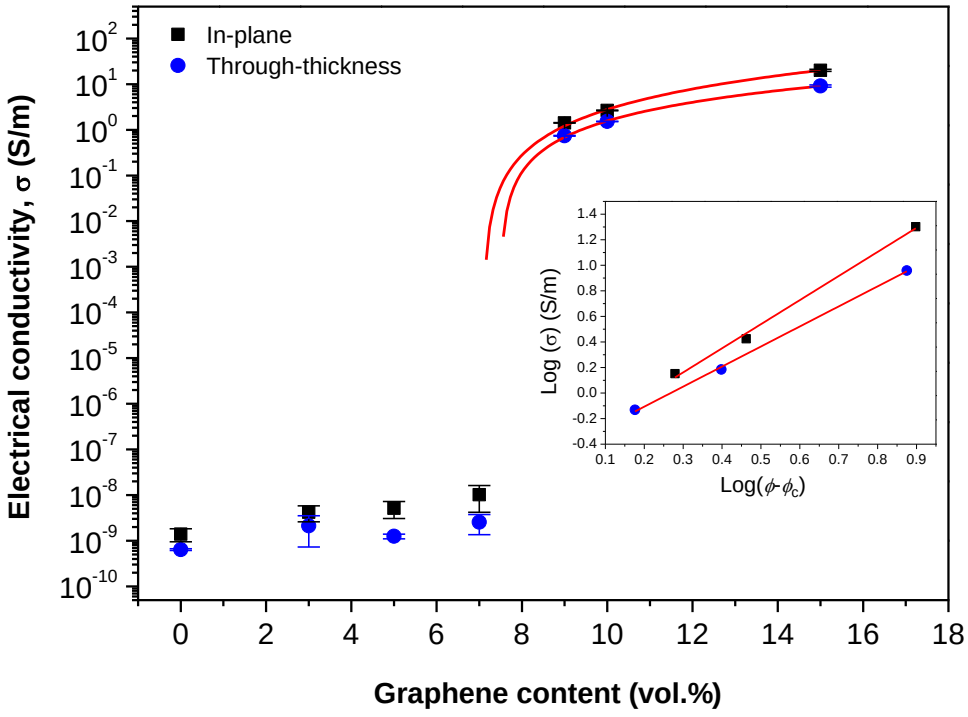

Figure 4.12. In-plane and through-thickness electrical conductivities of GPLs/Al_2O_3 nanocomposites at room temperature. The solid lines are fittings to Eqn.(6). Inset is the double-logarithmic plot of electrical conductivity versus (ϕ-ϕ_c), showing a linear relationship (R^2 is 0.992 and 0.998 for the in-plane and through-thickness directions, respectively).

Table 4.5. Fitting parameters of the electrical conductivity data depending on the GPLs content determined both in the in-plane and through-thickness directions by fitting the experimental data to the classical percolation theory (Eqn.(4.6)).

	σ_0	ϕ_c	t_c	Adj R^2
In-plane	0.343 ± 0.56	7.1 ± 1.36	1.97 ± 0.62	0.9993
Through-thickness	0,360 ± 0.18	7.5 ± 0.46	1.60 ± 0.2	0.9997

Even though there is an obvious preferential orientation of GPLs throughout the matrix as it was confirmed by the SEM micrographs and Raman analyses, the electrical conductivity of the nanocomposites exhibited a slight anisotropy depending on the orientation of GPLs with a slightly lower resistivity in the in-plane direction. The in-plane conductivity of the nanocomposites is ~2-3 times of the conductivity in through-thickness direction. The lower anisotropy than expected could be attributed to the presence of some misaligned/rotated GPLs with respect to the alignment plane (in-plane direction) of most of the GPLs which oriented during SPS process, as suggested by Ramirez et al. [126], who reported in-plane to through-thickness electrical conductivity ratio of 10-25 for their GPLs/Si_3N_4 composites. Moreover, the electrical conductivity of a composite can be improved by filler material either through establishing a new conductive path in the matrix or through increasing the cross area of the formed path, which is the thickness of graphene flakes in case of graphene-based nanocomposites [127]. At high graphene-based material loadings, the probability of agglomeration and overlapping increases resulting in an increment in the thickness of graphene flakes [127]. In this case, second mechanism becomes dominant and the electrical conductivity increases in the through-thickness direction, as well as in the in-plane direction. This phenomenon is also supposed to be effective in the relatively low anisotropy observed for the electrical conductivity of the GPLs/Al_2O_3 nanocomposites. Thin few-layer graphene flakes, which locate at the grain boundaries and around the matrix grains and cannot be easily observed in the SEM micrographs, could also affect the anisotropy in the electrical conductivity. The fitting of the experimental data yielded t_c values of

1.97 ± 0.62 and 1.60 ± 0.2 for the in-plane and through-thickness directions, respectively. The slope of the linear fits in the log-log plots shown in the inset (Fig. 4.12) gave t_c values of 1.89 and 1.57 for the in-plane and through-thickness directions, respectively, confirming the t_c values found by fitting the data to Eqn. (4.6). The t_c value determined for the in-plane direction is in excellent fit with the expected value (~1.94) for three-dimensional percolating systems indicating the three-dimensional network of GPLs in the nanocomposites above the percolation threshold. This result is in agreement with the relatively low anisotropy in electrical conductivity and with similar ϕ_c values observed in both directions. The lower t_c value observed for the through-thickness direction in comparison to the in-plane direction could be attributed to a percolation which takes place in a network with more 'dead arms' or weakly connected parts than a classical random network [104, 107] or to a quasi-two-dimensional network of GPLs with a combination of two- and three-dimensional organizations. Fan et al. [108] reported t_c value of 1.54 for the GPLs/Al_2O_3 composites and attributed the low value of t_c to some preferential orientation of GPLs in the in-plane direction. However, the authors did not make orientation dependent measurements [108]. Ramirez et al. [126] estimated t_c = 0.89 and t_c = 2.05 for the in-plane and through-thickness electrical conductivity data of their GPLs/Si_3N_4 composites and attributed the observation of larger t_c exponent for the through-thickness direction compared to the in-plane direction to a broader range of inter-particle connectivity.

The maximum electrical conductivities achieved in the present study are ~20.1 and ~9.1 S/m for the 15 vol.% GPLs/Al_2O_3 nanocomposite in the in-plane and through-thickness directions, respectively (Fig. 4.11). Although these values are sufficiently high for EDM process, they are much lower than the one reported by Fan et al. [108], who achieved 5709 S/m electrical conductivity for the same amount of graphene-based material in the Al_2O_3 matrix. This difference can be attributed to the preferential orientation of graphene flakes throughout the matrix which may raise the percolation threshold [111], and also to different characteristics of the graphene-based materials used for the composite production, such as lower lateral size and aspect ratio which may affect the percolation

threshold and electrical conductivity. Fan et al. [108] used ball milling to grind expanded graphite with Al_2O_3 and obtained graphene-based material with mostly ~2.5-20 nm in thickness; however, they did not give information about the lateral size of these flakes. The GPLs utilized in the present study are small in lateral size (mostly <1 μm) and it is known that smaller graphene flakes result in more junctions and consequently in lower conductivity due to the effect of inter-flake junction resistances [39, 68]. Moreover, higher amount of GPLs is required to form a conductive network when flakes with a smaller lateral size are used. Recently, Fan et al. [127] produced few-layer graphene (<5 nm)/Al_2O_3 nanocomposites by spark plasma sintering of graphene oxide/Al_2O_3 hybrids prepared by colloidal processing with a simultaneous reduction of GO. The authors achieved a percolation threshold as low as 0.38 vol.% and obtained a conductivity of 1038.15 S/m by increasing the graphene content to 2.35 vol.% [127]. They attributed this lower percolation to homogeneous dispersion of very thin few-layer graphene in the matrix, high quality of the as prepared few-layer graphene and better contact between conductive nanoparticles [127]. However, Porwal et al. [109] suggested that the method that Fan et al. [127] used for measuring the graphene-based material volume content in the alumina matrix is not well established. The authors determined the filler volume fraction in composites by loading a certain amount of dried graphene oxide into a graphite die and sintered it by SPS in the same condition used for the few-layer graphene/Al_2O_3 nanocomposites. They found that 35% mass remained after sintering. This mass loss percentage was then used to estimate the filler volume fraction in composites [127]. Rul et al. [104] prepared SWNT-$MgAl_2O_4$ composites with a homogeneous distribution of SWNTs between matrix grains by in-situ catalytic chemical vapor deposition method. They investigated the electrical conductivity of SWNT-$MgAl_2O_4$ composites with 0.23 and 24.5 vol.% CNT content and showed that the classical percolation theory is valid for these composites up to 11 vol.%. A percolation threshold of 0.64 vol.% and t = 1.73 was reported for these systems and conductivity was measured in the range of 0.4 – 850 S/m depending on the CNT content. On the other hand, Zhan et al. [128]

reported electrical conductivity of 3345 S/m for 15 vol.% SWNT containing Al_2O_3 nanocomposite.

4.3.5. Thermal Properties

Thermal properties of the GPLs/Al_2O_3 nanocomposites were investigated as a function of temperature, graphene content and orientation of GPLs in the matrix. Figure 4.13 shows the C_p values of the monolithic Al_2O_3 and the GPLs/Al_2O_3 nanocomposites as a function of temperature determined by DSC measurements and also calculated by the help of HSC Chemistry software [132], for comparison. The C_p of all the samples increased with temperature (Fig. 4.13). Heat is generally stored by phonons and free electrons of a material; however, for graphite and graphene, phonons dominate the specific heat at all practical temperatures (>1 K), and the phonon specific heat increases with temperature [144, 145]. Figure 4.13 revealed that both the measured and the calculated C_p values increase with graphene addition, as in agreement with Miranzo et al. [115]. Similar behavior was also reported by Kumari et al. [146] for the CNT-Al_2O_3 nanocomposite systems, the heat capacity of which is much higher than that of the monolithic Al_2O_3. It was observed that the experimental C_p of the monolithic Al_2O_3 is lower than that of the calculated one, while the experimental measurements revealed generally much higher C_p than the calculated ones for the GPLs/Al_2O_3 nanocomposites (Fig. 4.13). The experimentally determined C_p values were taken into account for the thermal conductivity calculations, since they may give more realistic results.

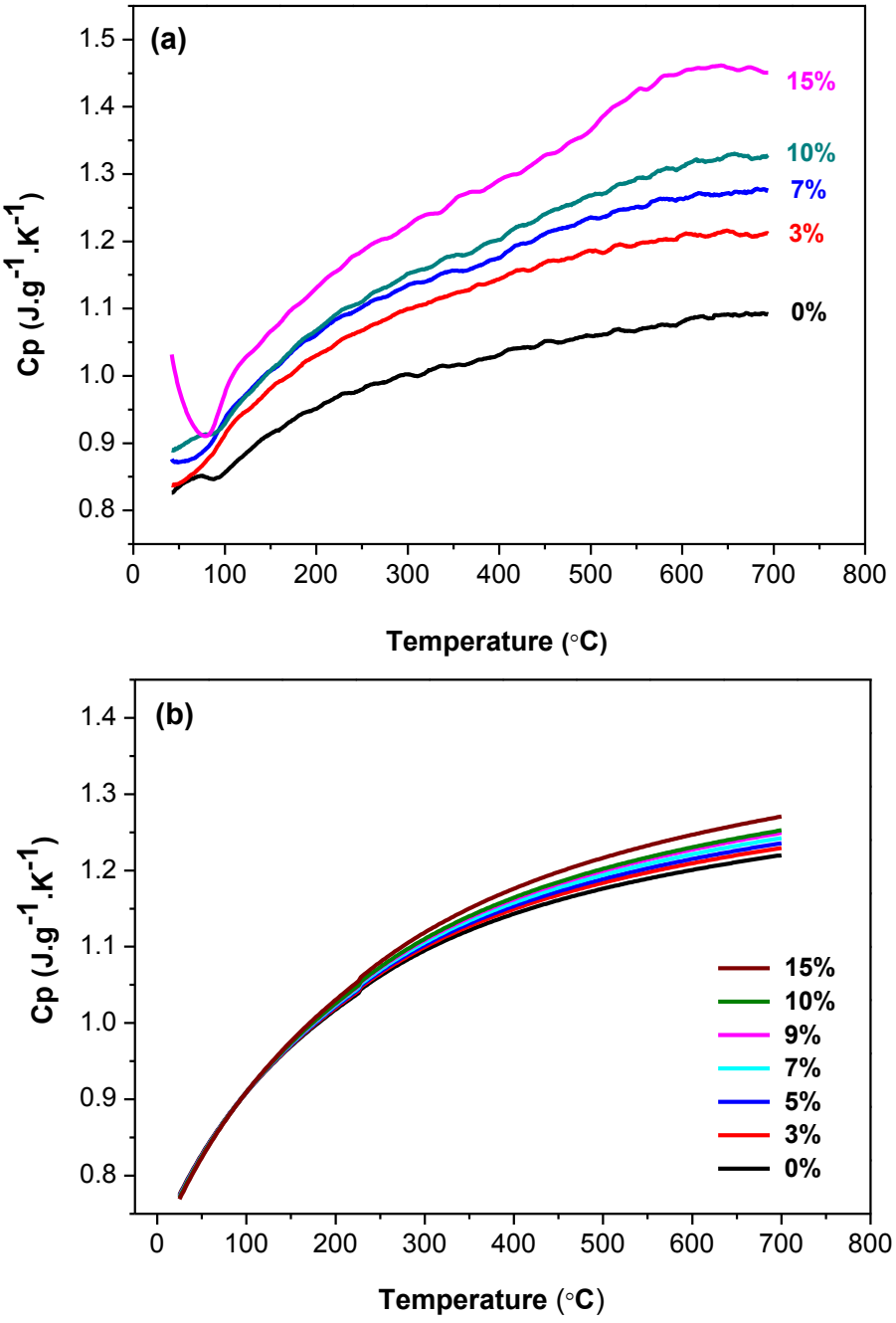

Figure 4.13. Specific heat values of the monolithic Al_2O_3 and the GPLs/Al_2O_3 nanocomposites **(a)** experimental values, **(b)** calculated values obtained by the rule of mixtures using the C_p data of Al_2O_3 (corundum) and graphite determined by the HSC Chemistry [132].

The thermal diffusivity and the thermal conductivity of the monolithic Al_2O_3 and the GPLs/Al_2O_3 nanocomposites decreased with increasing temperature both in the in-plane and the through-thickness directions (Figs. 4.14 and 4.15). This behavior is characteristic of crystalline solids and is attributed to phonon-phonon Umklapp scattering, which makes major contribution to thermal conductivity at high temperatures as reducing the phonon mean free path [23, 146, 147]. In through-thickness direction, the monolithic Al_2O_3 exhibited higher thermal diffusivity and thermal conductivity than that of the GPLs/Al_2O_3 nanocomposites within the measured temperature range, and both the thermal diffusivity and the thermal conductivity values decreased with increasing GPLs amount (Figs. 4.14(a) and 4.15(a), respectively). The decrease in the thermal diffusivity and the thermal conductivity of monolithic Al_2O_3 with GPLs addition could be attributed mainly to interfacial thermal resistance between GPLs and Al_2O_3 grains [23, 147, 148]. Interfacial thermal resistance, also known as thermal boundary resistance, at the interface of graphene with other materials, has a non-zero value even at the perfect interfaces owing to differences in the phonon density of states [23]. This effect is known as Kapitza resistance [149]. The actual thermal boundary resistance is usually higher than the Kapitza resistance owing to interface imperfections. Graphene thermal coupling to other materials depend on the surface roughness, presence or absence of suspended regions in graphene layers, and methods of graphene preparation [23]. Although graphene has extremely high intrinsic thermal conductivity in its suspended form (~5000 $W.m^{-1}.K^{-1}$ at room temperature) [10], the final thermal properties of its potential applications, such as nanocomposites, are strongly affected by the interfacial thermal barrier. As shown in Fig. 4.4, GPLs addition into monolithic Al_2O_3 led to a much finer microstructure; consequently, the amount of grain boundaries and interfaces, which act as scattering regions for phonons leading to a reduction in lattice thermal conductivity, increased. Interfacial thermal resistance decreases with temperature following a typical trend for Kapitza resistance [23]. This could be the reason of the reduced difference within the thermal diffusivity/the thermal conductivity values of the monolithic Al_2O_3 and the nanocomposites with increasing temperature in through-thickness direction (Figs. 4.14(a) and 4.15(a)).

The contacts between GPLs, the defects within GPLs and the presence of the bended GPLs at the Al_2O_3 grain boundaries also limit the thermal transport in the through-thickness direction [115]. In the in-plane direction, the thermal diffusivity and the thermal conductivity of the GPLs/Al_2O_3 nanocomposites were slightly lower than that of the monolithic Al_2O_3 at room temperature; however, they showed an increasing trend with GPLs content (Figs. 4.14(b) and 4.15(b)). At higher temperatures, these values got closer to or even exceeded the thermal diffusivity and especially the thermal conductivity values of the monolithic Al_2O_3 depending on the volume fraction of GPLs, which could be attributed to a decrease in interfacial thermal resistance at high temperatures. The thermal conductivity curves of the monolithic Al_2O_3 and the 15 vol.% GPLs/Al_2O_3 nanocomposite coincided at 100°C, and above that temperature the thermal conductivity of the 15 vol.% GPLs/Al_2O_3 nanocomposite got higher than that of the monolithic Al_2O_3 and the difference between them increased with temperature (Fig. 4.15(b)). It is very clear that GPLs form a less resistive heat conduction path in the in-plane direction, as in agreement with Miranzo et al. [115], who studied the thermal conduction of Si_3N_4 composites with different types of carbon nanostructures (CNTs and GPLs) and investigated the effect of nanostructure orientation with respect to heat flux, testing temperature and α/β Si_3N_4 phase ratio. The authors reported that the addition of both CNTs and GPLs reduced the thermal conductivity in the through-thickness direction, and they obtained a significant improvement in the in-plane thermal conductivity for platelets addition up to 40 $W.m^{-1}.K^{-1}$, twice the thermal conductivity of the Si_3N_4 matrix [115]. In the only study which investigated both the in-plane and through thickness thermal conductivity of CNTs containing ceramic nanocomposites, Zhan and Mukherjee [147] observed that incorporation of single-wall CNTs ropes does not change the in-plane thermal conductivity of the Al_2O_3, while it decreases thermal diffusivity in through-thickness direction.

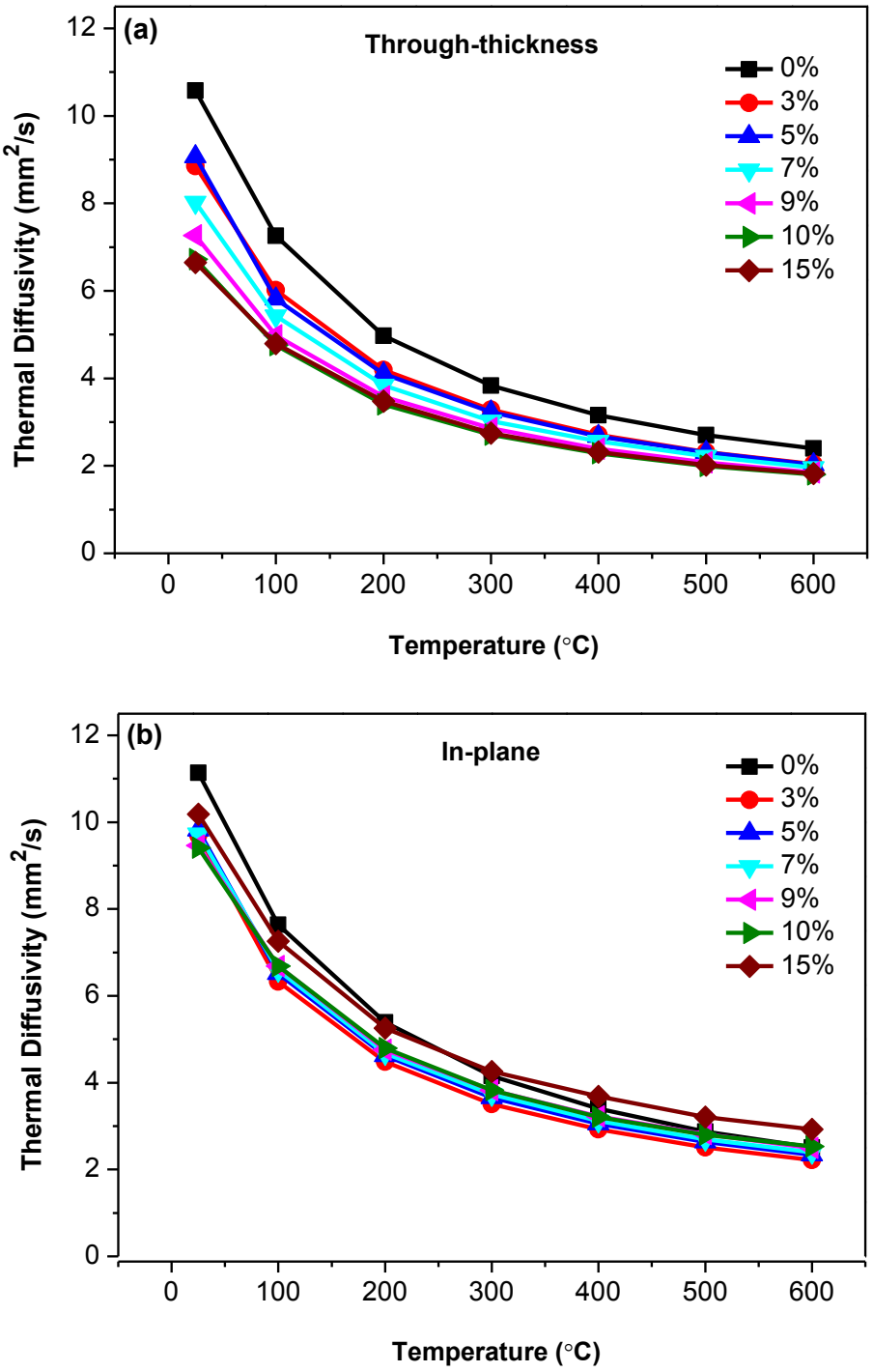

Figure 4.14. Through-thickness and in-plane thermal diffusivities of the monolithic Al_2O_3 and of the GPLs/Al_2O_3 nanocomposites as a function of temperature.

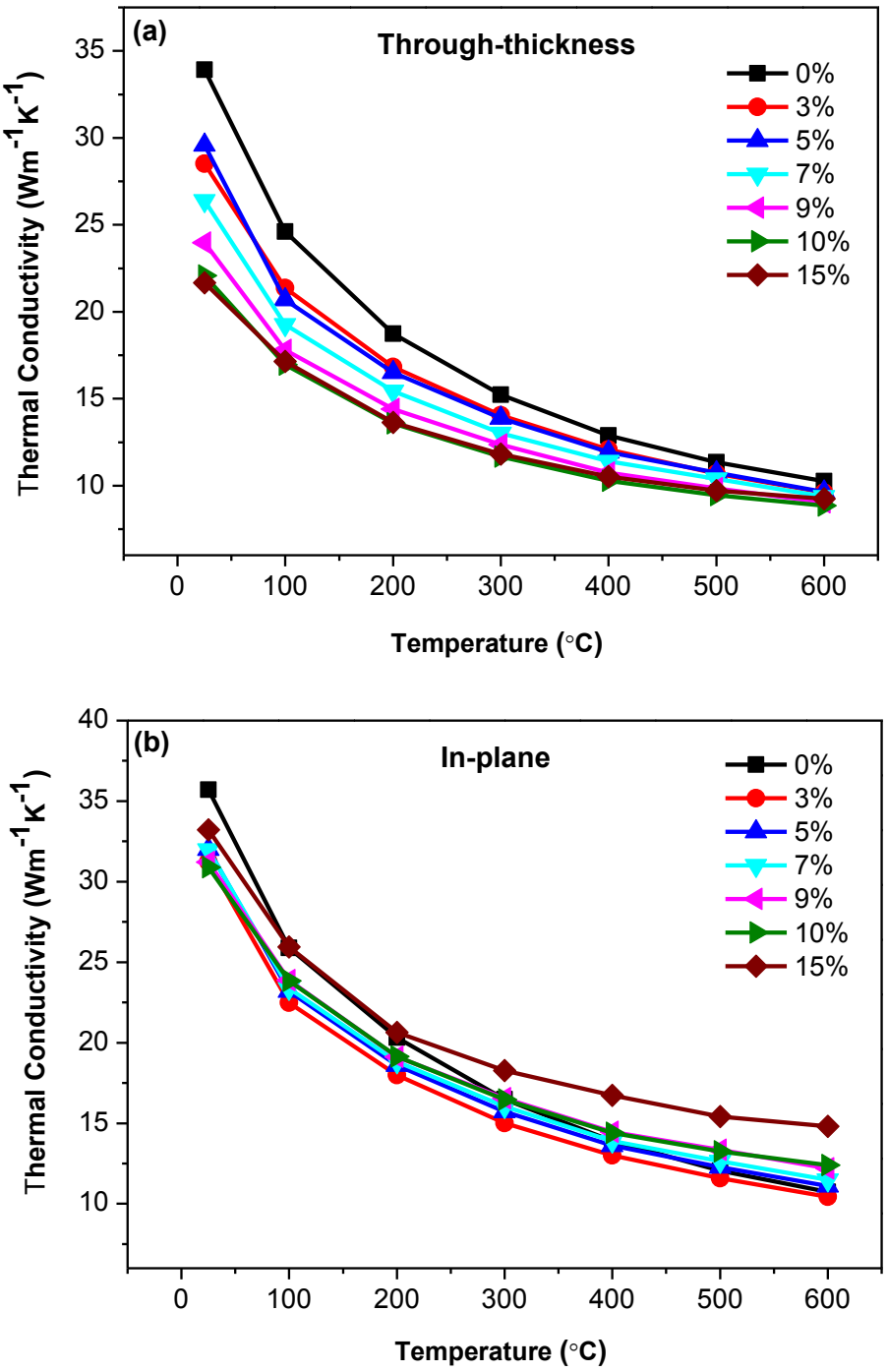

Figure 4.15. Through-thickness and in-plane thermal conductivities of the monolithic Al_2O_3 and of the GPLs/Al_2O_3 nanocomposites as a function of temperature.

Figure 4.16 shows the in-plane thermal conductivity values of the nanocomposites as a function of GPLs volume fraction at 600°C. As from 3 vol.% GPLs, the thermal conductivity increased almost linearly with graphene content without showing any clear thermal percolation threshold, as in agreement with the observations of Shahil and Balandin for the multilayer graphene-epoxy composite systems [130]. ~44% increase in the in-plane thermal conductivity at 600°C was achieved with 15 vol.% GPLs addition into the monolithic Al_2O_3 (Fig. 4.16). The difference between the thermal and the electrical transport behaviors mainly arises from differences in conductivity ratios of filler to matrix. For thermal transport, this ratio is ~10^3 – 10^4 even for a very conductive filler material; while it can be up to ~10^{12} – 10^{16} in terms of electrical conductivities [148]. Therefore, the effective conduction path is through the filler material in case of electrical conductivity; however, heat can also be transmitted through the matrix [148]. That is, thermal conductivity is a bulk property, while electrical conductivity is a line property.

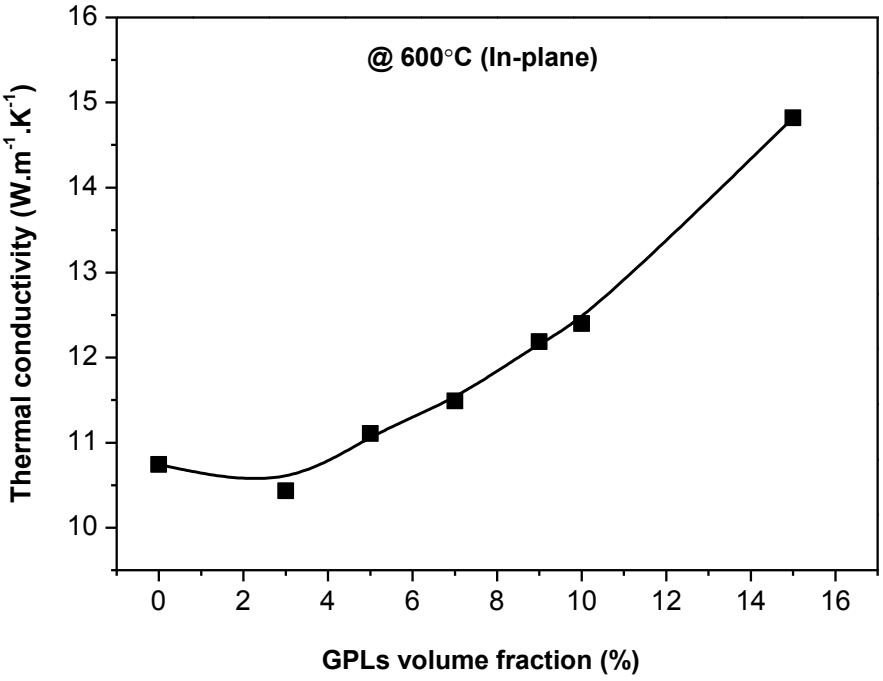

Figure 4.16. In-plane thermal conductivity of GPLs/Al_2O_3 nanocomposites at 600°C as a function of graphene content (vol.%).

Figure 4.17 demonstrates the comparison of the in-plane and through thickness thermal conductivities of the monolithic Al_2O_3 and the nanocomposites with different GPLs volume fractions as a function of temperature. It can be clearly seen that the anisotropy between the in-plane and through-thickness thermal conductivities increases with GPLs amount. This anisotropy increase arises from decrement of through-thickness thermal conductivity and improvement of in-plane thermal conductivity simultaneously with increasing GPLs content. Figure 4.18 shows the in-plane to through-thickness thermal conductivity ratio ($k_{\text{in-plane}}/k_{\text{through-thickness}}$) at 600°C for the GPLs/$Al_2O_3$ nanocomposites depending on the GPLs content. ~52% increase in the $k_{\text{in-plane}}/k_{\text{through-thickness}}$ ratio was observed for the 15 vol.% GPLs/Al_2O_3 nanocomposite in comparison to the monolithic Al_2O_3 at 600°C (Fig. 4.18). Similar $k_{\text{in-plane}}/k_{\text{through-thickness}}$ ratios were also observed for the room temperature thermal conductivity values. Figure 4.19 shows the thermal behavior of 15 vol.% GPLs/Al_2O_3 nanocomposite in air, indicating its stability up to ~700°C.

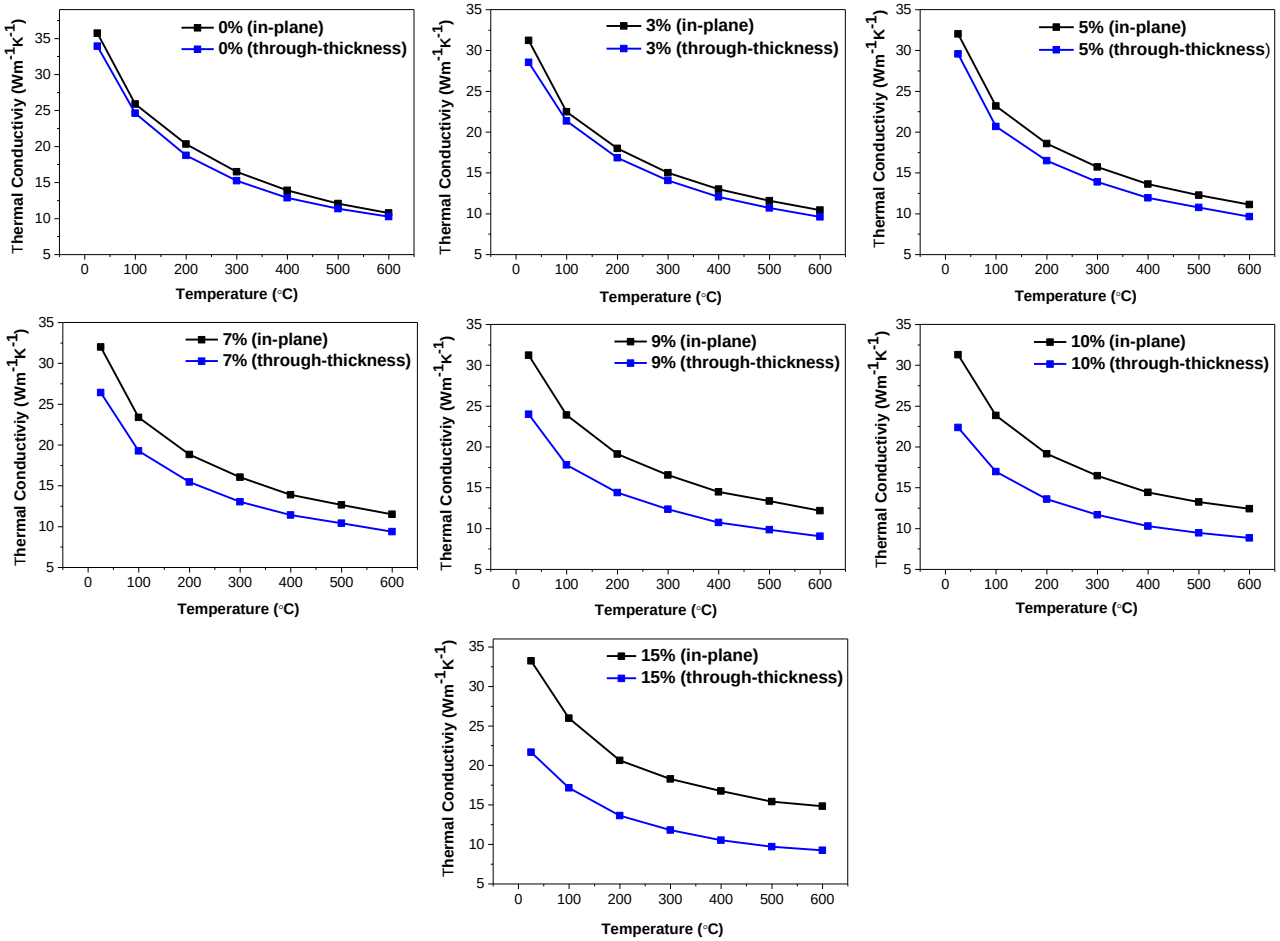

Figure 4.17. In-plane and through thickness thermal conductivities of the monolithic Al_2O_3 and the nanocomposites as a function of temperature showing anisotropy increase with increasing GPLs volume fraction (%).

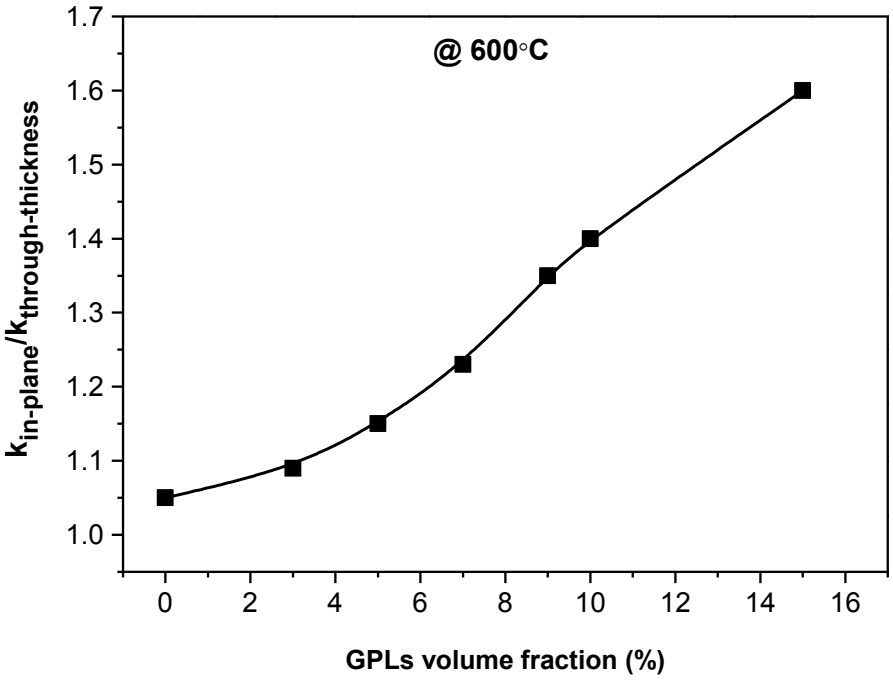

Figure 4.18. In-plane to through-thickness thermal conductivity ratio at 600°C for the GPLs/Al_2O_3 nanocomposites depending on the GPLs content (vol.%).

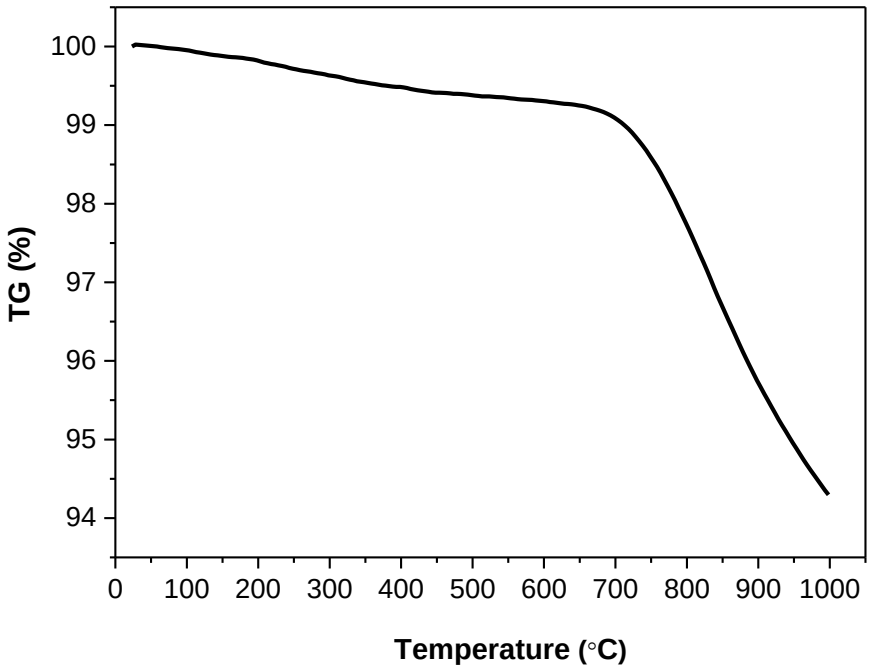

Figure 4.19. TG of 15 vol.% GPLs/Al_2O_3 nanocomposite in air.

4.4. Conclusions

GPLs containing Al_2O_3 nanocomposites, which exhibit anisotropic mechanical, thermal and electrical properties due to preferential orientation of GPLs throughout the matrix, have been successfully prepared by SPS.

3 vol.% GPLs addition into monolithic Al_2O_3 resulted in an increase in fracture toughness by ~27.5% in the in-plane direction (perpendicular to the SPS pressing axis) and a decrease by ~17.7% in through thickness direction (parallel to the SPS pressing axis) depending on the interface strength between GPLs and matrix grains. Pull-out is the main toughening mechanism in the in-plane direction for this nanocomposite. Further increase in GPLs content starts to decrease the in-plane fracture toughness due to weakening of the interface as a result of agglomeration/overlapping of GPLs, while increasing it in the through-thickness direction as a result of crack bridging and crack deflection mechanisms. Crack branching appears at high GPLs loadings as a dominant toughening mechanism, especially for the 15 vol.% GPLs containing nanocomposite resulting in ~9% and ~33% increase in fracture toughness in through-thickness direction compared to the monolithic Al_2O_3 and the 3 vol.% GPLs containing Al_2O_3, respectively.

The electrical conductivity of the nanocomposites exhibited a slight anisotropy with a lower resistivity in the in-plane direction. An electrical percolation threshold was observed at ~7.1 and ~7.5 vol.% GPLs contents for the in-plane and through-thickness directions, respectively. The electrical conductivity values of the 15 vol.% GPLs containing Al_2O_3 nanocomposite are 20.1 and 9.1 S/m in the in-plane and through-thickness directions, respectively, which are sufficiently high for EDM process.

Thermal properties of graphene-based material containing Al_2O_3 nanocomposite systems have been investigated for the first time in the literature in this study. Oriented GPLs led to a less resistive heat conduction path in the in-plane direction. The thermal conductivity values of nanocomposites in the in-plane direction get higher than that of the monolithic Al_2O_3 at high temperatures (>100°C), especially for high GPLs loadings. The anisotropy in thermal conductivity increases with GPLs amount due to reduction in through-thickness

thermal conductivity and increase in in-plane thermal conductivity simultaneously with increasing GPLs content. ~44% increase in the in-plane thermal conductivity was achieved at 600°C with 15 vol.% GPLs addition into the monolithic Al_2O_3 and this resulted in ~52% increase in the $k_{\text{in-plane}}/k_{\text{through-thickness}}$ ratio. This higher in-plane thermal conductivity can be beneficial for dissipation of heat from one direction. The improvement in high temperature thermal conductivity can be advantageous to minimize heat accumulation in material during applications, such as cutting tools, where the material is exposed to high loads at high temperatures.

5. LOW PRESSURE CVD GROWTH OF GRAPHENE OVER CU FOILS

5.1. Introduction

Chemical vapor deposition (CVD) of hydrocarbons on transition metal substrates is a promising method for large-area graphene production at a large scale with low defects, good uniformity and controlled number of graphene layers. The graphene films made on metal film or foil surfaces can be easily removed and transferred onto dielectric substrates. This enables one to produce large area, planar graphene films with relatively low defect density and is well-suited for flexible transparent electrodes and electronic applications where the growth can be patterned precisely in combination with lithographical methods.

There are two different growth mechanisms proposed for CVD graphene growth which have been mainly attributed to the carbon solubility limit in the metal. Li *et al.* [150] used isotopic labelling of the carbon precursor ($^{12}CH_4$, $^{13}CH_4$) to study the mechanism and kinetics of CVD growth of graphene on Ni and Cu substrates. They observed segregation/precipitation and surface adsorption mechanisms for Ni and Cu, respectively. In the case of very low carbon solubility catalysts (<0.001 atomic %) such as Cu, the synthesis of graphene is limited to the surface of the catalyst. The carbon precursor is decomposed at high temperatures (>1000°C) on Cu, leading to primarily single layer graphene. In the case of intermediate-high solubility (> 0.1 atom %) metal catalysts, such as Co and Ni, graphene synthesis is proposed to proceed via dissociation of carbon precursor on the substrate, diffusion of carbon into the metal thin film at the growth temperature, and a precipitation of carbon as graphene on the metal substrate upon cooling [151].

Ni and Cu have received the most attention as a graphene substrate material because of their cost, grain size, etchability, and their use and acceptance by the semiconductor industry [150]. Ni has the best lattice match with graphene among the metal substrates. The smallest mismatch is for grains with the (111) orientation (1.2%) [152]. However, Ni foils or Ni films usually yields non-uniform graphene layers, that is, they have a wide variation in thickness over the metal surface from a monolayer to many layers [150]. On the other hand, Cu is a

very promising catalyst substrate for production of high-quality graphene films with uniform thickness due to the low solubility of C in Cu. However, different from the growth on Ni, a low pressure CVD process, with a total pressure of 0.5–50 Torr, is usually used for the growth of graphene films on Cu foils [153]. The low pressure growth of graphene on Cu foils is known to be advantageous in terms of controlled thickness and quality.

The quality, thickness and uniformity of CVD-grown graphene films depend on various parameters such as gas flow rates, growth temperature and time, pressure during the entire growth process, cooling rate, etc. The surface morphology and purity (amount of impurities) of the Cu foil play a critical role in the graphene growth, as well. These characteristics of Cu foils can be very different depending on various suppliers or different batches, resulting in reproducibility problems [154]. This may also affect the quality of the graphene significantly [154]. Disorders, defects and impurities originating from both the synthesis process (i.e., from process parameters and transfer process) and/or from the metal catalyst used act as active sites for graphene nucleation, enhancing the catalytic activity of the Cu surface and leading to thickness non-uniformities across the grown film [155]. They may also affect the mobility of the CVD-synthesized graphene significantly. To be able to improve the thickness uniformity and enhance the transport properties of CVD graphene, the amount of disorders, defects or impurities have to be eliminated or at least minimized by controlling the process parameters, transfer route and Cu foil properties.

The objective of this study was to perform low-pressure CVD growth experiments of graphene films on two different Cu foils (belonging to two different batches) by controlling the H_2 and/or Ar flows rates during ramping in order to investigate the influence of ramping atmosphere on the impurity level, quality of the synthesized graphene films and their uniformity in terms of number of layers. The effect of differences in Cu foil characteristics (depending on using foils from different batches) on the amount of impurities was also examined and different pre-cleaning routes were investigated in order to minimize the amount of impurities.

5.2. Experimental Procedure

Graphene synthesis was carried out in a commercial CVD system with a 4 inch quartz tube inside a horizontal tube furnace (EasyTube 3000 Ext., First Nano, USA) using Cu foils as a catalyst substrate. 25 μm thick and 99.8% pure Alfa Aesar foils with the same lot number (13382), but supplied from two different sources at different times (i.e., from different batches) were used as catalysts in this study. These foils were denoted as 'B1' for batch 1 and 'B2' for batch 2.

Prior to loading the Cu foils into the reaction chamber, they were cleaned using acetone, deionized (DI) water, acetic acid (glacial-100%) or nitric acid (5.4 (w/w)), DI water, acetone and isopropyl alcohol, subsequently. After loading the samples into the chamber, the system was purged with Ar gas (purity 99.999%). Then, the sample was heated to 1000°C at a pressure of 0.5 torr (unless otherwise stated). Heating was performed under different gas environments such as Ar, Ar/H_2 or H_2 (purity 99.999%) to clarify the effect of ramping atmosphere on the quality of the Cu foil and graphene growth. The system was maintained at 1000°C for 30 min under 300 standard cubic centimeters per minute (sccm) H_2 flow at 0.5 torr (unless otherwise stated) in order to reduce any oxide layer, to remove organic residues (oil contaminations, lubricants, etc.) originating from metal processing and to obtain Cu grains as large as possible. After annealing, H_2 flow rate was decreased to 100 sccm and CH_4 (purity 99.995%) was introduced into the system as carbon source for graphene growth for 5 min at 0.5 torr. During growth, 100 sccm H_2: 20 sccm CH_4 flow was mostly used. For the B2 Cu foil, 100 sccm H_2: 17 sccm CH_4 flow was also applied. The system was then cooled down to 940°C and the sample was unloaded from the reaction chamber for a quick cooling. Figure 5.1 shows the schematic of CVD graphene growth process.

After graphene growth, one side of the copper foil was spin-coated with ~500 nm thick polymethyl-methacrylate (PMMA C4 950, Microchem Corp.) by using Specialty Coating Systems G3P-8 spin coater. The sample was then let for drying overnight in air. Since graphene is grown on both sides of the Cu foil, the graphene layer on the backside of the foil was removed by oxygen plasma etching at ~100 W for 3 min by Gala Instrumente Plasma $Prep_2$, Germany equipment.

Then, Cu was etched in 1 M $FeCl_3$ solution for a few hours. Once the Cu was removed completely, the PMMA/graphene film was soaked in deionized water (as the PMMA side up) in order to clean the residual $FeCl_3$ solution. This step was repeated several times with refreshed DI water. The PMMA/graphene film was then soaked in $H_2O/H_2O_2/HCl$ solution for ~15 min in order to remove metal-based contaminants that arise from Cu etchants followed by DI water rinse [156]. The PMMA/graphene film was then transferred onto a pre-cleaned Si wafer with a 300 nm thick SiO_2 layer. After drying the sample overnight in air, it was baked at 150°C for 30 min to improve the contact between the graphene film and the substrate and to reduce the number of cracks, as suggested by Liang et al. [156]. The PMMA was removed by immersing the sample in acetone at ~50°C. The sample was then rinsed in isopropyl alcohol and dried by N_2 blowing.

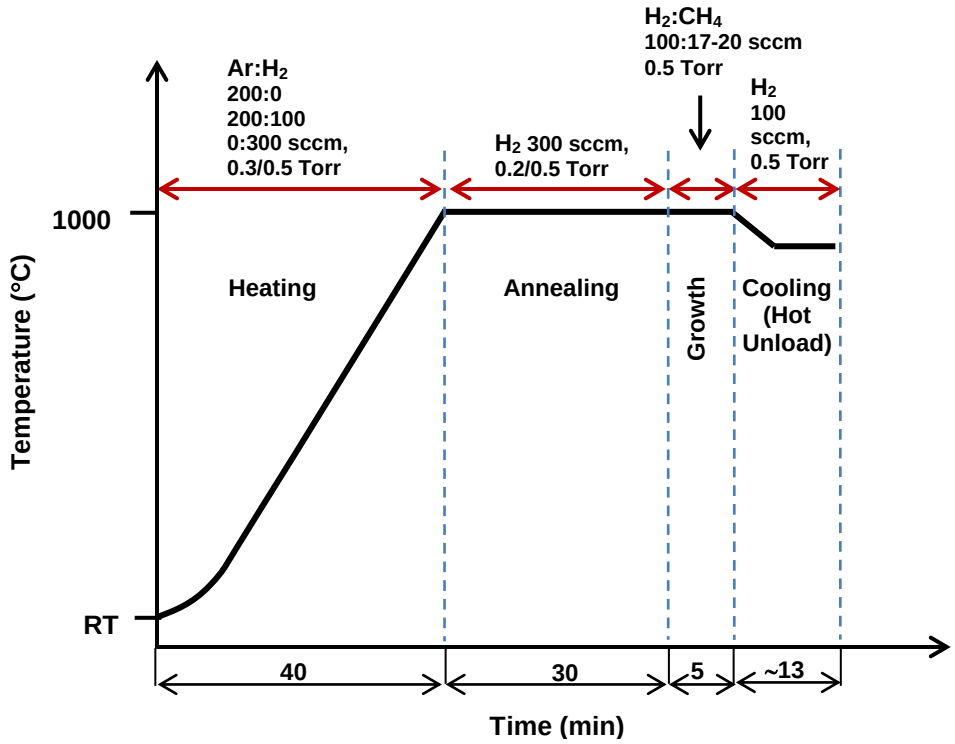

Figure 5.1. Schematic of CVD graphene growth process on Cu foils.

As-grown graphene films on Cu foils and the transferred graphene films onto SiO_2/Si substrate were characterized by field emission gun – scanning

electron microscope (FEG-SEM, Supra 50 VP). Energy-dispersive x-ray spectroscopy (EDX) analyses of these samples were also performed. Optical microscopy and micro-Raman analyses of the graphene films were performed on a Renishaw Invia spectrometer using 532 nm laser (2.33 eV) excitation and 100x objective lens. The laser power was kept below 1 mW in order to prevent sample damage. At least three Raman spectra were recorded at different spots for each sample. Raman measurements were performed on as-grown graphene films on Cu foils, as well as on transferred graphene films onto SiO_2/Si substrate for some of the samples. Costa et al. [157] showed that the acquisition of Raman spectra of graphene on Cu substrates is a practical and fast way to characterize as-grown graphene on Cu. The authors compared the results with graphene samples transferred onto SiO_2/Si and found no significant differences, indicating that the transfer process does not significantly change the properties of graphene and hence, Raman measurements of graphene samples can be directly performed on the Cu foil to save time [157]. Transmission Electron Microscopy (TEM) analyses (both low magnification and high resolution) were performed with a Jeol JEM 2100F at ‘‘service commun TEMSCAN’’ in Université Paul-Sabatier. TEM samples were prepared by following the graphene transfer route that described above. In this case, the PMMA/graphene film was transferred onto holey carbon coated copper grids (200 mesh).

5.3. Results and Discussion

Low-pressure CVD growth experiments of graphene films on Cu foils were performed using H_2 and/or Ar with different flow rates during ramping to growth temperature in order to investigate the influence of ramping atmosphere on quality of the synthesized graphene films and their uniformity in terms of number of layers. Therefore, while the ramping atmosphere was varied, the other process parameters were fixed, i.e., 0.5 torr pressure during the whole process, 300 sccm H_2 flow during annealing for 30 min, 100 sccm H_2/20 sccm CH_4 flow during 5 min of growth time, cooling down to 940°C under 100 sccm H_2 and hot unloading of the sample at 940°C.

Figure 5.2 shows FEG-SEM micrographs of B1-Cu foil subjected to CVD graphene growth process under different ramping atmospheres. It was observed that ramping at 300 sccm H_2 and 200 sccm Ar/100 sccm H_2, or hot loading the Cu foil directly into the preheated furnace at 1000°C for annealing under 300 sccm H_2 resulted in formation of spherical dark features in nm size on the surface. The corresponding Raman spectra of these foils revealed mostly a strong D-band, which arises from breathing modes of sp^2 atoms in rings and requires a defect for its activation [14, 90], at ~1368-1397 cm^{-1} and a broad G-band, which correspond to in-plane C-C bond stretching in graphitic materials and is common to all sp^2-bonded carbon systems [90], shifted to higher frequencies compared to that of graphene (~1600 cm^{-1}) (e.g., Fig. 5.3 – H_2 ramped sample). The intensity ratio of the D-band to that of the G-band (I_D/I_G) which is generally used to characterize the defect content [90] is ~0.4 - 0.6, indicating that the samples are highly defective. Almost no 2D-band was observed in the Raman spectra of these samples, confirming that there is no graphene. 2D-band is attributed to a second-order process related to a phonon near the K point in graphene and activated by double resonance process and strongly depends on any perturbation on the electronic and/or phonon structure of graphene [90]. It should be noted that there were a few spots recorded for the Ar/H_2 ramped and the hot loaded (at 1000°C) samples with a 2D-band positioned at ~2709 - 2724 cm^{-1} (Fig. 5.3); however,

I_{2D}/I_G ratios were very low (~0.2 - 0.3), indicating the presence of some multilayer graphene regions.

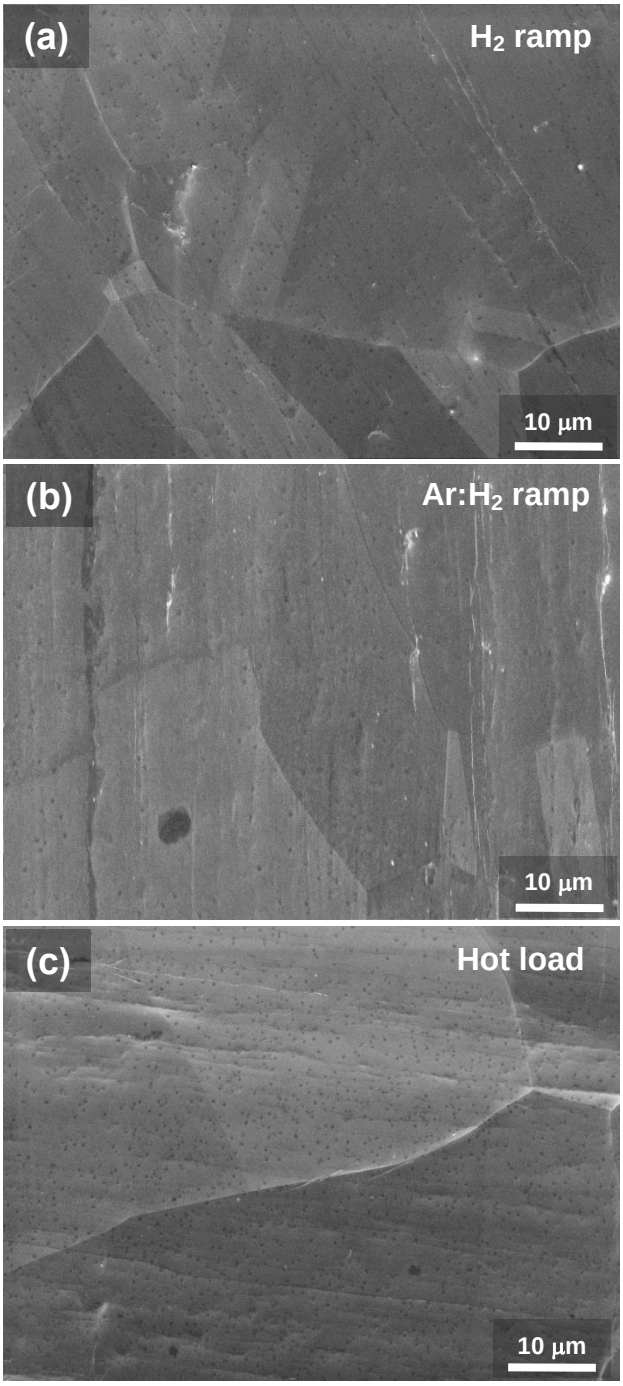

Figure 5.2. FEG-SEM micrographs of B1 Cu foils after being subjected to CVD growth process under different ramping conditions **(a)** 300 sccm H_2 ramp, **(b)** 200sccm Ar/100 sccm H_2 ramp, and **(c)** hot loading into a preheated furnace at 1000°C for annealing at 300 sccm H_2 flow.

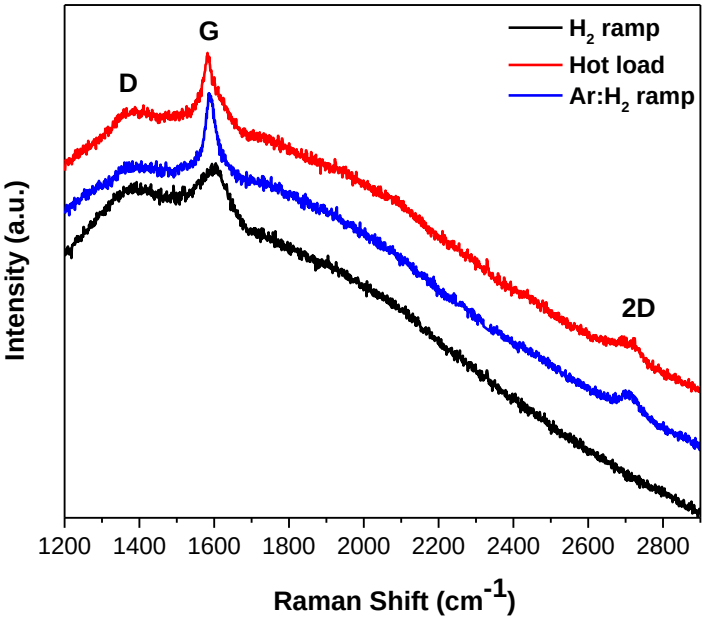

Figure 5.3. Raman spectra of B1 Cu foils after being subjected to CVD growth process under different ramping conditions (300 sccm H_2 ramp, 200sccm Ar:100 sccm H_2 ramp or hot load). The spectra show a background caused by the luminescence of the copper in this region.

These results indicated that if there is only H_2 in the ramping atmosphere or if there is not enough Ar as a buffer gas in the Ar/H_2 mixture during ramping, the surface of the Cu foil is deactivated; therefore CH_4 molecules cannot dissociate to promote graphene growth. The same situation is also valid when the sample is directly loaded into the reactor at 1000°C and annealed in H_2 environment. Jung et al. [158] performed atmospheric-pressure CVD growth of graphene domains on Cu foil using the various volume ratios of H_2 and Ar during annealing to investigate the influence of partial pressure of H_2 on the growth rate and shape of the graphene domains. The authors reported the synthesis of snowflake-shaped carbon aggregates when only H_2 was used during the annealing process. They attributed this to coverage of the surface completely by surface-bound active hydrogen atoms preventing the CH_4 molecules to bind to the surface to form active carbon species for graphene growth, which could possibly be the case in the present study, as well. Consequently, once the surface is covered by such hydrogen atoms, the active carbon species cannot transport and adsorbed onto the

Cu surface [158]. The authors suggested that if Ar coexist with H_2 in the reaction chamber, it collides with H_2 frequently, preventing H_2 molecules from binding to the surface. As a result, CH_4 has higher opportunity to bind the Cu surface to lead a proper graphene synthesis [158].

Figure 5.4 shows FEG-SEM micrograph of the graphene film grown on B1 Cu foil using 200 sccm Ar flow during ramping, revealing no dark spherical features across the surface. The representative Raman spectra measured at different spots across this graphene film on the Cu foil are shown in Fig. 5.5. The Raman spectrum in Figure 5.5(a) revealed a negligible D-band and a high I_{2D}/I_G ratio (~2.3) with a symmetric 2D-band (FWHM is ~25 cm^{-1}) at 2691 cm^{-1} and a G-band at 1589 cm^{-1}, confirming the presence of a monolayer graphene [91, 92]. Figure 5.5(b) revealed a bilayer graphene with a lower I_{2D}/I_G ratio (~1.7) and a broader FWHM of the 2D-band (~35cm^{-1}). G-band (~1593 cm^{-1}) and the 2D-band (~2703 cm^{-1}) shifted to higher frequency values. In addition, D-band was observed at ~ 1365 cm^{-1} with I_D/I_G ratio of 0.37. In Fig.5.5(c), the Raman spectrum of a highly defective few-layer or multilayer graphene was observed with I_D/I_G and I_{2D}/I_G ratios of 1.0 and 1.1, respectively. These results indicate that 200 sccm Ar flow promote graphene growth on B1 Cu foil; however, with some non-uniformity in the number of layers across the film.

Although Ar ramping was observed to be highly advantageous for graphene growth, irregular shaped, large (a few μm in diameter) impurity particles appeared on the surface when the ramping was performed only in Ar environment (Fig. 5.4). In order to investigate the composition of these impurity particles EDX analyses were performed. Figure 5.6 shows the FEG-SEM micrographs of these impurities and their EDX analysis results. Both secondary electron (SE) and back scattered electron (BSE) images of the impurities revealed the presence of two different phases in these particles (Fig. 5.6(a)). EDX analyses showed that these particles consist of C, O, Cu and Si elements and brighter regions are Cu-rich phase with a small amount of SiO_2 (Fig. 5.6(b)), while darker regions contain higher amount of SiO_2, as well as some CuO (Fig. 5.6(c)).

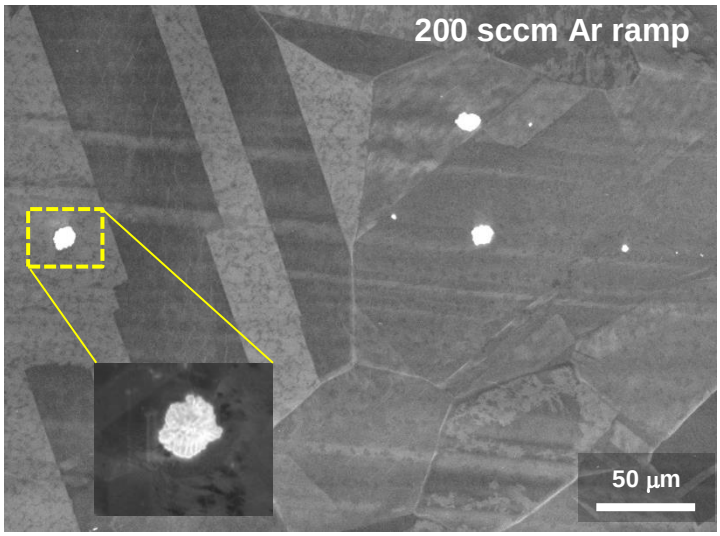

Figure 5.4. FEG-SEM micrograph of the graphene film grown on B1 Cu foil using 200 sccm Ar flow during ramping. Inset shows higher magnification of the impurity particle indicated by a dashed rectangle.

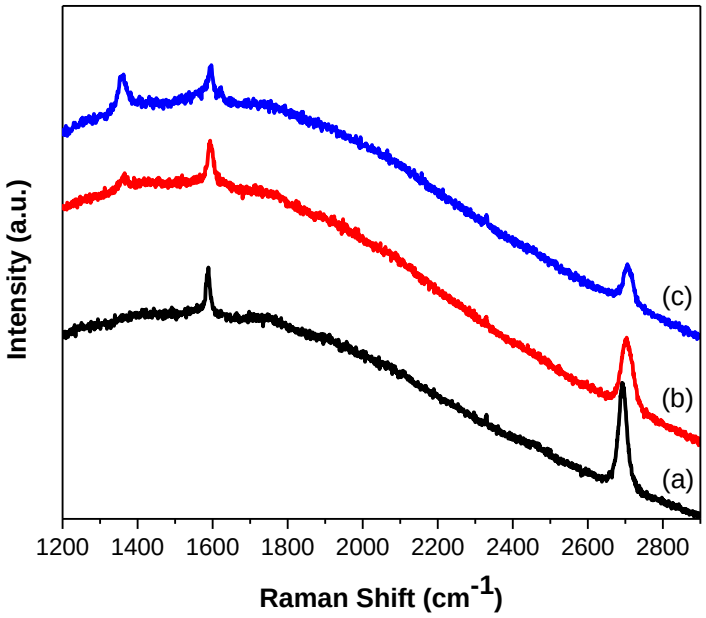

Figure 5.5. Raman spectra recorded at different spots on the graphene film grown on B1 Cu foil using 200 sccm Ar flow during ramping showing **(a)** Monolayer graphene, **(b)** Bilayer graphene and **(c)** Few-layer (3-5 layers) graphene.

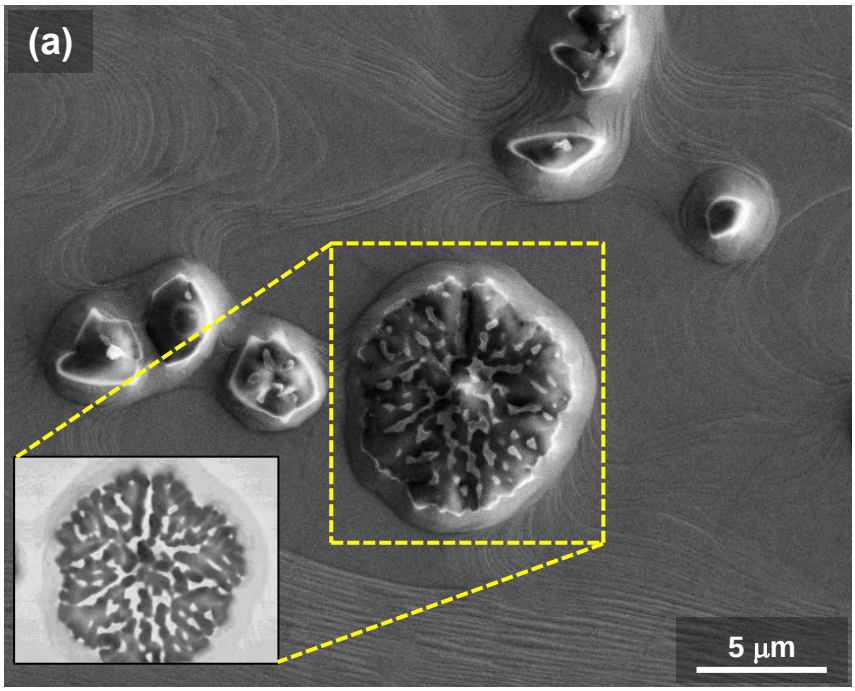

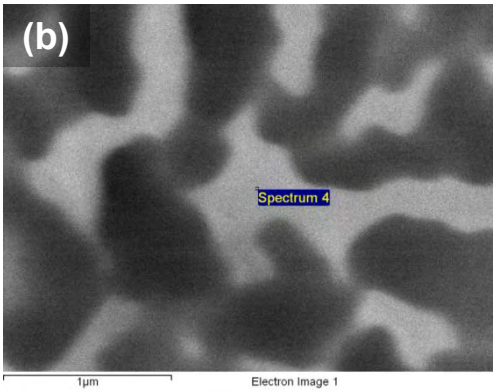

Element	Weight%	Atomic%
C K	3.20	14.10
O K	1.74	5.77
Si K	0.82	1.56
Cu L	94.24	78.57
Totals	100.00	

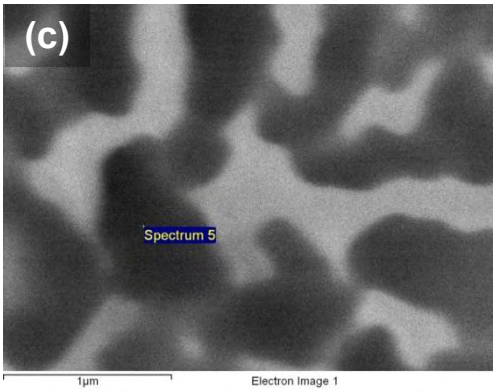

Element	Weight%	Atomic%
C K	2.89	7.78
O K	22.61	45.66
Si K	13.53	15.56
Cu L	60.96	31.00
Totals	100.00	

Figure 5.6. (a) Secondary electron image of impurity particles on Cu foil surface after CVD graphene growth process, the ramping step of which was performed under 200 sccm Ar. Inset shows the back scattered electron image of the impurity particle indicated by a dashed rectangle, revealing the presence of two different phases. **(b)**, **(c)** EDX analysis results of these two phases.

Jung et al. [158] also observed SiO_2 particles in the center of the carbon aggregates that were formed when only H_2 was used during the annealing step of the CVD process as confirmed by EDX, and they proposed that these SiO_2 particles were introduced to the sample from the quartz tube of the CVD chamber. However, their SiO_2 particles were spherical and much smaller (in nm size) than those observed in the present study when ramping was performed under only Ar gas. Impurity nanoparticles that appear white in color on the surface of the Cu foil after graphene growth have been commonly observed during SEM analyses [154, 156]. Kim et al. [154] performed EDX and Auger electron spectroscopy which showed that these white particles on the Cu surface are mostly metal particles, such as Si, Ca, Pt, Ru and Ce. They suggested that there are two possibilities for the origin of these impurities. They could either come from impurities distributed inside the copper foil and be driven out to the surface during high temperature growth process or they are on the Cu surface even before the CVD synthesis. The authors found that the impurity particles were significantly removed when the Cu foil was pre-cleaned with nitric acid; therefore they concluded that the impurity particles were on the Cu surface from the beginning [154].

In the present study, the Cu foils were already pre-cleaned using acetic acid as described in Section 5.2. However, in order to investigate the influence of different cleaning procedures on the amount of impurities, nitric acid cleaning and mechanical scrubbing of the Cu foil surface using acetone and isopropyl alcohol (IPA) soaked tissues prior to acetic acid cleaning were also performed. Figure 5.7 shows FEG-SEM micrographs of these pre-cleaned Cu foils after subjecting to the CVD process with 200 sccm Ar flow during ramping. Large, anisometric impurities were observed on the foils treated by nitric acid (Fig. 5.7 (a) and (b)), while pre-cleaning of the Cu foil surface by acetone and IPA soaked tissues helped to reduce the amount of these large, irregular shaped SiO_2 impurities, which may indicate that some of the impurities containing Si were on the surface of the Cu foil prior to the CVD graphene growth process, as in agreement with Kim et al [154]. However, it should be noted that some nanometer-sized spherical impurity particles still remain on the surface, indicating that some of the impurities present inside the copper foil are driven out to the surface during high

temperature CVD process, in contrast to the observations of Kim et al. [154]. These impurities then activate the formation of graphene islands of more than one layer across the surface (Figs. 5.7 (c) and (d)).

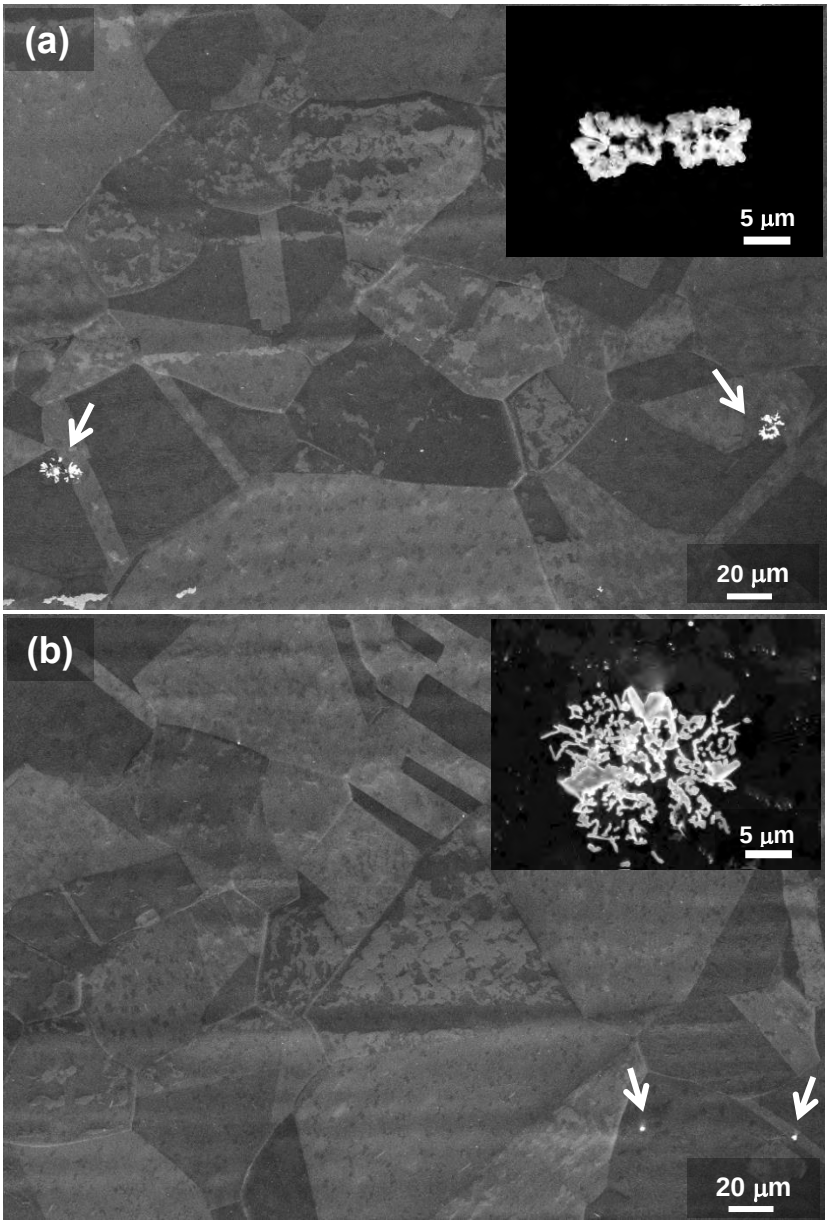

Figure 5.7. FEG-SEM micrographs of graphene grown on Cu foils that were pre-cleaned by **(a)** Nitric acid for 30 s, **(b)** Nitric acid for 60 s, and **(c)** Mechanical scrubbing of the foil surface using acetone and IPA soaked tissues. **(d)** Higher magnification image of (c). Ramping was performed at 200 sccm Ar flow. Insets in (a) and (b) show higher magnification of the impurities observed on the surface.

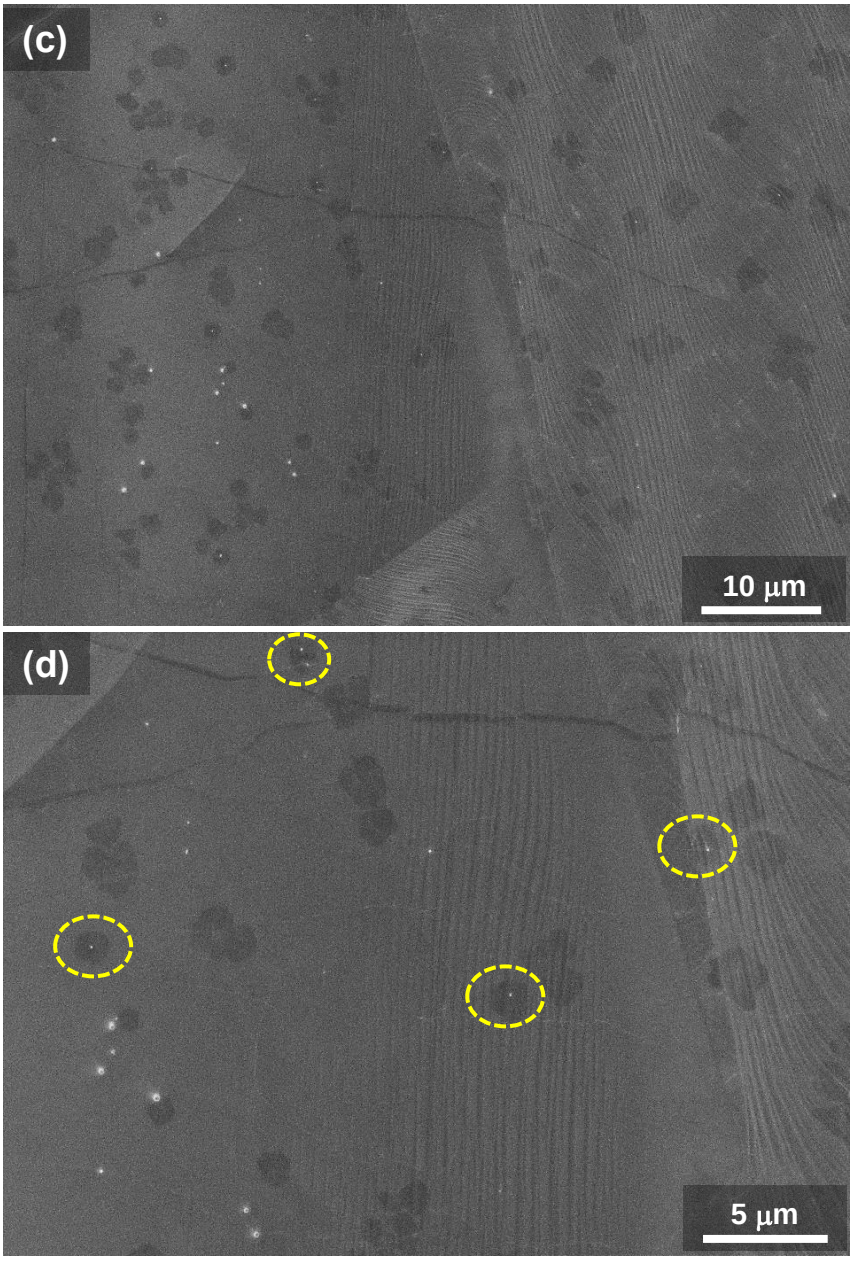

Figure 5.7. (Continued) FEG-SEM micrographs of graphene grown on Cu foils that were pre-cleaned by **(a)** Nitric acid for 30 s, **(b)** Nitric acid for 60 s, and **(c)** Mechanical scrubbing of the foil surface using acetone and IPA soaked tissues. **(d)** Higher magnification image of (c). Ramping was performed at 200 sccm Ar flow. Insets in (a) and (b) show higher magnification of the impurities observed on the surface.

Figure 5.8(a) shows representative Raman spectra recorded at different spots across the graphene film grown on pre-cleaned B1 Cu-foil with acetone and IPA soaked tissues and transferred onto a SiO_2 (300 nm)/Si substrate. Accordingly, a symmetrical 2D-band centered at 2676 cm^{-1} with a FWHM of 34 cm^{-1}, a high intensity ratio of the 2D-band to G-band, I_{2D}/I_G (~3.8) and the absence of any D-band, are the signature of single layer (monolayer) graphene (Fig. 5.8(a)) [91, 92]. On the other hand, observation of a larger 2D-band at 2685 cm^{-1} with a FWHM of 42 cm^{-1}, a decreased I_{2D}/I_G ratio (~2.8) and a small D-band (I_D/I_G : ~0.09) confirms the presence of bilayer graphene. This is in agreement with the SEM micrographs in Figs. 5.7(c) and (d)) that there are bilayer islands on the single layer graphene film. Figure 5.8(b) shows optical image of this graphene film transferred onto a SiO_2/Si substrate with alignment marks on it. It is seen from the optical image that graphene film is continuous over a large area, indicating a successful transfer process (without any cracks, holes, etc.), which is a very critical step since the graphene film can be mechanically damaged during transfer (Fig. 5.8(b)).

Figure 5.9 shows high resolution TEM (HRTEM) images of the graphene film grown on pre-cleaned B1 Cu-foil with acetone and IPA soaked tissues. There are impurity nanoparticles (~5 nm in diameter) on the graphene film. Fast Fourier transform (FFT) of the dashed area revealed hexagonal spot patterns indicating the six-fold symmetry feature of graphene (Inset in Fig. 5.9 (a)). A higher magnification image shows the impurity nanoparticles more clearly (Fig. 5.9 (a)). The corresponding FFT of this image (at the inset) revealed the contribution of these nanoparticles, as well as the graphene.

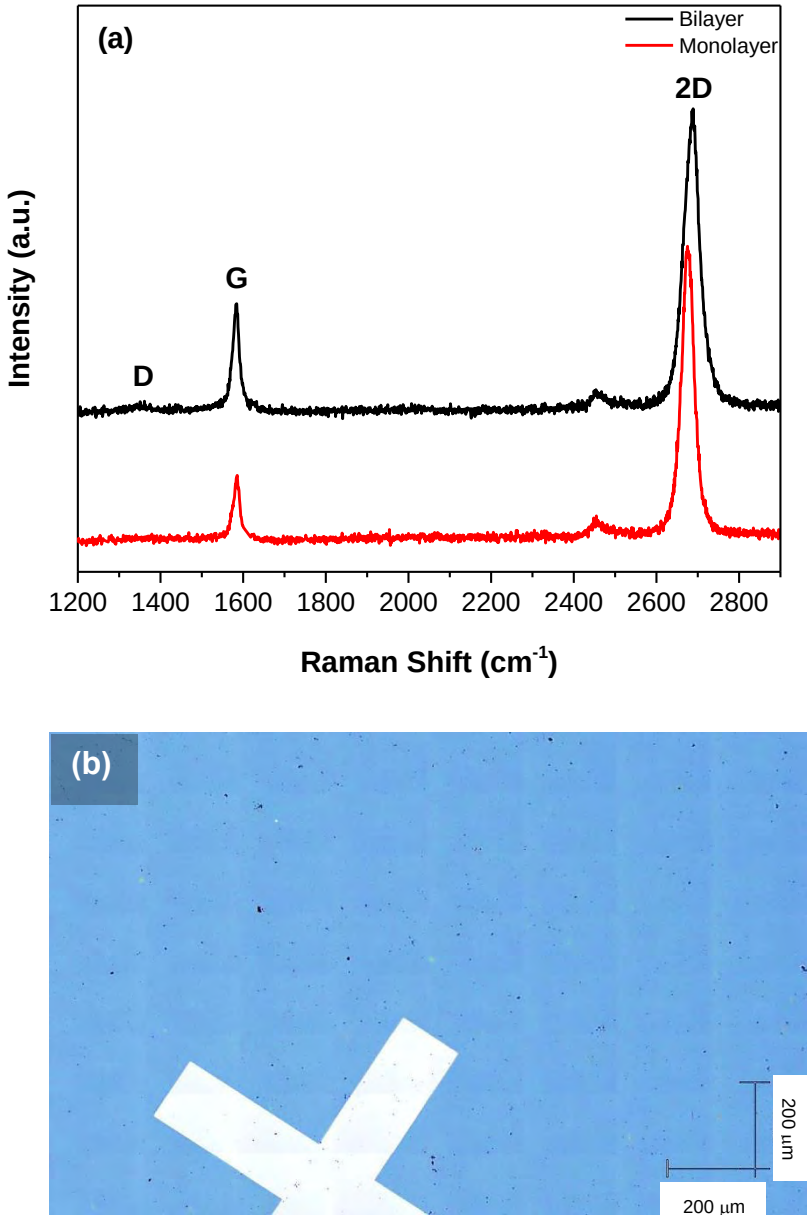

Figure 5.8. **(a)** Representative Raman spectra (recorded at different spots) of the graphene film grown on pre-cleaned B1 Cu-foil with acetone and IPA soaked tissues and transferred onto a SiO_2 (300 nm)/Si substrate, revealing the presence of bilayers, as well as monolayer graphene. **(b)** Optical image of this graphene film transferred onto a SiO_2 (300 nm)/Si substrate with alignment marks on it. Graphene film is continuous over a large area, indicating a successful transfer process.

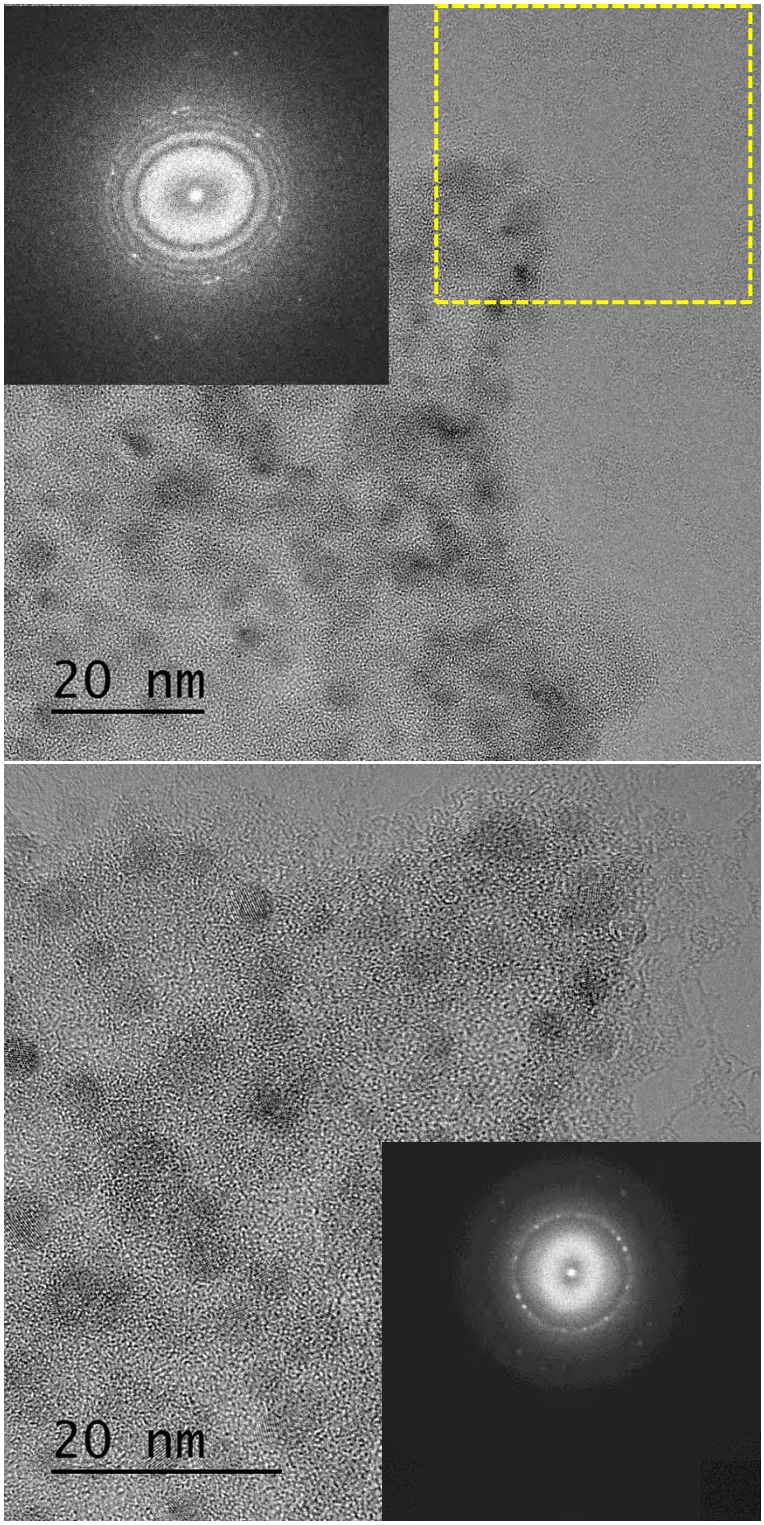

Figure 5.9. (a) HRTEM image of the graphene film grown on pre-cleaned B1 Cu-foil with acetone and IPA soaked tissues. Impurity nanoparticles are present on the graphene film. Inset shows the FFT of the area showed by a dashed square, indicating six fold symmetry of graphene. **(b)** Higher magnification of (a). Inset shows the FFT of the corresponding HRTEM image, revealing the contribution of nanoparticles, as well as graphene.

These results indicate that the SiO_2 impurities most probably do not come from the system (e.g., quartz tube), in contrast to what Jung et al. [158] suggested, but originate from the Cu foil itself and are promoted to form with different shapes and size depending on the ramping atmosphere and pre-cleaning of the Cu foil.

In order to investigate the origin of these impurities further and whether the amount of them vary from batch to batch, another Cu foil belonging to a different batch (but with the same lot number), denoted as B2 Cu foil, was used in the further CVD graphene growth studies. B2 Cu foil was precleaned using acetic acetic for 10 min, unless otherwise stated.

FEG-SEM micrographs of the B2 Cu foil subjected to the CVD process under a 200 sccm Ar flow during ramping revealed the appearance of much higher amount of impurities with irregular shape (Fig. 5.10(a) and (b)). All the process parameters (ramping, annealing and growth conditions) were same with that of B1 foil - 0.5 torr pressure during the whole process, 300 sccm H_2 flow during annealing for 30 min, 100 sccm H_2/20 sccm CH_4 flow during 5 min of growth time, cooling down to 940°C under 100 sccm H_2 and hot unloading of the sample at 940°C. EDX analysis of an impurity particle revealed the presence of C, O, Si and Cu, similar to the composition of the impurities observed on the B1 foil (Fig. 5.10(c), confirming that the impurities are SiO_2 particles with some CuO regions around them.

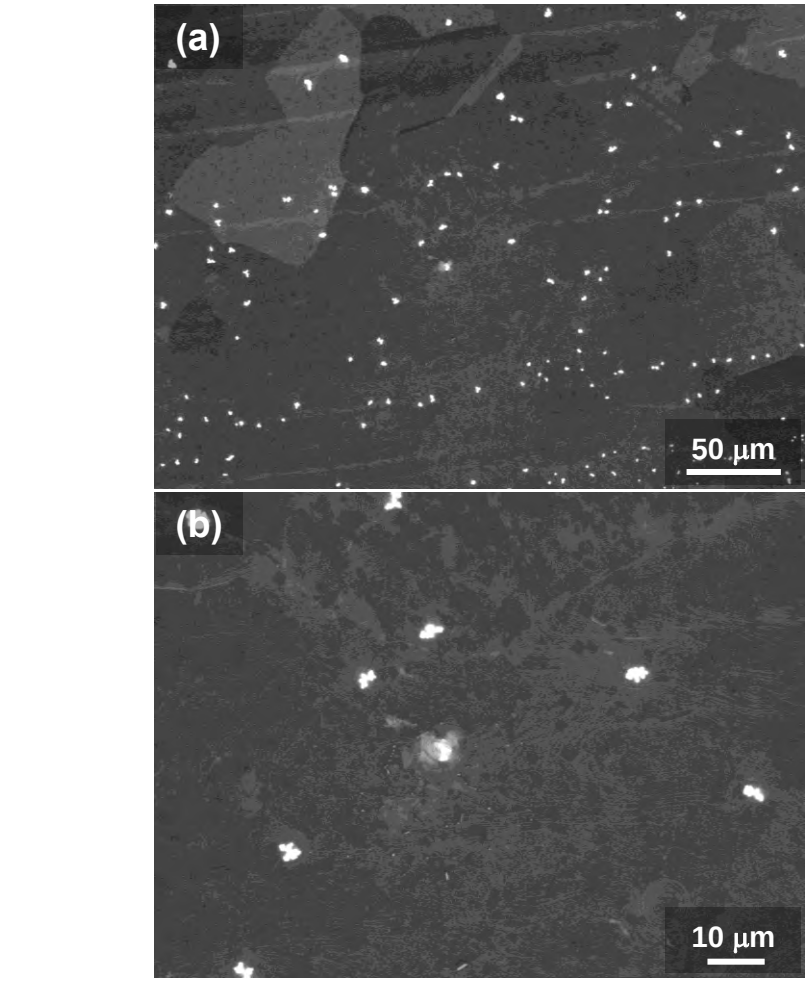

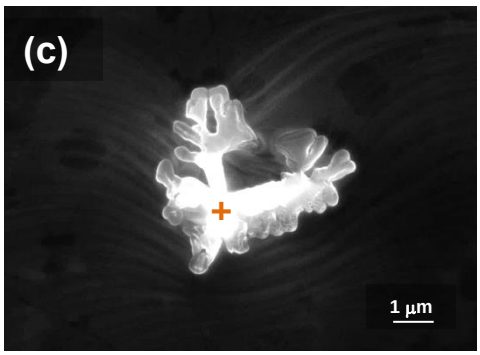

Element	Weight%	Atomic%
C K	2.24	4.93
O K	34.92	57.71
Si K	21.35	20.10
Cu L	41.48	17.26
Totals	100.00	

Figure 5.10. (a), (b) FEG-SEM micrographs (In-lens images) of the B2 foil after CVD graphene growth process. (b) is higher magnification of (a) showing the impurities and bilayer/few-layer graphene islands more clearly. **(c)** EDX analysis result of an impurity particle.

It should be noted that these SiO_2 particles are transferred onto the SiO_2/Si substrate together with the graphene film (Fig. 5.11).

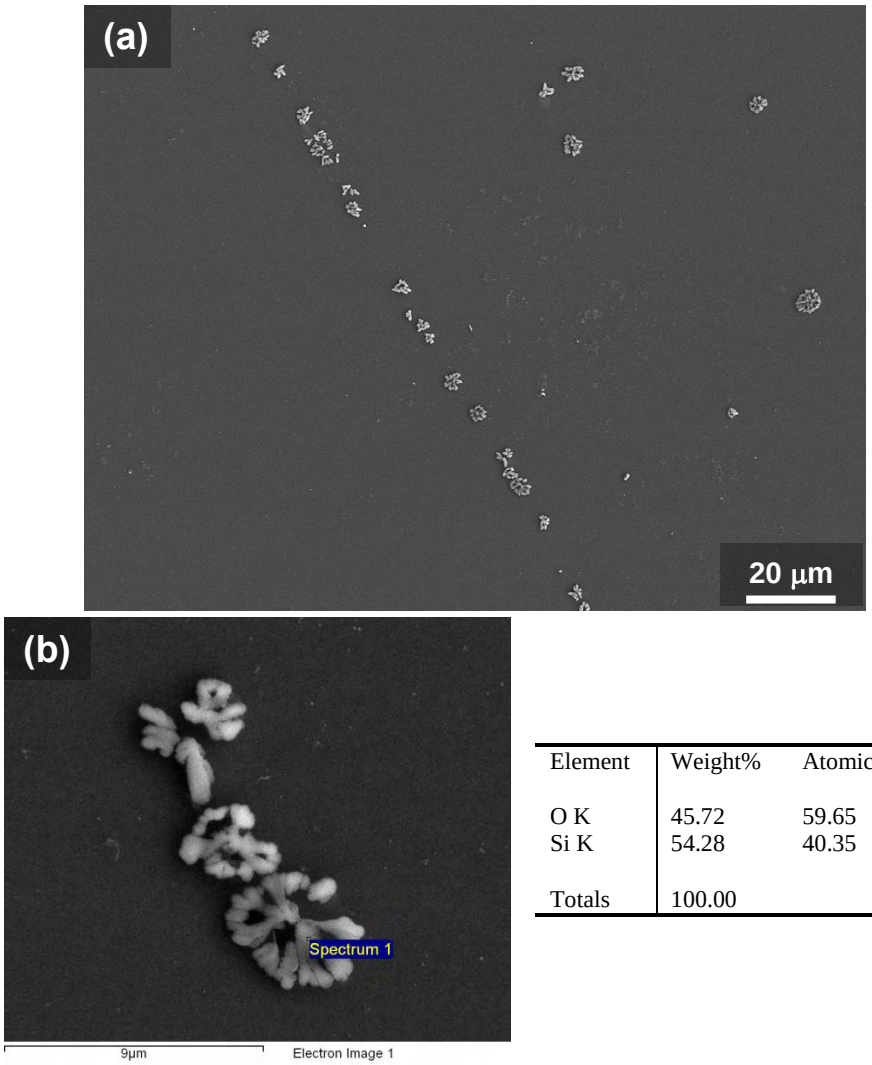

Element	Weight%	Atomic%
O K	45.72	59.65
Si K	54.28	40.35
Totals	100.00	

Figure 5.11. (a) FEG-SEM micrograph of CVD-grown graphene film transferred from B2 Cu foil onto a SiO_2(300nm)/Si substrate. The impurity particles are also transferred together with the graphene film. **(b)** EDX analysis of an impurity particle transferred onto SiO_2/Si substrate, confirming that it is a SiO_2 particle.

Figures 5.12(a) and (b) show the FEG-SEM micrographs of graphene films grown on B2 Cu foil using 300 sccm H_2 and 200 sccm Ar/100 sccm H_2 in the ramping atmosphere, respectively. Interestingly, the dark features which were formed when the B1 foil subjected to a CVD process at H_2 and Ar/H_2 ramping, resulting in deactivation of the Cu surface for graphene growth, have not formed on the B2 foil (Fig. 5.12). This suggests that characteristics of each batch are different. It is known that reproducibility is affected from batch to batch. The surface morphology and conditions of the copper foil can be very different depending on various suppliers or different batches [154]. These surface properties of Cu strongly affect the growth behavior of graphene, thus making the growth conditions irreproducible when different batches of Cu foil are used. This may also affect the quality of the graphene significantly [154]. The difference between the B1 and B2 foils could be their oxygen content; therefore, each batch may need a separate process tuning. Hao et al. [159] discovered that oxygen impurities on the Cu surface suppress graphene nucleation density by passivating Cu surface active sites, such as step edges, defects, impurities, etc, enabling the growth of cm-scale single-crystal graphene domains. The deactivation of the B1 foil surface under H_2 or Ar/H_2 ramping atmosphere could be related with the low oxygen level of this foil, which may result in the deactivation of the surface by complete coverage of the surface-bound active hydrogen atoms preventing the CH_4 molecules to bind to the surface to form active carbon species for graphene growth, as suggested by Jung et al. [158]. On the other hand, the higher oxygen content of the B2 foil could have prevented the complete coverage of the surface by surface-bound hydrogen atoms, enabling the graphene growth even when ramping at only H_2 flow.

Figures 5.12(a) and (b) also show that these two samples do not exhibit irregular shaped large SiO_2 particles, in contrast to the case when ramping in only Ar flow. These results are in agreement with those observed for the B1 Cu foil, confirming that the irregular-shaped, large SiO_2 particles are formed when the ramping is carried out only at Ar atmosphere. However, spherical impurity nanoparticles were observed especially on the Ar/H_2 ramped sample. Figure 5.12(c) shows the EDX analysis result for one of these nanoparticles, indicating

that it contains O, Si, Ca and Cu elements. The presence of oxygen indicates the presence of oxides in these nanoparticles, as well.

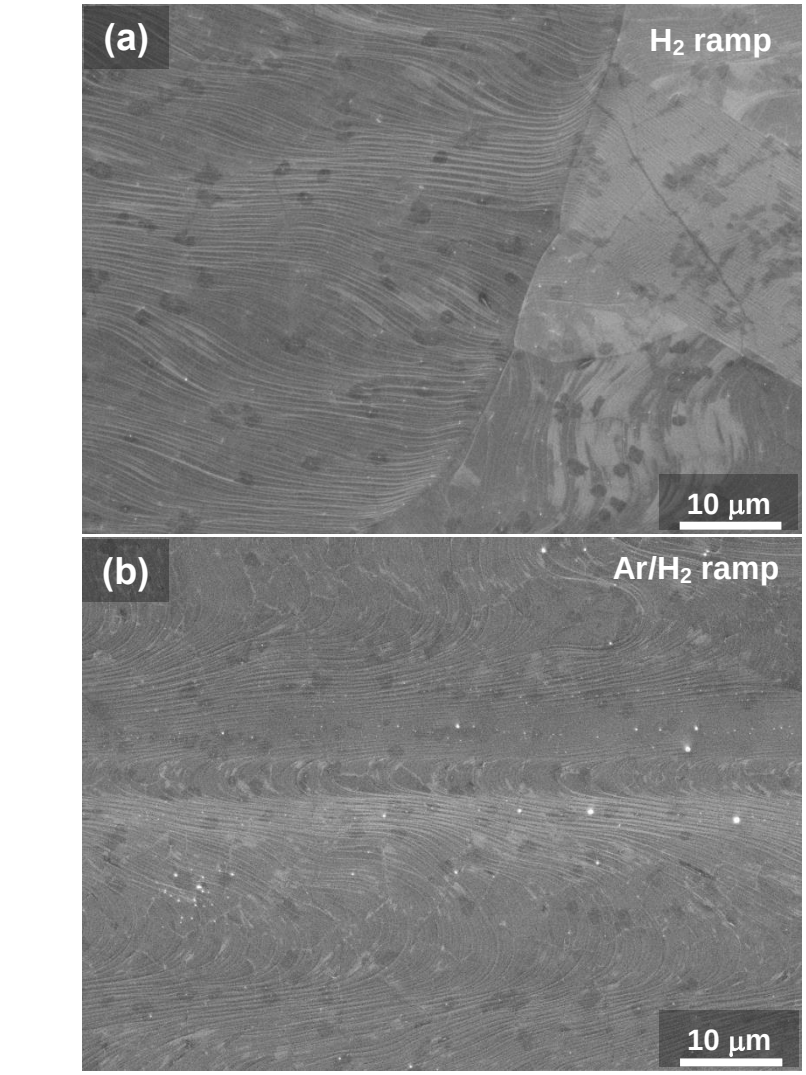

Element	Weight%	Atomic%
O K	11.40	31.04
Si K	6.56	10.17
Ca K	6.30	6.84
Cu L	75.75	51.94
Totals	100.00	

Figure 5.12. FEG-SEM micrographs of graphene films on B2 Cu foil subjected to a CVD growth process at ramping atmospheres of **(a)** 300 sccm H_2 flow and **(b)** 200 sccm Ar/100 sccm H_2. **(c)** EDX analysis result of a spherical impurity nanoparticle.

The SiO_2 impurity appearance could be attributed to oxidation of Si impurities that were already present in the Cu foil before the CVD process due to presence of residual O_2 in the ramping atmosphere when the ramping atmosphere contains only Ar gas. The basic function of annealing atmosphere is to protect the sample from oxidation, so as the function of the ramping atmosphere. Therefore, the oxygen partial pressure of the atmosphere must be below a specific level, which is required to form an oxide. The oxygen partial pressure, above which oxidation occurs, and below which metal is stable, is known for each metal and can be determined by using the corresponding Ellingham diagram, which gives the standard free energies of formation of oxides as a function of temperature [160]. As it can be seen from the Ellingham diagram shown in Fig. 5.13, Si oxidizes at any oxygen partial pressure (pO_2) higher than ~10^{-26} atm at 1000°C. Using an inert gas such as Ar decreases the oxygen level in the atmosphere significantly; however, even 99.999% pure Ar contains 1-2 ppm of oxygen, which is enough to oxidize Si. In order to reduce the oxygen level further, it is necessary to react it with hydrogen:

$$1/2O_2 + H_2 \longrightarrow H_2O$$

In this case, the oxygen partial pressure depends on the H_2:H_2O ratio. Accordingly, if this ratio is higher, the atmosphere becomes more reducing.

Zhu et al. [161] have studied floating zone refining of commercially available 99.9999% pure Cu under reduced hydrogen pressure. They observed SiO_2 inclusions in the molten zone and concluded that these inclusions originate from the starting material. The authors reported that if Si is present as solid solution in the starting material, to reduce them below 0.005 ppm, the oxygen partial pressure in the chamber should be higher than 1.6×10^{-11} Pa (~1.6×10^{-17} atm.) at 1473 K, respectively [161]. However, they determined that oxygen partial pressure in the hydrogen atmosphere is only 1.3×10^{-20} Pa (~1.3×10^{-25} atm.) at 1473 K. Therefore, the authors concluded that the SiO_2 inclusions are not due to the reaction of Si with trace oxygen in liquid copper during refining in hydrogen atmosphere, but come from the starting material [161]. Lim et al. [162] carried out experiments to remove impurities from Cu metal by Ar and Ar-20%H_2 plasma arc

melting. Impurity concentrations in the Cu metal after refining were determined by glow discharge mass spectroscopy and it was revealed that the oxygen content of the starting material increased from 15 to 33.5 mass ppm after 60 min Ar treatment, but decreased to 6.8 mass ppm after Ar-20%H_2 plasma arc melting for 60 min, indicating that the Ar introduces oxygen into the system [162]. The concentration of Si showed a slight decrease from 0.31 to 0.28 ppm after Ar plasma arc melting, while Ar-20%H_2 was found to be slightly more effective with a Si concentration of 0.22 after refining. The authors reported that Si impurities in Cu molten metal cannot be separated easily due to the formation of SiO_2 inclusions in the starting material itself [162].

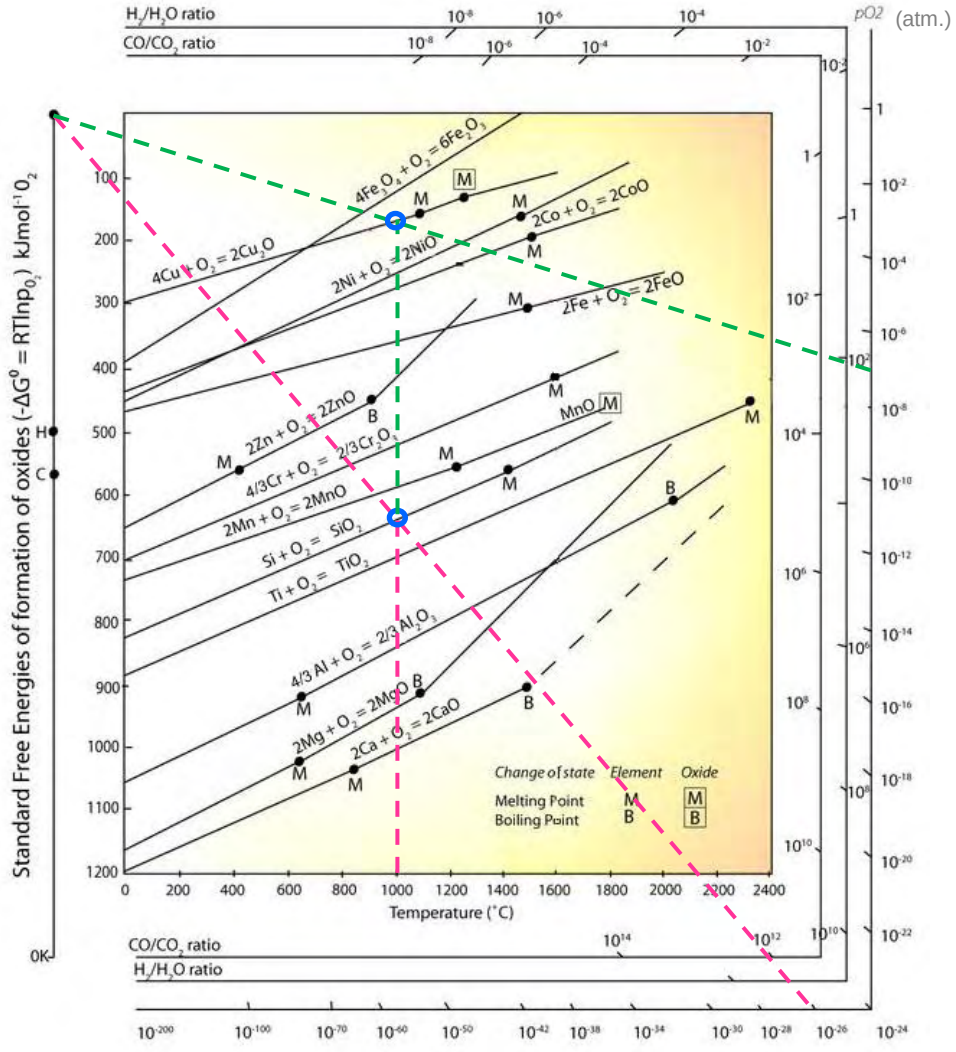

Figure 5.13. Standard free energies of formation of oxides as a function of temperature [160, 163]

The Cu foil impurities affect not only the quality but also the catalytic decomposition of CH_4, consequently the thickness uniformity of the grown graphene film, since the impurities enhance the catalytic activity of the Cu surface [155]. As it can be seen in Fig. 5.12(a) and (b), the impurity nanoparticles promote nucleation of more than one layer graphene islands on the surface (the darker regions on the SEM images). Therefore, in order to improve the thickness uniformity of CVD grown graphene films, it is critical to minimize the amount of these impurities, as well as controlling the process parameters.

In order to examine the effect of CH_4 concentration on thickness uniformity of graphene film grown on the B2 Cu foil, 100 sccm H_2/17 sccm CH_4 gas flow was used during graphene growth for 5 min (ramping atmosphere is 200 sccm Ar/100 sccm H_2 and the other parameters were kept fixed). FEG-SEM micrograph of this sample indicated that decreasing the concentration of CH_4 resulted in a decrease in the amount of bilayer/multilayer islands (Fig. 5.14(a)). Decreasing the process pressure from 0.5 torr to ~0.3 and ~0.2 torr for the ramping and annealing steps, respectively, resulted in a smoother surface (Fig. 5.14(b)). It should be noted that this foil was mechanically cleaned using acetone and IPA soaked tissues [164], prior to cleaning by acetic for 10 min. Figures 5.14(c) and (d) shows the SEM micrographs of the graphene film grown at exactly the same conditions as indicated for the sample shown in Fig. 5.14(b); however, the B2 Cu foil was pre-cleaned in nitric acid solution (5.4 % (w/w)) for 60 s, resulting in a cleaner Cu foil surface with a significantly reduced impurity and bilayer/few-layer island amounts.

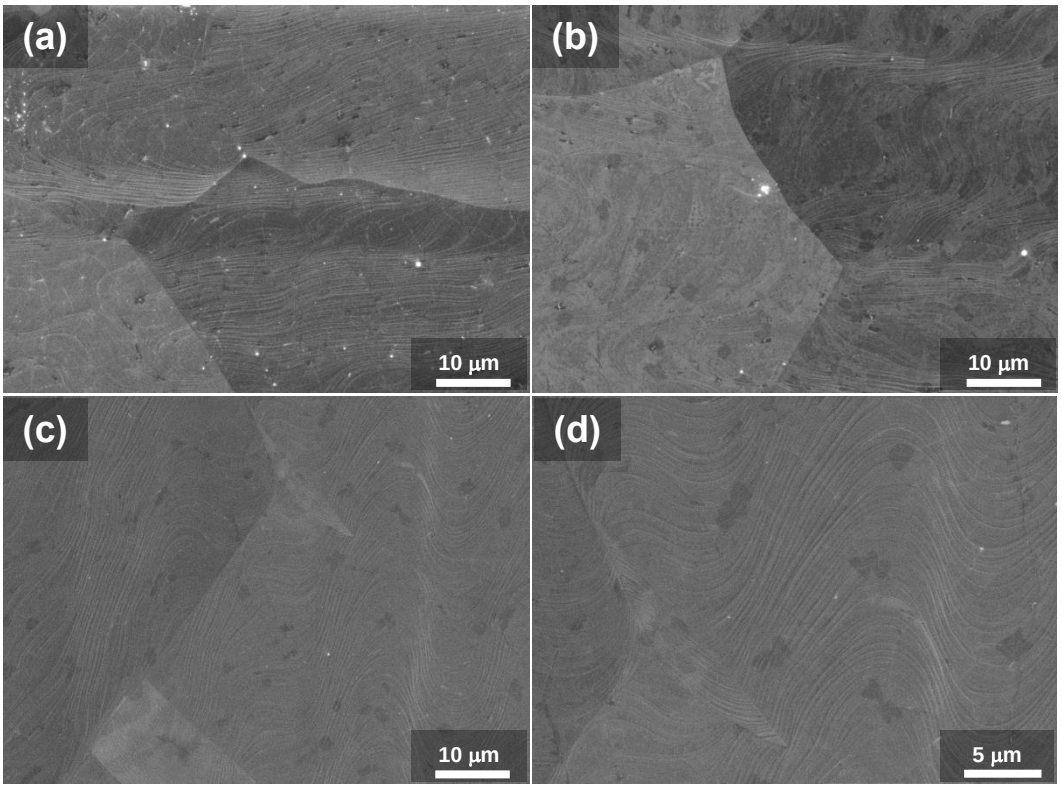

Figure 5.14. FEG-SEM micrographs of graphene films grown on B2 Cu foil using **(a)** 200 sccm Ar/100 sccm H_2 during ramping and 100 sccm H_2/17 sccm CH_4 gas flow during graphene growth (the other parameters were kept fixed), **(b)** the same process conditions as indicated in (a), but at a 0.3 and 0.2 torr during ramping and annealing, instead of 0.5 torr. The Cu foil was mechanically cleaned prior to acetic acid cleaning and **(c)** the same conditions as indicated in (b), but the Cu foil was pre-cleaned in a nitric acid solution for 60 s instead of acetic acid. **(d)** Higher magnification of (c).

Figure 5.15 shows representative Raman spectra recorded at different spots across the graphene film grown on B2 Cu-foil, which was pre-cleaned by nitric acid for 60 s, using 200 sccm Ar/100 sccm H_2 during ramping, 100 sccm H_2/17 sccm CH_4 during graphene growth for 5 min, and 0.3 torr and 0.2 torr pressure during ramping and annealing steps, respectively. A symmetrical 2D-band that can be fit with a single Lorentzian (as shown in the inset) centered at 2679 cm^{-1} with a FWHM of 38 cm^{-1}, a high intensity ratio of the 2D-band to G-band, I_{2D}/I_G (~2.3) and an almost negligible D-band are all the hallmarks of single layer

graphene (Fig. 5.15(a)) [91, 92]. On the other hand, Fig. 5.15(b) shows a Raman spectrum (recorded at a different spot) with a larger 2D-band (FWHM of 46 cm^{-1}) at 2674 cm^{-1}, a lower I_{2D}/I_G ratio (~1.9) and a small D-band (I_D/I_G : ~0.04), confirming that the islands observed on the corresponding SEM micrographs (Figs. 5.14(c) and (d)) are bilayer graphene. Figure 5.16(a) shows optical image of this graphene film transferred onto a SiO_2 (300 nm)/Si substrate. It is seen from the optical image that graphene film is continuous over a large area, except very few empty regions, indicating a successful transfer process (Fig. 5.16(a)). The FEG-SEM micrograph of the transferred graphene film onto SiO_2/Si substrate reveals the bilayer islands, as well as the grain boundaries and the wrinkles across the surface (Fig. 5.16(b)).

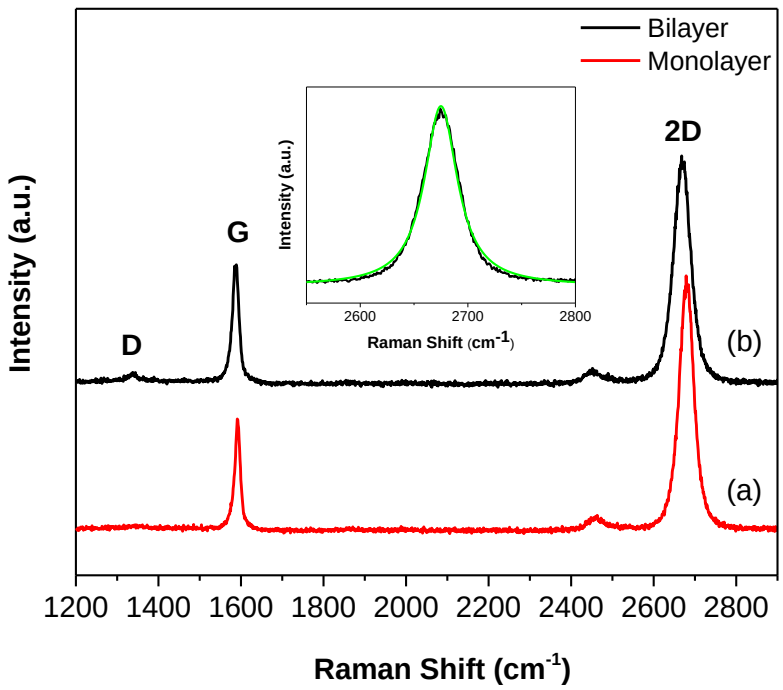

Figure 5.15. Representative Raman spectra recorded at different spots across the graphene film grown on B2 Cu-foil, which was pre-cleaned by nitric acid for 60 s, using 200 sccm Ar/100 sccm H_2 during ramping, 100 sccm H_2/17 sccm CH_4 during graphene growth for 5 min, and 0.3 torr and 0.2 torr pressure during ramping and annealing steps, respectively.

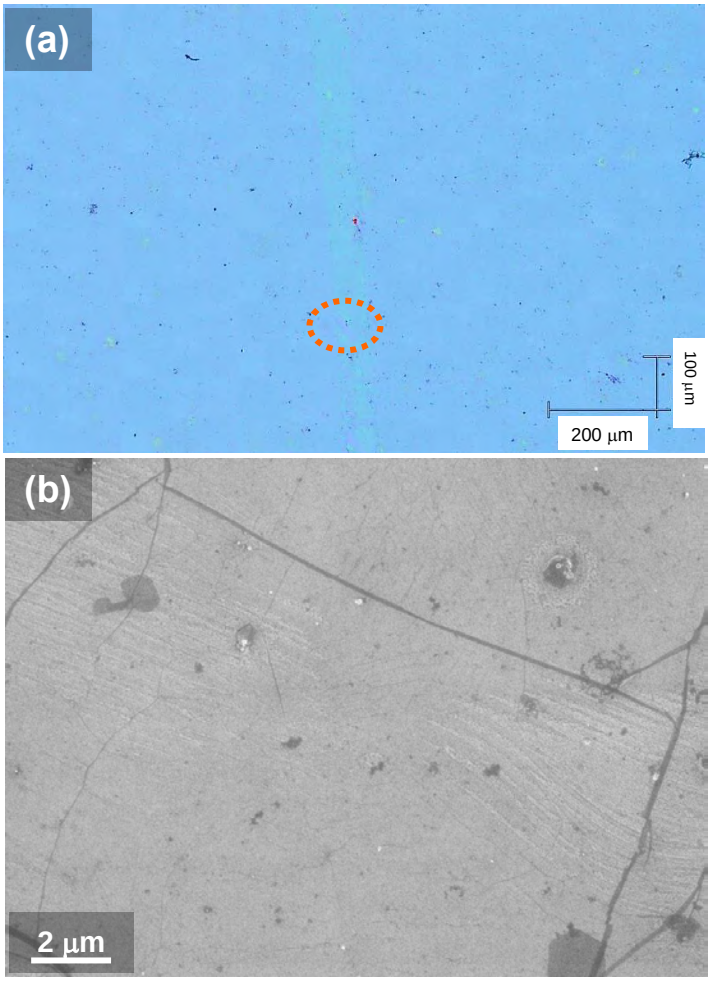

Figure 5.16. (a) Optical image and (b) FEG-SEM micrograph of the graphene film grown on B2 Cu foil, which was pre-cleaned by nitric acid for 60 s (using 200 sccm Ar/100 sccm H_2 during ramping, 100 sccm H_2/17 sccm CH_4 during graphene growth for 5 min, and 0.3 torr and 0.2 torr pressure during ramping and annealing steps, respectively) and transferred onto a SiO_2 (300 nm)/Si substrate.

Figure 5.17 shows low magnification TEM and HRTEM images of a bilayer graphene island grown on B2 Cu foil. The number of layers of this island can be easily observed at the edge of it (Fig. 5.17(b)). HRTEM image shows high crystallinity of the sample (Fig. 5.17(c)), and the FFT image of this HRTEM micrograph reveals hexagonal spot patterns indicating the six-fold symmetry feature of graphene (Fig. 5.17(d))

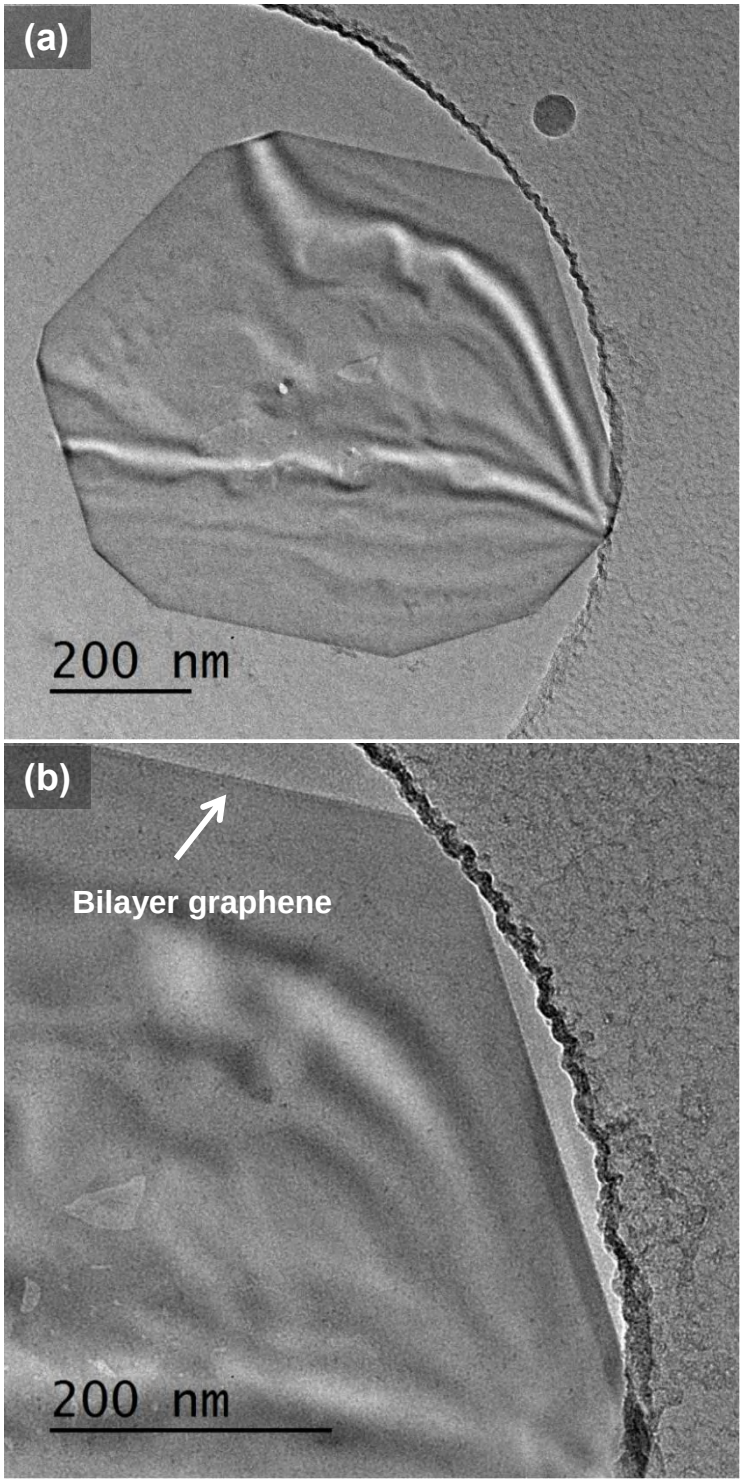

Figure 5.17. (a), (b) Low magnification TEM and **(c)** HRTEM images of a bilayer graphene island grown on B2 Cu-foil which was pre-cleaned by nitric acid for 60 s (using 200 sccm Ar/100 sccm H_2 during ramping, 100 sccm H_2/17 sccm CH_4 during graphene growth for 5 min, and 0.3 torr and 0.2 torr pressure during ramping and annealing steps, respectively). **(d)** FFT of the corresponding HRTEM image shown in (c).

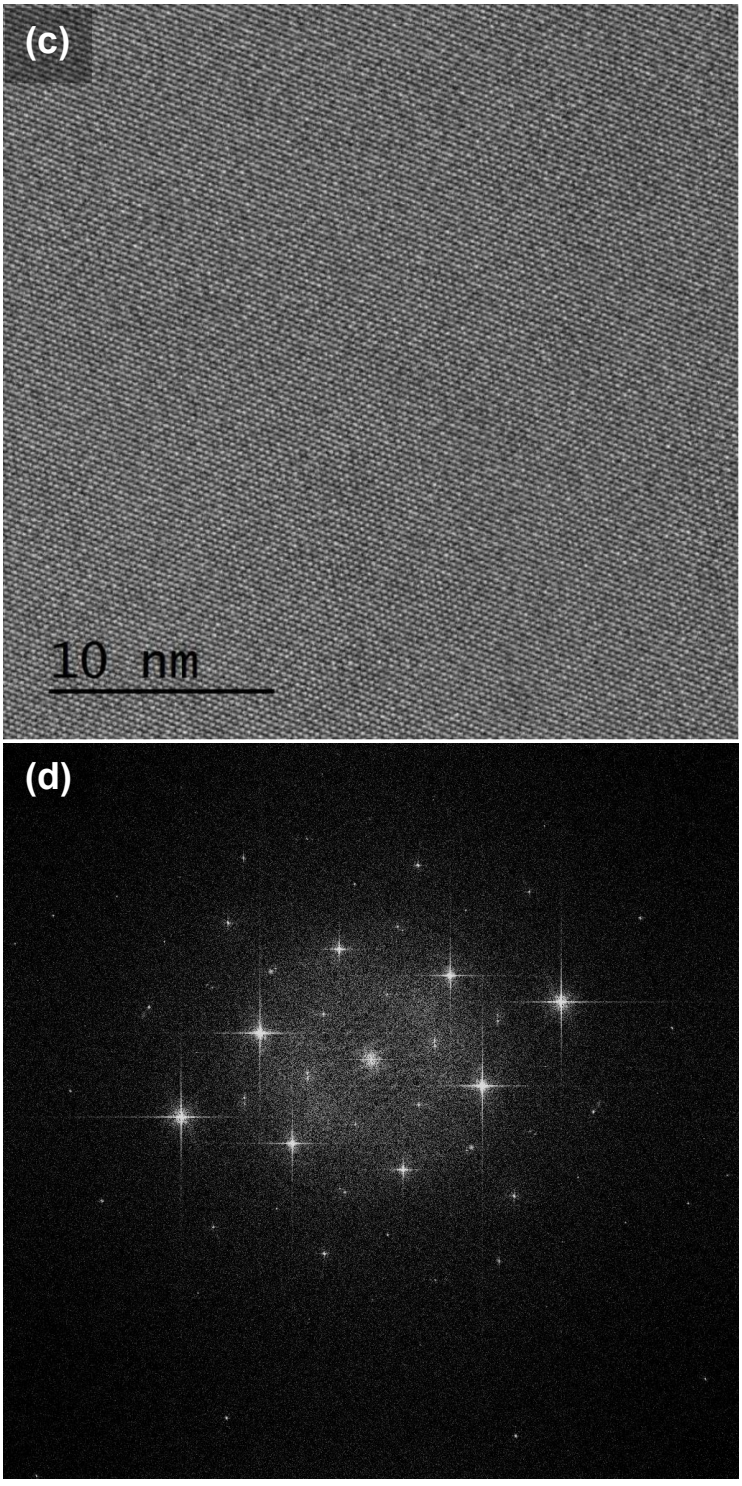

Figure 5.17. (Continued) (a), (b) Low magnification TEM and **(c)** HRTEM images of a bilayer graphene island grown on B2 Cu-foil which was pre-cleaned by nitric acid for 60 s (using 200 sccm Ar/100 sccm H_2 during ramping, 100 sccm H_2/17 sccm CH_4 during graphene growth for 5 min, and 0.3 torr and 0.2 torr pressure during ramping and annealing steps, respectively). **(d)** FFT of the corresponding HRTEM image shown in (c).

Figure 5.18 gives a summary of the effect of ramping atmosphere on graphene growth by CVD method on two different Cu foils (belonging to different batches), the surface oxygen content of which was supposed to be different. Graphene growth was promoted on oxygen-free Cu foil when the ramping was performed only in Ar flow. The presence of H_2 in the ramping atmosphere resulted in deactivation of the foil surface by surface bound hydrogen atoms. However, ramping in Ar atmosphere caused formation of large, irregular-shaped SiO_2 impurities, which was attributed to oxidation of Si impurities that were already present in the Cu foil due to presence of residual O_2 in the ramping atmosphere. On the other hand, Ar ramping resulted in much higher amount of SiO_2 impurities on oxygen-rich Cu foil compared to oxygen-free Cu foil. The presence of H_2 in the ramping atmosphere did not prevent the graphene growth on oxygen-rich Cu foil, and even promoted high quality graphene growth without large SiO_2 impurities. The dashed rectangles indicate the ramping atmospheres that provided the highest quality graphene growth on the corresponding Cu foils in the present study. It should be noted that effective pre-cleaning helped to reduce the amount of impurities on both foils.

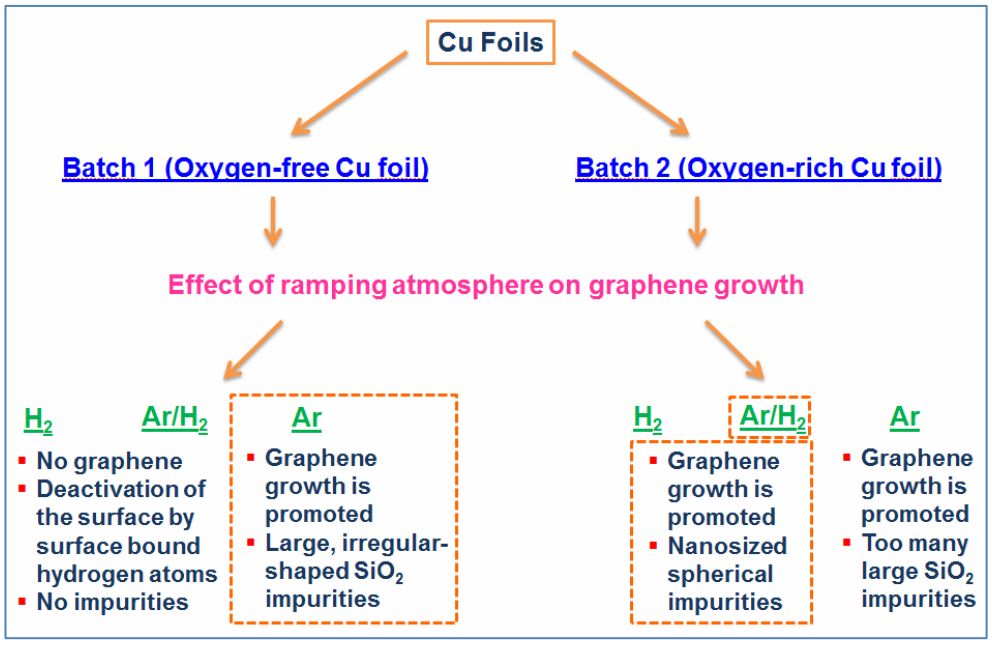

Figure 5.18. Summary of the effect of ramping atmosphere on graphene growth by CVD method on two different Cu foils (belonging to different batches) with different surface oxygen content.

5.4. Conclusions

Low-pressure CVD growth experiments of graphene films on two different Cu foils (belonging to two different batches - denoted as B1 and B2 Cu foils) were performed by controlling the H_2 and/or Ar flows rates during ramping in order to investigate the influence of ramping atmosphere on the impurity level, quality of the synthesized graphene films and their uniformity in terms of number of layers. The effect of differences in Cu foil characteristics depending on using foils from different batches was also examined and different pre-cleaning routes were investigated in order to minimize the amount of impurities.

It was observed that ramping atmosphere has a strong influence on the graphene growth process. It affected not only the nucleation of graphene, but also the type and amount of the impurities formed on the surface. H_2 and Ar/H_2 ramping resulted in appearance of spherical nanometer-sized impurities, while irregular-shaped, large (a few μm) SiO_2 impurities were observed when there is only Ar flow during ramping. The formation of SiO_2 particles was attributed to oxidation of Si impurities that were already present in the Cu foil before the CVD process due to presence of residual O_2 in the ramping atmosphere, when the ramping atmosphere contains only Ar gas. The presence of H_2 as well as Ar during ramping eliminated the formation of these large impurities by reducing the oxygen level in the system.

Monolayer graphene with few amounts of bilayer graphene islands on it was successfully synthesized using two different Cu foils belonging to same lot number, but different batches. However, these two foils exhibited different characteristics both in terms of the reaction that they showed against process conditions such as ramping atmosphere and of the amount of impurities. Therefore, they needed separate process adjustments. The difference between these two Cu foils was attributed to the possible difference in their oxygen impurity content.

Pre-cleaning of the Cu foil was observed to reduce the amount of impurities. However, the most effective pre-cleaning route may change depending on the surface characteristics of the Cu foil used.

The electrical characterization and high magnetic field experiments of the graphene films grown on B1 Cu foil *(pre-cleaned by acetic acid for 10 min) using 200 sccm Ar flow during ramping, 100 sccm H_2/20 sccm CH_4 during graphene growth for 5 min and 0.5 torr pressure during the entire process*, and on B2 Cu foil *(pre-cleaned by nitric acid for 60 s) using 200 sccm Ar/100 sccm H_2 during ramping, 100 sccm H_2/17 sccm CH_4 during graphene growth, and 0.3 torr and 0.2 torr pressure during ramping and annealing steps, respectively*, were discussed in Chapter 6. These two graphene samples were denoted as B1 and B2 samples in Chapter 6.

6. ELECTRICAL CHARACTERIZATION AND HIGH MAGNETIC FIELD MEASUREMENTS OF CVD-GROWN GRAPHENE FILMS

6.1. Introduction

Anomalous quantum Hall effect (QHE) is one of the most remarkable properties of graphene [16, 21].

In conventional integer QHE observed in two-dimensional semiconductor systems, when charge carriers are forced to move in a plane and are subjected to a perpendicular magnetic field B of appropriate magnitude at low temperature (Fig. 6.1(a)), the Hall (transverse) resistance ($R_H \equiv R_{xy}$) is quantized and shows plateaus at values R_K/i, where i is an integer and R_K theoretically equals h/e^2 ('e' is the electron charge and 'h' is the Planck constant). Simultaneously, the longitudinal resistance, R_{xx}, drops to zero, reflecting the absence of dissipation in the two-dimensional electron gas (Fig. 6.1(b)) [165, 166]. This integer QHE relies on the charge carriers in the system occupying a series of discrete energy levels known as Landau levels (LLs), which correspond to the quantization of the cyclotron motion of charge carriers in the magnetic field [166].

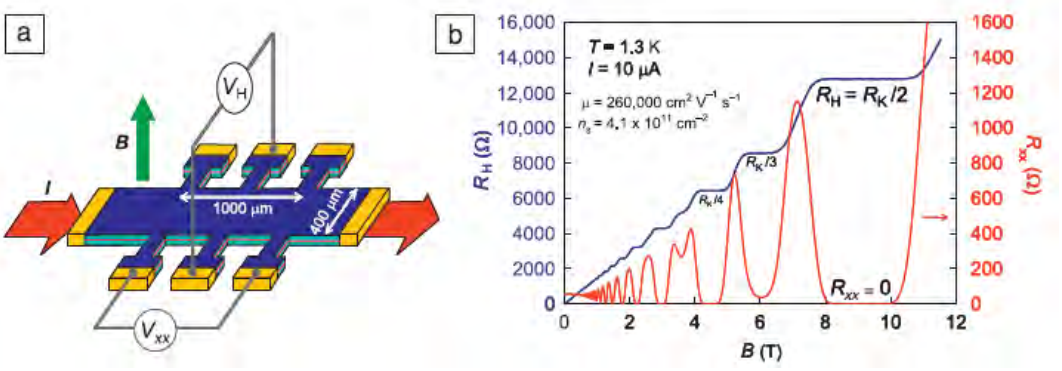

Figure 6.1. (a) Drawing of a typical Hall bar, fabricated from a two-dimensional electron gas (formed in a GaAs/AlGaAs heterostructure). **(b)** Longitudinal (R_{xx}) and Hall resistance (R_H) measured in the device at T=1.3K.The value of the Hall resistance on the plateaus is a very reproducible resistance reference [166].

In graphene, charge carriers mimic massless Dirac fermions; therefore graphene exhibits anomalous QHE resulting in shifted positions of the Hall

plateaus [167]. In anomalous QHE observed in graphene, the Hall resistance displays quantized plateaus at $R_{xy}=h/[g.(n+1/2).e^2]$ (where g=4 stands for spin and valley degeneracy) as a function of the magnetic field. It should be noted that the QHE depends on the electronic band structure of the system, which is directly related to the number of layers. In bilayer graphene, charge carriers have a parabolic energy spectrum, consequently they exhibit a different form of QHE where the Landau quantization of the fermions results in plateaus in Hall conductivity at standard integer positions [167]. The use of magnetic field has been proven extremely useful for addressing the fundamental properties of graphene as it provides an external and adjustable parameter which drastically modifies its electronic band structure [168].

The initial experiments revealing graphene's unique electronic transport properties were performed using micro-mechanically exfoliated graphite deposited on SiO_2 substrates. However, the exfoliation technique provides graphene flakes of the order of tens of micrometers and is not a scalable method for practical applications (e.g. integrated circuits, transparent electronics, quantum Hall resistance metrology, optical and scanning tunneling microscopy (STM) studies).

Chemical vapor deposition (CVD) is a promising method for the production of high quality wafer-scale graphene films. The CVD-grown graphene films can be transferred from the metal catalyst onto dielectric substrates enabling patterning the films precisely directly on the desired substrate for the electronic applications. It was shown that high quality and uniform CVD-grown graphene films exhibit anomalous QHE at low temperature and high magnetic field [169]. However, the structural characteristics and disorders at the microscopic and macroscopic scale have a strong influence on the transport properties of graphene. The mobility of CVD-grown graphene is limited by disorder originating from both the growth and the transfer processes.

As discussed in Chapter 5 of this thesis, large-area graphene films with improved quality were produced via CVD method by optimizing the process and the transfer conditions. The objective of this study was to perform electrical characterization and to measure transport properties of CVD-grown graphene

films transferred onto SiO_2/Si substrate at low temperature and high magnetic field, as well as at room temperature. It was aimed to take advantage of high field magneto-transport measurements to characterize the CVD graphene samples, in particular in the Quantum Hall regime which is one of the hallmarks of graphene.

6.2. Experimental Procedure

Chips were prepared using two different CVD-grown graphene samples, named B1 and B2 samples, the production and characterization details of which were discussed in Chapter 5.

P-type silicon with 300 nm SiO_2 layer, the resistivity of which is ~0.01-0.1 Ω cm, was used as a substrate. The SiO_2 layer acts as a back-gate to be able to change the carrier density in the sample when required. First, alignment marks were created on the SiO_2 (300 nm)/Si substrate (5 cm in diameter) by photolithography (Fig. 6.2(a)). Graphene transfer process from Cu foils to SiO_2 (300 nm)/Si substrate with alignment marks was carried out by following the transfer procedure described in Chapter 5, Section 5.2 (Fig. 6.2(b)). The transferred graphene films were then etched into a Hall bar by reactive ion etching (RIE) process using oxygen plasma through a photoresist (mask) which was then removed by lift-off in acetone (Fig. 6.2(c)). Then metal electrodes (10 nm of Pd and 50 nm of Au) were deposited on top of graphene through another photoresist mask using evaporation by Joule effect (Fig. 6.2(d)). After cleaning the sample in acetone, it was diced into small chips. Since the residual photoresist may remain on the samples, an annealing process was carried out in 10% H_2/90% Ar atmosphere at 350°C for 8 h.

Once the device fabrication was done, mobility estimations were performed at room temperature before and after the annealing process with a 2-probe test-head probe station to check the device's conductance as a function of the gate voltage. Then, transport measurements were performed (at the Laboratoire National des Champs Magnetiques Intenses de Toulouse (LNCMI-T) under pulsed magnetic fields to investigate the QHE in the graphene films. The longitudinal and Hall resistances were measured by using the Hall bar type electrode configuration. For QHE measurements by pulsed magnetic field, the

sample was mounted on a ceramic support with gold pads by gluing it with G.E. varnish and silver paste (Fig. 6.3(a)). This provides that the bottom of the Si substrate is connected with the back-gate contact to control the charge carrier density in graphene. Then, wedge bonding was performed to electrically address the sample using golden wires (Fig. 6.3(b)).

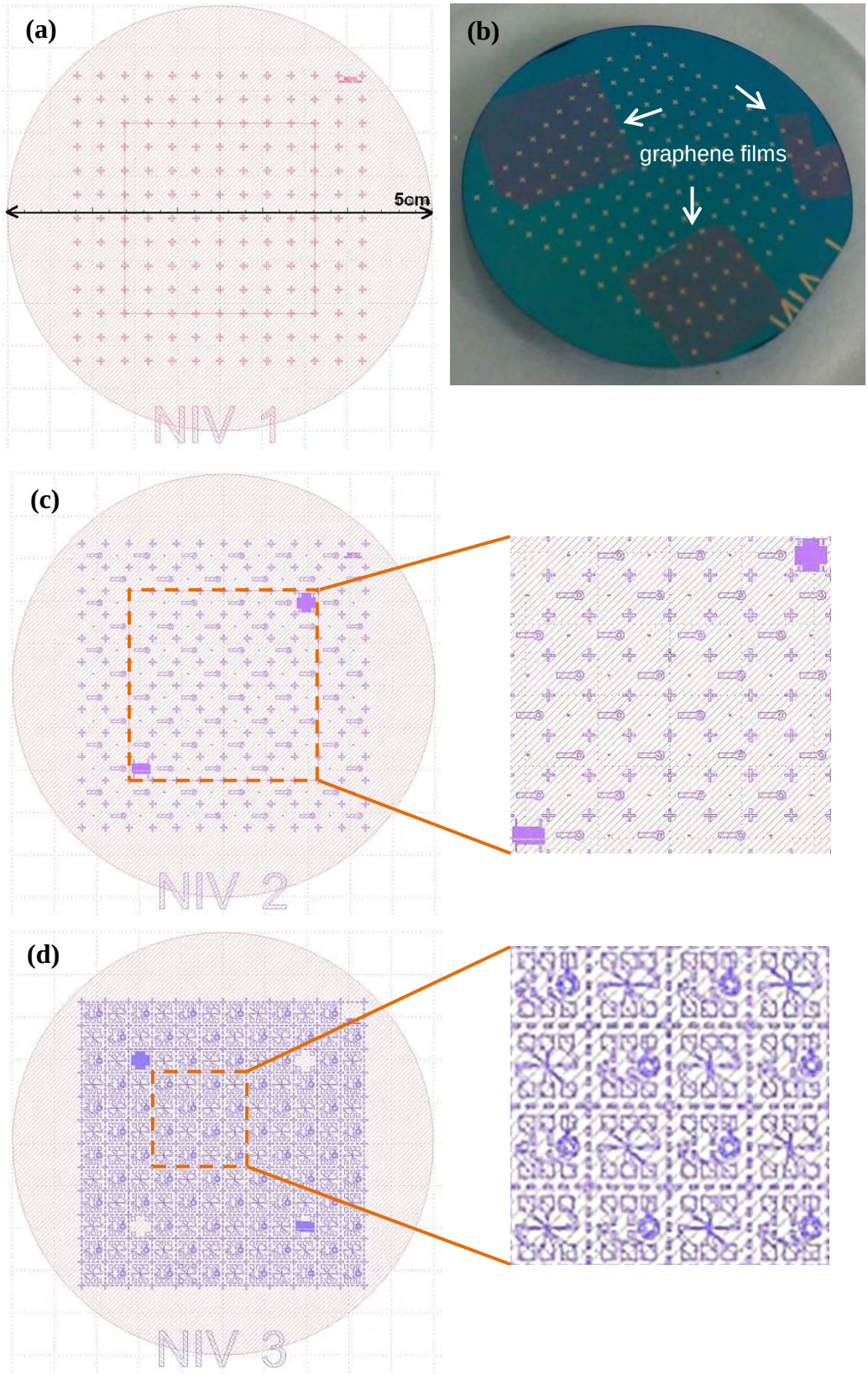

Figure 6.2. Device fabrication process. **(a)** Creating alignment marks on SiO_2/Si substrate, **(b)** Transferred CVD-grown graphene films onto the SiO_2/Si substrate, **(c)** Etching of graphene into Hall bar and **(d)** Connecting with metal electrodes.

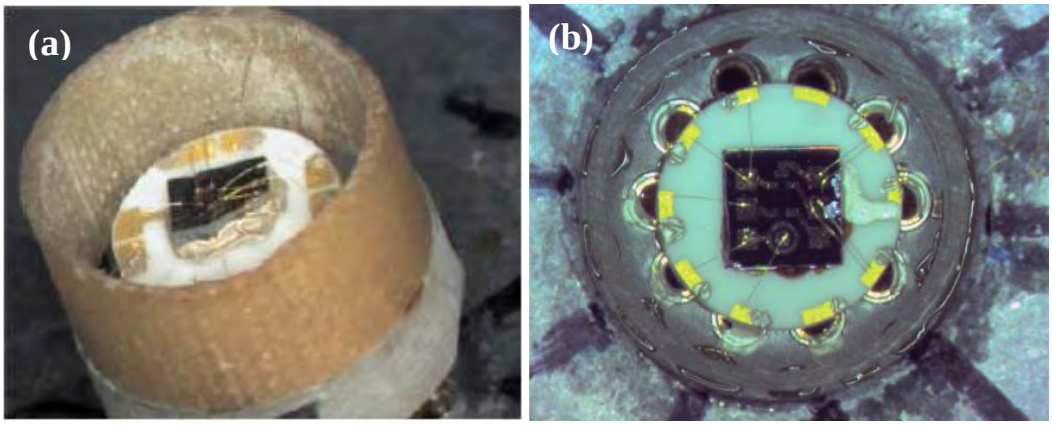

Figure 6.3. **(a)** The sample glued and electrically addressed by wedge bonding to the ceramic support for pulsed magnetic field measurements. **(b)** Top view of the sample holder (connector) with the ceramic support and the sample wedge bonded onto it.

6.3. Results and Discussion

Figure 6.4 shows the optical microscope images of the chips prepared from samples B1 and B2 revealing graphene connected into Hall bars. There are plenty of disorder/impurities on the chips, as well. These disorder/impurities could arise from the graphene synthesis and transfer processes as discussed in Chapter 5, and/or from the device fabrication process. The thickness non-uniformity of B1 sample can be even seen in the optical image (Fig. 6.4(b)).

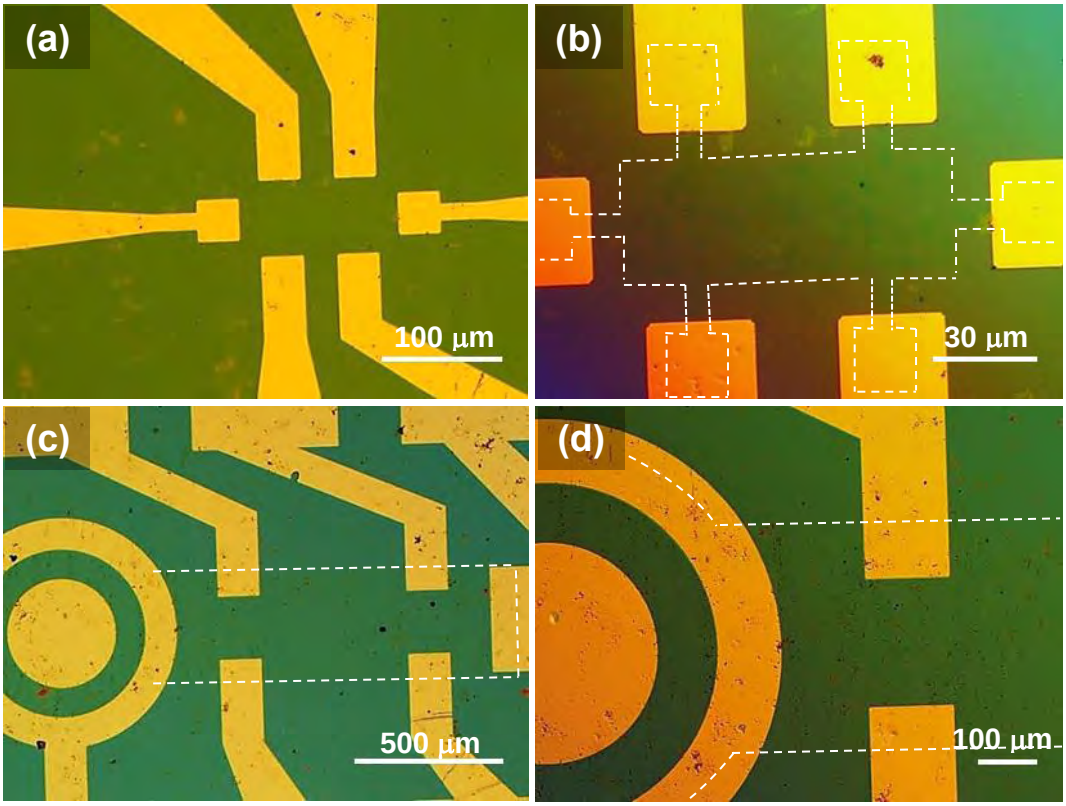

Figure 6.4. Optical microscope images of devices fabricated from **(a), (b)** Sample B1 and **(c), (d)** Sample B2. The edges of graphene were highlighted with a dashed line.

Figure 6.5 shows the resistance of the devices measured at room temperature as a function of the back-gate voltage before and after thermal annealing process. The R(Vg) characteristic of B1 sample responded to the gate voltage as shown in Fig. 6.5(a) and exhibited a resistance of the order of 6 kΩ. However, the Dirac point (the maximum resistance) is out of the experimental range and the resistance peak is quite broad, which is typical to disordered graphene with low electronic mobility. A high magnification optical microscope image reveals non-uniformity on the film and the presence of multi-layer graphene islands on the film, which could also be effective in the low mobility of this sample (Fig. 6.6). The R(Vg) characteristic was measured again just after the annealing process; however, the Dirac point was not recovered. On the other hand, the electrical characterization of the B2 sample revealed a Dirac point located at Vg = –0.1 V before annealing (Fig. 6.5(b)). This may indicate that the

sample is clean and almost free from charged impurities, which may arise from adsorbed water or molecules present in air or from fabrication process [165]. For pristine graphene Vg is expected as 0 V. The deviations from Vg = 0 V of the position of the Dirac point are linked to charged impurities located at the sample's surface or at the interface between graphene and the SiO_2 supporting layer [165]. The residual carrier density at charge neutrality point (CNP) (n_0, at the point where the resistance is maximum) and the carrier mobility (μ) was estimated by fitting the experimental data using Eqn.6.1, where n_0 and μ are the adjustable parameters [165].

$$R_{2p} = \frac{L/W}{e.\mu \times \sqrt{n_0^2 + \left[\frac{\varepsilon_0.\varepsilon_r.(V_g - V_{CNP})}{e.d}\right]^2}} + R_c \qquad \text{(Eqn. 6.1)}$$

where;

R_{2p} is resistance, L is length (was taken as 1120 μm), W is width (was taken as 350 μm), V_g = gate voltage, V_{CNP} is the back gate voltage corresponding to the system's charge neutrality point, $\varepsilon_0.\varepsilon_r$ is dielectric permittivity (3.45×10^{-11} $F.m^{-1}$ for SiO_2), d is the thickness of SiO_2 (300 nm) and R_c is the contact resistance.

Accordingly, n_0 and μ were determined as $0.03x10^{12}$ cm^{-2} and 46500 cm^2/Vs, respectively. This is a very high mobility value compared to the literature where the best mobility for SiO_2 deposited graphene is of the order of 15000 cm^2/Vs [3]. After annealing, the device characteristics of B2 sample improved so as to global resistance decreased; however, the shape of the R(Vg) curve became asymmetric and sharper. This effect can be attributed to charge injection mismatch between electron-type and hole-type quasi-particles due to the formation of Schottky barriers at the contacts or to the presence of disorder with selective scattering depending on the type of quasi-particles (electrons or holes). Table 6.1 gives a summary of the characteristics measured for the B2 sample.

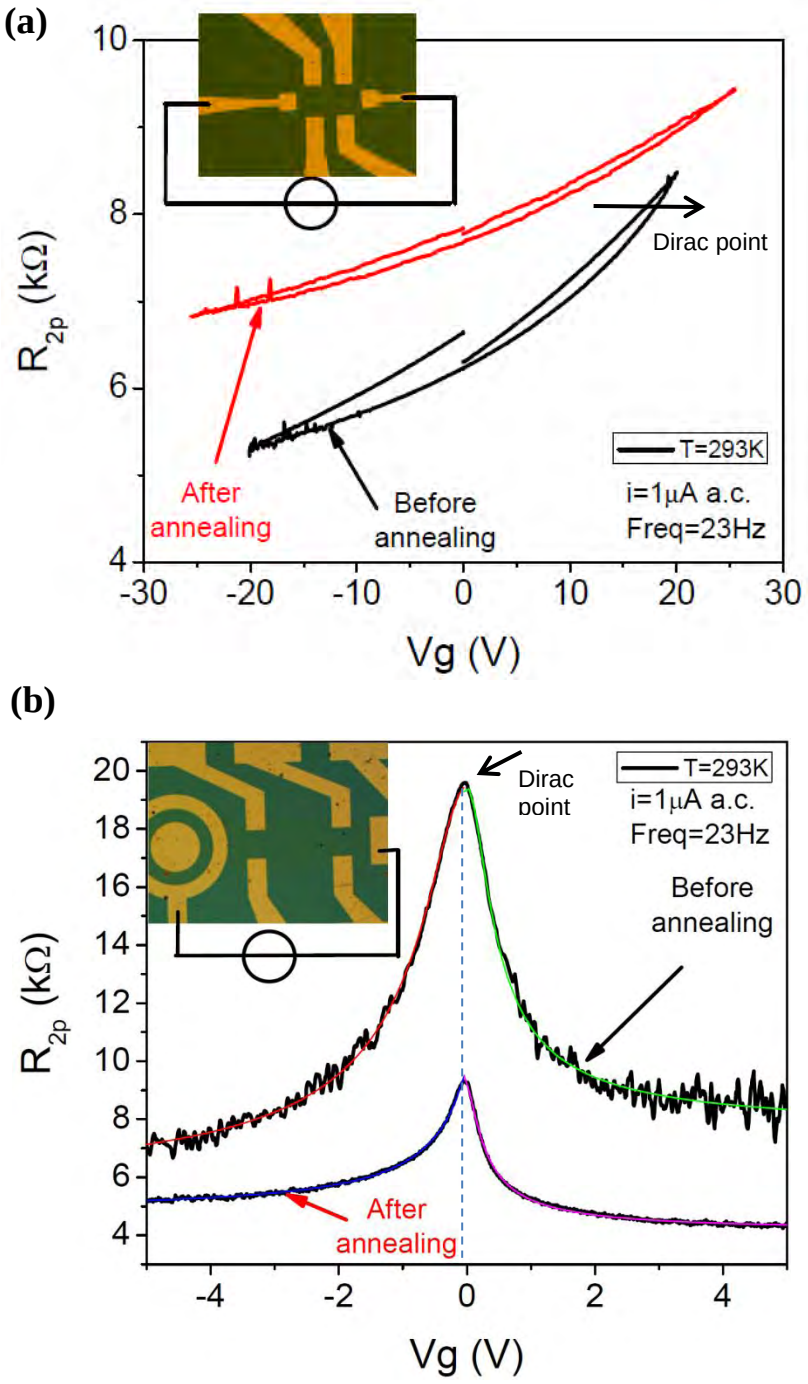

Figure 6.5. Resistance of the samples **(a)** B1 and **(b)** B2 measured at room temperature as a function of the back-gate voltage before and after thermal annealing process.

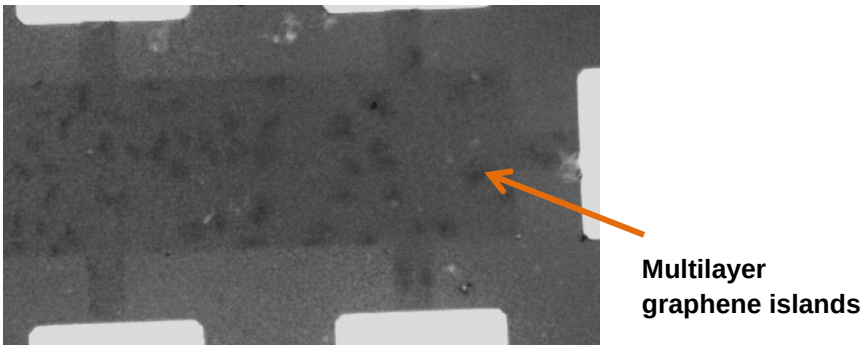

Figure 6.6. High magnification optical microscope image of B1 sample revealing multilayer graphene islands on the film.

Table 6.1. Summary of the electrical characterization of sample B2.

	Before Annealing			**After Annealing**		
	n_0 ($\times 10^{12}$ cm^{-2})	**μ (cm^2/Vs)**	**Contact (kΩ)**	**n_0 ($\times 10^{12}$ cm^{-2})**	**μ (cm^2/Vs)**	**Contact (kΩ)**
Holes	0.044	32029	5.4	0.022	112705	4.7
Electrons	0.023	73824	7.5	0.016	227149	4.11
Average	0.03	46500	6.0	N/A	N/A	N/A

n_o: residual carrier density at charge neutrality point
μ: field effect mobility

The R(V_g) characteristics of the B2 sample were measured again after mounting it onto the sample holder (chip carrier) for pulsed magnetic field measurements. Figure 6.7 reveals that the CNP is out of experimental range indicating that the sample degraded/contaminated significantly during its preparation for magnetic field experiments. Although an additional annealing process was performed in vacuum at 90°C for several days, the quality of the device could not be improved.

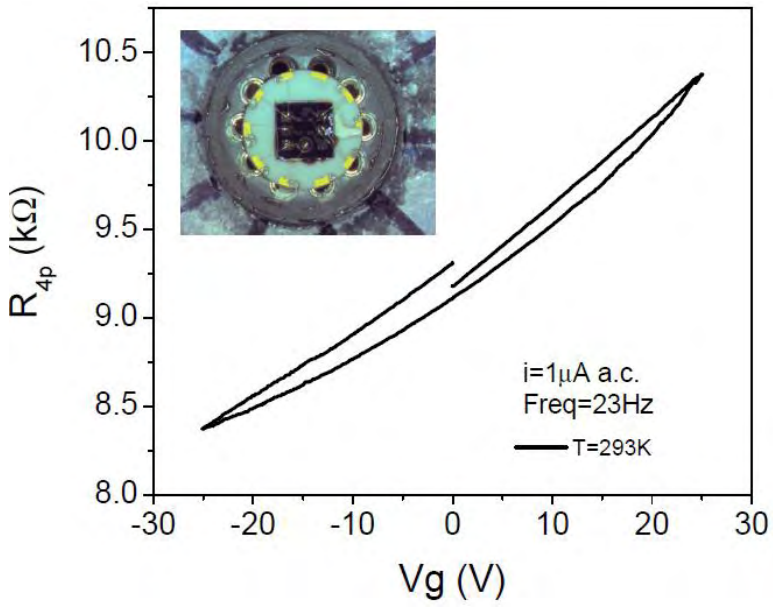

Figure 6.7. Resistance of the B2 sample measured at room temperature as a function of the back-gate voltage after mounting it onto sample holder for pulsed magnetic field measurements.

The B2 sample was then cooled down to 4.2K. The longitudinal $R_{xx}(B)$ and Hall $R_{xy}(B)$ resistances were recorded as a function of magnetic field, while the back gate voltage was held constant at V_g = 0 V (Fig.6.8). Both magneto-resistances exhibited oscillating behavior associated to the formation of Landau Level in graphene [21]. Quantum oscillations displayed by high field magneto-transport are typical for graphene, which confirms that the sample is a monolayer graphene. However, the carrier density and the electronic mobility were determined as 7.1×10^{12} cm^{-2} and 200 cm^2/Vs, respectively, indicating that the sample is highly doped. It can be clearly seen that the mobility value is much lower than that of before the processing for pulsed magnetic field measurements (~46500 cm^2/Vs). It is proposed that this mobility decrease and doping of the sample arose during mounting the sample onto sample holder. The Hall resistance is close to $R_K = h/2e^2$ at high magnetic field and R_{xx} is vanishing as expected for monolayer graphene in the Quantum Hall regime. However, the low mobility hindered observation of quantized plateaus in the Hall resistance clearly. It should

be noted that the carrier density could not be changed (only the Vg = 0 V was measured) due to failure of the back-gate.

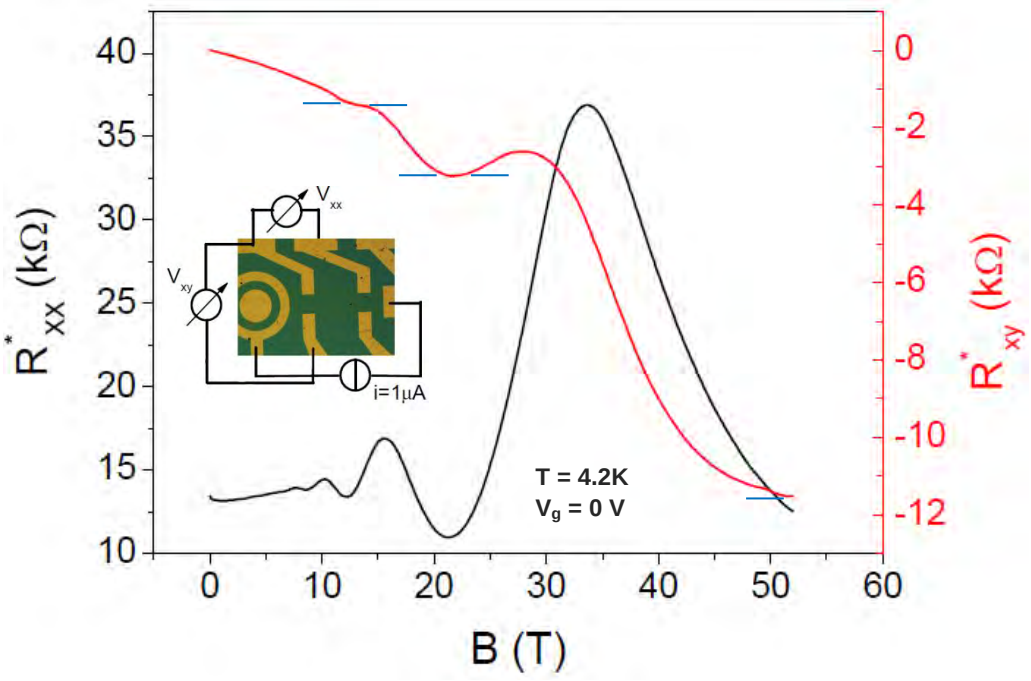

Figure 6.8. Longitudinal (R_{xx}) and Hall (R_{xy}) resistance measured as a function of magnetic field of up to 53T. The horizontal lines correspond to h/e^2v values, where the quantized plateaus are expected.

In order to fix the back-gate voltage electrode, the sample was warmed up to room temperature and the vacuum was released. After fixing, the sample was cooled down to 4.2K again. However, the sample was not re-annealed. Figure 6.9 shows the R(Vg) characteristic at 4.2K as well as the magneto-transport for three different values of back gate voltage (-30 V, +30 V and +60 V). Table 6.2 gives a summary of the calculated carrier density and electronic mobility. Due to quite high carrier density and low electronic mobility, the QHE was not well established. The sample could be polluted by air (absorption of H_2O, O_2 and N_2 molecules onto the graphene surface) when the sample was put back to air after H_2 annealing or polluted by the solvents used in the glue and/or silver past during mounting on sample holder.

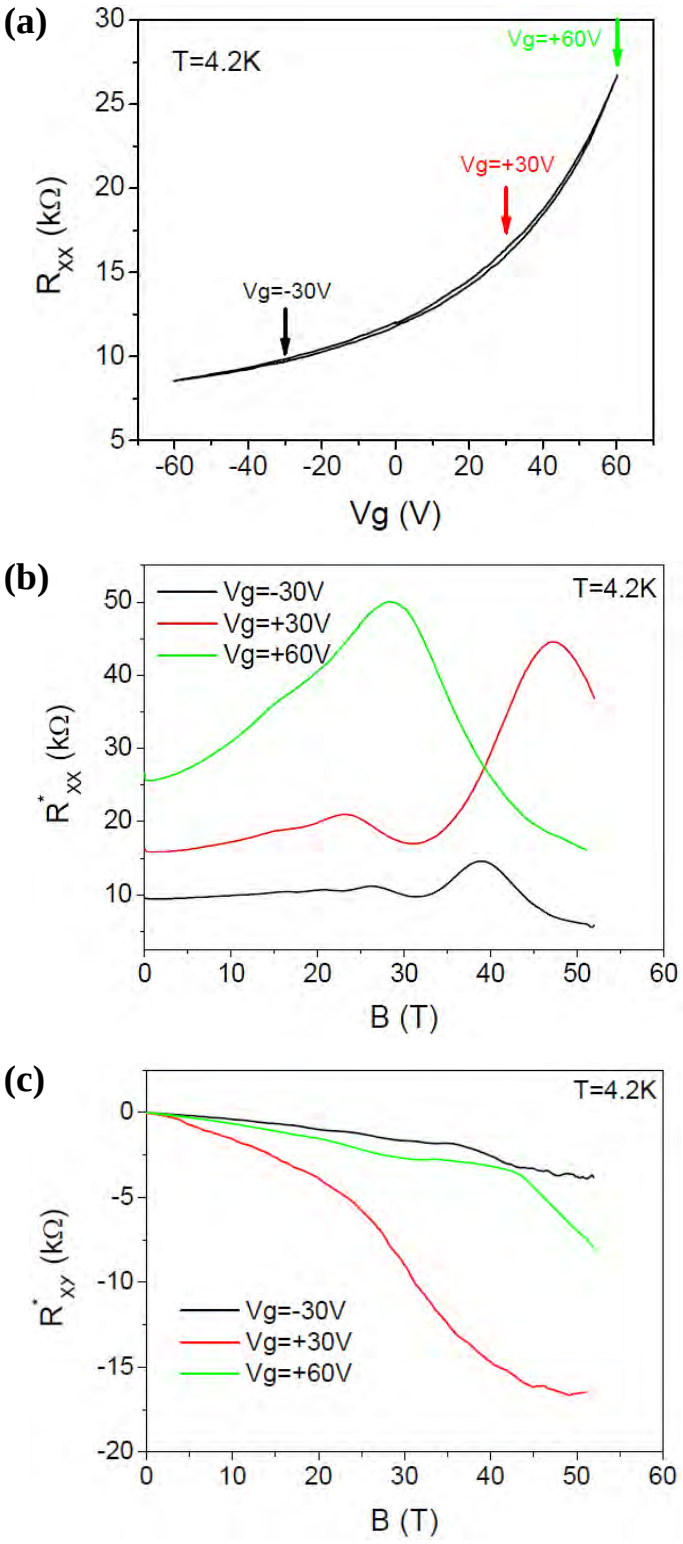

Figure 6.9. **(a)** R(Vg) characteristic of B2 sample at 4.2K after exposure to air. **(b)** Longitudinal and **(c)** Hall resistance as a function of magnetic field for three different back-gate voltage.

Table 6.2. Summary of the calculated carrier density and electronic mobility of B2 sample at 4.2K at three different back-gate voltages.

	n (cm^{-2})	**μ (cm^2/Vs)**
Vg = -30 V	1.63×10^{13}	320
Vg = +30 V	4.09×10^{12}	285
Vg = +60 V	N/A / Puddles	N/A / Puddles

n: carrier density μ: field effect mobility

6.4. Conclusions

The room temperature electrical characterization of the CVD-grown graphene films (named B1 and B2), the production and characterization details of which were discussed in Chapter 5 of this thesis, was performed. It was also aimed to take advantage of high field magneto-transport measurements to characterize the CVD graphene samples, in particular in the Quantum Hall regime which is one of the hallmarks of graphene.

The preliminary electrical characterization of these samples by two-probe measurements revealed a broad resistance peak where the Dirac point is out of the experimental range for sample B1, indicating a low mobility, while a significantly high mobility (~46500 cm^2/Vs) was estimated for the B2 sample with a Dirac point located at V_g = –0.1 V, indicating the sample is almost disorder free. High field magneto transport measurements of this sample revealed quantum oscillations typical to single layer graphene. However, the sample was damaged significantly during mounting onto the chip carrier for high magnetic field measurements. Moreover, the back gate voltage was broken during measurements. The sample was warmed up and put back to air in order to fix the back gate voltage, which could also have polluted the sample (by air molecules). Therefore, the quantum Hall effect could not be observed clearly. Further studies of high magnetic field experiments including preparation of samples without any damage are ongoing.

7. GENERAL CONCLUSIONS AND FUTURE WORK

In this thesis, graphene-based materials have been successfully produced by liquid phase exfoliation and chemical vapor deposition, which are two of the most promising graphene production methods in terms of mass production. In this way, a fundamental understanding has been developed on graphene production by using both top-down and bottom-up techniques. The critical parameters of these methods that affect the quality of the graphene-based materials, as well as their number of layers and uniformity were determined, and the graphene-based materials with required properties were prepared for the corresponding applications. CVD-grown graphene is a planar film which can be patterned precisely in combination with lithographical methods and well-suited for electronic applications, while the graphene-based materials produced by liquid phase exfoliation are more appropriate for applications where accurate positioning of the layers is not required, such as composites. Therefore, the graphene-based materials produced by liquid phase exfoliation method were incorporated into Al_2O_3 matrix to form nanocomposites which exhibit anisotropic electrical, thermal and mechanical properties, while CVD-grown graphene was used in device fabrication to measure its electrical properties and Quantum Hall Effect at high magnetic fields.

In liquid phase exfoliation studies, three different graphite-based materials, expanded graphite (EG) prepared from expandable graphite, and two different nano-graphite powders (SEFG and PA), were investigated as starting powders for an effective exfoliation process in a low boiling point solvent, isopropyl alcohol. The results have revealed that the starting material has a critical influence on the concentration, stability, quality, lateral size and number of layers of the prepared graphene-based materials. Exfoliation of EG in IPA for 90 min by tip sonication enabled production of graphene-based materials with a relatively large lateral sizes (~a few μm), very high quality (I_D/I_G <0.09) and high electrical conductivity (~3167 S/m with the corresponding sheet resistance of 7.3 kΩ/□), especially when annealed (~19200 S/m, 0.8 kΩ/□). However, graphene-based material concentration of the prepared dispersion was relatively low (~0.06 mg/ml) and it

exhibited a polydisperse character. On the other hand, nano-graphite powders provided much higher graphene-based material concentration in comparison to expanded graphite; however, with a smaller lateral size of the flakes in the form of folded and scrolled few-layer graphene sheets (3-5 layers) entangled each other and much lower electrical conductivity (~15 S/m, 808 kΩ/□ before annealing and 86 S/m, 145 kΩ/□ after annealing). Few-layer graphene dispersions ($I_D/I_G < 0.3$) with a relatively high concentration (up to 1.1 mg/ml) have been successfully prepared in IPA within 90 min of bath sonication by utilizing SEFG nano-graphite powder, which was derived from natural graphite. PA nano-graphite powder that was derived from synthetic graphite resulted in a concentration of ~0.45 mg/ml at the same conditions, although the SSA of it is ~twice that of the SEFG, indicating that the dispersibility of the nano-graphite powders decrease with increasing SSA.

As a future work of liquid phase exfoliation process, optimization studies can be performed to increase graphene concentration and to obtain graphene flakes with a more uniform thickness in EG-based dispersions, and to decrease the agglomeration level of folded and scrolled few-layer graphene sheets in SEFG-based dispersions. Moreover, with the help of understanding developed on liquid phase exfoliation process in this research, the exfoliation studies can be extended to investigate alternative dispersion routes such as milling and shear mixing, and better solvents in order to observe their effects on the yield, quality, lateral size and number of layers of the graphene-based materials.

Low-pressure CVD growth experiments of graphene films on two different Cu foils (belonging to different batches) were performed by controlling the H_2 and/or Ar flows rates during ramping in order to investigate the influence of ramping atmosphere on the impurity level, quality of the synthesized graphene films and their uniformity in terms of number of layers. It was shown that the Cu foils exhibited different characteristics in terms of the reaction that they showed against process conditions, such as ramping atmosphere, and of the amount of impurities observed after the CVD process. These differences were attributed to possible difference in oxygen impurity content of these foils; therefore, they needed separate process adjustments. Ramping atmosphere was also shown to have a strong influence on the graphene growth process. It affected not only the

nucleation of graphene, but also the type and amount of the impurities formed on the surface. H_2 and Ar/H_2 ramping resulted in appearance of spherical nanometer-sized impurities, while irregular-shaped, large (a few μm) SiO_2 impurities were observed on both foils, when there is only Ar flow during ramping.

The formation of SiO_2 impurities was attributed to the reaction of Si impurities that were already present in the Cu foils with the residual oxygen, when the ramping atmosphere contains only Ar flow. However, the mechanisms behind formation of these impurities should be better understood by further investigating the effect of other parameters such as the effect of quartz-wares in the reactor, temperature and pressure, etc., on the amount, shape and size of the impurities, as a future work. This understanding will allow production of disorder free graphene films with improved transport properties for electronic applications as a result of reduction in the amount of active sites for graphene nucleation with more than one layer and obtaining a more uniform thickness across the film surface. Different foils, such as Ni and Co, which have a relatively higher oxidation resistance than Cu, can also be utilized as an alternative catalyst to investigate and compare their performance on the amount of impurities, graphene thickness and uniformity in comparison to Cu.

APPENDIX A: RÉSUMÉ DE LA THÈSE EN FRANÇAIS

Le carbone, brique élémentaire de la vie sur Terre, est un élément unique, dont les atomes peuvent former jusqu'à quatre liaisons covalentes avec d'autres atomes, conduisant à la formation de matériaux extraordinaires. Le diamant et le graphite sont deux allotropes tridimensionnels du carbone, parmi les mieux connus, tandis que les fullerènes et les nanotubes de carbone sont des variétés à zéro et à une dimension, respectivement. Les découvertes de molécules de fullerènes en 1985 par Kroto et al. [1] puis des nanotubes de carbone en 1991 par Iijima [2] ont représenté des jalons dans le domaine de la nanotechnologie, qui ont stimulé la recherche fondamentale et les applications potentielles sur les nanomatériaux à base de carbone. La forme bidimensionnelle du carbone, le "graphène", a d'abord été obtenue et isolée en quantité suffisante par Novoselov et al. [3] en 2004 en utilisant une méthode d'exfoliation mécanique (scotch), permettant ainsi la mesure expérimentale (ceci étant déjà préalablement attendu au niveau théorique) de ses propriétés électriques uniques. Jusqu'à cette date, les matériaux 2D étaient supposés thermodynamiquement instables, d'après les calculs théoriques [4, 5]. Bien que, en 1962, Boehm et al. [6] avaient déjà rapporté l'obtention de minces feuilles de carbone par réduction de l'oxyde de graphite, il avait à cette époque été difficile expérimentalement d'isoler et d'identifier une couche de graphène unique et non fonctionnalisée. Le succès dans l'isolement et la caractérisation de graphène par Novoselov et al. [3] a ouvert la voie non seulement de l'exploration des propriétés exceptionnelles du graphène mais aussi du développement d'autres matériaux bidimensionnels [7]. Le graphène correspond à un plan d'atomes de carbone d'épaisseur atomique, disposés selon un réseau bidimensionnel en nid d'abeilles. En dépit d'une épaisseur atomique, ce matériau est le plus résistant au niveau mécanique (et thermodynamiquement stable) connu [8]. Il est un excellent conducteur électrique, avec des propriétés de transport balistique [9] et une conductivité thermique intrinsèque extrêmement élevée à température ambiante. Cette dernière est parmi les plus élevés de tous les matériaux connus, lorsque les dimensions sont suffisamment grandes, en suspension dans un liquide [10]. En raison de ces propriétés uniques, le graphène est un matériau prometteur pour de nombreuses applications telles que les

transistors à effet de champ, les électrodes transparentes, les capteurs, les systèmes de stockage d'énergie et les matériaux composites. Cependant, la production de matériaux à base de graphène de haute qualité à l'échelle industrielle est une condition préalable pour la réalisation des applications potentielles du graphène. Il existe de nombreuses méthodes pour la production de graphène. Toutefois, le nombre de couches, les dimensions latérales, la qualité et le rendement des dérivés de graphène ainsi obtenus présentent des variations considérables en fonction de la méthode de production utilisée. Par conséquent, une méthode appropriée de production du graphène doit être choisie en fonction des exigences d'une application spécifique.

Le graphène et ses dérivés sont communément produits soit par des techniques "bottom-up", telles que le dépôt chimique en phase vapeur (CVD) sur des substrats métalliques [11] et la croissance épitaxiale sur SiC [12], ou "top-down" par lesquelles des feuillets de graphène sont isolées à partir de graphite (naturel ou synthétique) par exfoliation mécanique avec du scotch [3], par d'exfoliation chimiques de l'oxyde de graphite [13] ou encore par exfoliation en phase liquide [14]. Parmi ces méthodes, l'exfoliation mécanique donne le graphène de meilleure qualité, pour autant que le graphite de meilleure qualité soit utilisé. Cependant, ce procédé présente un rendement extrêmement faible ; par conséquent, il ne peut être utilisé que pour la recherche fondamentale. Les techniques "bottom-up", en particulier la CVD, permettent quant à elles de produire des films de grande surface, avec une densité de défauts relativement faible, et sont bien adaptées pour la réalisation d'électrodes transparentes flexibles et les applications dans le domaine de l'électronique où la croissance peut être localisée précisément en combinaison avec des méthodes lithographiques. Cependant, les films de graphène CVD sont synthétisés principalement sur substrat (de cuivre) et doivent ensuite être transférés du substrat de synthèse sur des substrats diélectriques (arbitraires) en fonction des applications visées. La mobilité du graphène obtenu par synthèse CVD est limitée par les défauts et impuretés provenant à la fois du procédé de synthèse et de la technique de transfert. Par conséquent, il est nécessaire d'améliorer les propriétés de transport du graphène CVD en tout en permettant une croissance uniforme sur de grandes

surfaces. Quant à elles, les méthodes d'exfoliation chimique, par exemple l'exfoliation en phase liquide (LPE) de graphite, sont prometteuses pour la production à grande échelle et à faible coût de matériaux à base de graphène (de qualité cependant inférieure par rapport au graphène CVD). Ces méthodes permettent ainsi d'obtenir un matériau satisfaisant pour les applications dans lesquelles le positionnement exact des feuillets n'est pas nécessaire, telles que les matériaux composites, encres conductrices et stockage de l'énergie. Toutefois, l'obtention de graphène et dérivés de quelques couches seulement (□5) et de haute qualité, à grande échelle et avec des dimensions latérales raisonnables, représentent les défis majeurs de l'approche LPE.

Bien que la CVD et les méthodes LPE soient les méthodes les plus prometteuses de production de graphène en termes de qualité, d'extension à l'échelle industrielle et de coût, plusieurs défis doivent être relevés afin de rendre possible les applications potentielles du graphène et de ses dérivés. Par conséquent, les objectifs de cette thèse sont :

1. Acquérir une compréhension fondamentale des deux méthodes principales de production de graphène : l'exfoliation en phase liquide (LPE), qui est une technique top-down et le dépôt chimique en phase vapeur (CVD), qui est une technique bottom-up.
2. Déterminer les paramètres critiques de ces techniques qui influent sur la qualité, le nombre de couches, les dimensions latérales, l'homogénéité et les possibilités de production à grande échelle des matériaux à base de graphène.
3. Produire des matériaux à base de graphène ayant les propriétés requises pour des applications spécifiques comme les nanocomposites ou les dispositifs électroniques, en utilisant la méthode de production de graphène appropriée, et de montrer l'applicabilité des matériaux de graphène produites dans ces applications.

Avec ces objectifs, cette thèse a été organisée en deux parties principales et est divisée en deux parties réparties sur six chapitres :

(1) La production de matériaux à base de graphène selon la méthode LPE, leur caractérisation et enfin leur application aux nanocomposites à matrice céramique.

Le chapitre 2 présente un panorama des propriétés, méthodes de production, caractérisation et applications potentielles du graphène et de ses dérivés. Le **chapitre 3** présente les défis des méthodes LPE et présente une étude comparative dans laquelle trois poudres de graphites différents sont étudiées comme matières première dans un processus d'exfoliation mettant en œuvre un solvant de bas point d'ébullition. Une caractérisation détaillée des matériaux à base de graphène produits en fonction de leur stabilité en suspension et de leur concentration, du nombre de couches, des dimensions latérales et leur qualité est présentée, et le matériau à base de graphène le plus prometteur en termes à la fois de qualité et de quantité est déterminé. Dans le **chapitre 4**, l'application de ce matériau à base de graphène sélectionné en tant que charge (renforcement) pour la réalisation de nanocomposites à matrice Al_2O_3 est discutée. L'effet de ces nanoparticules sur les propriétés mécaniques, électriques et thermiques des nanocomposites ainsi préparés est discuté en tenant compte de l'anisotropie et étudié pour chaque propriété du matériau.

(2) La synthèse de graphène par procédé CVD, la caractérisation, l'optimisation des conditions de synthèse et l'application à des dispositifs électroniques.

Le Chapitre 5 détaille les expériences de synthèse de graphène par procédé CVD à basse pression et traite de l'influence de la nature du matériau catalytique (feuille de Cu) et de ses impuretés sur la qualité, le nombre de couches et l'uniformité des films de graphène. L'influence de la composition de l'atmosphère pendant la rampe de chauffage initiale et du pré-nettoyage du catalyseur sur la quantité et la nature des impuretés obtenues est détaillée. L'optimisation du transfert du graphène synthétisé à partir de feuilles de Cu sur des substrats diélectriques est également discutée. Le

chapitre 6 décrit la fabrication de dispositifs à partir des échantillons graphène CVD synthétisés au chapitre 5 et la caractérisation électrique de ces dispositifs (transport). Les mesures de résistance des dispositifs à la température ambiante en fonction de la tension de grille ainsi que des propriétés de transport en régime d'effet Hall quantique (EHQ) (à basse température et champ magnétique élevé) grâce à des expériences sous champ magnétique pulsé sont abordées dans ce chapitre.

Les chapitres 3-6 commencent par une revue de la littérature de la partie correspondante, suivie par les détails des procédures expérimentales, les résultats obtenus et leur discussion, et se terminent enfin par une conclusion partielle.

Dans le cadre de cette thèse en co-tutelle, la préparation des échantillons de graphène par LPE et CVD, la réalisation et la caractérisation des matériaux nanocomposites à base de graphène ont été effectuées à l'Université Anadolu, Eskisehir, Turquie. Pour les expériences de CVD et la caractérisation des échantillons préparés par cette méthode, un laboratoire incluant l'équipement de CVD ainsi qu'un Raman couplé AFM a été établi à l'Université Anadolu, Département de Science des Matériaux et d'Ingénierie, avec le soutien financier de la Commission des Projets de Recherche de l'Université Anadolu (bourse 1110F155). La caractérisation par microscopie électronique à transmission (MET) et les analyses de MET haute résolution ont été effectuées au Service Commun TEMSCAN à l'Université Paul Sabatier, Toulouse, France, avec l'aide de Lucien Datas et Pierre Lonchambon. La fabrication de dispositifs à partir des échantillons de graphène CVD a été effectuée à l'AIME (Atelier Interuniversitaire de Micro-nano Électronique) et en collaboration avec le Pr Christophe Vieu au LAAS (Laboratoire d'Analyse et d'Architecture des Systèmes) à Toulouse. Les mesures de résistance à la température ambiante et de magnéto-transport sous haut champ magnétiques des dispositifs ont été menées au Laboratoire National des Champs Magnétiques Intenses (LNCMI-Toulouse) en collaboration avec le Dr Walter Escoffier.

A.1. Production de graphène à faible nombre de feuillets (FLG) par exfoliation en phase liquide dans un solvant à bas point d'ébullition

Le graphite est facilement disponible et représente la source la moins coûteuse pour la production de matériaux à base de graphène (simple feuillet, quelques feuillets (FLG), oxyde de graphène, oxyde de graphène réduit, etc.). Le principal défi que représente la production de graphène à partir de graphite est de surmonter les forces de Van der Walls, qui maintiennent les feuillets de graphène ensemble [67]. L'exfoliation en phase liquide est un procédé prometteur pour exfolier le graphite en flocons minces dispersés sous forme de suspensions colloïdales dans des solvants, avec ou sans ajout d'agent tensio-actif [68]. Ce procédé élimine la nécessité d'utiliser un substrat. Comme il n'y a donc plus d'étape de transfert du graphène, les matériaux à base de graphène ainsi produits peuvent être facilement incorporés dans d'autres matériaux tels que des polymères, des métaux ou des céramiques pour former des nanocomposites. Le point critique dans l'exfoliation en phase liquide est d'être en mesure d'augmenter la concentration de graphène autant que possible, tout en conservant la qualité du matériau (en particulier les dimensions latérales).

L'objectif de cette étude était d'examiner trois graphites différents (graphite expansible, poudre de nano-graphite dérivé de graphite naturel (SEFG) et poudre de nano-graphite dérivé de graphite synthétique) comme matériaux de départ pour une exfoliation en phase liquide dans un solvant à bas point d'ébullition, l'alcool isopropylique (IPA), afin de produire des matériaux à base de graphène de bonne qualité à une grande échelle tout en se limitant à de relativement courtes durées de traitement par ultrasons (<120 min). Les dispersions à base de graphène préparées ont été caractérisées et comparées en fonction de leur concentration et de leur stabilité, du nombre de feuillets, de la qualité et de la conductivité électrique des matériaux à base de graphène, conduisant aux résultats suivants:

- Des suspensions de graphène de bonne qualité (I_D/I_G = 0,3) avec une concentration relativement élevée (jusqu'à 1,1 mg/ml) ont été préparées avec succès dans de l'IPA après 90 minutes au bain à ultrasons en utilisant une poudre de nano-graphite de haute surface (SEFG), dérivée de graphite naturel. Des

mesures électriques ont révélé une résistance relativement élevée (807,8 kΩ/□) et une faible conductivité électrique (15 S/m) pour un film mince (80 nm d'épaisseur) préparé à partir de cette suspension (SEFG-IPA-90min). Après recuit de ce film mince au 400°C dans une atmosphère Ar/H_2 pendant 4 h, nous avons mis en évidence une diminution de la résistance à 144,8 kΩ/□ et une valeur de conductivité de 86 S / m. Bien que cette valeur de conductivité électrique soit trop faible pour des applications en tant qu'électrodes conductrices transparentes, elle est cependant suffisante pour les applications dans des nanocomposites. La conductivité électrique relativement faible de cet échantillon peut être attribuée aux dimensions latérales limitées (D_{50}: 403 nm) des flocons, ainsi qu'aux défauts intrinsèques du matériau de départ et à la présence possible de solvant résiduel. Les analyses MET et HR-MET de cet échantillon ont mis en évidence principalement la présence de FLG de quelques feuillets (3-5), essentiellement repliés et enroulés, ainsi que de FLG bifeuillets et une très faible quantité de flocons de graphite (<10 feuillets) (Fig. A.1). Les mesures de sédimentation de cette suspension, qui présentait la plus forte concentration parmi toutes celles que nous avons préparées, a révélé une stabilité modérée avec 35% de nanoparticules toujours en suspension après 8 semaines.

- D'autre part, l'exfoliation de graphite expansible (EG) dans l'IPA avec une sonde à ultrasons pendant 90 minutes a permis la production de matériaux à base de graphène avec des dimensions latérales relativement importantes (quelques μm), de très bonne qualité structurale (I_D/I_G = 0,09) et présentant une bonne conductivité électrique (3167 S / m, la résistance du film mince correspondant étant de 7,3 kΩ/□), en particulier après recuit (19200 S/m, 0,8 kΩ/□). Cependant, la concentration en FLG de la suspension ainsi préparée est relativement faible (0,06 mg/ml) et l'échantillon présente un caractère polydispersé. L'observation au MET-HR du matériau présent dans ces suspensions a révélé la présence de graphène mono et bifeuillets, ainsi, à l'opposé, que de grandes paillettes de graphite (Fig. A.2). Les analyses par transformée de Fourier (FFT) des micrographies de MET-HR révèlent la présence de graphène turbostratique (désorienté) dans cet échantillon.

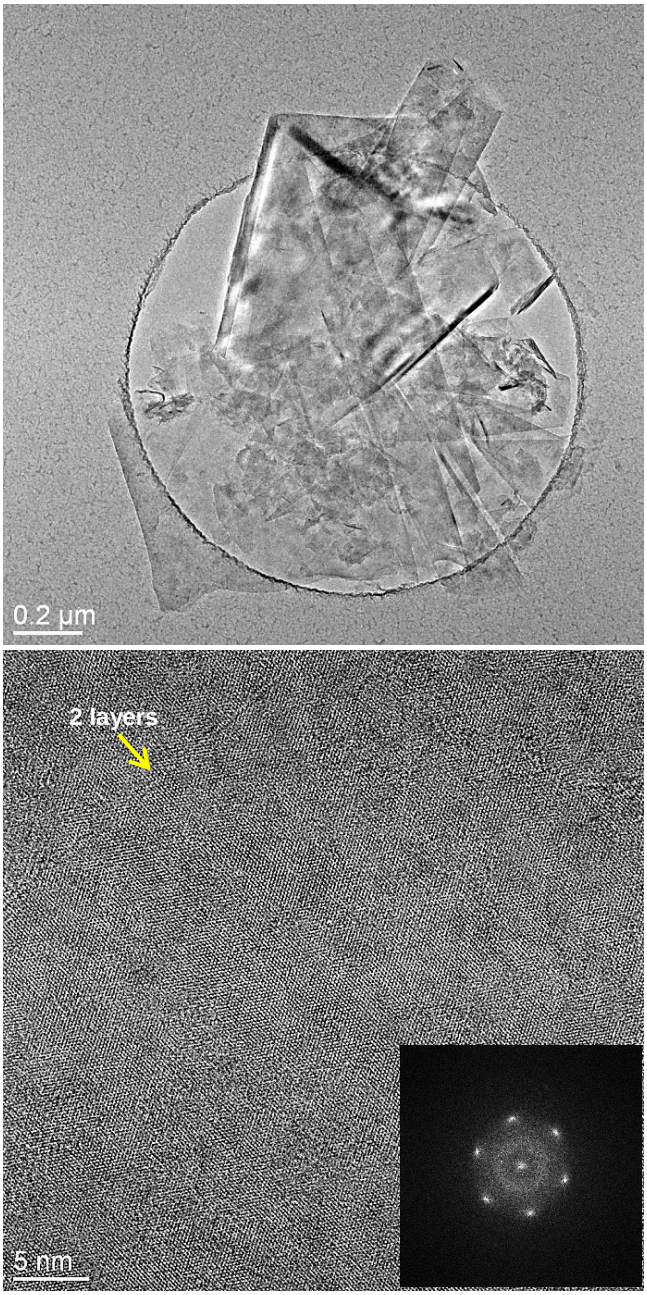

Figure A.1. (a) Image MET à faible grossissement de la poudre de nano-graphite naturel SEFG. **(b)** Image MET-HR d'un échantillon SEFG-IPA-90m montrant un graphène bifeuillets (l'encart montre la FFT correspondant à la micrographie).

L'analyse Raman a également confirmé la présence de FLG ne comportant quelques feuillets (<5), ainsi que de flocons de graphite. Des études d'optimisation pourraient être effectués comme travaux futurs afin d'augmenter la concentration et d'obtenir une meilleure uniformité en termes de nombre de feuillets.

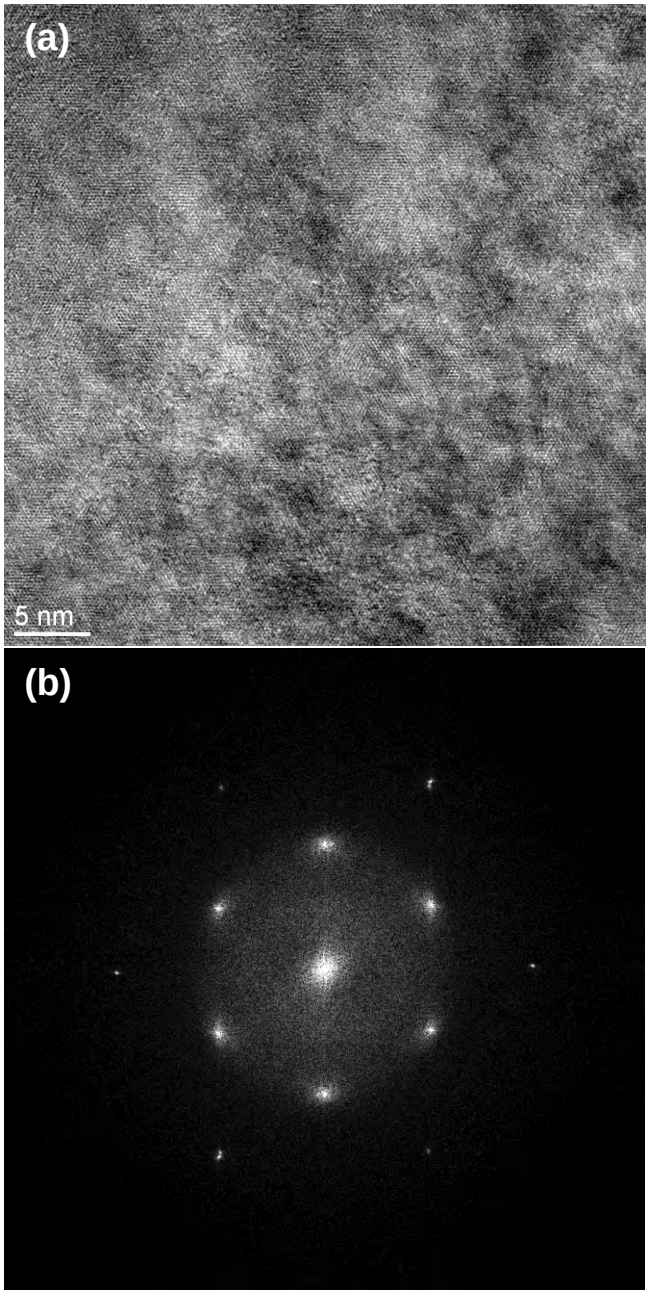

Figure A.2. (a) Image MET-HR de graphène obtenu par exfoliation de graphite expansible (EG-IPA-90min), **(b)** FFT de (a).

- Les observations au MET-HR ont révélé les structures très cristallines des matériaux à base de graphène obtenus par exfoliation des poudres EG et SEFG, mais avec une certaine non-uniformité sur la surface des paillettes. Cependant, une très forte contribution d'une phase amorphe a été observée pour l'échantillon préparé à partir de la poudre de nano-graphite d'origine synthétique (référence

PA). Bien que les suspensions préparées à partir de la poudre de PA dans l'IPA aient présenté une stabilité relativement élevée, leur concentration est beaucoup plus faible (0.45 mg/ml) que celle des suspensions préparées à partir de la poudre SEFG.

- En conséquence, la poudre SEFG s'est révélée être un matériau de départ prometteur pour la production de masse de matériaux à base de graphène à l'un d'un procédé par exfoliation en phase liquide à haut rendement, respectueux de l'environnement et a priori rentable, permettant d'obtenir des matériaux à base de graphène facilement applicables dans des domaines tels que celui des nanocomposites. Dans le chapitre 4, l'applicabilité de l'échantillon SEFG-IPA-90m pour la réalisation de nanocomposites à matrice céramique dans le but d'améliorer les propriétés mécaniques, électriques et thermiques du matériau de la matrice, a été étudiée.

A.2. Propriétés mécaniques et fonctionnelles anisotropes de nanocomposites à matrice alumine contenant du graphène

Les nanocomposites, qui présentent des propriétés mécaniques et physiques supérieures par rapport à leurs matériaux de matrice respectifs, sont parmi les matériaux les plus prometteurs pour répondre à la demande mondiale en applications de haute performance dans de nombreux domaines. À cet égard, le développement de nouveaux matériaux nanocomposites avec des propriétés améliorées joue un rôle crucial pour étendre leur utilisation dans l'industrie. Les études portant sur les nanocomposites contenant des matériaux à base de graphène ont été principalement axées sur des matrices polymères et il a été montré que d'importantes améliorations des propriétés multifonctionnelles sont possibles même à des taux de charge faibles. Les réalisations récentes et les progrès dans le domaine des nanocomposites à matrice polymère à base de graphène ont été rapportées par de nombreux auteurs [110-112]. En outre, le potentiel des charges à base de graphène dans nanocomposites à matrice céramique a été démontré au cours des dernières années. Cependant, bien que l'alumine soit l'un des matériaux les plus largement utilisés, la conductivité thermique des nanocomposites à base alumine contenant des matériaux à base de graphène n'a pas été étudiée à ce jour.

En conséquence, l'objectif de cette étude était de préparer des nanocomposites à matrice alumine en utilisant les plaquettes de graphène (GPLs) produites par exfoliation en phase liquide (chapitre 3) en tant que charge, afin d'étudier les effets de l'orientation préférentielle des GPLs dans la matrice sur les propriétés à la fois mécaniques, thermiques et électriques, et ce pour la première fois dans la littérature.

Les nanocomposites à matrice alumine contenant des GPLs, qui présentent des propriétés mécaniques, thermiques et électriques anisotropes en raison de l'orientation préférentielle de la charge carbonée dans la matrice, ont été préparés avec succès par SPS (Fig. A.3).

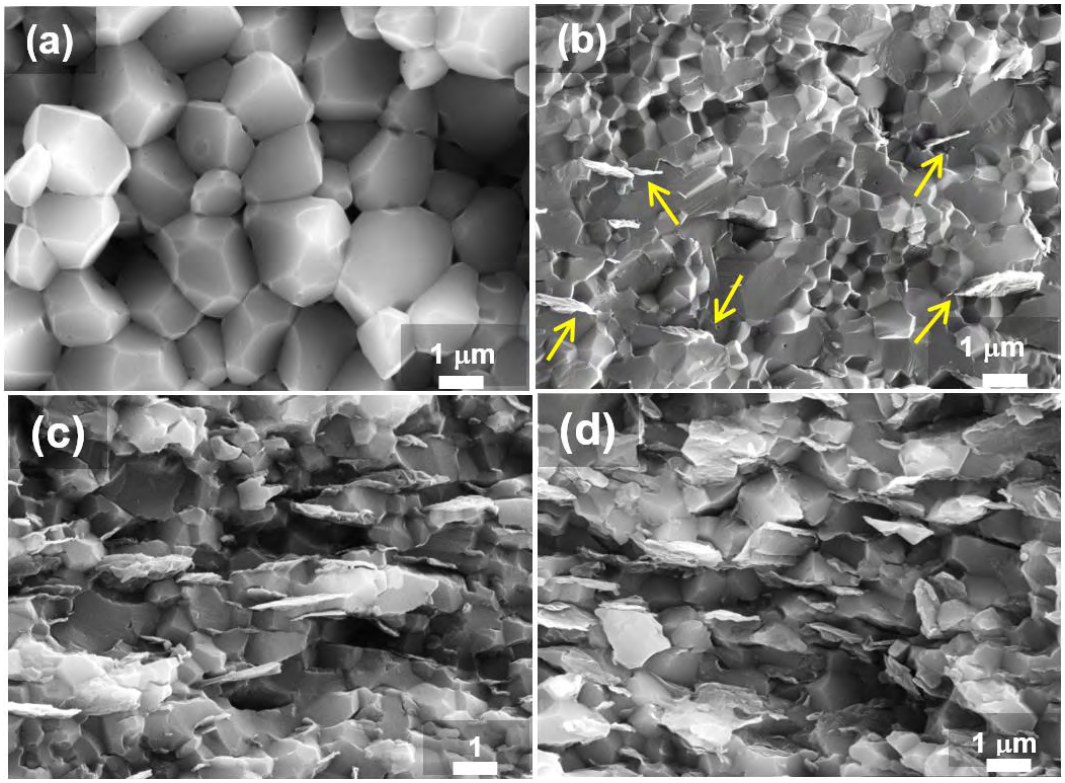

Figure A.3. Images MEB-FEG de surfaces de fracture de (a) alumine et de nanocomposites avec une teneur en GPLs de (b) 3% en vol., (c) 10% en vol. et (d) 15% en vol. Les flèches jaunes indiquent les protrusions de GPLs orientées.

L'ajout de 3% vol. de GPLs dans la matrice alumine a conduit à une augmentation de la ténacité à la rupture d'environ 27,5% dans la direction dans le plan (perpendiculaire à l'axe de pressage SPS) mais dans le même temps à une

diminution d'environ 17,7% dans la direction parallèle à l'axe de pressage SPS, ce qui s'explique par la différence de force d'interaction à l'interface entre la matrice et les GPLs (Fig. A.4). L'arrachement est le principal mécanisme de renfort dans la direction dans le plan de ce nanocomposite. L'augmentation de la teneur en GPLs conduit à diminuer la ténacité à la rupture dans le plan en raison de l'affaiblissement de l'interface à la suite de l'agglomération / chevauchement des GPLs, tout en l'augmentant dans la direction perpendiculaire du fait des mécanismes de pontage et de déviation des fissures. Aux forts taux de charge en GPLs, le fait que les fissures finissent par se rejoindre apparaît comme le mécanisme de renfort dominant, en particulier pour 15% vol., résultant en une augmentation de 9% et 33% de la ténacité à la rupture dans la direction parallèle à l'axe de pressage SPS, comparativement à la matrice alumine seule d'une part et le nanocomposite chargé à hauteur de 3% vol. de GPLs d'autre part.

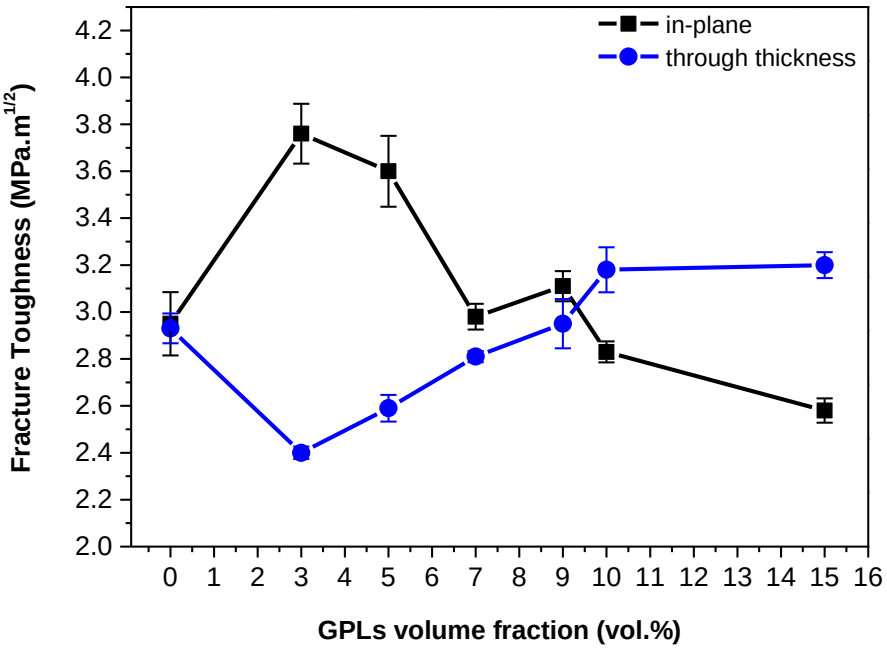

Figure A.4. Ténacité à la rupture dans le sens perpendiculaire (in plane) et parallèle (through-thickness) à l'axe de pressage SPS pour les nanocomposites alumine–GPLs en fonction de la fraction volumique en GPLs

La conductivité électrique des nanocomposites a montré une légère anisotropie avec une résistivité plus faible dans la direction dans le plan. Un seuil de percolation électrique a été observé à 7,1 et 7,5% vol. de GPLs pour les directions d'une part dans le plan et d'autre part perpendiculairement au plan (Fig. A.5). Les valeurs de conductivité électrique du nanocomposite contenant 15% vol. de GPLs sont de 20,1 S / m dans la direction du plan, et de 9,1 S / m dans la direction perpendiculaire; ce qui demeure suffisant par exemple pour un usinage de ces nanocomposites par électro-érosion.

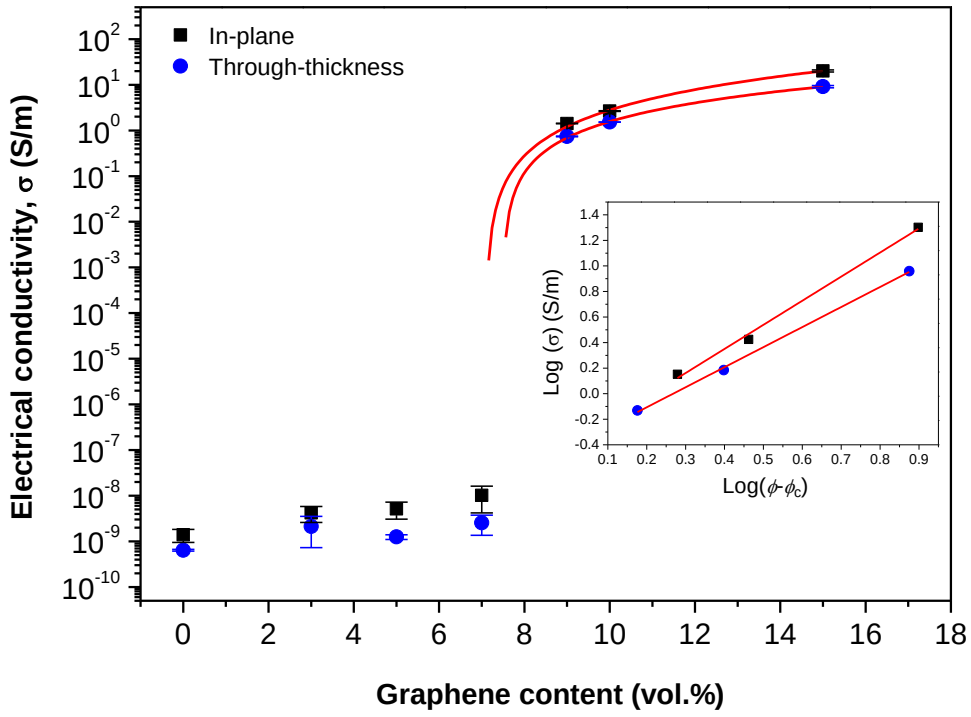

Figure A.5. Conductivité électrique à la température ambiante dans le plan et à travers l'épaisseur des nanocomposites alumine-GPLs. Les courbes pleines correspondent au fit des données par l'équation (6) proposée dans ce manuscrit. En insert, tracé en échelle log/log de la conductivité électrique en fonction de (ϕ-ϕ_c), montrant une relation linéaire (R^2 = 0,992 et 0,998 pour les directions dans le plan et à travers l'épaisseur, respectivement).

Les propriétés thermiques des nanocomposites alumine–GPLs ont été étudiés pour la première fois dans ces travaux. L'orientation des GPLs conduit à un chemin de conduction de chaleur moins résistif dans la direction dans le plan. Les valeurs de conductivité thermique des nanocomposites dans la direction dans

le plan sont supérieures à celle de l'alumine à haute température (>100°C), en particulier pour des charges élevées GPLs. L'anisotropie de la conductivité thermique augmente avec la teneur en GPLs en raison de la diminution de la conductivité thermique à travers l'épaisseur et de son augmentation conjointe dans le plan. Une augmentation de 44% de la conductivité thermique dans le plan a été obtenue à 600°C à 15% vol. de GPLs, conduisant à une augmentation de 52% du rapport $k_{plan}/k_{épaisseur}$ (Fig. A.6 (a) et (b)). Cette valeur plus élevée de la conductivité thermique dans le plan peut être bénéfique pour la dissipation de chaleur dans cette direction. L'amélioration de la conductivité thermique à température élevée peut être avantageuse pour minimiser l'accumulation de chaleur dans la matière lors de certaines applications, comme par exemple dans les outils de coupe, où le matériau est exposé à des contraintes élevées à haute température.

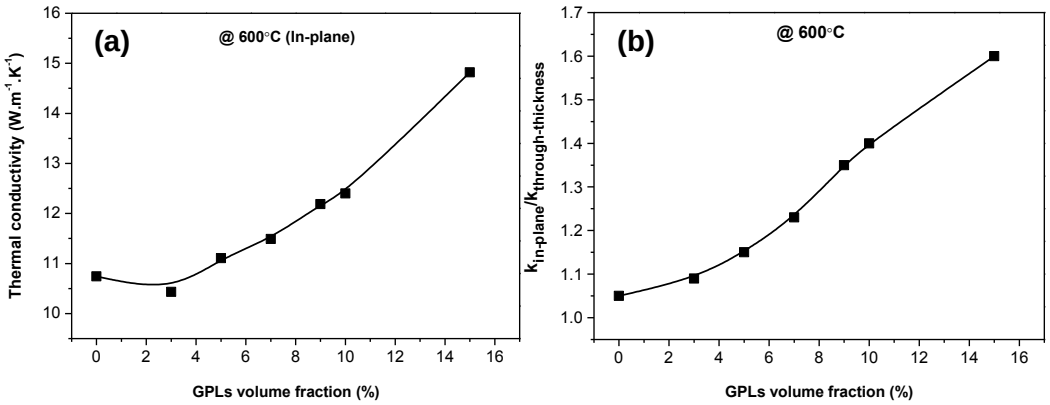

Figure A.6. **(a)** Variation de la conductivité thermique des nanocomposites alumine- GPLs à 600°C en fonction de la fraction volumique en GPLs. **(b)** Variation du rapport de conductivité thermique $k_{plan}/k_{épaisseur}$ à 600°C en fonction de la fraction volumique en GPLs.

A.3. Croissance de graphène sur cuivre par CVD basse pression

Le dépôt chimique en phase vapeur (CVD) d'hydrocarbures sur des substrats de métaux de transition est une méthode prometteuse pour la production à grande échelle de grandes surfaces de graphène avec peu de défauts, une bonne uniformité et un nombre contrôlé de feuillets. Les films de graphène synthétisés sur des surfaces métalliques peuvent être facilement transférés sur des substrats diélectriques, ce qui est bien adapté pour la réalisation d'électrodes transparentes flexibles ou encore des applications en électronique où la croissance peut être contrôlée précisément (motifs) en combinaison avec des méthodes lithographiques.

L'objectif de cette étude était de réaliser des expériences de croissance CVD basse pression de films de graphène sur deux feuilles de Cu différentes (provenant de deux lots différents) en contrôlant le flux de H_2 et/ou d'Ar pendant le traitement thermique afin d'étudier l'influence de la composition de l'atmosphère sur le niveau d'impuretés, la qualité des films de graphène synthétisés et leur uniformité en termes de nombre de feuillets. L'influence des différences de caractéristiques de feuille de Cu provenant de différents lots a été également été examinée, et différents traitements de nettoyage ont été étudiés afin de minimiser la quantité d'impuretés.

Il a été observé que l'atmosphère de traitement thermique a une forte influence sur le processus de croissance de graphène. Elle joue non seulement sur la nucléation de graphène, mais également sur le type et la quantité des impuretés formées à la surface. Des traitements sous H_2 et Ar/H_2 ont entraîné l'apparition d'impuretés sphériques de taille nanométrique, tandis que des impuretés SiO_2 de forme irrégulière et de grande taille (quelques μm) ont été observées lorsque l'Ar est utilisé seul (Fig. A.7). La formation de particules de SiO_2 a été attribuée à l'oxydation des impuretés de Si qui étaient déjà présentes dans la feuille de Cu avant le processus de CVD, du fait de la présence d'O_2 résiduel dans l'atmosphère d'Ar seul. La présence de H_2 en plus de l'Ar lors des traitements thermiques a supprimé la formation de ces grosses impuretés en réduisant la teneur en oxygène dans le système.

Des monocouches de graphène avec de faibles quantités d'îlots de graphène bifeuillets ont été synthétisées avec succès en utilisant deux feuilles de Cu différentes appartenant à même numéro de lot, mais issues de séquences différentes. Cependant, ces deux feuilles de Cu ont présenté des comportements différents vis-à-vis des conditions de procédé telles que l'atmosphère de traitement thermique ou la quantité d'impuretés. Par conséquent, il s'est avéré nécessaire d'optimiser le procédé. La différence de comportement entre ces deux feuilles de Cu a été attribuée à la différence possible dans leur teneur en impuretés oxygénées (Fig. A.8).

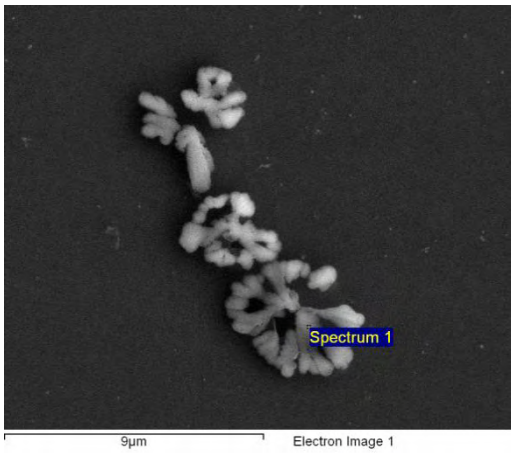

Element	Weight%	Atomic%
O K	45.72	59.65
Si K	54.28	40.35
Totals	100.00	

Figure A.7. Analyse EDX d'une particule d'impureté (particule de SiO_2) formée sur une feuille de Cu (traitement sous Ar uniquement).

Le nettoyage préalable de la feuille de Cu a permis de réduire la quantité d'impuretés. Cependant, nous avons montré que la méthode de nettoyage la plus efficace peut dépendre des caractéristiques de surface de chaque feuille de Cu utilisée.

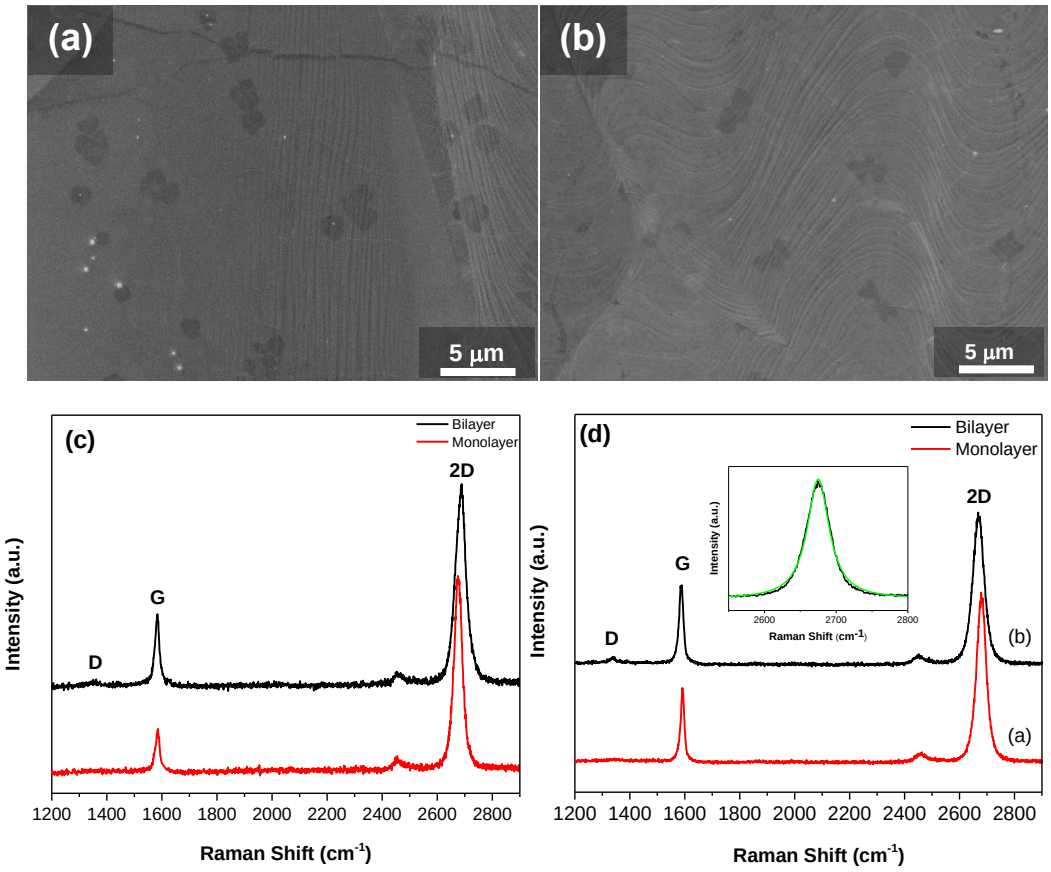

Figure A.8. Images MEB-FEG de graphène synthétisé sur les feuilles de cuivre B1 **(a)** et B2 **(b)**. La feuille B1 été nettoyée par de l'acide acétique pendant 10 minutes puis soumise à une CVD mettant en œuvre 200 sccm d'Ar seul au départ Ar puis un mélange de 100 sccm H_2/20 sccm CH_4 pendant la croissance du graphène pour une durée de 5 min et une pression de 0,5 torr pendant tout le processus. La feuille de cuivre B2 a été nettoyée par de l'acide nitrique pendant 1 min puis soumise à une CVD mettant en œuvre 200 sccm Ar/100 sccm H_2 au départ, puis 100 sccm H_2/17 sccm de CH_4 pendant la croissance du graphène, et 0,3 torr et 0,2 torr pendant les étapes de réduction puis de recuit. **(c), (d)** Spectres Raman correspondant aux échantillons montrés en (a) et (b), enregistrés à différents emplacements.

A.4. Caractérisation électrique et mesures sous champ magnétique élevé de films de graphène CVD

Le dépôt chimique en phase vapeur (CVD) est un procédé prometteur pour la production de films de graphène de haute qualité à l'échelle de wafers de silicium (ou plus). Les films de graphène CVD peuvent être transférés à partir du catalyseur métallique vers des substrats diélectriques en permettant le positionnement précis des motifs des films, pour les applications en électronique. Il a été montré que des films graphène CVD de haute qualité et uniformes présentent un effet Hall quantique (QHE) anormal à basse température et champ magnétique élevé [169]. Cependant, les caractéristiques structurales et les désordres aux échelles microscopique et macroscopique ont une forte influence sur les propriétés de transport du graphène. La mobilité du graphène CVD est limitée par le désordre provenant à la fois de la croissance et des processus de transfert. Comme discuté au chapitre 5 de cette thèse, des films de graphène de grande surface de bonne qualité ont été produits au cours de ces travaux par synthèse CVD en optimisant le processus et les conditions de transfert. L'objectif de cette étude était de réaliser la caractérisation électrique et de mesurer les propriétés de transport de ces films de graphène CVD une fois transférés sur substrat SiO2 / Si, à basse température et champ magnétique élevé, ainsi qu'à la température ambiante. Nous souhaitions profiter de mesures de magnéto-transport sous fort champ magnétique pour caractériser les échantillons de graphène CVD, en particulier dans le régime d'effet Hall quantique.

La caractérisation électrique préliminaire de ces échantillons par des mesures à deux électrodes a révélé un large pic de résistance où le point de Dirac est hors de la gamme expérimentale pour l'échantillon B1, indiquant une faible mobilité, tandis qu'une mobilité importante (46500 cm²/Vs) a été estimée pour l'échantillon préparé sur le substrat B2, avec un point situé à Dirac Vg = -100 mV, indiquant que l'échantillon est presque sans défaut (Fig. A.9). Des mesures de transport magnéto-transport de cet échantillon sous fort champ ont révélé des oscillations quantiques typiques d'un seul feuillet de graphène. Toutefois, l'échantillon a malheureusement été endommagé de façon significative au cours

de montage sur le support pour réaliser des mesures D'autres caractérisations sous champ magnétique élevé sont en cours.

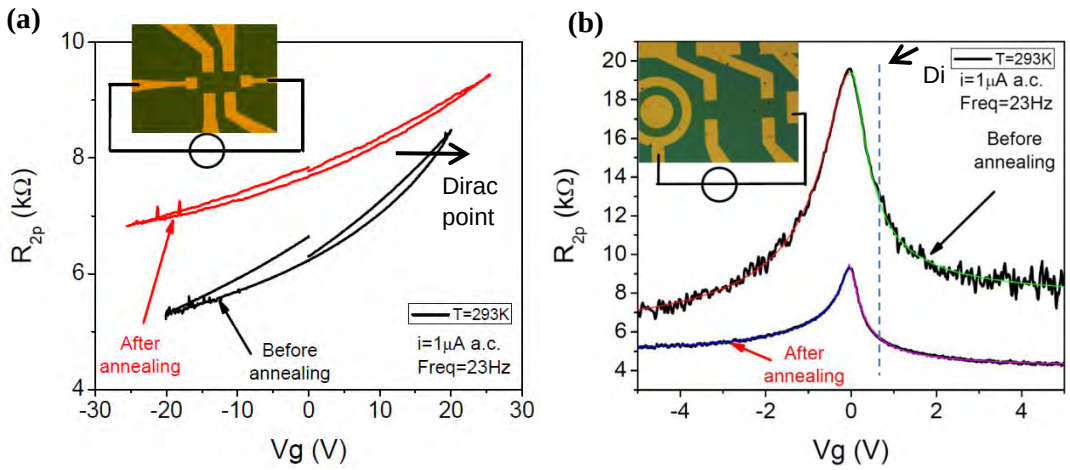

Figure A.9. Résistance des échantillons **(a)** B1 et **(b)** B2 mesurée à température ambiante en fonction de la tension de grille, avant et après le processus de recuit thermique.

REFERENCES

[1] Kroto, H. W., Heath, J. R., Obrien, S. C., Curl, R. F., and Smalley, R. E., "C-60 - Buckminsterfullerene," *Nature,* **318**, 162-163, 1985.

[2] Iijima, S., "Helical Microtubules of Graphitic Carbon," *Nature,* **354**, 56-58, 1991.

[3] Novoselov, K. S., Geim, A. K., Morozov, S. V., Jiang, D., Zhang, Y., Dubonos, S. V., *et al.*, "Electric field effect in atomically thin carbon films," *Science,* **306**, 666-669, 2004.

[4] Peierls, R. E., "Quelques proprietes typiques des corpses solides," *Ann. I. H. Poincare,* **5**, 177-222, 1935.

[5] Landau, L. D., "Zur Theorie der phasenumwandlungen II," *Phys. Z. Sowjetunion,* **11**, 26-35, 1937.

[6] Boehm, H. P., Clauss, A., Fischer, G. O., and Hofmann, U., "Das Adsorptionsverhalten sehr dünner Kohlenstoff-Folien," *Zeitschrift für anorganische und allgemeine Chemie,* **316**, 119-127, 1962.

[7] Novoselov, K. S., Jiang, D., Schedin, F., Booth, T. J., Khotkevich, V. V., Morozov, S. V., *et al.*, "Two-dimensional atomic crystals," *Proceedings of the National Academy of Sciences of the United States of America,* **102**, 10451–10453, 2005.

[8] Lee, C., Wei, X. D., Kysar, J. W., and Hone, J., "Measurement of the elastic properties and intrinsic strength of monolayer graphene," *Science,* **321**, 385-388, 2008.

[9] Geim, A. K. and Novoselov, K. S., "The rise of graphene," *Nat. Mater.,* **6**, 183-191, 2007.

[10] Balandin, A. A., Ghosh, S., Bao, W. Z., Calizo, I., Teweldebrhan, D., Miao, F., *et al.*, "Superior thermal conductivity of single-layer graphene," *Nano Lett.,* **8**, 902-907, 2008.

[11] Reina, A., Thiele, S., Jia, X., Bhaviripudi, S., Dresselhaus, M. S., Schaefer, J. A., *et al.*, "Growth of large-area single- and bi-layer graphene by controlled carbon precipitation on polycrystalline Ni surfaces," *Nano Res.,* **2**, 509-516, 2009.

[12] Hass, J., de Heer, W. A., and Conrad, E. H., "The growth and morphology of epitaxial multilayer graphene," *J Phys.-Condens. Matter*, **20**, 323202, 2008.

[13] Eda, G., Fanchini, G., and Chhowalla, M., "Large-area ultrathin films of reduced graphene oxide as a transparent and flexible electronic material," *Nat. Nanotechnol.*, **3**, 270-274, 2008.

[14] Hernandez, Y., Nicolosi, V., Lotya, M., Blighe, F. M., Sun, Z. Y., De, S., *et al.*, "High-yield production of graphene by liquid-phase exfoliation of graphite," *Nat. Nanotechnol.*, **3**, 563-568, 2008.

[15] Dubois, S. M. M., Zanolli, Z., Declerck, X., and Charlier, J. C., "Electronic properties and quantum transport in Graphene-based nanostructures," *Eur. Phys. J. B*, **72**, 1-24, 2009.

[16] Novoselov, K. S., Geim, A. K., Morozov, S. V., Jiang, D., Katsnelson, M. I., Grigorieva, I. V., *et al.*, "Two-dimensional gas of massless Dirac fermions in graphene," *Nature*, **438**, 197-200, 2005.

[17] Castro Neto, A., Guinea, F., Peres, N., Novoselov, K., and Geim, A., "The electronic properties of graphene," *Rev. Mod. Phys.*, **81**, 109-162, 2009.

[18] Mayorov, A. S., Gorbachev, R. V., Morozov, S. V., Britnell, L., Jalil, R., Ponomarenko, L. A., *et al.*, "Micrometer-scale ballistic transport in encapsulated graphene at room temperature," *Nano Lett.*, **11**, 2396-2399, 2011.

[19] Morozov, S., Novoselov, K., Katsnelson, M., Schedin, F., Elias, D., Jaszczak, J., *et al.*, "Giant intrinsic carrier mobilities in graphene and its bilayer," *Phys. Rev. Lett.*, **100**, 016602, 2008.

[20] Avouris, P. and Xia, F., "Graphene applications in electronics and photonics," *MRS Bull.*, **37**, 1225-1234, 2012.

[21] Zhang, Y., Tan, Y. W., Stormer, H. L., and Kim, P., "Experimental observation of the quantum Hall effect and Berry's phase in graphene," *Nature*, **438**, 201-204, 2005.

[22] Seol, J. H., Jo, I., Moore, A. L., Lindsay, L., Aitken, Z. H., Pettes, M. T., *et al.*, "Two-dimensional phonon transport in supported graphene," *Science*, **328**, 213-216, 2010.

[23] Balandin, A. A., "Thermal properties of graphene and nanostructured carbon materials," *Nat. Mater.,* **10**, 569-581, 2011.

[24] Nair, R. R., Blake, P., Grigorenko, A. N., Novoselov, K. S., Booth, T. J., Stauber, T., *et al.*, "Fine structure constant defines visual transparency of graphene," *Science,* **320**, 1308-1308, 2008.

[25] Peigney, A., Laurent, C., Flahaut, E., Bacsa, R. R., and Rousset, A., "Specific surface area of carbon nanotubes and bundles of carbon nanotubes," *Carbon,* **39**, 507-514, 2001.

[26] Fuhrer, M. S., Lau, C. N., and MacDonald, A. H., "Graphene: Materially better carbon," *MRS Bull.,* **35**, 289-295, 2010.

[27] McCann, E. and Fal'ko, V., "Landau-level degeneracy and Quantum Hall Effect in a graphite bilayer," *Phys. Rev. Lett.,* **96**, 086805, 2006.

[28] Partoens, B. and Peeters, F., "From graphene to graphite: Electronic structure around the K point," *Phys. Rev. B,* **74**, 075404, 2006.

[29] Castro Neto, A. H., "The carbon new age," *Mater. Today,* **13**, 12-17, 2010.

[30] Nakada, K., Fujita, M., Dresselhaus, G., and Dresselhaus, M., "Edge state in graphene ribbons: Nanometer size effect and edge shape dependence," *Phys. Rev. B,* **54**, 17954-17961, 1996.

[31] Han, M., Özyilmaz, B., Zhang, Y., and Kim, P., "Energy band-gap engineering of graphene nanoribbons," *Phys. Rev. Lett.,* **98**, 206805, 2007.

[32] Li, X. L., Wang, X. R., Zhang, L., Lee, S. W., and Dai, H. J., "Chemically derived, ultrasmooth graphene nanoribbon semiconductors," *Science,* **319**, 1229-1232, 2008.

[33] Jiao, L., Zhang, L., Wang, X., Diankov, G., and Dai, H., "Narrow graphene nanoribbons from carbon nanotubes," *Nature,* **458**, 877-880, 2009.

[34] Ryu, S., Han, M. Y., Maultzsch, J., Heinz, T. F., Kim, P., Steigerwald, M. L., *et al.*, "Reversible basal plane hydrogenation of graphene," *Nano Lett.,* **8**, 4597-4602, 2008.

[35] Sofo, J. O., Chaudhari, A. S., and Barber, G. D., "Graphane: A two-dimensional hydrocarbon," *Phys. Rev. B,* **75**, 153401, 2007.

[36] Castro, E., Novoselov, K., Morozov, S., Peres, N., dos Santos, J., Nilsson, J., *et al.*, "Biased bilayer graphene: semiconductor with a gap tunable by the electric field effect," *Phys. Rev. Lett.*, **99**, 216802, 2007.

[37] Novoselov, K. S., Fal'ko, V. I., Colombo, L., Gellert, P. R., Schwab, M. G., and Kim, K., "A roadmap for graphene," *Nature*, **490**, 192-200, 2012.

[38] Lin, Y. M., Dimitrakopoulos, C., Jenkins, K. A., Farmer, D. B., Chiu, H. Y., Grill, A., *et al.*, "100-GHz transistors from wafer-scale epitaxial graphene," *Science*, **327**, 662-662, 2010.

[39] Lyons, P. E., De, S., Blighe, F., Nicolosi, V., Pereira, L. F. C., Ferreira, M. S., *et al.*, "The relationship between network morphology and conductivity in nanotube films," *J. Appl. Phys.*, **104**, 044302, 2008.

[40] Bae, S., Kim, H., Lee, Y., Xu, X., Park, J. S., Zheng, Y., *et al.*, "Roll-to-roll production of 30-inch graphene films for transparent electrodes," *Nat. Nanotechnol.*, **5**, 574-578, 2010.

[41] Subrina, S., Kotchetkov, D., and Balandin, A. A., "Heat removal in silicon-on-insulator integrated circuits with graphene lateral heat spreaders," *IEEE Electr. Device L*, **30**, 1281-1283, 2009.

[42] Schedin, F., Geim, A. K., Morozov, S. V., Hill, E. W., Blake, P., Katsnelson, M. I., *et al.*, "Detection of individual gas molecules adsorbed on graphene," *Nat. Mater.*, **6**, 652-655, 2007.

[43] Ha, S. H., Jeong, Y. S., and Lee, Y. J., "Free standing reduced graphene oxide film cathodes for lithium ion batteries," *ACS Appl. Mater. Inter.*, **5**, 12295-12303, 2013.

[44] Yoo, E., Kim, J., Hosono, E., Zhou, H., Kudo, T., and Honma, I., "Large reversible Li storage of graphene nanosheet families for use in rechargeable lithium ion batteries," *Nano Lett.*, **8**, 2277-2282, 2008.

[45] Stoller, M. D., Park, S. J., Zhu, Y. W., An, J. H., and Ruoff, R. S., "Graphene-based ultracapacitors," *Nano Lett.*, **8**, 3498-3502, 2008.

[46] Lu, W., Soukiassian, P., and Boeckl, J., "Graphene: Fundamentals and functionalities," *MRS Bull.*, **37**, 1119-1124, 2012.

[47] Jaber-Ansari, L. and Hersam, M. C., "Solution-processed graphene materials and composites," *MRS Bull.*, **37**, 1167-1175, 2012.

[48] Brodie, B. C., "On the atomic weight of graphite," *Phil. Trans. R. Soc. Lond.*, 249-259, 1859.

[49] Hummers, W. S. and Offeman, R. E., "Preparation of graphitic oxide," *J. Am. Chem. Soc.*, **80**, 1339, 1958.

[50] Kovtyukhova, N. I., Ollivier, P. J., Martin, B. R., Mallouk, T. E., Chizhik, S. A., Buzaneva, E. V., *et al.*, "Layer-by-layer assembly of ultrathin composite films from micron-sized graphite oxide sheets and polycations," *Chem. Mater.*, **11**, 771-778, 1999.

[51] Compton, O. C. and Nguyen, S. T., "Graphene oxide, highly reduced graphene oxide, and graphene: versatile building blocks for carbon-based materials," *Small*, **6**, 711-723, 2010.

[52] Guardia, L., Fernandez-Merino, M. J., Paredes, J. I., Solis-Fernandez, P., Villar-Rodil, S., Martinez-Alonso, A., *et al.*, "High-throughput production of pristine graphene in an aqueous dispersion assisted by non-ionic surfactants," *Carbon*, **49**, 1653-1662, 2011.

[53] Bonaccorso, F. and Sun, Z., "Solution processing of graphene, topological insulators and other 2d crystals for ultrafast photonics," *Opt. Mater. Express*, **4**, 63-78, 2014.

[54] Lotya, M., King, P. J., Khan, U., De, S., and Coleman, J. N., "High-concentration, surfactant-stabilized graphene dispersions," *ACS Nano*, **4**, 3155-3162, 2010.

[55] Khan, U., O'Neill, A., Lotya, M., De, S., and Coleman, J. N., "High-concentration solvent exfoliation of graphene," *Small*, **6**, 864-871, 2010.

[56] First, P. N., de Heer, W. A., Seyller, T., Berger, C., Stroscio, J. A., and Moon, J. S., "Epitaxial graphenes on silicon carbide," *MRS Bull.*, **35**, 296-305, 2010.

[57] Forbeaux, I., Themlin, J. M., and Debever, J. M., "Heteroepitaxial graphite on 6H-SiC(0001): Interface formation through conduction-band electronic structure," *Phys. Rev. B*, **58**, 16396-16406, 1998.

[58] Berger, C., Song, Z. M., Li, T. B., Li, X. B., Ogbazghi, A. Y., Feng, R., *et al.*, "Ultrathin epitaxial graphite: 2D electron gas properties and a route

toward graphene-based nanoelectronics," *J. Phys. Chem. B,* **108**, 19912-19916, 2004.

[59] Sutter, P., "Epitaxial graphene: How silicon leaves the scene," *Nat Mater.*, **8**, 171-172, 2009.

[60] Miao, C., Zheng, C., Liang, O. and Xie, Y.-H., 2011, "Chemical vapor deposition of graphene," *Physics and applications of graphene - Experiments*, (Ed: Mikhailov, S.), InTech. Available: http://www.intechopen.com/books/physics-and-applications-of-graphene-experiments/chemical-vapor-deposition-of-graphene

[61] Zhang, Y., Gomez, L., Ishikawa, F. N., Madaria, A., Ryu, K., Wang, C. A., *et al.*, "Comparison of graphene growth on single-crystalline and polycrystalline Ni by chemical vapor deposition," *J. Phys. Chem. Lett.*, **1**, 3101-3107, 2010.

[62] Vázquez de Parga, A., Calleja, F., Borca, B., Passeggi, M., Hinarejos, J., Guinea, F., *et al.*, "Periodically rippled graphene: growth and spatially resolved electronic structure," *Phys. Rev. Lett.*, **100**, 056807, 2008.

[63] Coraux, J., T N'Diaye, A., Engler, M., Busse, C., Wall, D., Buckanie, N., *et al.*, "Growth of graphene on Ir(111)," *New J. Phys.*, **11**, 023006, 2009.

[64] Li, X., Cai, W., An, J., Kim, S., Nah, J., Yang, D., *et al.*, "Large-area synthesis of high-quality and uniform graphene films on copper foils," *Science,* **324**, 1312-1314, 2009.

[65] Taghioskoui, M., "Trends in graphene research," *Mater Today,* **12**, 34-37, 2009.

[66] Zhong, Y. L., Tian, Z., Simon, G. P., and Li, D., "Scalable production of graphene via wet chemistry: progress and challenges," *Mater Today,* **18**, 73-78, 2015.

[67] Dhakate, S. R., Chauhan, N., Sharma, S., Tawale, J., Singh, S., Sahare, P. D., *et al.*, "An approach to produce single and double layer graphene from re-exfoliation of expanded graphite," *Carbon*, **49**, 1946-1954, 2011.

[68] Khan, U., O'Neill, A., Porwal, H., May, P., Nawaz, K., and Coleman, J. N., "Size selection of dispersed, exfoliated graphene flakes by controlled centrifugation," *Carbon*, **50**, 470-475, 2012.

[69] Du, W. C., Jiang, X. Q., and Zhu, L. H., "From graphite to graphene: direct liquid-phase exfoliation of graphite to produce single- and few-layered pristine graphene," *J. Mater. Chem. A,* **1**, 10592-10606, 2013.

[70] Notley, S. M., "Highly concentrated aqueous suspensions of graphene through ultrasonic exfoliation with continuous surfactant addition," *Langmuir,* **28**, 14110-14113, 2012.

[71] Behabtu, N., Lomeda, J. R., Green, M. J., Higginbotham, A. L., Sinitskii, A., Kosynkin, D. V., *et al.*, "Spontaneous high-concentration dispersions and liquid crystals of graphene," *Nat. Nanotechnol.,* **5**, 406-411, 2010.

[72] Khan, U., Porwal, H., O'Neill, A., Nawaz, K., May, P., and Coleman, J. N., "Solvent-exfoliated graphene at extremely high concentration," *Langmuir,* **27**, 9077-9082, 2011.

[73] Catheline, A., Valles, C., Drummond, C., Ortolani, L., Morandi, V., Marcaccio, M., *et al.*, "Graphene solutions," *Chem. Commun.,* **47**, 5470-5472, 2011.

[74] O'Neill, A., Khan, U., Nirmalraj, P. N., Boland, J., and Coleman, J. N., "Graphene dispersion and exfoliation in low boiling point solvents," *J. Phys. Chem. C*, **115**, 5422-5428, 2011.

[75] Park, S., An, J. H., Piner, R. D., Jung, I., Yang, D. X., Velamakanni, A., *et al.*, "Aqueous suspension and characterization of chemically modified graphene sheets," *Chem. Mater.*, **20**, 6592-6594, 2008.

[76] Kozhemyakina, N. V., Eigler, S., Dinnebier, R. E., Inayat, A., Schwieger, W., and Hirsch, A., "Effect of the structure and morphology of natural, synthetic and post-processed graphites on their dispersibility and electronic properties," *Fuller. Nanotub. Car. N.*, **21**, 804-823, 2013.

[77] Ingle, J. D. and Crouch, S. R., *Spectrochemical Analysis*. Prentice Hall, Englewood Cliffs, NJ, 1988.

[78] Yu, A., Su, C.-C. L., Roes, I., Fan, B., and Haddon, R. C., "Gram-scale preparation of surfactant-free, carboxylic acid groups functionalized, individual single-walled carbon nanotubes in aqueous solution," *Langmuir,* **26**, 1221-1225, 2009.

[79] Available: http://www.asbury.com

[80] Chiang, C. L. and Hsu, S. W., "Synthesis, characterization and thermal properties of novel epoxy/expandable graphite composites," *Polym. Int.*, **59**, 119-126, 2010.

[81] Wang, G. X., Yang, J., Park, J., Gou, X. L., Wang, B., Liu, H., *et al.*, "Facile synthesis and characterization of graphene nanosheets," *J. Phys. Chem. C*, **112**, 8192-8195, 2008.

[82] Dresselhaus, S., Dresselhaus, G., and Eklund, P. C., *Science of fullerenes and carbon nanotubes: Their properties and applications*. Academic Press, Inc., New York, 1996.

[83] Yasmin, A., Luo, J. J., and Daniel, I. M., "Processing of expanded graphite reinforced polymer nanocomposites," *Compos. Sci. Technol.*, **66**, 1182-1189, 2006.

[84] Gu, W. T., Zhang, W., Li, X. M., Zhu, H. W., Wei, J. Q., Li, Z., *et al.*, "Graphene sheets from worm-like exfoliated graphite," *J. Mater. Chem.*, **19**, 3367-3369, 2009.

[85] Hernandez, Y., Lotya, M., Rickard, D., Bergin, S. D., and Coleman, J. N., "Measurement of multicomponent solubility parameters for graphene facilitates solvent discovery," *Langmuir*, **26**, 3208-3213, 2010.

[86] Liu, W. W., Wang, J. N., and Wang, X. X., "Charging of unfunctionalized graphene in organic solvents," *Nanoscale*, **4**, 425-428, 2012.

[87] "Zeta Potential of Colloids in Water and Waste Water," ASTM Standard D, American Society for Testing and Materials, 4187-82, 1985.

[88] Nicolosi, V., Vrbanic, D., Mrzel, A., McCauley, J., O'Flaherty, S., McGuinness, C., *et al.*, "Solubility of $Mo_6S_{4.5}I_{4.5}$ nanowires in common solvents: A sedimentation study," *J. Phys. Chem. B*, **109**, 7124-7133, 2005.

[89] Ferrari, A. C., "Raman spectroscopy of graphene and graphite: Disorder, electron-phonon coupling, doping and nonadiabatic effects," *Solid State Commun.*, **143**, 47-57, 2007.

[90] Dresselhaus, M. S., Jorio, A., Hofmann, M., Dresselhaus, G., and Saito, R., "Perspectives on Carbon Nanotubes and Graphene Raman Spectroscopy," *Nano Lett.*, **10**, 751-758, 2010.

[91] Ferrari, A. C., Meyer, J. C., Scardaci, V., Casiraghi, C., Lazzeri, M., Mauri, F., *et al.*, "Raman spectrum of graphene and graphene layers," *Phys. Rev. Lett.*, **97**, 2006.

[92] Malard, L. M., Pimenta, M. A., Dresselhaus, G., and Dresselhaus, M. S., "Raman spectroscopy in graphene," *Phys. Rep.*, **473**, 51-87, 2009.

[93] Afanasov, I. M., Shornikova, O. N., Kirilenko, D. A., Vlasov, I. I., Zhang, L., Verbeeck, J., *et al.*, "Graphite structural transformations during intercalation by HNO_3 and exfoliation," *Carbon*, **48**, 1862-1865, 2010.

[94] Yi, M., Shen, Z. G., Ma, S. L., and Zhang, X. J., "A mixed-solvent strategy for facile and green preparation of graphene by liquid-phase exfoliation of graphite," *J. Nanopart. Res.*, **14**, 1003, 2012.

[95] Zan, R., *Microscopy and spectroscopy of graphene: Atomic scale structure and interaction with foreign atom species*, PhD Thesis, University of Manchester, School of Physics and Astronomy, 2012.

[96] Wong, H. S. and Durkan, C., "Unraveling the rotational disorder of graphene layers in graphite," *Phys. Rev. B*, **81**, 045403, 2010.

[97] Zan, R., Bangert, U., Ramasse, Q., and Novoselov, K. S., "Imaging of Bernal stacked and misoriented graphene and boron nitride: experiment and simulation," *Journal of Microscopy*, **244**, 152-158, 2011.

[98] Wang, G. X., Shen, X. P., Yao, J., and Park, J., "Graphene nanosheets for enhanced lithium storage in lithium ion batteries," *Carbon*, **47**, 2049-2053, 2009.

[99] Park, S., Floresca, H. C., Suh, Y., and Kim, M. J., "Electron microscopy analyses of natural and highly oriented pyrolytic graphites and the mechanically exfoliated graphenes produced from them," *Carbon*, **48**, 797-804, 2010.

[100] Wang, Z. L., Liu, Y., and Zhang, Z., *Handbook of nanophase and nanostructured materials: Materials systems and applications II. Vol. 4*. Kluwer Academic/Plenum Publishers, 2003.

[101] Niihara, K. and Nakahira, A., "Particulate strengthened oxide ceramics-nanocomposites," In *Advanced Structural Inorganic Composites* (Ed:

Vincenzini, P.), Elsevier Scientific Publishing Co., London, 637-664, 1990.

[102] Pandey, G. and Thostenson, E. T., "Carbon nanotube-based multifunctional polymer nanocomposites," *Polym. Rev.*, **52**, 355-416, 2012.

[103] Samal, S. S. and Bal, S., "Carbon nanotube reinforced ceramic matrix composites - A review," *Journal of Minerals and Materials Characterization and Engineering (JMMCE)*, **7**, 355-370, 2008.

[104] Rul, S., Lefevre-schlick, F., Capria, E., Laurent, C., and Peigney, A., "Percolation of single-walled carbon nanotubes in ceramic matrix nanocomposites," *Acta Mater.*, **52**, 1061-1067, 2004.

[105] Flahaut, E., Peigney, A., Laurent, C., Marliere, C., Chastel, F., and Rousset, A., "Carbon nanotube-metal-oxide nanocomposites: Microstructure, electrical conductivity and mechanical properties," *Acta Mater.*, **48**, 3803-3812, 2000.

[106] Peigney, A., Laurent, C., Flahaut, E., and Rousset, A., "Carbon nanotubes in novel ceramic matrix nanocomposites," *Ceram. Int.*, **26**, 677-683, 2000.

[107] Barrau, S., Demont, P., Peigney, A., Laurent, C., and Lacabanne, C., "DC and AC conductivity of carbon nanotubes-polyepoxy composites," *Macromolecules*, **36**, 5187-5194, 2003.

[108] Fan, Y. C., Wang, L. J., Li, J. L., Li, J. Q., Sun, S. K., Chen, F., *et al.*, "Preparation and electrical properties of graphene nanosheet/Al2O3 composites," *Carbon*, **48**, 1743-1749, 2010.

[109] Porwal, H., Grasso, S., and Reece, M. J., "Review of graphene-ceramic matrix composites," *Adv. Appl. Ceram.*, **112**, 443-454, 2013.

[110] Kuilla, T., Bhadra, S., Yao, D. H., Kim, N. H., Bose, S., and Lee, J. H., "Recent advances in graphene based polymer composites," *Prog. Polym. Sci.*, **35**, 1350-1375, 2010.

[111] Potts, J. R., Dreyer, D. R., Bielawski, C. W., and Ruoff, R. S., "Graphene-based polymer nanocomposites," *Polymer*, **52**, 5-25, 2011.

[112] Das, T. K. and Prusty, S., "Graphene-based polymer composites and their applications," *Polym-Plast. Technol.*, **52**, 319-331, 2013.

[113] Kim, H. J., Lee, S. M., Oh, Y. S., Yang, Y. H., Lim, Y. S., Yoon, D. H., *et al.*, "Unoxidized graphene/alumina nanocomposite: Fracture- and wear-resistance effects of graphene on alumina matrix," *Sci. Rep.*, **4**, 5176, 2014.

[114] Malek, O., Gonzalez-Julian, J., Vleugels, J., Vanderauwera, W., Lauwers, B., and Belmonte, M., "Carbon nanofillers for machining insulating ceramics," *Mater. Today*, **14**, 496-501, 2011.

[115] Miranzo, P., Garcia, E., Ramirez, C., Gonzalez-Julian, J., Belmonte, M., and Osendi, M. I., "Anisotropic thermal conductivity of silicon nitride ceramics containing carbon nanostructures," *J. Eur. Ceram. Soc.*, **32**, 1847-1854, 2012.

[116] Walker, L. S., Marotto, V. R., Rafiee, M. A., Koratkar, N., and Corral, E. L., "Toughening in graphene ceramic composites," *ACS Nano*, **5**, 3182-3190, 2011.

[117] Wang, K., Wang, Y. F., Fan, Z. J., Yan, J., and Wei, T., "Preparation of graphene nanosheet/alumina composites by spark plasma sintering," *Mater. Res. Bull.*, **46**, 315-318, 2011.

[118] Liu, J., Yan, H. X., and Jiang, K., "Mechanical properties of graphene platelet-reinforced alumina ceramic composites," *Ceram. Int.*, **39**, 6215-6221, 2013.

[119] Liu, J., Yan, H. X., Reece, M. J., and Jiang, K., "Toughening of zirconia/alumina composites by the addition of graphene platelets," *J. Eur. Ceram. Soc.*, **32**, 4185-4193, 2012.

[120] Tapaszto, O., Kun, P., Weber, F., Gergely, G., Balazsi, K., Pfeifer, J., *et al.*, "Silicon nitride based nanocomposites produced by two different sintering methods," *Ceram. Int.*, **37**, 3457-3461, 2011.

[121] Dusza, J., Morgiel, J., Duszova, A., Kvetkova, L., Nosko, M., Kun, P., *et al.*, "Microstructure and fracture toughness of Si_3N_4 + graphene platelet composites," *J. Eur. Ceram. Soc.*, **32**, 3389-3397, 2012.

[122] Fan, Y. C., Estili, M., Igarashi, G., Jiang, W., and Kawasaki, A., "The effect of homogeneously dispersed few-layer graphene on microstructure

and mechanical properties of Al_2O_3 nanocomposites," *J. Eur. Ceram. Soc.*, **34**, 443-451, 2014.

[123] Centeno, A., Rocha, V. G., Alonso, B., Fernandez, A., Gutierrez-Gonzalez, C. F., Torrecillas, R., *et al.*, "Graphene for tough and electroconductive alumina ceramics," *J. Eur. Ceram. Soc.*, **33**, 3201-3210, 2013.

[124] Yamamoto, G., Omori, M., Hashida, T., and Kimura, H., "A novel structure for carbon nanotube reinforced alumina composites with improved mechanical properties," *Nanotechnology*, **19**, 315708, 2008.

[125] Zhan, G. D., Kuntz, J. D., Wan, J. L., and Mukherjee, A. K., "Single-wall carbon nanotubes as attractive toughening agents in alumina-based nanocomposites," *Nat. Mater.*, **2**, 38-42, 2003.

[126] Ramirez, C., Figueiredo, F. M., Miranzo, P., Poza, P., and Osendi, M. I., "Graphene nanoplatelet/silicon nitride composites with high electrical conductivity," *Carbon*, **50**, 3607-3615, 2012.

[127] Fan, Y. C., Jiang, W., and Kawasaki, A., "Highly conductive few-layer graphene/Al_2O_3 nanocomposites with tunable charge carrier type," *Adv. Funct. Mater.*, **22**, 3882-3889, 2012.

[128] Zhan, G. D., Kuntz, J. D., Garay, J. E., and Mukherjee, A. K., "Electrical properties of nanoceramics reinforced with ropes of single-walled carbon nanotubes," *Appl. Phys. Lett.*, **83**, 1228-1230, 2003.

[129] Bianco, A., Cheng, H. M., Enoki, T., Gogotsi, Y., Hurt, R. H., Koratkar, N., *et al.*, "All in the graphene family - A recommended nomenclature for two-dimensional carbon materials," *Carbon*, **65**, 1-6, 2013.

[130] Shahil, K. M. F. and Balandin, A. A., "Thermal properties of graphene and multilayer graphene: Applications in thermal interface materials," *Solid State Commun.*, **152**, 1331-1340, 2012.

[131] Evans, A. and Charles, E., "Fracture toughness determinations by indentation," *J. Am. Ceram. Soc.*, **59**, 371-372, 1976.

[132] Roine, A., *HSC Chemistry 7.0 User's Guide*. Finland, 2009.

[133] Parker, W., Jenkins, R., Butler, C., and Abbott, G., "Flash method of determining thermal diffusivity, heat capacity, and thermal conductivity," *J. Appl. Phys.*, **32**, 1679-1684, 1961.

[134] Ovid'ko, I. A. and Sheinerman, A. G., "Micromechanisms for improved fracture toughness in nanoceramics," *Rev. Adv. Mater. Sci.*, **29**, 105-125, 2011.

[135] Richerson, D., *Modern Ceramic Engineering: Properties, Processing, and Use in Design*, 2nd Ed., Marcel Dekker Inc., 1992.

[136] Quinn, G. D. and Bradt, R. C., "On the Vickers indentation fracture toughness test," *J. Am. Ceram. Soc.*, **90**, 673-680, 2007.

[137] Aguilar-Elguezabal, A. and Bocanegra-Bernal, M. H., "Fracture behaviour of alpha-Al_2O_3 ceramics reinforced with a mixture of single-wall and multi-wall carbon nanotubes," *Composites Part B-Eng.*, **60**, 463-470, 2014.

[138] Garcia, F. L., Estournes, C., Peigney, A., Weibel, A., Flahaut, E., and Laurent, C., "Spark-plasma-sintering of double-walled carbon nanotube-magnesia nanocomposites," *Scripta Mater.*, **60**, 741-744, 2009.

[139] Pisana, S., Lazzeri, M., Casiraghi, C., Novoselov, K. S., Geim, A. K., Ferrari, A. C., *et al.*, "Breakdown of the adiabatic Born-Oppenheimer approximation in graphene," *Nat. Mater.*, **6**, 198-201, 2007.

[140] Kirkpatrick, S., "Percolation and conduction," *Rev. Mod. Phys.*, **45**, 574-588, 1973.

[141] Stauffer, D. and Aharony, A., *Introduction to percolation theory*, 2nd Ed., Taylor & Francis, London, 1994.

[142] Fesenko, O. and Yatsenko, L. (Eds.), *Nanocomposites, Nanophotonics, Nanobiotechnology, and Applications*, Springer Proceedings in Physics, Vol.156, 2015.

[143] Littlejohn, S. D., *Electrical properties of graphite nanoparticles in silicone: Flexible oscillators and electromechanical sensing*, Springer Theses, 2014.

[144] Pop, E., Varshney, V., and Roy, A. K., "Thermal properties of graphene: Fundamentals and applications," *MRS Bull.*, **37**, 1273-1281, 2012.

[145] Hone, J., "Phonons and thermal properties of carbon nanotubes," In *Carbon Nanotubes* (Ed: Dresselhaus, M., Dresselhaus, G., and Avouris, P.). Vol. 80, Springer Berlin Heidelberg, 273-286, 2001.

[146] Kumari, L., Zhang, T., Du, G. H., Li, W. Z., Wang, Q. W., Datye, A., *et al.*, "Thermal properties of CNT-alumina nanocomposites," *Compos. Sci. Technol.*, **68**, 2178-2183, 2008.

[147] Zhan, G. D. and Mukherjee, A. K., "Carbon nanotube reinforced alumina-based ceramics with novel mechanical, electrical, and thermal properties," *Int. J. Appl. Ceram. Tec.*, **1**, 161-171, 2004.

[148] Ahmad, K. and Pan, W., "Electrical, mechanical, and thermal properties of multiwalled carbon nanotube reinforced alumina composites," In *Nanostructured Materials and Nanotechnology II: Ceramic Engineering and Science Proceedings, Vol. 29, Issue 8* (Ed: Mathur, S. and Singh, M.) John Wiley & Sons, Inc., Hoboken, NJ, USA, 49-59, 2008.

[149] Kapitza, P. L., *Collected papers of P.L. Kapitza* vol. II (Ed: Ter Haar, D.). Pergamon Press, Oxford, 1965.

[150] Li, X. S., Cai, W. W., Colombo, L., and Ruoff, R. S., "Evolution of graphene growth on Ni and Cu by carbon isotope labeling," *Nano Lett*, **9**, 4268-4272, 2009.

[151] Bhaviripudi, S., Jia, X. T., Dresselhaus, M. S., and Kong, J., "Role of kinetic factors in chemical vapor deposition synthesis of uniform large area graphene using copper catalyst," *Nano Lett.*, **10**, 4128-4133, 2010.

[152] Thiele, S., Reina, A., Healey, P., Kedzierski, J., Wyatt, P., Hsu, P. L., *et al.*, "Engineering polycrystalline Ni films to improve thickness uniformity of the chemical-vapor-deposition-grown graphene films," *Nanotechnology*, **21**, 015601, 2010.

[153] Gao, L. B., Ren, W. C., Zhao, J. P., Ma, L. P., Chen, Z. P., and Cheng, H. M., "Efficient growth of high-quality graphene films on Cu foils by ambient pressure chemical vapor deposition," *Appl. Phys. Lett.*, **97**, 183109, 2010.

[154] Kim, S. M., Hsu, A., Lee, Y. H., Dresselhaus, M., Palacios, T., Kim, K. K., *et al.*, "The effect of copper pre-cleaning on graphene synthesis," *Nanotechnology*, **24**, 365602, 2013.

[155] Luo, Z. Q., Yu, T., Shang, J. Z., Wang, Y. Y., Lim, S., Liu, L., *et al.*, "Large-scale synthesis of bi-layer graphene in strongly coupled stacking order," *Adv. Funct. Mater.*, **21**, 911-917, 2011.

[156] Liang, X. L., Sperling, B. A., Calizo, I., Cheng, G. J., Hacker, C. A., Zhang, Q., *et al.*, "Toward clean and crackless transfer of graphene," *ACS Nano*, **5**, 9144-9153, 2011.

[157] Costa, S. D., Righi, A., Fantini, C., Hao, Y. F., Magnuson, C., Colombo, L., *et al.*, "Resonant Raman spectroscopy of graphene grown on copper substrates," *Solid State Commun.*, **152**, 1317-1320, 2012.

[158] Jung, D. H., Kang, C., Kim, M., Cheong, H., Lee, H., and Lee, J. S., "Effects of hydrogen partial pressure in the annealing process on graphene growth," *J. Phys. Chem. C*, **118**, 3574-3580, 2014.

[159] Hao, Y. F., Bharathi, M. S., Wang, L., Liu, Y. Y., Chen, H., Nie, S., *et al.*, "The role of surface oxygen in the growth of large single-crystal graphene on copper," *Science*, **342**, 720-723, 2013.

[160] Ellingham, H. J. T., "Reproducibility of oxides and sulphides in metallurgical processes," *J. Soc. Chem. Ind.*, **63**, 125-133, 1944.

[161] Zhu, Y. F., Mimura, K., Ishikawa, Y., and Isshiki, M., "Effect of floating zone refining under reduced hydrogen pressure on copper purification," *Mater. Trans.*, **43**, 2802-2807, 2002.

[162] Lim, J. W., Kim, M. S., Munirathnam, N. R., Le, M. T., Uchikoshi, M., Mimura, K., *et al.*, "Effect of Ar/Ar-H_2 plasma arc melting on Cu purification," *Mater. Trans.*, **49**, 1826-1829, 2008.

[163] Available: http://www.doitpoms.ac.uk/tlplib/ellingham_diagrams/printall.php

[164] Vlassiouk, I., Fulvio, P., Meyer, H., Lavrik, N., Dai, S., Datskos, P., *et al.*, "Large scale atmospheric pressure chemical vapor deposition of graphene," *Carbon*, **54**, 58-67, 2013.

[165] Escoffier, W., Poumirol, J., Amado, M., Rossella, F., Kumar, A., Diez, E., *et al.*, "High field quantum Hall effect in disordered graphene near the Dirac point," In *GraphITA 2011, Carbon Nanostructures* (Ottaviano, L. and Morandi, V., Ed), Springer, Verlag Berlin Heidelberg, 61-73, 2012.

[166] Schopfer, F. and Poirier, W., "Graphene-based quantum Hall effect metrology," *MRS Bull.*, **37**, 1255-1264, 2012.

[167] Novoselov, K. S., McCann, E., Morozov, S. V., Fal'ko, V. I., Katsnelson, M. I., Zeitler, U., *et al.*, "Unconventional quantum Hall effect and Berry's phase of 2 pi in bilayer graphene," *Nat. Phys.*, **2**, 177-180, 2006.

[168] Orlita, M., Escoffier, W., Plochocka, P., Raquet, B., and Zeitler, U., "Graphene in high magnetic fields," *Comptes Rendus Physique*, **14**, 78-93, 2013.

[169] Cao, H. L., Yu, Q. K., Jauregui, L. A., Tian, J., Wu, W., Liu, Z., *et al.*, "Electronic transport in chemical vapor deposited graphene synthesized on Cu: quantum Hall effect and weak localization," *Appl. Phys. Lett.*, **96**, 2010.